Multi-Modal Microstructural Imaging of Brain White Matter

Andersson, Mariam

Publication date:
2021

Document Version
Publisher's PDF, also known as Version of record

Link back to DTU Orbit

Citation (APA):
Andersson, M. (2021). *Multi-Modal Microstructural Imaging of Brain White Matter*. Technical University of Denmark.

Multi-Modal Microstructural Imaging of Brain White Matter

Mariam Andersson

Kongens Lyngby 2021

Technical University of Denmark
Department of Applied Mathematics and Computer Science
Richard Petersens Plads, building 324,
2800 Kongens Lyngby, Denmark
Phone +45 4525 3031
compute@compute.dtu.dk
www.compute.dtu.dk

Summary (English)

The diameters of axons, the communication cables of the brain, determine the conduction velocity at which signals are communicated within the brain network. Some neurodegenerative diseases manifest as damage to axons of a particular size, and axon diameter is thus an indicator of brain health and a potential biomarker of disease. Diffusion magnetic resonance imaging (MRI) methods can non-invasively provide estimates of axon diameter in the living brain, but many rely on the assumption that axons can be described as cylindrical.

Imaging white matter regions of the vervet monkey brain with synchrotron X-Ray Nano-Holotomography reveals how blood vessels, cell clusters and vacuoles modulate the three-dimensional morphologies of axons. The findings challenge current knowledge of the signal conduction process in axons and shed light on the validity of enforcing a cylindrical axon shape in biophysical models.

Axonal connections could be traced with structure tensor tractography on X-ray nanotomography images of healthy and diseased tissue from the mouse brain, providing a characterisation of the macroscopic organisation of axonal bundles. Experiments using x-ray nanotomography on the hydrated genu of the vervet monkey brain revealed features that were difficult to distinguish in samples treated with conventional sample processing techniques involving dehydration, indicating a need to image the hydrated white matter environment.

Lastly, powder average approaches to axon diameter estimation with diffusion MRI were validated using segmented axons from a crossing fibre and splenium region of the vervet monkey brain. Even in extremely complex white matter architectures, accurate estimates of axon diameter could be obtained for different sequence parameters and diffusion times. At sufficiently low b-values, the acquisition was sensitive to axonal microdispersion and the intra-axonal parallel diffusivity showed time dependence, which could be an interesting biomarker of white matter health and pathology. Ultimately, the signal-to-noise ratio determined the range of measurable axon diameter.

Summary (Danish)

Diameteren af aksoner, hjernens kommunikationskabler, afgør ledningshastigheden for signaler, der kommunikeres inden for hjernenetværket. Flere neurodegenerative sygdomme manifesteres som skader på aksoner af en specifik størrelse, og aksondiameter er dermed en indikator for hjernesundhed og en potentiel biomarkør for sygdom. Metoder baseret på diffusionsvægtet magnetisk resonans billeddannelse (MRI) kan på ikke-invasiv vis bidrage med estimater af aksondiametre i den levende hjerne, men mange afhænger af antagelsen om, at aksoner kan beskrives som cylindere.

Billeddannelse af regioner af hvid substans fra en abehjerne med synkroton-røntgen-nano-holotomografi afslører, hvordan blodårer, celleklynger, og vakuoler modulerer den tredimensionelle aksonmorfologi. Fundene udfordrer den etablerede viden om signaltransmissionsprocesserne i aksoner, og kaster lys over, hvorvidt det i biofysiske modeller kan antages at aksoner er cylindriske.

Aksonale forbindelser kunne spores med strukturtensortraktografi af røntgen-nanotomografi-billeder af raskt og patologisk væv fra mussehjernen, hvilket bidrager til karakterisering af den makroskopiske organisering af aksonbundter. Eksperimenter med røntgen-nanotomografi af den hydrerede genu fra en abehjerne afslørede egenskaber, som var svære at adskille i prøver behandlet med konventionel processeringsteknik, som er betinget af dehydrering. Dette indikerer et behov for at udføre billeddannelse af det hydrerede hvid-substans-miljø.

Afsluttende, pulvergennemsnitstilgange til estimering af aksondiametre i diffusionsvægtet MRI blev valideret ved brug af segmenterede aksoner fra den krydsende fiber, og regioner fra splenium fra en abehjerne. Selv i ekstremt komplekse hvid substans-strukturer kan nøjagtige estimater af aksondiametre opnås for forskellige sekvensparametrer og diffusionstider. Ved tilstrækkeligt lave b-værdier var målingen følsom overfor aksonal mikrodispersion, og den intra-aksonale parallelle diffusivitet viste tidsafhængighed, hvilket kunne være en interessant biomarkør for sundhed og patologi i hvid substans. Endeligt, afgjorde signal-støj-forholdet intervallet af målbare aksondiametre.

Preface

This thesis was prepared in partial fulfilment of the requirements for the *Doctor of Philosophy degree* (Ph.D) at the Department of Applied Mathematics and Computer Science of the Technical University of Denmark (DTU Compute) and the Danish Research Centre for Magnetic Resonance (DRCMR), Copenhagen University Hospital Hvidovre. The research presented in this thesis was carried out from October 2017 to February 2021.

The project was carried out under the primary supervision of Associate Professor Tim B. Dyrby from DTU Compute and DRCMR, and was co-supervised by Associate Professor Vedrana Andersen Dahl from DTU Compute, Associate Professor Martin Bech from the Division of Medical Radiation Physics at Lund University and Senior Researcher Henrik Lundell from DRCMR. Funding was provided partly ($\frac{2}{3}$) from the Capital Region Research Foundation Grant to Tim B. Dyrby (grant number A5657), and partly ($\frac{1}{3}$) by DTU Compute.

This thesis aims to explore and analyse the three-dimensional microstructure of the brain white matter in order to improve diffusion magnetic resonance imaging methods of measuring axon diameter.

Lyngby, 15-February-2021

Mariam Andersson

Acknowledgements

First and foremost, I would like to thank my main supervisor, Tim B. Dyrby. Thank you for your patience, guidance and for forming such a creative learning environment. Your enthusiasm is as contagious as it is convincing. I have absolutely loved these past years, and am so grateful for the opportunities you have put in front of me.

Secondly, I would like to thank my co-supervisors Vedrana Andersen Dahl, Martin Bech and Henrik Lundell. How lucky I have been to have supervisors from different fields to turn to when in doubt! Thank you for all your advice and support, ranging from image analysis, to synchrotron imaging to diffusion MRI.

Hans Martin Kjer, postdoctoral researcher on the same project with a flair for stunning visualisations and an eagle eye for errors. Thank you for sharing so much of your knowledge and so many of your coffee breaks with me. Working together been a lovely journey. Thank you also to Christian Skoven, with whom it has been a pleasure to share an office at DRCMR.

Thank you to my colleagues at DRCMR, especially the Microstructure and Plasticity group, for such a wonderful environment – always with lots of cake! An equally big thank you goes to all my colleagues from the Image Analysis and Computer Graphics section at DTU Compute. It has been great to spend time at two such different institutions.

A thank you also goes to Jean-Philippe Thiran for welcoming me to his group, the LTS5 Signal Processing Laboratory, at EPFL. My time in Switzerland has a special place in my heart, and many thanks go to the entire LTS5 group who made me feel at home from the very beginning with their hospitality and friendship. To Giorgio Innocenti, I am so grateful for the opportunity I received to get to know you and learn from you. A special thank you also goes to Jonathan Rafael-Patino for hours and hours of ideas and discussions that have stretched far beyond my time in Lausanne. Marco Pizzolato, I am so happy to have met you in Lausanne and to have later had the chance to work with you

in Copenhagen. It is always fun to discuss with you.

The project would not have been possible without the involvement of Bente Pakkenberg and the Research Laboratory for Stereology and Neuroscience at Bispebjerg Hospital. Thank you especially to Susanne Sørensen, for helping with all of the sample processing; I am sorry for all of the teeny tiny tissue samples! Thanks are in order to Tim Salditt and his group in helping to plan, prepare and execute the synchrotron experiments at P10 of DESY, and to Alexandra Pacureanu for experiments at beamline ID16A of ESRF.

A huge thank you goes to all of my wonderful friends and family for their encouragement during these years.

To my parents, Zahra and Lars, and my brother, David. You are my pillars. Your unconditional support, love and belief in me means the world.

Lastly, Simon – my very best friend, partner in crime, my polar opposite and my kindred spirit. Thank you for bringing laughter and magic into my life every single day, come rain, shine or raging global pandemic.

Contributions

Contributions Included in Thesis

Contribution I:

Mariam Andersson, Hans Martin Kjer, Jonathan Rafael-Patino, Alexandra Pacureanu, Bente Pakkenberg, Jean-Philippe Thiran, Maurice Ptito, Martin Bech, Anders Bjorholm Dahl, Vedrana Andersen Dahl, Tim B. Dyrby. *Axon morphology is modulated by the local environment and impacts the noninvasive investigation of its structure–function relationship.* Proceedings of the National Academy of Sciences of the United States of America 117 (52) 33649-33659 (2020); DOI: 10.1073/pnas.2012533117

Contribution II:

Mariam Andersson, Marco Pizzolato, Hans Martin Kjer, Henrik Lundell, Tim B. Dyrby. *Does powder averaging remove dispersion bias in diameter estimates within realistic axonal architectures?* (In preparation).

Contribution III:

Hans Martin Kjer, Mariam Andersson, Yi He, Marie Louise Elkjaer, Alexandra Pacureanu, Zsolt Illes, Bente Pakkenberg, Anders Bjorholm Dahl, Vedrana Andersen Dahl, Tim B. Dyrby. *Streamline tractography for 3D mapping of axon bundle organization in one MRI voxel using ultra-high resolution synchrotron radiation imaging* in Proceedings of the 2020 ISMRM & SMRT Virtual Conference & Exhibition.

Other Contributions by Author

Niccolò Peruzzi, Béla Veress, Lars B. Dahlin, Tim Salditt, Mariam Andersson, Marina Eckermann, Jasper Frohn, Anna-Lena Robisch, Martin Bech & Bodil Ohlsson (2020) *3D analysis of the myenteric plexus of the human bowel by X-ray phase-contrast tomography – a future method?*, Scandinavian Journal of Gastroenterology, 55:10, 1261-1267, DOI: 10.1080/00365521.2020.1815079

Sidsel Winther, Henrik Lundell, Mariam Andersson, Tim Dyrby. *Orientation-dependent biases in powder averaging caused by inhomogeneous distributions of magnetic susceptibility in white matter* in Proceedings of the 2020 ISMRM & SMRT Virtual Conference & Exhibition.

Mariam Andersson, Jonathan Rafael-Patino, Hans Martin Kjer, Vedrana Andersen Dahl, Alexandra Pacureanu, Martin Bech, Anders Bjorholm Dahl, Jean-Philippe Thiran, Tim B. Dyrby. *The impact of axon orientation dispersion and 3D diameter variations on the transverse apparent diffusion coefficient* in Proceedings of the 2020 ISMRM & SMRT Virtual Conference & Exhibition.

Jonathan Rafael-Patino, Thomas Yu, Mariam Andersson, Hans Martin Kjer, Vedrana Andersen Dahl, Alexandra Pacureanu, Anders Bjorholm Dahl, Tim B. Dyrby, Jean-Philippe Thiran. *Phantoms for Diffusion Simulations: Multi-Objective Differential Evolution for Realistic Numerical (MODERN) Phantoms* in Proceedings of the ISMRM 27th Annual Meeting & Exhibition, 2019.

Mariam Andersson, Hans Martin Kjer, Jonathan Rafael-Patino, Vedrana Andersen Dahl, Alexandra Pacureanu, Jean-Philippe Thiran, Martin Bech, Anders Bjorholm Dahl, Tim B. Dyrby. *Uncovering 3D Axonal Morphologies with Synchrotron Imaging: Impact on Microstructure Imaging with Diffusion MRI* in Proceedings of the ISMRM 27th Annual Meeting & Exhibition, 2019.

Mariam Andersson, Hans Martin Kjer, Vedrana Andersen Dahl, Martin Bech, Alexandra Pacureanu, Anders Bjorholm Dahl, Tim B. Dyrby. *Using X-Ray Imaging to Visualise the 3D Architecture of White Matter* in Proceedings of the 69th Annual Conference of the Nordic Microscopy Society, 2018.

Abbreviations

Abbreviations

ADC Apparent Diffusion Coefficient.
ADD Axon Diameter Distribution.
AP Action Potential.

CC Corpus Callosum.
CNN Convolutional Neural Network.
CNS Central Nervous System.
CPZ Cuprizone.
CV Conduction Velocity.

DT Diffusion Tensor.
DWI Diffusion Weighted Imaging.

ECS Extra-Cellular Space.
EM Electron Microscopy.

FID Free Induction Decay.
FOD Fibre Orientation Distribution.
FOV Field Of View.

IAS Intra-Axonal Space.

LM Light Microscopy.

MC Monte Carlo.
MMWMD Minimal Model of White Matter Diffusion.
MRI Magnetic Resonance Imaging.
MSD Mean-Squared Displacement.

NAWM Normal Appearing White Matter.
NMR Nuclear Magnetic Resonance.

OD Orientation Dispersion.

PA Powder Average.
PDF Probability Density Function.
PGSE Pulsed Gradient Spin Echo.
PL Power Law.

RF Radio Frequency.

SE Spin Echo.
SMT Spherical Mean Technique.
SNR Signal-to-Noise Ratio.
ST Structure Tensor.

TE Echo Time.

WM WM.

XNH X-Ray Nano-Holotomography.

Contents

CHAPTER 1

Introduction

Immense volumes of information are constantly processed and communicated by the brain to ensure our cognitive and physiological function. The workhorse behind brain communication is the neuron, a cell consisting of a soma that sends and receives signals, and an axon that connects different brain regions and relays signals between them. Together, many neurons form the extremely complex brain network whose exact configuration and function remains elusive.

Although the complex neuronal network has yet to be fully mapped and comprehended, it is clear that the structure of different brain regions is adaptable and related to function. The structure has been shown to change with age [1], learning of visuo-motor tasks such as juggling [2], training of working memory [3] and in response to other experiences e.g. exercise or the learning of new languages [4]. Neurodegenerative diseases such as Multiple Sclerosis and Alzheimer's disease also incur structural changes in the brain tissue [5, 6].

The coupling between structure and function exists also on the single-axon level. Axons, the communication cables of the brain, are long, tubular structures that constitute a large portion of the brain's white matter (WM). In the WM, many axons are wrapped in a fatty layer of myelin that acts to insulate the axon from the extra-axonal environment. The morphology of an axon – especially its diameter and the thickness of the myelin sheath – controls the conduction velocity (CV) with which signals are propagated [7–9]. Axon diameter is thus indicative of brain function and the speed with which signals are conducted within the brain network. Furthermore, some neurodegenerative diseases attack certain sizes of axon. In Multiple Sclerosis, the degeneration of axons with small diameters has been observed [10, 11], whereas in Amyotrophic Lateral Sclerosis [12] it is the largest axons that degenerate. Hence, axon diameter could be a valuable biomarker for the diagnosis of such conditions.

At present, the only technique to measure axon diameter in the living brain is diffusion magnetic resonance imaging (MRI). Diffusion MRI utilises the diffusion of water molecules to probe the WM microstructure. However, axons in the brain have diameters on the order of micrometres, whereas MRI voxels for in-vivo studies are on the order of millimetres. To extract microscale information, therefore, biophysical models that describe the expected geometries of the WM compartments must be fitted to the acquired diffusion MRI signal. The axons are often modelled as straight cylinders – just like they were described by Otto Friedrich Karl Deiters upon their discovery over 150 years ago. The question is: *is this a sufficiently valid description of axonal morphology on the scale of MRI voxels, or do we need to update our models and methods?* Studies show that diffusion MRI-based axon diameter estimates [13–15] are larger than those obtained by histology [16]. One potential reason is a mismatch between the biophysical models and the actual architecture of the WM.

A validation of the three-dimensional (3D) WM anatomy would thus shed light on the validity of modelling axons as cylinders for diffusion MRI applications, but also for axonal structure-function relations. 3D electron microscopy (EM) studies of tissue from the mouse brain confirm that axons, in fact, have inherently complex morphologies with varying diameters, shapes and trajectories [17, 18]. The axons are only tracked for up to 20 μm, however, a fraction of their length in MRI voxels.

1.1 Aim

The work presented in this thesis has two main aims. The second builds directly on the first:

1. To map the 3D WM environment on scales that approach those of MRI voxels with x-ray nanotomography. This involves a characterisation of axonal morphologies against the backdrop of other WM structures, such as cells and blood vessels.

2. To validate powder-averaging of the diffusion MRI signal as a way of removing orientation bias from axon diameter estimates in the realistic axonal geometries obtained from Aim 1. This involves an investigation of how sequence parameters, signal-to-noise and angular resolution of the diffusion MRI measurement determine which diameters can be measured – and which cannot.

1.2 Thesis Structure

The thesis is divided into the following chapters:

Chapter 1. Introduction and motivation.

Chapter 2. Theory: The Structure and Function of Axons

Chapter 3. Theory: Axon Diameter Estimation with Diffusion Magnetic Resonance Imaging

Chapter 4. Theory: Synchrotron X-Ray Nanotomography

Chapter 5. Investigations into 3D White Matter Morphology

Chapter 6. Investigation into Powder Averaging as a Means of Reducing Bias in MRI Axon Diameter Estimates

Chapter 7. Conclusion

Chapters 1-4 provide the background for Chapters 5-6, which describe the results of this thesis. Chapter 1 introduces the motivation behind studying axons and their morphologies. Chapter 2 focusses on the relationship between axon structure and axon function, methods to image axons and expected axon diameters in the corpus callosum – a reoccurring WM region throughout this thesis. Chapter 3 summarises the principles of diffusion MRI, the challenges of axon diameter estimation and the theory behind powder averaging to removing dispersion bias from the signal. Chapter 4 describes the synchrotron X-ray Nanotomography techniques used to study the WM in this thesis. Chapter 5 is to a large extent based on Contributions I and III, and presents findings of the synchrotron X-Ray Nanotomography investigations into the structure and organisation of the WM and its compartments. Chapter 6 is a summary of Contribution II; it validates and investigates the use of powder averaging techniques in the complex WM architectures presented in Chapter 5.

CHAPTER 2

The Structure and Function of Axons

"As long as our brain is a mystery, the universe, the reflection of the structure of the brain will also be a mystery."
Santiago Ramón y Cajal (1852-1934)

The above statement by the father of modern neurobiology, Santiago Ramón Cajal, rings true to this day. To better understand how the brain functions, how *we* function, a deeper knowledge and understanding of the structure of the brain must be obtained. This chapter aims to outline the basics of brain and white matter anatomy. To provide a context for the results of the PhD studies, focus is placed on what is known about axonal physiology and function, the methods used to study it, and – importantly – what is *not* yet known.

2.1 Brain Anatomy

The brain, the control centre of the body, is an extremely complex network of neuronal circuits. It is constantly processing a multitude of information to regulate both cognitive and physiological processes. Together with the spinal cord, the brain comprises the central nervous system (CNS). Brain tissue can be divided into two categories: grey matter and WM.

The grey matter is present in the cerebral cortex – the outer layer of the brain – as shown in Figure 2.1, the cerebellar cortex as well as other regions of the cerebrum, cerebellum and brainstem. On the microstructural level, the grey matter contains neuronal cell bodies and dendrites, glial cells e.g. astrocytes and oligodendrocytes, blood vessels and synapses. In terms of function, the role of the grey matter is to *process* signals in the brain network.

The WM, on the other hand, is the cabling of the brain. It is organised into tracts or fascicles of myelinated axons – the tubular bodies of the neuron – that connect the grey matter regions. Like the grey matter, it also contains blood vessels, astrocytes, oligodendrocytes and other glial cells. Although sparse, a population of neuronal cell bodies has also been shown to exist in WM tracts like the corpus callosum (CC) [19]. The role of the WM is to *communicate* signals in the brain network.

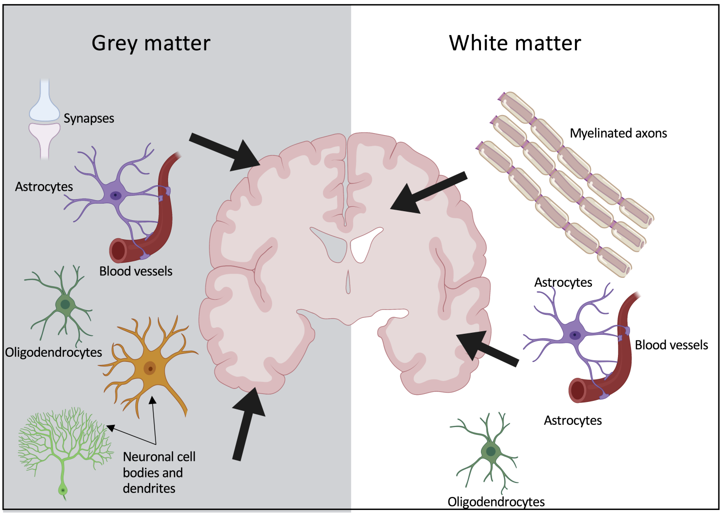

Figure 2.1: Brain tissue can be divided into two types: "grey matter", whose role is to process signals in the brain network, and "white matter", whose role is to transfer or communicate signals. The different tissue types contain different microstructures, with grey matter containing a high density of neuronal cell bodies and WM containing a high density of myelinated axons.

Between the different membrane-bound cellular components is the highly complex extra-cellular space (ECS). The ECS provides structural support and an ideal chemical environment for the cellular structures. In the brain, the ECS consists of a network of macromolecules, including polysaccharides and proteins, and has been shown to occupy approximately 20% of the volume [20]. Secreted by the neurons and glia themselves, the ECS is vital to proper cellular function and is involved in cell migration, growth of neurites and synaptic plasticity [21].

The neuron, shown in Figure 2.2, is essentially the building block of the brain. It consists of a soma (cell body), dendrites that receive signals from other cells, an axon along which the signal is conducted and axon terminals that conduct the signal on to other neurons. Many of the axons in WM are "myelinated" and are wrapped in layers of the lipid, myelin, by an oligodendrocyte. Myelination occurs in segments, with each myelinated segment called an "internode", separated from other internodes by shorter segments of unmyelinated axon called "Nodes of Ranvier". The myelin layers are termed "lamallae". The cytoplasm of the axon, the axoplasm, contains neurofilaments and microtubules which facilitate the transport of nutrients along the axon, and mitochondria which cater to the energy requirements of the axon.

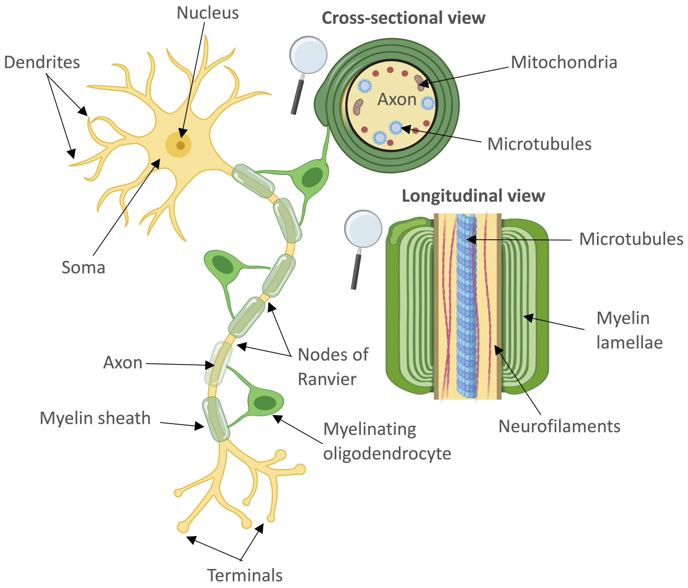

Figure 2.2: The neuron consists of a soma with dendrites, and a long, tubular axon along which signals are conducted. The axon branches out into axon terminals. In myelinated axons, myelinating oligodendrocytes wrap layers of myelin around segments of the axon called internodes. Between these internodes are "Nodes of Ranvier" – short, umyelinated segments of the axon that are important to the signal conduction.

2.1.1 Signal Conduction Along Axons

Communication in the brain network takes place via the transmission of signals and generation of action potentials (AP). APs can be generated in response to sensory cues, but most commonly, APs are caused by presynaptic neurons. The dendrites of the neuron receive an incoming chemical signal from a presynaptic neuron, triggering ion channels in the dendrite to open. At resting state, the interior of the neuron is negatively charged compared to the ECS around it, but the change in ionic permeability due to the opening of the ion channels changes the membrane potential and the membrane becomes either de-polarised or hyperpolarised. In the case of depolarisation, the change in the potential propagates to other membrane areas and may also depolarise the axon hillock – the segment of axon that connects to the soma. If the depolarisation is strong enough to overcome a threshold, a new AP is created and propagated along the axon.

In unmyelinated axons, the AP causes a depolarisation of the axonal membrane further downstream. This triggers the opening of voltage-gated sodium ion channels in the membrane, allowing positive sodium cations to flow into the axoplasm. The cations thereafter flow further downstream, depolarising more distal parts of the axon membrane, and the process is repeated until the AP reaches the terminals, as shown in Figure 2.3. This is dubbed "continuous" conduction.

Once the axon hillock has been depolarised, the AP is propagated via a continued depolarisation of the initial segment of the axon membrane as a result of the opening of voltage-gated sodium ion channels. However, due to the existence of the myelin, this cycle of depolarisation and influx of sodium cations cannot occur continuously along the axon. The presence of myelin has two effects. Firstly, it increases the membrane resistance of the axon and reduces the number of cations that can exit or "leak" out into the ECS across the axonal membrane, leaving a higher number of cations to depolarise more distal segments of the axonal membrane than in unmyelinated axons. Secondly, the myelin insulates the axon from negative charges in the ECS and decreases the capacitance of the axonal membrane. Essentially, the myelin decreases the amount of charge that can be stored in the axonal membrane and, again, this entails that there are more cations available to depolarise more distal segments of the axons. In practise, the sodium cations are able to passively diffuse further along the axon and they can depolarise the axonal membrane at larger distances than in the unmyelinated axons. Importantly, depolarisation of the membrane – and a new influx of sodium cations – can only occur at the exposed Nodes of Ranvier, and not within the internodes. As such, the signal is said to jump from node to node. In summary, the myelin boosts the conduction process, and the AP can be propagated faster than in unmyelinated axons. For fibres more than few microns in diameter, the conduction velocity (CV) increases by more than a factor of 10, compared to in unmyelinated axons of the same diameter [22].

Knowledge of the mechanisms behind the propagation of APs is important when considering which factors affect the CV of the signal. However, the explanation of AP propagation and saltatory conduction given above is simplified, and does not take into account other important aspects such as the effects of the sodium-potassium pump and potassium channel. For a comprehensive review of axon physiology, the reader is referred to Debanne et al. [23].

2.2 The Axonal Structure-Function Relationship

The structure of an axon is innately related its function and CV. Structural factors that affect axon CV include axon diameter [7], thickness of the CV-boosting myelin sheath [8], internodal distance [9], Node of Ranvier length [9], and g-ratio [24,25] – the ratio of the outer fiber diameter (inclusive of the myelin sheath) to the inner axon diameter.

In unmyelinated axons, the CV increases with the square root of the axon diameter [26], whereas in myelinated axons of the CNS, the relationship between CV (in ms^{-1}) and outer fiber diameter, D is formulated to be [27]:

$$CV = 5.5 \cdot D \tag{2.1}$$

D is related to the axon diameter, d, through the g-ratio, $g = \frac{d}{D}$. The g-ratio is thought to be constant across axons, and optimised at a value that promotes high CVs while minimising energy consumption and taking into account spatial constraints [28]. Histological studies [29, 30] confirm the findings of simulation studies [24, 25] – that the g-ratio in the CNS has a value around 0.7.

Although it is assumed to be constant, it was shown already in early studies that the g-ratio depends on axon diameter [28, 31–33]. Berthold et al. formulated a linear and logarithmic function relating the number of myelin lamellae, nl, to the axon diameter [31]:

$$nl = C_0 + C_1 d + C_2 \log d \tag{2.2}$$

where C_0, C_1 and C_2 are the regression coefficients of the fit. Had the g-ratio been constant for axons of different diameters, the number of lamellae would

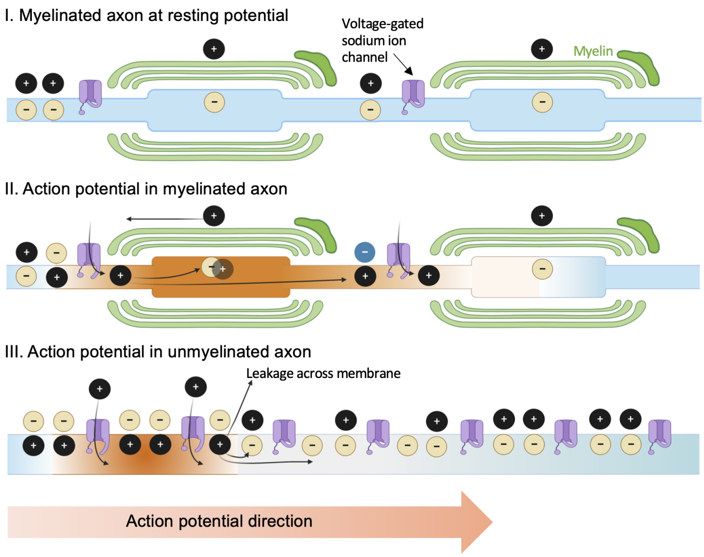

Figure 2.3: I. At resting potential, the interior axon membrane is negatively charged and the exterior is positively charged. The voltage-gated Sodium ion channels are closed. II. When an AP propagates along a myelinated axon it depolarises the axonal membrane at the Nodes of Ranvier. The voltage-gated Sodium ion channels open to allow an influx of positively charged Sodium ions. Some ions "neutralise" negative ions at the membrane, while others propagate to the next node to cause another depolarisation and continue the propagation of the AP. III. In an unmyelinated axon, the membrane capacitance is higher and the membrane can hold more charge. Furthermore, voltage-gated Sodium ion channels are present along the entire axonal membrane. Here, the AP is propagated continuously along the axon. The lack of myelin entails that there is a larger leakage of Sodium ions to the ECS and that the positive Sodium ions diffuse a shorter distance along the axon membrane than in the myelinated case.

scale linearly with axon diameter, assuming that the spacing between the myelin layers remains constant.

Through their electrophysiological experiments on the excised peroneal nerves of rabbits, Sanders et al. showed that nerves with smaller diameters, but thicker myelin sheaths conducted APs faster than nerves with larger diameters, but thinner myelin sheaths. This demonstrated the dependence of CV on the thickness of the myelin, and not only the axon diameter. Considering the effect of myelin on signal conduction, as described in Section 2.1.1, it is intuitive that it increases CV.

Further keeping in mind the signal conduction mechanism described in Section 2.1.1, it is reasonable that the internodal length also affects CV. If the internodal length were too long, it would take longer time to depolarise the Nodes of Ranvier. If it were too short, the signal would need to make more jumps or "saltations" along the axon length. This would slow down the CV [34, 35], and the relationship between internodal distance and CV therefore exhibits a maximum at one internodal distance [34]. The effect of internode and Node of Ranvier length on the CV is demonstrated by simulations in Arancibia-Cárcamo et al. 2017 [9], where it is found that an increasing node length decreases CV if the number of ion channels remains constant. With increasing node length, the nodal capacitance increases and the node thus takes longer time to depolarise. However, if the density of ion channels were to remain constant, the number of ion channels at each node also increases and the relationship between CV and node length exhibits a maximum at one particular length, similar to the internodal distance.

Not only are the structural properties of axons closely linked to CV – they are also linked to each other. For instance, in an axon that has a large axon diameter, the flow of charge along the axon experiences less resistance and can depolarise more distal segments of the membrane, meaning that the internodal distance should also increase to optimise the signal conduction. The different properties of the axonal system can be modelled using cable theory [34, 36, 37], and such formulations are integral to understanding the function of axons and interplay of the different structural features.

This section has aimed to couple the structural properties of axons to the signal conduction process, but has not delved into the implications of the diameters and CVs on the computational properties of the axons within the greater context of the brain network. For a detailed review of this, the reader is referred to Innocenti et al. [38, 39].

2.3 Imaging Axons

Axons have been imaged in a variety of modalities that reveal different structural or chemical properties. Even so, the classic techniques of light microscopy (LM) and electron microscopy (EM) are those most widely used to observe and quantify axon morphology in the dense WM of the CNS.

Conventional Light Microscopy Axons were discovered by Otto Friedrich Karl Dieters in ca. 1860 – using a light microscope. Conventional LM is 2D and has a resolution limit of approximately 200 nm under the best conditions, but in practise is it difficult to achieve resolutions below 1 μm [40]. An example of LM in a sample from the splenium of the vervet monkey brain is provided in Figure 2.4. Commonly, samples of brain tissue are fixed to preserve structural features, dehydrated with an alcohol series and embedded in paraffin or EPON (EPOXY resin), after which they are sectioned into thin slices of a few microns in thickness. With LM it is possible to apply a multitude of different stains to enhance different features of the tissue, such as cell nuclei or the myelin around the axons. Histological tracer studies, for example, have been used to show that the diameter – and thus CV – of an axon depend on its origin [41] and target [30]. Tracer studies also demonstrate the non-straight trajectories of axonal projections over long distances [41–43].

Electron Microscopy Due to its high resolution, down to a few nanometres, conventional EM is commonly used to image axons. In particular, by also being able to image smaller axons, EM has been widely used to quantify axon diameter distributions (ADD) in tissue. Recent studies on axon morphology have used 3D EM, based on serial imaging of 2D EM sections, to image the WM in the mouse brain [17, 18], segmenting and demonstrating axonal geometries up to 20 μm in length. These studies reveal that axons have non-uniform axon diameters and – as the LM investigations also demonstrate – varying trajectories. Figure 2.5 shows an example of EM used to image myelinated axons in a section from the corpus callosum of the monkey brain.

2.3.1 Other Techniques

There are many techniques that have emerged and have the capability to image structural characteristics of axons. Some of these are: structured illumination microscopy [45], two photon microscopy [46], coherent anti-Stokes Raman scat-

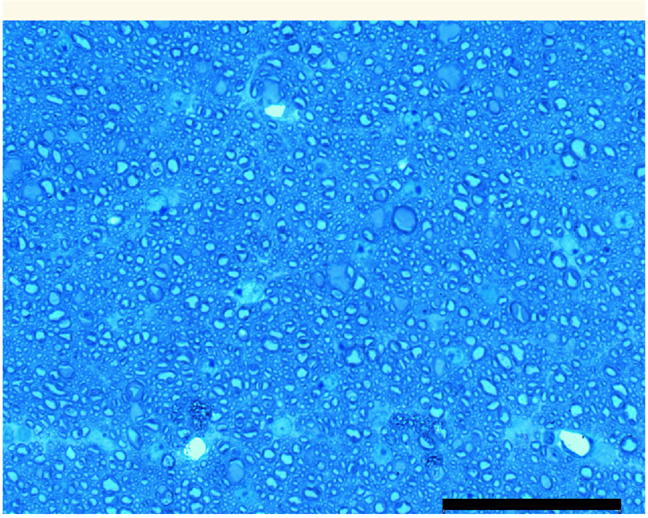

Figure 2.4: LM of EPON embedded tissue from the vervet monkey splenium [44], stained with 0.5% osmium tetroxide to give contrast to the myelin sheaths of the axons, and imaged with a Toluidine blue stain. The scale bar is 50 μm.

tering microscopy [47] and confocal microscopy [48]. Expansion microscopy [49] implements an isotropic expansion of tissue to overcome the resolution limits of light microscopy. Many of these techniques, however, employ some form of fluorescence imaging and thereby only structures that are stained for are imaged. This is excellent for investigating the chemical properties of axons or isolating specific structures, but as the images only provide information on select markers/structures, LM and EM constitute a more all-encompassing alternative to image general axon morphology, providing intensity information on all light/electron absorbing (or deflecting, in the case of scanning electron microscopy) structures in the tissue. In WM, this includes cell nuclei, cell membranes, structures within the axoplasm, the myelin and also the ECS. Diattenuation imaging and 3D polarised light imaging [50] provide information on axon orientation, axon diameter and myelination in entire, hydrated tissue sections, without any form of staining. The resolution, however, is too low to reconstruct and analyse single axons.

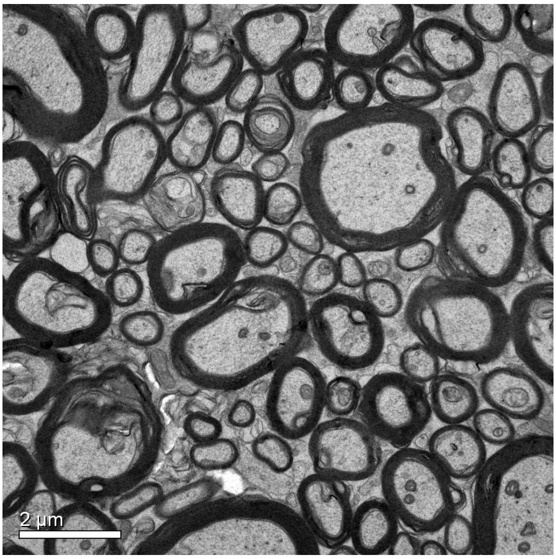

Figure 2.5: EM of a section of the monkey CC. Compared to LM, EM provides more details and reveals internal axonal structure, as well the organisation of the myelin sheath.

2.3.2 Artifacts and Biases

Imaging neural tissue with LM or EM involve tissue preparation procedures that may cause artifacts in tissue. The tissue needs to be extracted, fixed, processed, sectioned and/or stained prior to imaging. Each of these steps can incur tissue artefacts, some of which are outlined below.

The tissue needs to be fixed to prevent its deterioration via autolysis [51] or putrefaction. It can be either immersion fixated or perfusion fixated. Immersion fixation involves the extracting the tissue and then placing it in fixative. Perfusion fixation involves the injection of fixative into the cardiac muscle, whereby the fixative is pumped into the brain and the tissue does not die before it is fixed, preventing autolysis artifacts. Fixation arifacts can be caused by the use of an incorrect fixative, inadequate quantities of fixative, or insufficient time spent in fixative [52]. The most commonly used fixative is formaldehyde, which has been show to cause some shrinkage in neural tissue [53], although it is unknown if this shrinkage affects all WM compartments equally [15]. Glutaraldehyde, another common fixative, has been shown to cause shrinkage and distortion of the shapes of red blood cells [54]. Furthermore, the procedure by which the tissue is extracted may cause "pressure effects" if care is not taken [52] e.g. if the tissue is squeezed by tweezers. To prevent shrinkage and preserve the sample to as near-native state as possible, cryofixation of the tissue is possible ahead of LM and EM experiments, and can involve high-pressure freezing in combination with freeze substitution [55].

After regular fixation, the tissue is typically processed for embedding in paraffin wax or EPOXY resin (EPON). This involves first dehydrating the sample through an alcohol series, which causes additional shrinkage. Artifacts in the embedding stage can be caused by inadequate infiltration of the embedding medium [52].

The resolution and field-of-view (FOV) of the imaging technique may incur sampling bias. For example, the limited resolution of conventional LM biases morphological measurements to structures significantly larger than 200 nm, but the relatively narrow FOV of EM images – typically tens of microns – reduces the probability of sampling sparse structures, such as very large axons. Large structures, such as blood vessels or cell bodies may also be difficult to robustly characterise. In particular, metrics derived from 2D measurements may not accurately represent the 3D environment [56]. However, morphological metrics are not exempt from bias even if they are obtained in 3D. In their 3D EM studies of the mouse CC, Abdollahzadeh et al. [17] demonstrated that the volume fraction of axons present in their volumes heavily depended on the presence of cells or cellular processes. In this case, the EM volumes of dimension $\sim 15 \times 15 \times 15 \mu\text{m}^3$ were not large enough to robustly characterise the cells, of which there were between 1-4.

2.4 Axons in the Corpus Callosum

The CC, shown in Figure 2.6, is the largest WM structure in the human brain and can be found in all placental mammals. It connects the left and right hemispheres of the brain, making it integral to their communication. Studies in patients in which the CC is to some degree severed, causing a partial disconnection of the hemispheres, show that it is essential in the communication of perceptual, motor and cognitive information [57]. The axons in the CC are well aligned and are often assumed to be parallel to each other. It has thus been the subject of many LM/EM [30, 41, 58–63] and MRI studies [13, 14, 64–67] on axon diameter or axon diameter distribution. The CC can be divided into three regions: the genu, in the anterior part of the CC; the midbody, in the central region of the brain; and the splenium, in the posterior part of the CC. In general, the axon diameter is believed to increase moving from the genu to the midbody, to then decrease again moving from the midbody to the splenium. This is a simplification of the axon diameter trend in the CC and a more comprehensive division of the CC can be made [63]. Throughout this thesis, however, the three-region division is referred to.

Across species, the number of axons in the CC scales with brain size [68]. Although the median axon diameter does not show significant variability with species, the CC regions of animals with larger brains exhibit a larger population of large axons [68], which may impact the mean diameter. Figure 2.6 shows the mean diameters and standard deviations of axons in the genu, midbody and splenium regions as calculated from EM of the mouse CC in Sepehrband et al. 2016 [69] and LM of the macaque/human CC from Caminiti et al. 2013 [59].

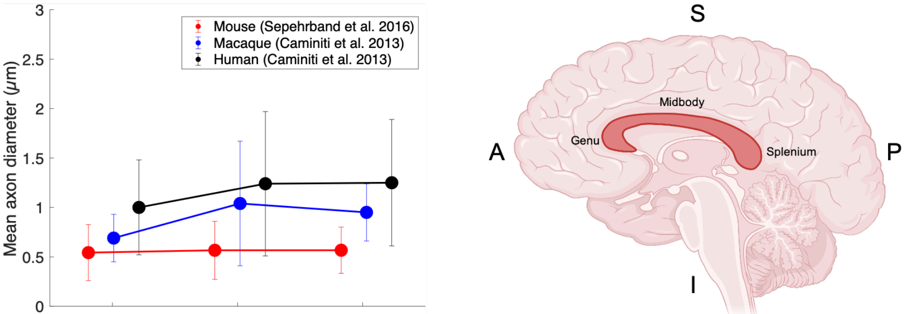

Figure 2.6: Left: Axon diameters in different regions of the CC, as reported in [69] from EM of the mouse CC, and in [59] from LM of the macaque and human brains. Error bars represent the standard deviations of the measurements. For the mouse data, the CC was divided into the three regions genu, midbody and splenium. For the LM measurments, the category "genu" consists of axons projecting to the prefrontal cortex, axons in the "midbody" project to the motor cortex and axons in the "splenium" project to the visual cortex. Right: the CC (dark red) in a mid-sagittal view of the human brain. The approximate locations of the genu, midbody and splenium are indicated.

For the mouse data, Sepehrband et al. CC had pre-divided the freely available data into the three regions genu, midbody and splenium [69]. However, for the LM in the macaque and human brains, the measurements were reported differently [59]. Measurements labelled here as "genu" are from tracts projecting to the prefrontal cortex, those labelled here as "midbody" project to the motor cortex and those labelled here as "splenium" project to the visual cortex, as reported by Caminiti et al. Thus, the mean diameters shown in Figure 2.6 for the macaque/human CC are not representative of all subregions within the genu, midbody or splenium. In particular, axons projecting to the visual cortex have been found to be larger than those projecting to the parietal/temporal cortices, also from the splenium [43, 59].

Chapter 3

Axon Diameter Estimation with Diffusion Magnetic Resonance Imaging

---

3.1 Principles and Measures of Diffusion

Above a temperature of absolute zero, all liquids and gases experience motion as a result of their thermal energy. This is termed *molecular diffusion* and was first described by Albert Einstein [70] in 1905, almost 80 years after the Scottish botanist Robert Brown described Brownian motion in 1827 – the apparently completely random motion of pollen particles suspended in water. Not only did Einstein's description of diffusion explain Brownian motion, it also proved the existence of the atom.

However, already in 1855, German physicist Adolf Fick derived "Fick's laws of diffusion" to describe diffusion of particles along a concentration gradient. Fick related the flux of particles along the gradient to the diffusion coefficient, D, which quantifies the flux, J, of particles through a defined area over a defined period of time in Fick's first law:

$$J = -D\frac{dC}{dx} \tag{3.1}$$

where x is the position, the flux, J, has units of "substance quantity per unit area per unit time", the diffusivity, D has units of area per unit time and C, which describes the concentration, has units of "substance quantity per unit volume". In the presence of no concentration gradient, as seemed to be the case for Brownian motion, this would result in zero net flux and motion.

The conservation of mass states that rate of change of the concentration within a closed surface is equal to the net flux that crosses its boundaries.

$$\frac{dC}{dt} = -\nabla \cdot J \tag{3.2}$$

Substituting Equation 3.1 into Equation 3.2, and assuming that the D is constant, one obtains Fick's second law in the form of a partial differential equation:

$$\frac{dC}{dt} = D\nabla\frac{dC}{dx} = D\frac{d^2C}{dx^2} \tag{3.3}$$

Fick's second law describes how the concentration gradient changes with time. The solution to the partial differential equation in Fick's second law takes the following form:

$$C(x,t) = \frac{1}{\sqrt{4\pi Dt}}e^{-\frac{x^2}{4Dt}} \tag{3.4}$$

with initial conditions/boundary conditions

$$\begin{cases} C(x=0, t=0) \rightarrow \text{inf} \\ C(x \neq 0, t=0) = 0 \\ C(x \neq 0, t \rightarrow \text{inf}) = 0 \end{cases} \tag{3.5}$$

By likening the diffusion process to introducing a drop of ink into a pool of water at time $t = 0$ and position $x = 0$, the boundary conditions can be explained by considering that the concentration gradient is infinitely high at $x = 0$ in the instance when the ink droplet is introduced into the water, but 0 at all other positions $x \neq 0$. After an infinite amount of time, the ink has spread out and the concentration gradient at $x \neq 0$ is 0.

Now, a Gaussian probability density function (PDF) has the form:

$$f(x) = \frac{1}{\sigma\sqrt{2\pi}}e^{-\frac{1}{2}(\frac{(x-\mu)}{\sigma})^2} \tag{3.6}$$

where μ is the mean of the distribution and σ is its standard deviation. Comparing Equations 3.4 and 3.6, it becomes apparent that they are very similar and that the solution to Fick's second law in Equation 3.4 takes the form of a Gaussian that is centred on 0 ($\mu = 0$) with standard deviation $\sigma = \sqrt{2Dt}$.

In the case of a diffusing spin, we can use the solution to Fick's second law to express that the probability of finding a particle at a position x over a time t is given by:

$$C(x - x_0, t) = \frac{1}{\sqrt{4\pi Dt}} e^{-\frac{(x-x_0)^2}{4Dt}} \tag{3.7}$$

where x_0 is the initial position ($x = 0$ in Fick's second law). To find the time-dependent mean-squared-displacement (MSD) of a spin over a time t, we now consider the definition of the MSD:

$$MSD \equiv \langle (x(t) - x_0)^2 \rangle \tag{3.8}$$

The angle brackets $\langle ... \rangle$ represent that the displacement of the spin during the time t is averaged over many small time intervals. Expanding Equation 3.8, we obtain:

$$\langle (x(t) - x_0)^2 \rangle = \langle x(t)^2 \rangle + x_0^2 - 2x_0 \langle x(t) \rangle \tag{3.9}$$

where $\langle x \rangle$ and $\langle x(t)^2 \rangle$ are the first and second moments of the PDF in Equation 3.7. By calculating them, we can find the expression for the MSD of a freely diffusing spin. By definition, the first moment of a Gaussian is equal to its μ and the second is equal to $\sigma^2 + \mu^2$. Thus, the moments can be expressed as follows:

$$\begin{cases} \langle x(t) \rangle = x_0 \\ \langle x(t)^2 \rangle = 2Dt + x_0^2 \end{cases} \tag{3.10}$$

Plugging these values for the first and second moments into the definition of the MSD in Equation 3.8, we obtain:

$$\langle (x(t) - x_0)^2 \rangle = 2Dt + x_0^2 + x_0^2 - 2x_0(x_0) = 2Dt \tag{3.11}$$

The above is the MSD in one spatial dimension. In n spatial dimensions, it becomes:

$$\langle x(t)^2 \rangle = 2nDt \tag{3.12}$$

In his 1905 paper, Einstein presented this formulation. Importantly, he (but also, independently, Australian physicist William Sutherland in 1904 and Polish physicist Marian Smoluchowski in 1906) connected D to the properties of the fluid medium through:

$$D = \mu k_B T \tag{3.13}$$

where k_B is the Boltzmann constant, T is the absolute temperature and μ is now the fluid mobility – the ratio of a particle's drift velocity through a medium to the force applied to it.

For the particular case of the diffusion of spherical particles in a liquid with low Reynolds number (in which laminar, and not turbulent, flow is likely to occur), Einstein used Stokes law describing the frictional force on the particles to formulate the Stokes-Einstein equation:

$$D = \frac{k_B T}{8\pi \nu r^3} \tag{3.14}$$

where ν is the viscosity of the medium and r is the particle radius.

This connection of D to the thermal energy of a medium explained the motion of pollen observed by Robert Brown in the case of zero net concentration gradient. In the presence of no net concentration gradient, the thermal energy of the particles in a fluid or gas, along with their collisions, give rise to microscopic, instantaneous concentration gradients and fluxes. Thus, diffusion – as that exemplified by Brownian motion – still occurs.

3.2 Free, Hindered and Restricted Diffusion

For an ensemble of spins, the PDF in Equation 3.7 is sometimes referred to as the ensemble average propagator [71]. The Gaussian nature of propagator is only valid when the particles are permitted to diffuse freely. In the case of the neural tissue, within and around the cellular microstructures described in 2.1, the diffusion process is either restricted or hindered, as shown in 3.1. This assumes that the boundaries of the cellular microstructures are impermeable. Allowing permeability further changes the hallmark of the diffusion process.

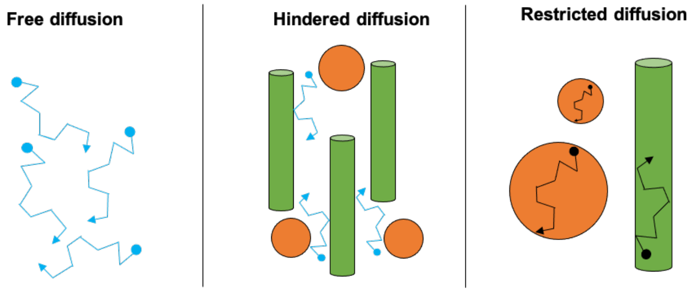

Figure 3.1: In neural tissue, the diffusion process can be either free, hindered (occuring in the ECS, for example) or restricted to cellular compartments such as axons.

The nature of the diffusion process may also depend on the diffusion time. For example, on very short time scales, diffusion occurring in hindered or restricted compartments may appear to be free, whereas at longer diffusion times, the particles are further displaced from their starting positions and have probed more of the hindrances/restrictions.

At diffusion times sufficiently long for the trajectories of the spins to be impacted by any obstacles, the diffusion propagator will no longer be Gaussian. The shape of the diffusion propagator will reflect the geometry of the environment. It is this property of the diffusion propagator that microstructural diffusion MRI exploits to characterise the microstructural environment of neural tissue.

3.2.1 The Diffusion Tensor

Diffusion can be modelled in three dimensions x,y and z by the *diffusion tensor* (DT):

$$\mathbf{D} = \begin{pmatrix} D_{xx} & D_{xy} & D_{xy} \\ D_{yx} & D_{yy} & D_{yz} \\ D_{zx} & D_{zy} & D_{zz} \end{pmatrix} \tag{3.15}$$

The diagonal elements of **D** represent the diffusion coefficients along the x, y and z axes, while the off-diagonals represent the correlation between the directions. In uncharged media such as water in tissue, the correlation between the directions is symmetrical such that $D_{yx} = D_{xy}$, $D_{yz} = D_{zy}$ and $D_{xz} = D_{zx}$ [72]. To calculate the full DT, therefore, only six measurement directions are needed. In the case of diffusion that is equal in all directions – isotropic diffusion – $\mathbf{D}$ is formulated as:

$$\mathbf{D} = D \cdot I = \begin{pmatrix} D & 0 & 0 \\ 0 & D & 0 \\ 0 & 0 & D \end{pmatrix} \tag{3.16}$$

where I is the identity matrix and D is the diffusion coefficient, which is the same in all directions.

Now, departing from the x, y, z laboratory reference frame, we model the diffusion tensor as an ellipsoid whose main axis is aligned with the direction of principal diffusion. The ellipsoid can be described in terms of its three, orthogonal diffusion directions – called eigenvectors – and its eigenvalues $\lambda_1, \lambda_2, \lambda_3$, that describe the magnitude of the apparent diffusion coefficient (ADC) in each eigenvector direction. This formalism allows the set of eigenvalues to be written as a diagonal matrix, $\mathbf{\Lambda}$:

$$\mathbf{\Lambda} = \begin{pmatrix} \lambda_1 & 0 & 0 \\ 0 & \lambda_2 & 0 \\ 0 & 0 & \lambda_3 \end{pmatrix} \tag{3.17}$$

Depending on the eigenvalues, $\mathbf{\Lambda}$ can describe both isotropic and anisotropic diffusion, and is related to the diffusion coefficient, D, by the Einstein formulation in Equation 3.12.

3.3 Diffusion Weighted Magnetic Resonance Imaging

The geometries of different compartments can be characterised using their diffusion propagators, as mentioned in Section 3.2. By using diffusion times on the order of milliseconds, diffusion weighted magnetic resonance imaging (DWI) can be used to non-invasively probe the microstructural features of the intact brain, such as axon diameter. This is predominantly done through an estimation of the ADC – the observed value of D in Fick's laws.

3.3.1 Nuclear Magnetic Resonance

Depending on their composition of neutrons and protons, some atomic nuclei have an intrinsic spin, or angular momentum. Given that nuclei are positively charged due to the protons, and all charges in motion generate a magnetic field, the angular momentum of the nucleus creates a magnetic field around the nucleus and it acts as a dipole.

If an ensemble of nuclei are placed in a strong, constant magnetic field, their magnetic moments will precess around the direction of the external magnetic field. This precession is not in phase, and as such, the net magnetisation of all spins is in the direction of the static magnetic field. If the nuclei are then exposed to an oscillating magnetic field of an appropriate frequency, usually a radio frequency (RF) pulse, two things occur. They begin to precess in phase, and the axis around which they precess is now perturbed from the direction of the static magnetic field, meaning that the net magnetisation changes direction. Due to interactions with its environment, the nucleus will eventually return to precessing around the direction of the static magnetic field again. During the time from excitation (application of RF pulse) to equilibrium (once the net magnetisation of the spins is in line with the static magnetic field once more), the spins cause detectable changes in the magnetic field. This is what is known as Nuclear Magnetic Resonance (NMR), and was first reported by Rabi et al. in 1938 [73].

The power of the RF pulse affects the initial angle, α with which the net magnetisation is rotated away from the axis of the static magnetic field. The angle, named *flip angle*, can be estimated by:

$$\alpha = \gamma \cdot B_1 \cdot t_{RF} \tag{3.18}$$

where γ is the nucleus-specific gyromagnetic ratio, B_1 is the amplitude of the RF pulse and t_{RF} is its duration.

A nucleus with angular moment (due to spin), I, has a magnetic dipole moment, μ as follows:

$$\mu = \gamma \mathbf{I} \tag{3.19}$$

For the most commonly used nucleus for MRI, the Hydrogen nucleus – a single proton, $\gamma = 42.58$ MHzT^{-1}.

In the presence of a static magnetic field, $\mathbf{B_0}$, the nuclei precess around the magnetic field direction with frequency, ω_0:

$$\omega_0 = \gamma|\mathbf{B_0}| \tag{3.20}$$

ω_0 is also known as the Larmor frequency.

We now refer to the direction of initial magnetisation as the z-axis. If an RF pulse that has magnetic field B_1 with frequency equal to the Larmor frequency and a flip angle of 90° compared to the B_0 direction is applied, the nuclei become excited, and the net magnetisation is rotated into the transverse $x - y$ plane. The spins are no longer in equilibrium and will return to the equilibrium state via two mechanisms: T_1 and T_2 relaxation, describing the interaction of nuclei with their surroundings (spin-lattice relaxation) and the dephasing of spins due to local magnetic field fluctuations (spin-spin relaxation), respectively. The recovery of longitudinal magnetisation is governed by the T_1 time constant, whereas the decay of the transverse magnetisation is governed by the T_2 time constant.

The Bloch equations [74] describe the time-dependent net magnetisation, $\mathbf{M}$, of an ensemble of spins in all three dimensions as factors of the T_1 and T_2 time constants:

$$\frac{dM_x(t)}{dt} = \gamma(\mathbf{M}(t) \times \mathbf{B}(t))_x - \frac{M_x(t)}{T_2} \tag{3.21}$$

$$\frac{dM_y(t)}{dt} = \gamma(\mathbf{M}(t) \times \mathbf{B}(t))_y - \frac{M_y(t)}{T_2} \tag{3.22}$$

$$\frac{dM_z t)}{dt} = \gamma(\mathbf{M}(t) \times \mathbf{B}(t))_z - \frac{M_z(t) - M_0}{T_1} \tag{3.23}$$

Here M_0 is the equilibrium net magnetisation. Moving to the rotating (precessing) frame of reference, these equations are simplified and become:

$$\frac{dM_{xy}(t)}{dt} = \frac{M_{xy}(t)}{T_2} \tag{3.24}$$

$$\frac{dM_z(t)}{dt} = \frac{M_0 - M_z(t)}{T_1} \tag{3.25}$$

with solutions:

$$M_{xy}(t) = M_{xy}(0) \cdot e^{\frac{-t}{T_2}} \tag{3.26}$$

$$M_z(t) = M_0(1 - e^{\frac{-t}{T_1}}) + M_z(0) \cdot e^{\frac{-t}{T_1}} \tag{3.27}$$

where $M_{xy}(0)$ and $M_z(0)$ represent the transverse or longitudinal magnetisation present at $t = 0$ as a result of any previous application of an RF pulse. The decay of the transverse magnetisation is sensitive to inhomogeneities in the $\mathbf{B_0}$ field. B_0 inhomogeneities can be caused by either a non-perfect generation of $\mathbf{B_0}$ due to the MRI hardware (coils) or interfaces between different tissue types that cause susceptibility artifacts (perturbations of the field). These imperfections cause a faster decay of the transverse magnetisation than that defined by the T_2 constant, and a T_2^* time constant, including both the standard T_2 decay and the additional decay caused by field inhomogeneities, is defined. However, the effects of field inhomogeneities can be eliminated in some sequences, such as spin echo (SE) sequences, and in these, the transverse magnetisation decays according to the T_2 constant as in Equation 3.26.

3.3.2 Obtaining a Diffusion Weighted MRI Signal

The MRI Signal Magnetic Resonance Imaging (MRI) refers to a measurement of the NMR signal. After an ensemble of nuclei have been excited by an RF pulse at the Larmor (resonant) frequency, motion of the magnetisation vector occurs as described by Equations 3.21 to 3.23. According to the laws of Faraday and Lenz, this motion will generate a magnetic flux, and thereby a current, in a coil whose axis is placed in the transverse plane. This signal, first demonstrated by Erwin Hahn [75], and predicted by the Bloch equations, is called free induction decay (FID).

Almost immediately following his demonstration of the FID, Hanh described the SE method [76]. A single 90° RF pulse gives rise to a FID, but if it is followed soon after by a second 180° RF pulse, a SE that is insensitive to inhomogeneities in the static magnetic field can be measured. As previously mentioned, a rotation of the net magnetisation vector into the transverse plane, as is the case when a 90° RF pulse is used, the transverse magnetisation (which gives rise to the measured signal) decays due to T_2^* interactions and a dephasing of the spins. However, upon application of a second 180° RF pulse, the spins precess in the opposite direction to before and begin to *refocus*. The effect of the component of the $T2^*$ decay attributed to field inhomogeneities is reversed, and after a time defined as the echo time (TE), the nuclei are once more in phase. After this point, the signal decays according to the $T2$, and not $T2^*$, constant. However, Hahn also outlined one additional feature that impacted the measured signal: that is, the diffusion of spins in the presence of magnetic field gradients.

Diffusion-Weighting the MRI Signal In 1954, Carr and Purcell further outlined the effects of diffusion on the NMR signal, and suggested that a magnetic field gradient could be employed to measure the ADC of fluids [77]. In 1956, Torrey incorporated the effects of diffusion into the Bloch equations [78]. He derived the rate of change of the magnetisation upon application of a magnetic field gradient due to diffusion of spins described by diffusion tensor $\mathbf{D}$ to be:

$$\left(\frac{d\mathbf{M}}{dt}\right)_D = \nabla \cdot \mathbf{D}\nabla(\mathbf{M} - \mathbf{M_0}) \tag{3.28}$$

This term was added to the Bloch equations in Equations 3.21 to 3.23, and the modified equations are referred to as the Bloch-Torrey equations.

Using the idea of a magnetic field gradient to sensitize the MRI signal to diffusion, Stejskal and Tanner proposed the Pulsed Gradient Spin Echo (PGSE) in 1965 [79]. The PGSE sequence is essentially a SE, with two gradient pulses on either side of the 180° RF pulse, as shown in Figure 3.2.

After excitation by the 90° RF pulse, the application of the magnetic field gradient pulse of strength G and duration δ gives spins a position-dependent precession frequency (as in Equation 3.20). The spins thus accumulate phase according to their position in the magnetic field gradient. The 180° RF pulse reverses the precession direction, and the application of an identical second gradient pulse, a duration Δ after the first gradient pulse, once more gives spins a position-dependent precession frequency, and they again accumulate a phase according to their position.

If the spins remain stationary between the application of the two pulses, the phase accumulated by the spins just before the 180° pulse at time TE/2 will be opposite to that accumulated after a total time TE, and they should cancel. However, if diffusion has occurred, there will be a non-zero net phase and a lack of phase coherence, causing a reduction in the signal amplitude that is indicative of the ADC [79].

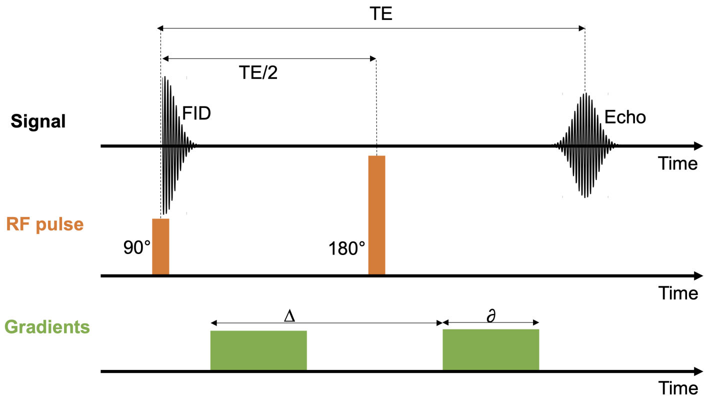

Figure 3.2: Simplified diagram of a PGSE sequence, showing the chronology of the application of RF pulses and gradients, as well as the registration of signals in the receiver coil. Upon generation of a 90° pulse, a FID is generated. A diffusion encoding gradient of duration δ is then applied. After a duration Δ from the start of the gradient pulse, a 180° RF pulse is generated. The spins then begin to dephase and a second diffusion encoding gradient is applied. After a time (TE) from the first RF pulse, an echo, the amplitude of which is indicative of the diffusion of spins that has taken place between the two gradient pulses, is registered at the receiver coil. Note that the amplitude of the second RF pulse is twice that of the first – the doubled amplitude doubles the flip angle.

Moving to the rotating frame of reference, as in Equations 3.24 to 3.25, the solution for the Bloch-Torrey evolution of the magnetisation in the transverse plane is similar to that in Equation 3.26 with the addition of a multiplicative "attenuation" term. Stejskal and Tanner formulated the solution to the Bloch-Torrey equations [79] as:

$$M_{xy}(t) = M_{xy}(0) \cdot e^{\frac{-TE}{T_2}} \cdot e^{-q^2(\Delta - \frac{1}{3}\delta)D} \tag{3.29}$$

where $q = \gamma^2 G^2 \delta^2$ is the diffusion encoding and $t_d = (\Delta - \frac{1}{3}\delta)$ is the diffusion time. The factor of $q^2 t_d$ is also referred to as the *b-value*, and is a quantification of the degree of diffusion weighting applied. The higher the b-value, the higher the diffusion weighting and the more dephasing a given displacement will cause. The signal, S, measured at the receiver coil can be formulated as a function of

b:

$$S(b) = S(0) \cdot e^{-bD} \tag{3.30}$$

where $S(0)$ is the signal acquired with the same TE as $S(b)$, but with no diffusion weighting. That is to say, $b = 0$.

Importantly, the value of D measured in Equation 3.30 with DWI is not necessarily the true diffusion coefficient, owing to the non Gaussian nature of diffusion within restricted spaces, as disussed in Section 3.2. Instead, it is the ADC – the *apparent* diffusion coefficient.

3.4 Biophysical Modelling of the White Matter Environment

MRI voxels can be up to several millimetres in side length, while the structures in brain tissue are on the order of micrometres. Therefore, the measured MRI signal in a single voxel of the WM, is the combined signal from all compartments: cells, axons, ECS, etc:

$$S = S(0) \sum_i f_i S_i \tag{3.31}$$

where $S(0)$ is the signal without diffusion weighting, i is the compartment index, f_i is the volume fraction of the ith compartment and S_i is the signal arising from it. This expression relies on the assumption that T_2 relaxation time is the same for all compartments.

In his PhD thesis, JE Tanner presented analytical predictions of the PGSE signal arising from different bounded geometries [80]. By modelling different compartments as different geometries, their expected signal contributions at different b-values can be predicted. This is necessary in order to explore the microstructure of the WM.

3.4.1 Diffusion within Cylinders

In the case of axons, they are often modelled as impermeable cylinders in which free diffusion occurs along the cylinder axis, and diffusion in all other directions is restricted. Neuman derived the PGSE signal perpendicular to a cylinder [81] to be:

$$\begin{aligned}\ln A = \ln A_0 - 2\gamma G^2 \sum_{m=1}^{\infty} \frac{1}{D_0^2 \alpha_m^6 (R^2 \alpha_m^2 - 1)} \\ \cdot [2D_0 \alpha_m^2 \delta - 2 + 2e^{-D_0 \alpha_m^2 \delta} + 2e^{-D_0 \alpha_m^2 \Delta} - e^{-D_0 \alpha_m^2 (\Delta - \delta)} - e^{-D_0 \alpha_m^2 (\Delta + \delta)}]\end{aligned} \tag{3.32}$$

where A is the diffusion-weighted signal, A_0 is the signal with no diffusion weighting, γ is the gyromagnetic ratio, G is the strength of the gradient pulse, D_0 is the intrinsic diffusion coefficient, δ is the duration of the gradient pulse, Δ is the separation of the gradient pulses, R is the radius of the cylinder and α_m is the mth root of the equation:

$$J_1'(\alpha_m R) = 0 \tag{3.33}$$

where J_1' is the derivative of the first order Bessel function of the first kind.

If $\delta \gg \frac{R^2}{D_0}$, the cylinders are said to fall within the Neuman limit [81, 82] and Equation 3.32 can be simplified to:

$$\ln S_\perp = -\frac{7}{48} \frac{\delta g^2 R^4}{D_0} \tag{3.34}$$

As demonstrated in the work of Van Gelderen et al. [83], it is possible to estimate the radius of a cylindrical restriction – D_0, given the PGSE sequence parameters and three orthogonal measurements of the DWI signal. Or – if the cylinder orientation is known – a single measurement perpendicular to the cylinder axis. The estimate of the radius improves if D_0 is known, and vice versa.

3.4.2 Multi-Compartment Models

There exist several multi-compartment WM models that aim to describe the signal arising from MRI voxels. Only a few are mentioned here; these are summarised in Table 3.1. A more comprehensive discussion of biophysical models for diffusion MRI is given in [16, 84, 85].

The AxCaliber method [14,65] uses the composite hindered and restricted models of diffusion (CHARMED) model [86,87] to estimate the ADD in each voxel. It has two compartments: a restricted compartment to represent the intra-axonal space IAS consisting of parallel cylinders with a gamma-distribution of radii, and a hindered compartment to represent the ECS, consisting of an anisotropic, axisymmetric DT whose principal axis is aligned with the main axon direction.

ActiveAx [13, 88] uses the minimal model of white matter diffusion (MMWMD) to provide orientationally invariant whole-brain estimates of the axon diameter index: an estimation of the volume-weighted average diameter. The MMWMD employs a four-compartment model, consisting of i) cylinders to model the (IAS), ii) DT for the ECS, iii) a freely diffusing compartment for the cerebrospinal fluid (CSF) and iv) a small stationary compartment in which there is no diffusion. The DT model is that from Basser et al. 1994 [89] and, contrary to the AxCaliber method, it is assumed that the same parallel diffusivity of the ECS is the same as that in the IAS. The perpendicular diffusivity of the hindered DT, $D_{h\perp}$ is given by the tortuosity model of Szafer et al. 1995 [90] in which:

$$D_{h\perp} = D_{h\|}\left(1 - \frac{f_a}{(f_a + f_h)}\right) \tag{3.35}$$

where f_a is the intra-axonal volume fraction and f_h is that of the hindered compartment. The freely diffusing isotropic compartment takes into account any contamination by the CSF, and the restricted dot compartment was found to be necessary to explain the MRI signal in ex-vivo tissue [13].

An extension of the CHARMED model takes into account the possible orientation dispersion (OD) of axons by representing axons as dispersed cylinders to estimate the diameter index, a' [91]. The model assumes that the axon OD follows a Watson distribution. As in the other models, the ECS is represented as a hindered, anisotropic (and cylindrically symmetrical) DT, and – like ActiveAx – the tortuosity model in Equation 3.35 is used.

As shown in Table 3.1, the techniques employ different MRI acquisition schemes and methods to fit the models to the MRI data. There are many ways to both acquire diffusion MRI data, and fit many different models to it to extract microstructural parameters of interest. However, the accuracy of the biophysical models in describing the anatomical WM environment can be disputed.

Table 3.1: Comparison of the biophysical models CHARMED, MMWMD, and the generalised CHARMED model, and the techniques that implement them: AxCaliber, ActiveAx and [91].

Model	CHARMED	MMWMD	Gen. CHARMED
Compartments	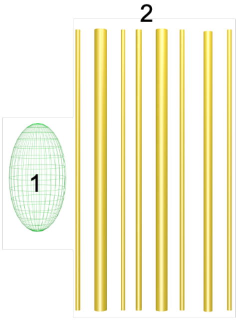 1. Diffusion tensor whose principal directions coincide with those of the axons. 2. Parallel cylinders with radii following a gamma distribution with parameters α and β.	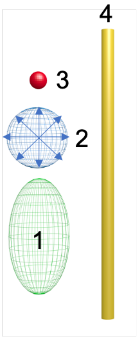 1. Dot 2. Isotropic, free diffusion. 3. Diffusion tensor. 4. Parallel cylinder with volume-weighted diameter index a'.	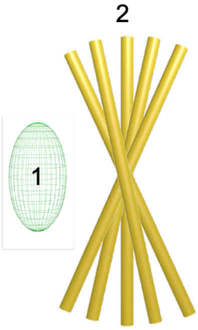 1. Diffusion tensor. 2. Dispersed cylinders with Watson distribution parameter κ and volume-weighted diameter index a'.
Technique	AxCaliber (can include an isotropic CSF compartment [14])	ActiveAx	*"Axon diameter mapping in the presence of orientation dispersion with diffusion MRI"* [91]
Fitted Parameters	$D_{h\perp}$, f_h, f_{iso}, f_a, α, β	**n** (principal fibre direction), f_a, f_h, a'	**n** (principal fibre direction), f_a, κ (OD parameter), a'
Fixed Parameters/Assumptions	• The axonal axial diffusivity, $D_{\parallel}$, is known and constant. • The principal direction of the DT coincides with that of the axons. • Measurement is made precisely perpendicular to fibre direction. • Fibres/axons are parallel.	• The axonal axial diffusivity, $D_{\parallel}$, is known and constant. • The principal direction of the DT coincides with that of the axons. • Fibres/axons are parallel.	• The axonal axial diffusivity, $D_{\parallel}$, is known and constant. • The OD can be characterised by a Watson distribution • One main fibre direction.
Fitting Optimisation	Non-linear least squares with Levenberg-Marquardt minimisation.	Rician MCMC procedure after an intial grid search and gradient descent algorithm for appropriate initialisation.	Rician MCMC procedure after an intial grid search and gradient descent algorithm for appropriate initialisation.
Image Acquisition Example	PGSE. 5 diffusion times for each of 16 values of G (80 parameter combinations) in a single direction perpendicular to fibre axis [14].	PGSE. 3-4 $b-$values or HARDI shells, 90 directions per shell [13].	PGSE. 4 $b-$values or HARDI shells, 90 directions per shell [91].

3.5 Challenges of Axon Diameter Estimation with Diffusion Magnetic Resonance Imaging

The extraction of microstructural features of interest, such as axon diameter, through the fitting of biophysical models to diffusion MRI data has its caveats and may not provide entirely accurate measures. Axon diameter estimates obtained with diffusion MRI [13, 14] are larger than LM- or EM-based axon diameter estimates [15, 16]. The sources of discrepancy between diffusion MRI- and histology-based estimates may be several, ranging from the design of the biophysical model to the potentially questionable validity of comparing the two metrics from two very different modalities and experimental conditions [15].

3.5.1 Compartment Morphology

The compartments of biophysical models are designed in part with knowledge of anatomical compartments from LM in mind, and in part with the diffusion MRI signal profile in mind e.g. the inclusion of the dot compartment in [13].

It would be somewhat unrealistic to expect real, anatomical compartments to adhere to perfect cylindrical, spherical or zeppelin shapes. However, for the purposes of microstructural diffusion MRI, it would be sufficient if the restricted and hindered diffusion occurring within the compartments *appears* as if it arises from these shapes. Consequently, the approximation of a certain geometrical shape may be appropriate at one diffusion time, but not another.

Axons have long been described as cylinders. Undisputably, they are tube-like. However, as mentioned in Section 2.3, both LM and EM studies [17, 18, 41–43] indicate non-constant diameters and trajectories of axons. In simulation studies, axonal undulations [92, 93] and general orientation dispersion [91] have been shown to cause an overestimation of axon diameter with diffusion MRI. Monte Carlo (MC) diffusion simulations within short segments of axons segmented from a 3D EM dataset of the mouse CC also indicate that realistic axonal geometries, with diameter and trajectory variations, exhibit a time dependent $D_{\|}$ within the IAS [94]. Furthermore, no consideration is taken to the effects of mitochondria or microtubules and neurofilaments on the intra-axonal diffusion.

3.5.2 Permeability

The estimation of axon diameter based on the diffusion occuring within cylinders described in Section 3.4.1 makes the assumption that myelinated axons are impermeable to the exchange of water across the axonal membrane. The same assumption is made for the other compartments shown in Table 3.1. It is possible that there is some exchange of water between the IAS and the ECS, meaning that myelinated axons are not fully impermeable, but it is likely to be negligible in healthy WM [95]. However, in cases of disease – for which axon diameter may be a biomarker – the assumption of impermeability becomes less valid [95].

3.5.3 Hardware Limitations

Limitations of the MRI hardware also affect the measurement of axon diameter. In Dyrby et al. [64], a dependence of the measured axon diameter index on the amplitude of the gradient pulse is demonstrated. Generally, the higher the available gradient strength, the smaller axon diameters that can be measured. At lower gradient strengths, large displacements are required to to produce detectable attenuation of the signal. As such diameters below a certain limit – which depends on the signal-to-noise ratio of the MRI signal and the gradient strength – are indistinguishable from each other [96].

There is an upper cap on the available MRI gradient strengths. Although technological advancement will most certainly see the development of coils that produce higher gradient strengths, the use of higher gradient strengths may not necessarily guarantee an unbiased estimate of axon diameter. The upper limit of measurable axon diameter depends on two variables: the diffusion time and also the SNR of the measurement. Sequence parameters that favour the measurement of small axons via a high gradient strength may cause the signal perpendicular to larger axons to be attenuated to the extent that it is no longer distinguishable from noise. Furthermore, elongating the diffusion time of a sequence is not either a guaranteed method of ensuring sensitivity to larger axons. An elongation of the diffusion time requires an elongation of the TE, entailing that more T2 decay has had time to occur, reducing the SNR of the measurement.

Therefore, for a given PGSE and realistic experimental conditions where there is some degree of noise (even in MC simulations), there is a "window" of sensitivity to axon diameter [64].

3.5.4 Compartmental T_2 Time Constants

Although it affects the estimated volume fraction of the IAS, and not the estimated axon diameter, another assumption that is worth mentioning is that the T_2 time constants are are assumed to the same for all compartments. Recent investigations studying the T_2 relaxation times of the IAS and ECS have shown that they may in fact differ [97–99]. Different T_2 relaxation times in different compartments could affect the estimation of their respective volume fractions, f_i in Equation 3.30, [100].

3.5.5 Validation Limitations

Lastly, there exists a disparity between the tissue that diffusion MRI probes, and that examined by LM. As outlined in Section 2.3.2, processing of tissue for LM or EM may cause shrinkage and/or artifacts, and it is unknown to which extent the IAS compartment is affected [15]. Therefore, there may exist differences in the axon diameters unrelated to measurement technique itself, but instead coupled to the tissue processing.

Furthermore, axon diameter distributions from LM and EM are often measured in 2D, while diffusion MRI is sensitive to the entire, 3D IAS. Measurements in 2D could be biased by a misalignment of the 2D imaging plane relative to the axonal trajectory.

3.6 Powder Averaging to Remove Orientation Bias

Powder averaging (PA) has been proposed and implemented as a model-free approach to remove OD bias in diffusion MRI metrics [101–111]. The PA involves calculating the arithmetic mean of the diffusion MRI signal in isotropically distributed directions on the unit sphere. The resulting PA signal represents the spherical mean of the set of micro-domains present in the voxel, regardless of their individual orientation.

Spins diffusing within a particular compartment will, at typical diffusion times, not probe the entire compartment. Instead they probe a micro-domain, represented by the orange arrows in Figure 3.3.

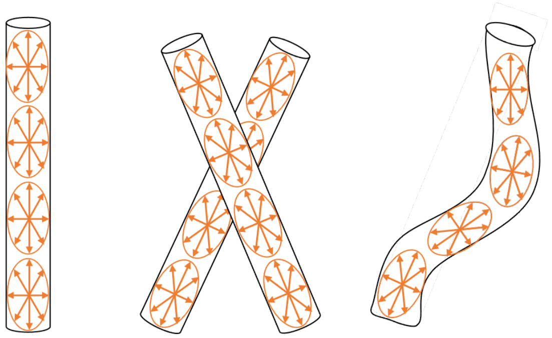

Figure 3.3: At typical diffusion times, spins will probe only a microdomain of a compartment (represented by the orange arrows).

If the diffusion MRI signal is measured in many different isotropically distributed directions, the signal profile of the three fibre configurations shown in Figure 3.3 will be very different. That is to say, the distribution of the signal over the different directions will differ. On the other hand, the signal obtained by averaging the signal in all directions will be the same for all fibre configurations, assuming that the spins do not probe too large a microenvironment. Thus, the PA diffusion MRI signal can be said to be free of OD bias to some extent. This approach can be extended to axon diameter estimation, but is not without its limitations, which we will explore further in Chapter 6. How well PA-based approaches can recover the axon diameter depends on diffusion time [111], and axonal dispersion on the scale of the microdomains probed by the spins may bias the axon diameter estimate.

3.6.1 The PA of the Diffusion MRI Signal in Cylinders

PA approaches to axon diameter estimation assume that the microdomains probed by spins within the IAS are cylindrical.

The analytical PA of the diffusion MRI signal from cylinders, $\overline{S_{SMT}}$, can be shown to be [112]:

$$\overline{S}_{SMT}(b) = f_a\left(e^{-bD_\perp}\cdot\sqrt{\frac{\pi}{4b\cdot(D_\parallel - D_\perp)}}\cdot erf\left(\sqrt{b\cdot(D_\parallel - D_\perp)}\right)\right) \tag{3.36}$$

where f_a is the relative contribution of the IAS to the total signal, b is the diffusion weighting, $D_{||}$ is the ADC parallel to the cylinder axis, $D_{\perp}$ is the ADC perpendicular to it and $erf(x)$ is the error function of x. Equation 3.36 is what is here referred to as the spherical mean technique (SMT) implementation.

In cylinders, $D_{||} > D_{\perp}$. At high $b-$values, it can thus be assumed that $b \cdot (D_{||} - D_{\perp}) \gg 1$ for cylinders, in which $D_{||} > D_{\perp}$. In these conditions, $erf(x) = 1$ and Equation 3.36 can be rearranged to take the form of a power law (PL) [113]:

$$\overline{S}_{PL}(b) = \beta e^{-bD_{\perp}} b^{-0.5} \tag{3.37}$$

where $\beta = f_a \sqrt{\frac{\pi}{4(D_{||} - D_{\perp})}}$. The value of β is constant with $b-$value. Equation 3.37 is what is here referred to as the "PL implementation" and is an alternative representation of the SMT at high $b-$values. The PL thus requires the fitting of only two variables (β and $D_{\perp}$), compared to the three variables (f_a, $D_{||}$ and $D_{\perp}$) of the SMT.

By fitting the PA signal to expressions for the PA of cylinders, an estimate of $D_{\perp}$, the ADC perpendicular to the cylinder axis, can be obtained. This can be converted into a diameter with Equation 3.30 and the expression for the analytical signal perpendicular to a cylinder of given diameter in Equation 3.32. As such, knowledge – or an assumption – of D_0 is needed. However, since the radius scales approximately as $R \sim (D_0)^{\frac{1}{4}}$ (Equation 3.34), it is relatively insensitive to small inaccuracies of D_0.

Chapter 4

Synchrotron X-Ray Nanotomography

4.1 Synchrotron Radiation

Synchrotrons are large-scale facilities, home to the brightest x-rays in the world. A cyclic particle accelerator accelerates electrons around a storage ring with the aid of magnetic fields. Broadly speaking, dipole magnets deflect the electrons to make sure they follow a circular orbit, while quadrupole and sextupole magnets focus the electron beam. The radial acceleration of the electrons results in synchrotron radiation, a type of bremsstrahlung. The radiation is guided out at tangents to the central ring into different beamlines or experimental stations. Using magnetic fields and different optical devices (mirrors, slits, monochromators, absorption filters), the energy, intensity and beam size of the radiation can be controlled.

During the PhD studies, experiments were conducted at two synchrotron facilities: Deutsches Elektronen-Synchrotron (DESY), beamline P10, and the European Synchrotron (ESRF), beamline ID16A.

4.2 X-ray Propagation-Based Phase Contrast Imaging in Soft Tissue

X-rays have wavelengths between 10^{-2} and 10 nm. For hard (high energy) x-rays, their propagation through a medium can be described by the complex refractive index, n, of the medium:

$$n = 1 - \delta_n + i\beta_n \tag{4.1}$$

where δ_n is the refractive index decrement and describes the phase shift ($\Delta\phi$) experienced by the x-rays as they traverse the medium, and the imaginary term with β_n is the absorption index, describing the amplitude change of the x-ray wave. Both δ_n and β_n depend on the electron density of the medium. In soft tissue, $\delta_n >> \beta_n$, and the interaction process is dominated by $\Delta\phi$ [114,115]. The phase shifted x-rays interact with reference x-rays that have not interfered with the medium (Figure 4.1). These interference effects become stronger the further the x-rays exiting the sample propagate, forming different imaging regimes at different sample-detector distances [116]. At short distances, phase contrast occurs due to diffraction associated with the high spatial frequencies of the electron density distribution in the sample e.g. edges between structures and materials, but preserves the lower frequency general shape of the sample. The intensity image resembles the sample, but exhibits an edge enhancement, and is sometimes referred to as the *direct contrast* regime. At longer propagation distances, even the low spatial frequencies are subject to diffraction and the intensity image no longer resembles the sample – this is the *holographic* regime. In the holographic regime, the observed intensity image at the detector mostly contains phase contrast, assuming that the sample is sufficiently small. This differs compared to conventional medical x-ray imaging in which the contrast is mostly given by absorption.

The phase information of the sample, δ_n and β_n, can then be reconstructed with appropriate phase retrieval algorithms for the experimental conditions and imaging regime, for which more details can be found in [114, 117–120].

4.3 Experimental Setups

X-ray nanotomography refers to the nano-resolution tomography of samples using x-rays to produce detailed, 3D maps of their inner structure. More specif-

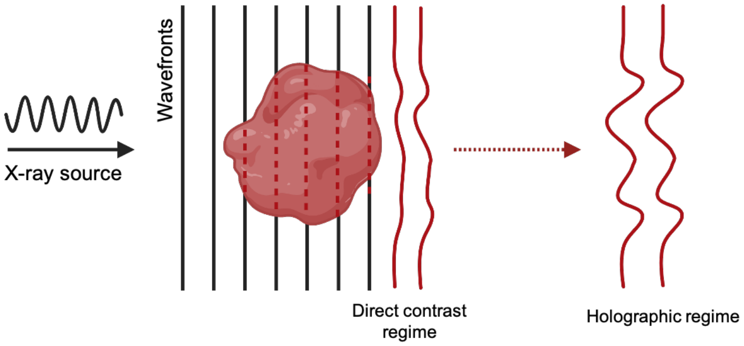

Figure 4.1: The entering x-rays (black wavefronts) accumulate both phase and amplitude changes as they interact with and traverse the sample (dashed red lines). The self-interaction of the x-rays with non-disturbed wavefronts gives rise to interference effects (red wavefronts) that are amplified by propagation in vacuum or free space. The intensity patterns in the image formed by the exiting x-rays encode the information of the complex refractive index of the medium. Figure inspired by Figure 1.3 of [120].

ically, x-ray nano-holotomography (also called x-ray holographic nanotomography [121]), XNH, refers to x-ray nanotomography in the holographic imaging regime.

The properties of the illuminating x-rays and the experimental setup determine the FOV and resolution of the acquired images. The GINIX endstation at beamline P10 of DESY had two possible configurations, shown in Figure 4.2. A parallel-beam configuration was used for imaging in the direct contrast regime (small d_2) and provided large FOVs (determined either by the detector size or the upstream slits) between 0.5-1 mm in each dimension, and an effective resolution that was determined by the detector pixel size of 550 nm. This configuration was ideal for overview scans of the tissue. The second configuration, the cone beam setup (Figure 4.2B), had variable effective pixel size and FOV (limited by the size of the detector). The divergent beam entailed that different geometrical magnifications $M = \frac{d_1+d_2}{d1}$ could be achieved by varying the focus-sample and sample-detector distances. The cone-beam setup provided resolutions of 50-200 nm and FOVs on the order of hundreds of micrometres, and is described in more detail in [122, 123]. At DESY, the free space propagation was in air and the x-ray energies used in the experiments was approximately 13 keV.

The XNH setup at beamline ID16A of ESRF used the cone-beam configuration shown in Figure 4.3. Contrary to at DESY, the free space propagation took

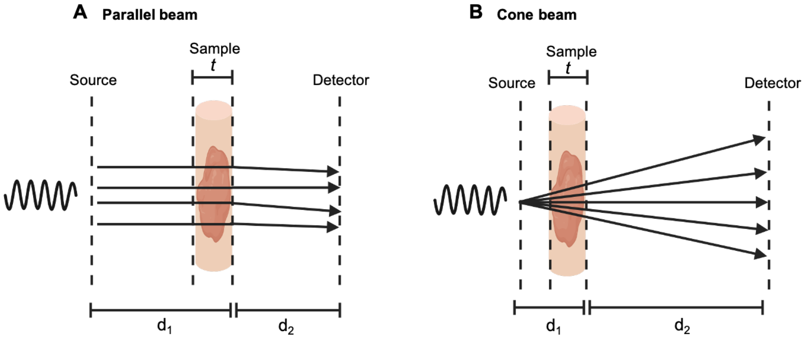

Figure 4.2: A) A parallel-beam configuration offers large FOV, but the resolution of the images is limited by the pixel size of the detector. Imaging is usually performed in the direct-contrast regime, with a small distance d_2 between the sample and the detector. B) A cone-beam geometry offers the possibility of geometrical magnification $M = \frac{d_1+d_2}{d1}$ to reduce the effective pixel size and increase resolution, at the cost of a smaller FOV.

place in vacuum. The x-ray energy used was approximately 17 keV and it was possible to image the sample at cryogenic temperatures. A pair of Kirkpatrick-Baez mirrors focussed the beam to a small spot size of around 30×30 nm^2. The sample was placed on a high-precision rotation stage and the samples were imaged with the nano-focussed cone beam [124, 125] at different distances with respect to the focus and the detector to obtain phase maps [117, 125]. The acquisition of tomograms at different distances serves to reduce artifacts in the reconstructed phase maps.

For experiments at both DESY and ESRF, rotation stages allowed the sample to be rotated through 180°, after which the 3D volumes were reconstructed by filtered backprojection or computed tomography algorithms.

4.4 Sample Preparation Considerations

The tissue samples had to be carefully prepared for the synchrotron experiments with the aim to reduce image artifacts and absorption of x-rays while maintaining contrast to the biological structures within the tissue.

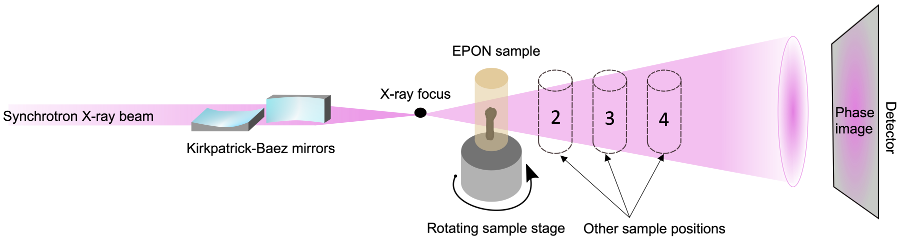

Figure 4.3: In the cone beam setup at ESRF, the x-ray beam is focused by a pair of Kirkpatrick-Baez mirrors into a small spot size. The sample is placed on a rotating sample stage, which rotates it through 180°. Holograms are acquired at different rotations and sample stage positions.

Heavy metal staining of tissue Osmium tetroxide is a common heavy metal stain, used to stain structures containing lipids, such as cell membranes or the myelin sheath around axons. Thus, it is an optimal stain for the study of WM, which contains a high density of myelinated axons. However, owing to its high electron density (and high Z – proton number), Osmium is highly absorbing and thus places limits on the the dimensions of the tissue samples. Ideally, the samples should be small enough to allow a high SNR in the acquired images, while being large enough to span at the very least, the maximum desired FOV. Furthermore, although many staining protocols recommend a 2% concentration of osmium tetroxide, preliminary experiments that we performed at the laboratory μ-CT setups at DTU and the Institut für Röntgenphysik at Georg-August-Universität Göttingen suggested that this caused excessive absorption, and that a 0.5% osmium tetroxide concentration would provide a good compromise between contrast and SNR for dense WM samples of approximately 1 mm in thickness.

Embedding medium The medium into which the sample is embedded, if any, impacts the morphological and absorption properties of the sample. As outlined in Section 2.3.2, embedding in EPON or paraffin involves processing the sample with an alcohol series, which causes shrinkage. The choice of EPON, paraffin, or other embedding medium also affects the contrast formation of microstructural features in tissue. In studies of the unstained mouse cerebellum, Töpperwien et al. investigated the structural and contrast differences between: i) hydrated samples stored in phosphate buffer solution, ii) samples housed in ethanol and ii) paraffin-embedded samples [126]. They found that the while there was significant shrinkage in the diameters of the Purkinje and granular cells when the tissue was embedded in ethanol or paraffin, the contrast was significantly improved compared to in the hydrated tissue. Further investigations into sample mounting and embedding strategies can be found in [127].

Sample geometry The algorithms used to retrieve the phase maps [117, 128] from the acquired holograms make several assumptions. Some assumptions are: that the sample is weakly absorbing, that the phase is slowly varying (smooth electron density distribution) throughout the sample, and that is symmetrical around its rotation axis. Violations of these assumptions can cause artifacts in the phase-reconstructed images. Thus, the sample should be designed to be as axisymmetrical as possible. Sharp edges should be avoided within the FOV of the scans and the embedding medium should have as smooth a surface as possible.

In the experiments outlined in this thesis, hydrated or paraffin-embedded samples were mounted on the rotation stage within cylindrical kapton tubes, while the EPON blocks were cut and polished to appropriate dimensions and smoothness.

Chapter 5

Investigations into 3D White Matter Morphology

To explore the morphology of axons and other microstructures in the white matter, synchrotron x-ray nanotomography was used to study brain tissue from different brain regions and animals. The first section of this chapter is a summary of the results of our study on the healthy WM in the vervet monkey brain with x-ray nano-holotomography (XNH) in Contribution I: *"Axon morphology is modulated by the local environment and impacts the noninvasive investigation of its structure–function relationship"* [44]. Next, what can x-ray nanotomography reveal about the organisation of WM in disease? The second section of this chapter takes the step from healthy WM to the diseased WM and summarises our findings from a structure-tensor (ST) tractography analysis in the CC of mice treated with a Cuprizone (CPZ) demyelination model, based on Contribution III [129]. The last section outlines the perspectives of the work, and potential next steps in imaging of the 3D tissue microstructure.

5.1 Contribution I: "Axon morphology is modulated by the local white matter environment and impacts the noninvasive investigation of its structure-function relationship"

This summary of Contribution I aims to give an overarching view of the results and implications of the study. As such, it excludes many of the technical and quantitative details that are present in [44] and included at the end of this thesis, to which the interested reader is referred.

5.1.1 Aim

Axon diameter and conduction velocity (CV) are closely related. Although diffusion MRI techniques can estimate axon diameter, a 3D validation of the biophysical models used is required. 3D EM studies report varying diameters and trajectories on scales up to 20 μm. The aim of Contribution I was to characterise axon morphology in relation to the WM environment and neighbouring axons. We sought to investigate the potential sources of morphological variation in axons on length scales up to several hundred micrometres, and consider the implications for their estimated physiological function.

The same monkey brain as in Alexander et al. [13] and Dyrby et al. [64] in which the MRI-derived axon diameter estimates were larger than those estimated by histology was scanned with the ActiveAx MRI protocol (CC diameters shown in Figure 5.1). With synchrotron XNH, we then mapped the WM microstructure. Several XNH volumes were acquired from different WM regions, as shown in Figure 5.1. The primary characterisation of the morphologies of 54 axons was performed in the XNH volume of the splenium region, with a cylindrical FOV of height and diameter 153.6 μm and isotropic voxel size of 75 nm. The combination of several adjacent XNH volumes enabled a segmentation of cells, blood vessels and vacuoles within a volume of approximately $\sim 150 \times 150 \times 585\ \mu\text{m}^3$. Axons longer than 660 μm could be tracked and analysed within this extended volume, providing information on long-range axon behaviour. Diffusion was simulated within the extracted axons, and the effects of diameter and trajectory variations on the measurement of axon diameter via the diffusion process were investigated.

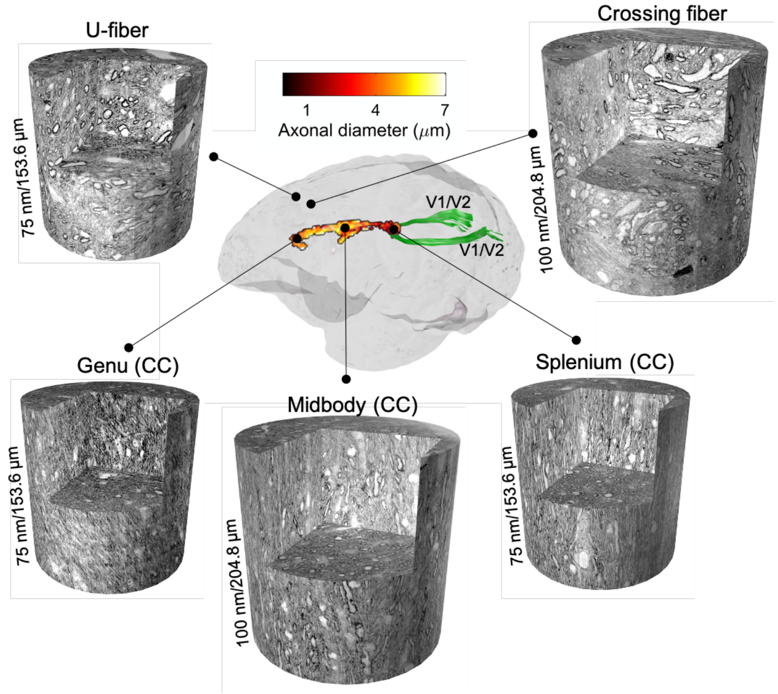

Figure 5.1: XNH volumes were acquired from several different WM regions of the vervet monkey brain in which ActiveAx overestimated axon diameter in the CC [13,64]. The colourbar represents the ActiveAx-estimated axon diameter. The splenium was selected for the primary analysis in Contribution I, and the interhemispheric tract connecting the visual cortices (V1/V2) and passing through the sample biopsy location was segmented by tractography (in green) as in Andersson et al. [44].

5.1.2 Methods

Diffusion Magnetic Resonance Imaging

The vervet monkey brain was scanned with the three-shell ActiveAx protocol using a maximal gradient strength of 300 mT/m for ex vivo tissue as in Dyrby et al. [64]. The acquisition used PGSE parameters: b-values, $b = [2011, 2957, 9529]$ s/mm^2; gradient durations $\delta = [5.6, 7.0, 10.5]$ ms; gradient separation, $\Delta = [12.1, 20.4, 16.9]$ ms and $G = [300, 219, 300]$ mT/m in $N_{dir} = [84, 87, 68]$ directions at echo time TE=36 ms. The voxel size of the MRI scans was isotropic 0.5 mm. After denoising [130] and the removal of Gibbs ringing artifacts [131] in MRTrix, the volume-weighted axon diameter was fitted to a region of interest spanning the midsagittal region of the CC. The interhemispheric connection linking the V1/V2 visual cortices and passing through the splenium was segmented with streamline-based deterministic tractography [132].

Synchrotron X-Ray Nano-Holotomography Imaging

The sample preparation process for the XNH experiments is shown in Figure 5.2 and was designed in line with the considerations described in Section 4.4.

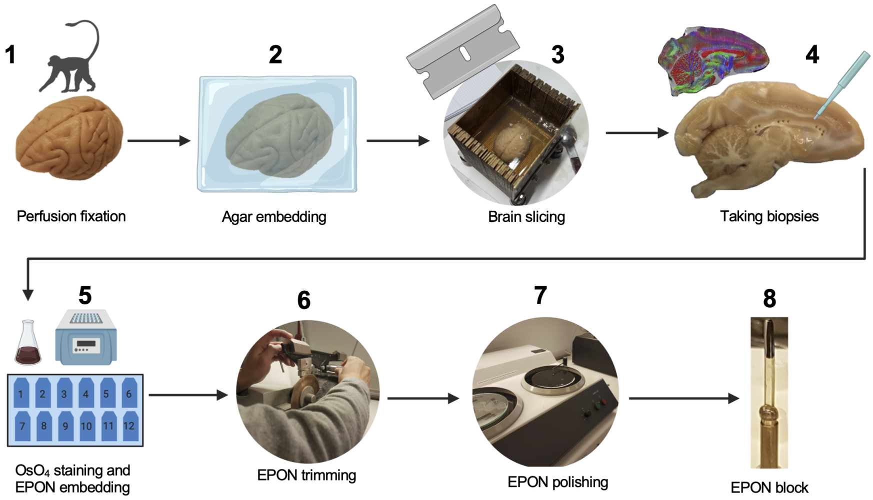

Figure 5.2: Schematic showing the tissue and sample preparation in preparation for XNH imaging. 1) Perfusion fixation of 32 month old female vervet monkey brain; 2) embedding of the brain in agarose for mechanical stability; 3) slicing of the brain into ~ 3 mm thick sagittal slices in a mold; 4) extracting Ø = 1 mm cylindrical biopsies from different WM locations, informed by a multi-fibre reconstruction of DWI images; 5) staining of the tissue samples with 0.5% osmium tetroxide and EPON embedding; 6) trimming of the EPON blocks with a circle saw; 7) polishing of the EPON blocks with a grinding-polishing machine equipped with sandpaper of varying fineness and 8) the final EPON-embedded sample.

XNH was performed at beamline ID16A of ESRF. A cone-beam setup (Figure

4.3) was used to acquire holograms at four different distances and an x-ray energy of 17 keV. Each XNH volume was acquired using 1800 rotation angles with an exposure time of 0.22 s, with a full scan taking ~ 4 hours. The phase retrieval and tomographic reconstruction were performed on-site.

Segmentation of Cell Clusters, Blood Vessels, Vacuoles and Axons

As described in cite [44], the XNH volumes were first downsampled by a factor of 5 to achieve volumes of dimension $410 \times 410 \times 410$ voxels with isotropic voxel size of 375 nm. This meant that the entire volumes, 32 GB large in their full resolution, could be loaded in image processing software. A rough segmentation of the axons from these volumes was then performed using the adaptive paintbrush in ITK-Snap. From the rough segmentation, the centreline of each axon could be estimated by calculating the slicewise centroid of the axonal cross section. With this as input, a MATLAB-based, in-house segmentation method was used to extract the axons and update their centerlines from the high-resolution volumes of voxel size 75 nm.

To segment the cell clusters, blood vessels and vacuoles, we used an intensity- and morphology-based approach in MATLAB. This was applied on the the downsampled (by a factor of 5) XNH volumes and made use of classic low-level image analysis operations such as intensity thresholds, morphological operations, and a connected components analysis [44].

Monte Carlo Simulations of Diffusion In Synthetic Axons

For each axon segmented from the XNH volumes, four morphological features were extracted. These were: i) the mean axon diameter, ii) the diameters along the axon trajectory (diameter variation), iii) the main axon direction (OD) and iv) the axon trajectory (microdispersion). By modelling the axons as deformable cylinders, five sets of synthetic substrates G1-G5 were created, with the axons in each substrate inheriting one or more of the aforementioned morphological features. Substrate G6 consisted of the XNH-segmented axons.

Simulations within the IAS of each axon were performed with the Monte Carlo Diffusion and Collision (MCDC) Simulator [133]. Each axon in each geometry G1-G6 was simulated separately, assuming an intrinsic ex-vivo diffusivity of $0.6 \cdot 10^{-10}$ m^{2}s^{-1} as measured in [64]. The positions of the uniformly initialised spins were recorded at integer diffusion times between 1 and 50 ms, at which point the mean-squared-displacements (MSD) parallel and perpendicular to the axon bundle (whole substrate) were saved. From the MSDs, the ADCs could be calculated using Equation 3.12 and the axon diameter could be estimated using $\lambda^2 = \frac{R^2}{2}$ [83], where R is the radius and λ^2 is the MSD in the perpendicular direction.

5.1.3 Results and Discussion

Volumetric Mesoscopic WM Features

Myelinated axons, cell nuclei and blood vessels were identifiable in the XNH volumes as shown in Figures 5.3A-D. A segmentation (Figure 5.3F) of the cell clusters (blue), blood vessels (red) and vacuoles (green) was performed within the extended volume in Figure 5.3F. The segmentation revealed an even spatial distribution of vacuoles (volume fraction 1.5%), but a clear clustering of the cells (volume fraction 4.6%) along the direction of the axons, with many appearing to be anchored in the blood vessels (volume fraction 0.6%). On average, the cell nuclei had a diameter of 5.5 μm (SD $=$ 0.73 μm, $N = 38$). Each cell cluster thus contained an average of 12 cells. A detailed morphological analysis of these structures is provided in [44]. A similar WM organisation was observed in the midbody (Figure 5.1). One WM feature that could not be observed, however, was the ECS – likely due to the dehydration of the tissue as part of the sample preparation. It is unknown how much, if any, shrinkage the various WM compartments are subject to as part of the tissue processing. In Töpperwien et al. [126], shrinkage of the diameters of different cell types in paraffin-embedded tissue to $63 - 93\%$ of their values in hydrated tissue is reported, but the authors stress that these values should be interpreted with caution as they are based on measurements of few cells. While it is possible that the reported volume fractions and quantitative measures of the WM structures are skewed as a result of the tissue processing, they shed light on the relative prevalence and spatial distribution of cells, blood vessels and vacuoles. Whether or not vacuoles are a WM feature or an artifact requires further investigation. Similar vacuoles are found in 3D EM studies of the mouse CC [17], but can also be associated with WM pathologies [134] and artifacts related to sample processing [52].

G-ratio variations along single axons are driven by axon diameter variations. Large axons (>2 μm in diameter) and their Nodes of Ranvier could also be segmented from the extended volume, as shown in Figure 5.3G. In six axons, each with two discernible Nodes of Ranvier, the g-ratios and CVs along the internode between the two nodes could be calculated according to Equation 2.1 through a quantification of the inner and outer axon diameters.

The results showed that individual internodes exhibit a distribution of g-ratios. Along the internodes, the myelin thickness was found to be stable, implying that the g-ratio – and thus CV – variations are driven by changes in axon diameter [44]. The average theoretical CVs are higher than those reported from LM in the larger macaque brain [59], but this can be attributed to the fact that we studied the largest – and thus, fastest – axons.

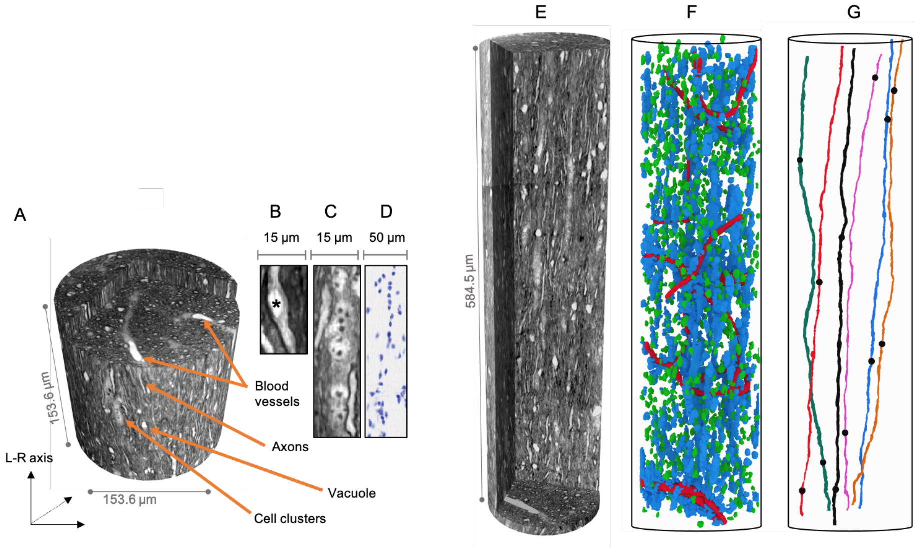

Figure 5.3: A) Axons, cells, blood vessels and vacuoles could be identified in the isotropic 75 nm resolution XNH volume of the vervet monkey splenium. B) Vacuoles (marked by asterisk) could sometimes be found within the axon. C) The cell nuclei clustered parallel to the axons and exhibited dense DNA inclusions. D) LM Nissl-stain light image showing cell nuclei in the splenium region of an age-matched monkey (BrainMaps: An Interactive Multiresolution Brain Atlas; brainmaps.org). E) Four consecutive XNH volumes like that shown in A were acquired and could be overlapped to form an extended volume of height 584.5 μm. F) The cells (blue), blood vessels (red) and vacuoles (green) were segmented in the extended volume. G) Six long axons, each with two identifiable Nodes of Ranvier (filled black circles) were segmented from the extended volume. Figure modified from [44].

Modulation of Axon Morphology by the Local Environment

Diameter variations. A high resolution quantification of the diameter variations of a 662 μm long axon, as shown in Figure 5.4A, revealed that diameter decreases occurred in conjunction with Nodes of Ranvier, as expected from literature [9, 135–137], and in response to vacuoles. Axon diameter has been shown to be regulated by the axonal cytoskeleton [138] which, when exposed to a decrease or increase in tension, can regulate diameter upwards or downwards, respectively [139, 140]. It is possible that extra-axonal structures such as vacuoles place tension on the cytoskeleteon, triggering a decrease in diameter. From their 3D EM studies, Abdollahzadeh et al. [17] and Lee et al. [94] could attribute local axon diameter increases to the presence of mitochondria, but they could not be identified here. Axon diameter increases have also been demonstrated as a result of signal firing in unmyelinated axons [23, 141, 142]. The XNH volumes provide a structural map of the WM environment, but since they provide only a static snapshot of the tissue, activity-dependent structural effects cannot be captured. The in-vivo morphologies of axons may thus be more varying and complex than those described here.

Trajectory variations. Cell clusters, other axons and blood vessels were found to cause significant trajectory changes in the axons, as illustrated in Figures 5.4B-D. The theoretical undulation of the IAS has been shown to cause an overestimation of axon diameter in [92–94]. Considering our findings on the relationship between cell clusters and axonal trajectories, the question of how axonal trajectories may be affected in a pathological case arises. Neuroinflammatory responses as a result of disease or trauma can cause an accumulation of microglia, macrophages and astrocytes in the ECS [143, 144]. An increased density of extra-axonal structures may potentially alter axonal trajectories and bias axon diameter measurements. Similar to how neurite beading has been shown to decrease the ADC after ischemic stroke [145], a reduced parallel ADC due to the the modulation of axonal trajectory could potentially act as a diffusion MRI-sensitive biomarker of inflammation.

Morphologies of Axons

To quantify the Morphologies of axons, 54 axons were segmented from the single XNH volume shown in Figure 5.3A in 75 nm isotropic resolution using a layered-surface segmentation algorithm, described in [44]. The segmentations are shown in Figure 5.5A. The equivalent diameters were quantified every 150 nm perpendicular to the local axon trajectory and calculated to be the diameter of a circle

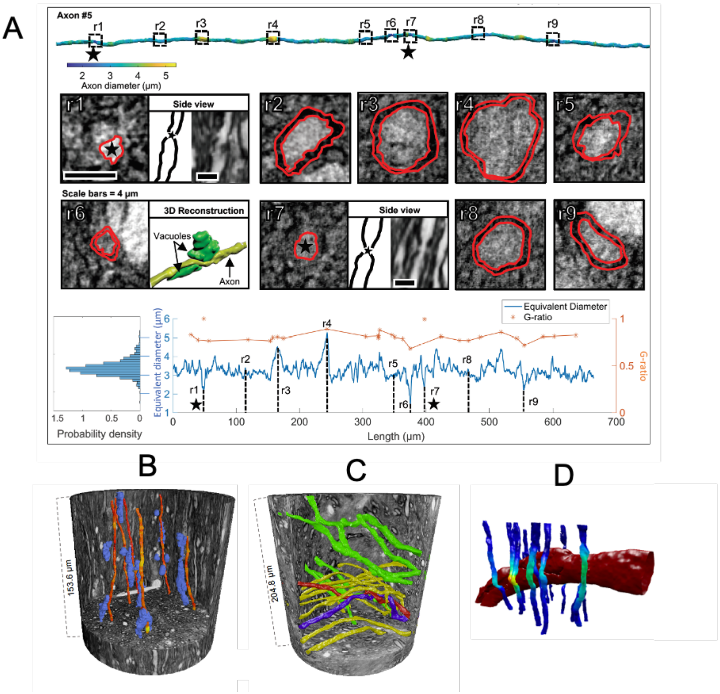

Figure 5.4: A) The equivalent diameter of single axon spanning the extended volume in Figures 5.3E-G was quantified every 150 nm of its 662 μm long trajectory. Along its length, the diameter varied between 1.5 and 5.3 μm and averaged at 3.3 μm. The axon is shown in the native XNH volume at ROIs labelled r1-r9. The lower plot shows how the calculated g-ratio (in orange) varies in tune with the equivalent axon diameter (in blue). For this axon, the most significant diameter decreases can be attributed to the presence of vacuoles or Nodes of Ranvier. B) The trajectories of segmented axons (orange) skirt around cell clusters (blue) – only a selection of the axons/cell clusters is shown for clarity. C) Segmentation of axons from a crossing fiber region show how axons travelling in different directions (yellow, green) navigate around each other. In particular, two axons (red, yellow) are seen to twist around each other. D) Axons bend around a blood vessel, deviating from their predicted linear trajectories based on their positions above and below the blood vessel. Strong deviation: yellow, little/no deviation: dark blue. Figure modified from [44].

with the same area as the local axonal cross-section, as in [17, 18]. All axons exceeded 120 μm in length and there were therefore at least 800 measurement points per axon.

Large axons have non-specific diameters. In referring to diameter variations occurring along individual axons, the terms "longitudinal" axon diameter and axon diameter distribution (ADD) are used. The segmented axons had mean diameters between 2 and 4 μm, and the ADD of all measured cross-sections in the 54-axon population is shown in Figure 5.5B. A positive correlation between mean axon diameter and the standard deviation of the longitudinal ADD was found. In other words, the larger axons exhibited larger diameter variations than the smaller ones, as demonstrated by the wider longitudinal ADD of the largest-diameter axon in Figure 5.5B compared to that of the smallest axon. From a computational point of view, the morphological non-specificity of large axons compared to their smaller counterparts could indicate that they encode different information [30, 146]. It may thus be valuable to consider a categorisation of axons by diameter, like that of the peripheral nervous system [147]. The correlation between axon diameter and neuron soma size [148] also supports a potential categorisation of axons into size-specific categories.

The wider longitudinal ADDs of large axons could potentially also explain the characteristic heavier tail of the ADD at large diameters, compared to at small diameters. Furthermore, this perspective on the longitudinal ADD of large axons suggests that the "giant axons" [16, 60] observed in 2D histological slices may not represent axons with very large mean diameters, but instead the diameter variations along large axons. This effect of sampling local diameter variations, combined with the observed constant myelin thickness along axons, may to some extent drive Berthold's observed log-linear relationship between axon diameter and the number of myelin lamellae [31] (Equation 2.2).

Implications for diameter and g-ratio measurements with classical histology. To shed light on the robustness of 2D measurements, like those performed with conventional LM and EM, we assessed how many measurements of axon diameter were required to accurately estimate the mean diameter of a) the single long axon in Figure 5.4A and b) the mean diameter of the 54-axon population. We found that the long axon required sampling (in the plane perpendicular to its local trajectory) for up to 200 μm at intervals of 150 nm until the cumulative mean diameter was stable to within ±150 nm of the mean. The length of the axon that required sampling depended on the position along the axon at which sampling commenced. This entails that local diameter variations can significantly bias the estimate of mean diameter, even when a dense sampling over large distances is available. This stability estimate assumes that an axon has a well-defined mean diameter over its 662 μm long trajectory. In this case, it seems that it does, since the mean axon diameter is accurately estimated beyond 200 μm of sampling. For the long axon, the equivalent diameter was approximated in the plane perpendicular to the local axonal trajectory to prevent bias. In 2D, this would not be possible and measurements would be performed in the available image plane, which is frequently chosen to be approximately perpendicular to the direction of axons. Abdollahzahdeh et al. [17] showed that this aspect of 2D imaging also incurs substantial bias in the estimation of axon diameter. In stark contrast to the quantification of mean diameter in a single axon, we found that measuring the mean of the ADD in the xy-plane of the XNH volumes – similar to what would be done in 2D EM/LM – consistently gave accurate estimates of the mean ADD throughout the subvolume in which all axons were present. This highlights how morphological measurements in a single 2D plane are a sampling of the entire 3D morphology. Thus, accurate estimates of the mean of the 3D ADD are accessible via 2D histology, provided that there is a sufficiently large FOV and number of measurement points to avoid any bias caused by the presence of mesoscale structures such as blood vessels or cell clusters.

Axons exhibit dispersion on all length scales. On the bundle level, the axons exhibited a mean OD of 7° compared to the average bundle direction (Figure 5.5C) in the splenium of the CC. On the single-axon level, we quantified the microdispersion, representing the average angle between axon segments of a given length and the mean axon orientation (Figure 5.5D). This showed that axon dispersion exists on all probed length scales, from 1 to 30 μm. Nonstraightness has previously been observed in tracer labelled axons in [41–43] and in growing axons of the frog and chick [15, 149]. The observed microdispersion could thus be a combination of the effects of axonal growth and the extra-axonal obstacles that cause trajectory variations.

Impact of Realistic Axon Morphology on Diffusion MRI Measurements

The MC simulations showed that any morphological deviation from cylinders causes a time-dependent overestimation of axon diameter, as shown in Figure 5.6B.

The need to account for a general OD, as exhibited in substrate G2, is thus confirmed [13, 14, 64, 150]. There exist methods to account for general OD effects [91, 113, 151], but none to remove the bias caused by microdispersion or diameter variations seen in substrates G2-G6. The realistic axonal geometries

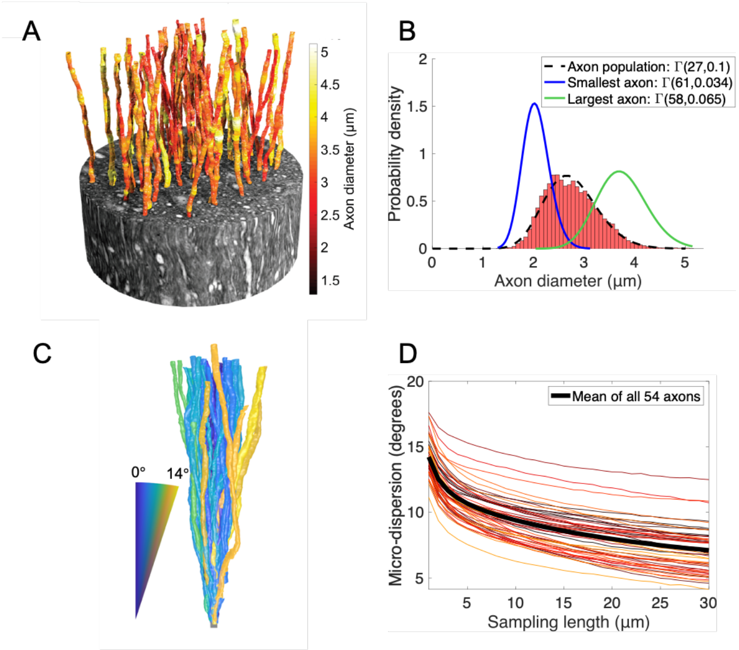

Figure 5.5: A) 54 segmented axons from the splenium of the vervet monkey, ranging between 2-4 μm in average diameter and >120 μm in length. B) Fits of a gamma distribution to the 3D ADD of all cross sections in the axon population (black striped line), and to the longitudinal ADDs of the thickest (green) and thinnest (blue) axons respectively. C) The axons are centred to a common origin to visualise their OD. The OD of each axon compared to the average bundle direction is represented by the colorbar. D) There exists microdispersion on all length scales from 1 to 30 μm. Figure modified from [44].

also cause a time-dependence of the parallel ADC which may be another source of bias in axon diameter measurements, as the parallel ADC is commonly used in place of the intrinsic diffusivity in Equation 3.32. For all diffusion times up to 50 ms, the difference between the intrinsic ADC and the estimated parallel ADC was most substantial for substrates that exhibited trajectory variations than for those that exhibited diameter variations e.g. substrate G4 vs. G3. However, the time dependence was steeper for substrates with diameter variations, and it is possible that diameter variations have a stronger effect on the parallel ADC than trajectory variations on longer time scales, although these are typically not applied in PGSE acquisitions for estimation of axon diameter. The time-dependence of the parallel ADC up to 100 ms is also demonstrated in

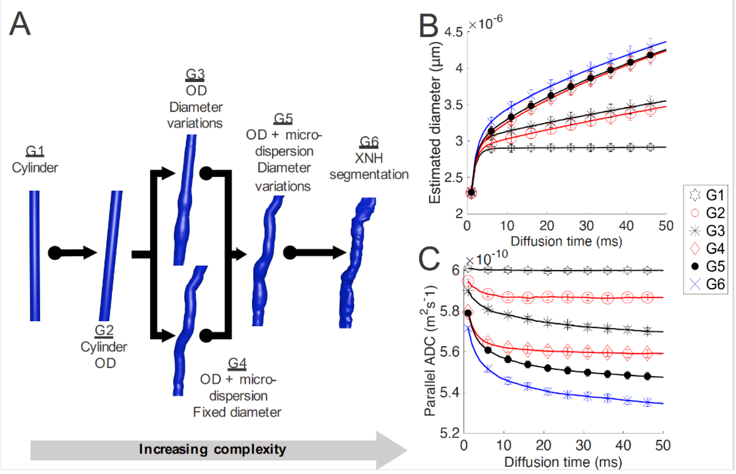

Figure 5.6: (A) The morphological features of the XNH-segmented axons in Figs. 3 and 4 are directly mapped to the six different axon classes generated for MC simulations. G1, straight cylinders of diameter corresponding to XNH axon mean diameters; G2, same as G1 plus segmented OD; G3, segmented OD and longitudinal ADD; G4, segmented OD and microdispersion; G5, segmented OD, microdispersion, and longitudinal ADD; and G6, the XNH segmentation. (B) The variation of estimated axon diameter and (C) parallel intra-axonal ADC with diffusion time for geometries G1–G6. Error bars represent the SE, reflecting the spread in diameters/ADCs across the individual axons. Figure from [44].

the axons from 3D EM of the mouse CC in Lee et al. [94]. In these, the diameter variations caused a larger discrepancy between the intrinsic ADC and parallel ADC than simply the trajectory variations. There may be several reasons for this difference, one of which could be that that smaller axons, like those in Lee et al., have a higher surface to volume ratio, meaning that a higher fraction of spins probe the effects of the diameter variations compared to in the larger axons. Regardless of source, the observed time dependence of the parallel ADC in the IAS could contribute to the time dependence observed in other studies [152], as is suggested by Fieremans et al. [153].

5.1.4 Conclusions

The interplay between extra-axonal structures and the micromorphology of axons was demonstrated through the segmentation and analysis of high resolution 3D XNH volumes from the WM of a vervet monkey brain. We find that axon diameter and trajectory vary along the length of the axon, often due to obstacles in the local microstructural environment. Consequently, we question the validity of enforcing cylindrical geometries in axonal structure–function relationships and postulate that the morphological non-specificity of large axons may entail non-specificity of their CVs. Furthermore, we show that 3D morphologies of axons may drive previously reported trends in 2D ADDs and g-ratio distributions. These results have significant impact for axon diameter determination with 2D techniques and — as we show here — diffusion MRI. The quantifications of OD, microdispersion and axon diameter variations could also be used to guide the construction of anatomically informed axonal phantoms for MC simulations.

Naturally, the study has several limitations that call for further investigation. Firstly, the combination of SNR and image resolution challenged the segmentation of axons smaller than $\sim 2\ \mu$m, and the morphological characteristics of smaller axons – believed to account for the majority of the ADD in WM – remains to be studied. Combination of XNH with methods like EM and diattenuation imaging [50] would be valuable for mapping fiber microstructure across different scales and resolutions. Secondly, it was not possible to segment the ECS from the XNH volumes. The structure and diffusion characteristics of the ECS is an important question in diffusion MRI. Techniques that preserve the hydrated tissue environment e.g. cryo-EM [154] and super-resolution shadow imaging [155] may provide avenues for characterisation and exploration of the ECS. As would tissue preparation procedures that preserve the architcture of the hydrated environment, for later imaging with XNH or EM. Chapter 5.3.1 further discusses imaging of the innate, hydrated WM environment. Lastly, we studied here the tissue from a single 32-mo old, female vervet monkey. The quantifications of axonal diameter and trajectory variation in Figure 5.5 may differ with species, age, gender, and disease, and it is relevant to pursue further studies into this matter.

5.2 Organisation of the White Matter in Health and Disease

5.2.1 Aim

To better understand how the microstructural architecture of WM couples to the diffusion MRI signal on the voxel scale, its micro-, meso- and macrostructural characteristics must be investigated. It is also important to identify how pathologies affect these structural characteristics and are expressed in the diffusion MRI signal to identify potential early biomarkers of disease. In Contribution I, the microstructural characteristics of axons were quantified. The aim of the work presented in this section and in Contribution III [129] was instead to study the meso- and macro-characteristics of axons through a 3D Structure Tensor (ST) analysis. The ST analysis was applied to X-ray nanotomography volumes of the CC of healthy mice and mice treated with a Cuprizone (CPZ) diet. CPZ diets are used as animal models of demyelination [156, 157], similar to what occurs in Multiple Sclerosis. The ST analysis provides among other things a measure of the local main direction. In fibre-rich samples such as the WM this enables deterministic tractography, which we perform to delineate and visualise tracts extending through the tissue samples.

5.2.2 Methods

Mouse Tissue

The tissue belonged to a) a 13 week-old female C57BL/6 mouse fed with a normal diet, and b) a 13 week-old female C57BL/6 mouse fed with a 0.2% CPZ diet for a duration of 5 weeks, beginning at age 7-8 weeks, before which it was fed a normal diet. The tissue was perfusion fixed with 4% paraformaldehyde, before being processed for synchrotron imaging.

Synchrotron Imaging

The sample preparation process for the synchrotron imaging experiments was similar to that shown in Figure 5.2. The mouse brains were sliced into 1 mm thick coronal slices with a stainless steel matrix and razor blades. Samples from the CC were extracted under a microscope by scalpel and excised to be approximately 500-800 μm thick and several millimetres long. Following this, the samples were fixed in Glutaraldehyde for 24 hrs, and subsequently stained with 0.5% osmium tetroxide for 2 hrs. After dehydration with an alcohol sequence, the samples were embedded in EPON and polished so that the final EPON blocks containing the sample were no more than 700 μm thick to prevent excessive absorption.

X-ray nanotomography was performed at beamline P10 of DESY using the parallel beam configuration at an energy of approximately 13 keV, shown in Figure 4.2A, producing volumes with large FOV and an isotropic voxel size of 550 nm. Additionally, the samples were scanned at beamline ID16A of ESRF with the cone-beam setup (Figure 4.3), giving XNH volumes of smaller FOV, but voxel sizes of 75-100 nm.

ST Analysis and Tractography

The 3D ST analysis was similar to that in Khan et al. [158]. The parameters σ and ρ control the degree of smoothing applied to the image and the neighbourhood size over which the ST is calculated, respectively. Appropriate values of σ and ρ are dataset-dependent and depend on the SNR and the size of the structure to which the ST should be sensitive. For the large FOV DESY datasets, the parameters were: $\sigma = 1$ and $\rho = 4$, but for the ESRF dataset the parameters were chosen to be $\sigma = 1$ and $\rho = 6$. These parameters resulted in patch sizes of 18.7 μm and 9.4 μm for the DESY/ESRF datasets respectively.

Similar to the DT in diffusion tensor imaging [159,160], the ST was decomposed into eigenvectors and eigenvalues, $\lambda' = [\lambda'_1, \lambda'_2, \lambda'_3]$. The STs from histological images, however, are different from those obtained from the diffusion MRI signal [158]. In the ST, the direction corresponding to the smallest eigenvalue represents the principle directions of highly anisotropic structures such as axons. In the DT, the principle direction of anisotropy is represented by the direction with the largest eigenvalue.

Deterministic tractography was performed based on the smallest eigenvector of the ST using the MRTrix3 toolbox [161]. For each dataset, seeding point regions were manually defined to control the start- and endpoints of the streamlines. Furthermore, rejection masks were implemented to limit where streamlines could travel and terminate, based on intensity thresholding of the images to eliminate regions or structures that did not include axons e.g. blood vessels, cells. This was followed by image closing or opening to remove holes or spurious voxels. To reduce the number of streamlines for visualisation, the QuickBundles streamline clustering algorithm [162] was used. The clustering entailed that the streamlines were likely to represent the direction of axon bundles, as opposed to individual axons.

5.2.3 Results and Discussion

In the large-FOV DESY image volumes, several fibre tracts were identifiable, including the CC and cingulum bundle. Although the axons were too small to segment, their general alignment in the left-right orientation was apparent (Figure 5.7). In the CPZ-treated tissue, the lesioned area was characterised by lower electron density owing to the demyelination, while the myelinated, normal appearing white matter (NAWM) was not visibly different to the tissue from the control brain. The higher resolution XNH volumes revealed cell processes, cell clusters and blood vessels in all volumes, and what appeared to be myelin debris in the CPZ-treated lesion area (Figure 5.7). Even at the higher resolutions of 50 to 70 nm, the axons were too small to be segmented, in contrast to those from the vervet monkey splenium in Figure 5.3. This agrees with the findings that mammalian species with larger brains have an increased number of large axons (see Section 2.4) [68].

Although they are not marked, there are potentially two other tracts just inferior to the CC: the dorsal fornix tract and the alveus tract. The existence of a tract inferior to the CC was more clear in Figure 5.7A where there was a discernible intensity difference in the CC and the tract underneath it, but the same was not true for the CPZ-treated tissue in Figure 5.7D. The difference in stucture of the tissue between the two volumes in Figures 5.7A and D could be due to slightly different positions of the tissue samples within the 1 mm thick coronal slice from which they were excised.

The calculated ST map for the large-FOV DESY volume of the CPZ-treated tissue is shown in Figure 5.8. The categorisation of different tracts becomes very clear with the ST; the CC region matched that of the CC axons which have a left-right orientation, while the cingulum bundle has an anterior-posterior orientation, as expected. The ST showed a predominant left-right orientation, even in the lesioned area. Thus, despite the myelin providing the primary source of image contrast, the ST could detect more subtle gradients that ensured a homogeneous ST orientation throughout the CC.

The tissue inferior to the CC, belonging to the hippocampus, showed a heterogeneous distribution of ST orientations. This is due to the high density of cells, the somewhat spherical shapes of which may cause the predominant ST orientation to be arbitrary and subject to local intensity fluctuations in the image,

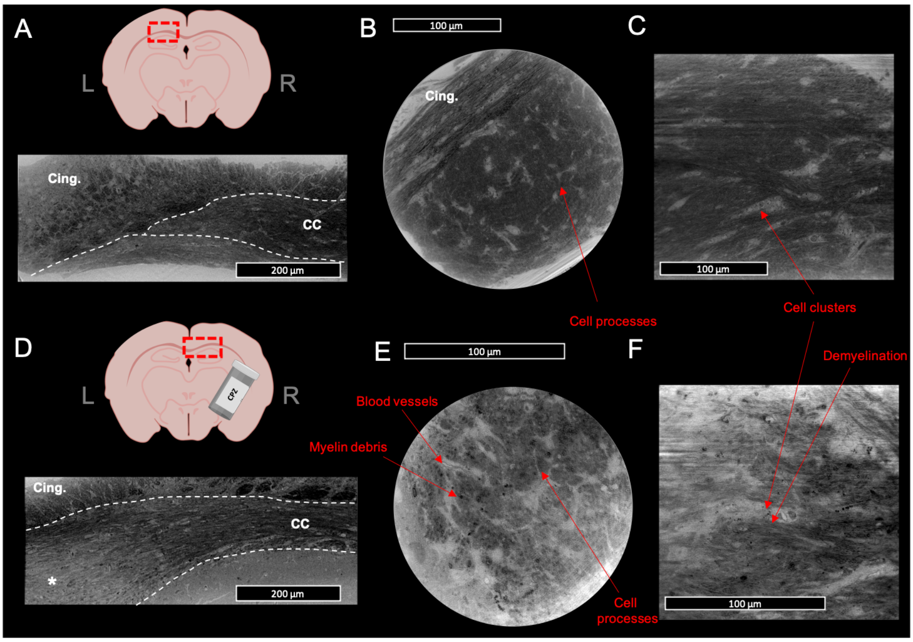

Figure 5.7: A) In a coronal slice of the control brain containing the splenium CC, tissue was extracted in the region of the red striped box. The large FOV DESY image volume shows the CC and cingulum. B-C) Orthogonal views of slices from the high resolution (75 nm) ESRF XNH volume, showing the cingulum, CC and with visible cell clusters and cell processes. D) In a coronal slice of the CPZ-fed mouse brain containing the splenium CC, tissue was extracted in the approximate region of the red striped box. The large FOV DESY image volume shows the CC and cingulum. The CC can be divided into two categories: NAWM and a lesioned area, marked by the asterisk. E-F) Orthogonal views of slices from the high resolution (50 nm) ESRF XNH volume in the lesioned area, with visible cell clusters, cell processes, blood vessels and myelin debris.

caused by e.g. noise.

The tractography streamlines for the image volumes in Figures 5.7A-D are shown in Figure 5.9..

In the large FOV volumes in Figures 5.9A and C, the CC streamlines projected through the entire CC in Figure 5.7A,D, including through the lesioned area of the CPZ-treated tissue. In the high resolution ESRF XNH volume in

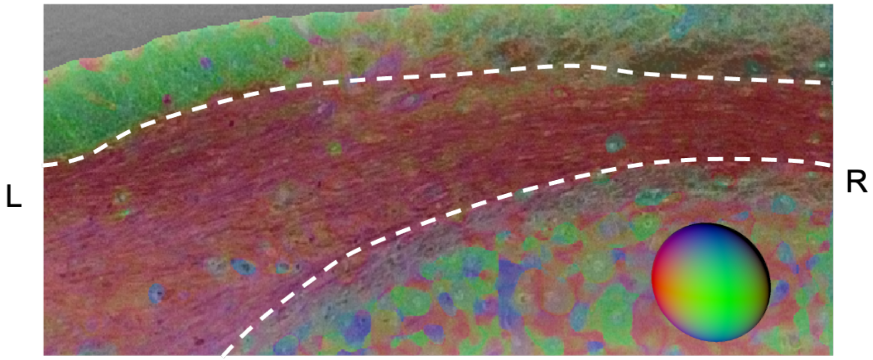

Figure 5.8: The ST for voxels in a slice of the large FOV DESY image volume of the lesioned tissue. The colour represents the ST orientation. Red: left-right, blue: inferior-superior, green: anterior-posterior. The STs in the CC region were predominantly oriented in the left-right direction, while the cingulum STs exhibited an anterior-posterior orientation.

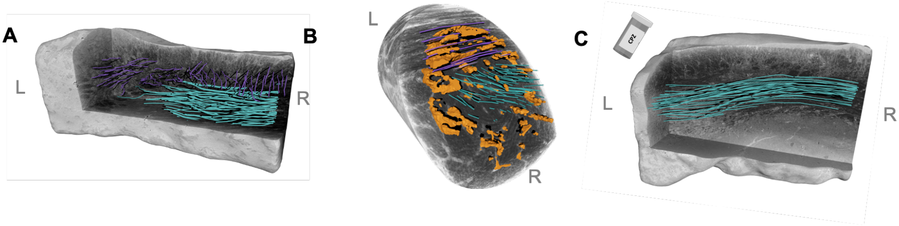

Figure 5.9: A) Tractography streamlines in the CC (cyan) and cingulum (purple) regions of the control tissue, in the large FOV DESY image volume. B) Tractography streamlines in the CC (cyan) and cingulum (purple) regions of the control tissue, in the high resolution (75 nm) ESRF image volume presented in [129]. Segmented cells are shown in orange. C) Tractography streamlines in the CC region of the CPZ-treated tissue. In the large FOV DESY image volume. The streamlines extended from myelinated region (NAWM) into the lesioned area.

which extra-axonal structures are visible, it was clear how the cells clustered and aligned with the axons, as found in the vervet monkey splenium [44].

The streamlines represent the paths of axon fascicles. The fascicular nature of the fibre organisation is most apparent in Figure 5.7C. Thus, even if the individual axons of the mouse brain cannot be tracked, it is possible to track individual tracts and fascicles. Their dispersion on different length scales could be quantified in the same way as the individual axons in Contribution I [44]. Such an analysis within large FOVs such as those presented in Figures 5.9A and C would be very valuable in determining the connectivity and organisation of different brain regions. Additionally, a fibre orientation dispersion (FOD) analysis could be performed on the data for comparison with diffusion MRI or histology derived FOD estimates [163–169].

5.2.4 Conclusion

A 3D ST analysis of x-ray nano-tomography and XNH volumes, combined with tractography, can reveal the macrostructural organisation of axonal fascicles in both healthy and pathological WM tissue samples across different FOVs and resolutions. Despite the demyelination in the CPZ treated tissue, the axonal organisation seems to be preserved and it is possible that the axoplasm itself remains intact. Had the axonal membranes been completely compromised, it is possible that the ST would resemble the hippocampal regions and exhibit a heterogeneous map of ST orientations, as opposed to the homogeneous ST orientation throughout the lesion area. The 3D ST and tractography analysis may, therefore, be a powerful tool for uncovering the microstructural signatures of pathology in cases where the image resolution is too small for segmentation of the structures of interest.

A future analysis of the FODs, like in the ST analysis of 3D EM volumes by Salo et al. [169], and a quantification of fractional anisotropies and fascicle trajectories could guide the development of new diffusion MRI biophysical models and act as ground-truth data for the validation of diffusion MRI derived FODs. Since axon morphology is affected by the presence of extra-axonal structures, such as cells, such metrics would give valuable information on the organisation of axon bundles in disease vs. health.

5.3 Towards a Characterisation of the Innate and Full White Matter Environment

5.3.1 Imaging the Innate White Matter Environment

There is uncertainty about the effects of different sample processing techniques on the microstructure. When we use imaging techniques such as XNH, LM or EM to validate diffusion MRI measurements, in which the tissue is always hydrated, we may be comparing two inherently different tissue environments. Ways to image the tissue microstructure without structural changes to all compartments are therefore of the utmost importance.

Imaging hydrated tissue with x-ray nanotomography is one alternative, as done for studies of the unstained mouse cerebellum in [126]. Using the direct-contrast parallel beam setup in Figure 4.2A, we imaged the hydrated genu of the vervet monkey brain, stained with 0.5% osmium tetroxide and stored in agar and PBS, at DESY. The reconstructed image volume is shown in Figure 5.10.

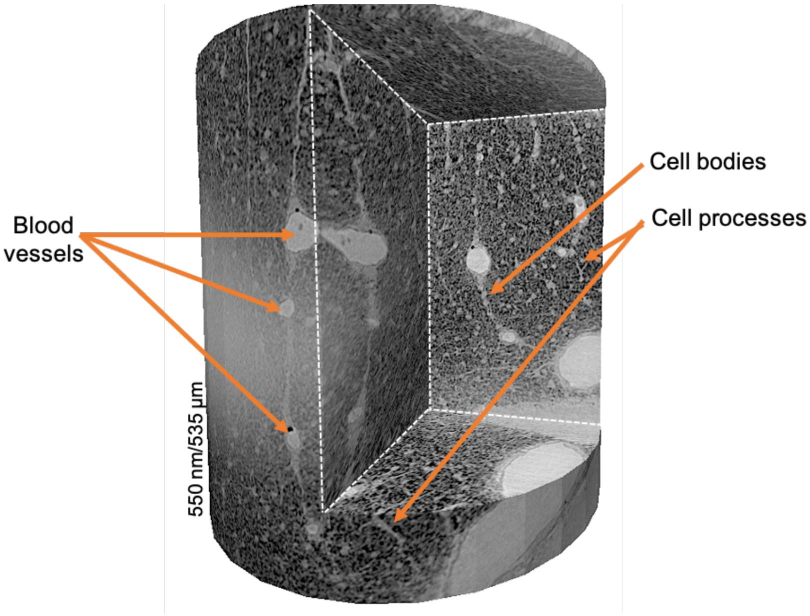

Figure 5.10: X-ray nanotomography volume of a hydrated sample from the vervet monkey genu, acquired at beamline P10 of DESY and stained with 0.5% osmium tetroxide. The brain is that used in [44]. The height of the cylindrical FOV is 535 μm and the voxel size is isotropic 550 nm. Blood vessels, cells and their processes are visible against the dense background of myelinated axons.

Inspection of the hydrated volume revealed the presence of the vessel system and cell clusters, confirming the finding in Contribution I [44] that cell clusters are closely associated with or "anchored" in blood vessels. Another identifiable feature in the hydrated volume was the cellular processes that manifested as 'star like', branching and bright tubular regions. These were not visible to the same extent in the dehydrated, EPON-embedded tissue samples of Contribution I. Furthermore, the voxel size of 550 nm entailed that a segmentation of the genu axons was not possible, but their density appeared to be high and the majority of image contrast arose from their stained myelin sheaths.

Imaging hydrated samples at higher resolution in an XNH cone-beam setup is problematic, since the high water content causes a significant absorption of the x-rays and a low SNR in the resulting reconstructed volume. Focussing the x-rays into a small volume, as is done in the cone-beam geometry in Figure 4.2, may heat and destruct the tissue during the process of the scan. It is, however, possible. Bartels et al. studied the stained and hydrated optic nerve of the mouse with XNH at beamline P10 of DESY using a cone-beam setup [170]. Although both the species and the WM regions are different, Bartels et al. also observe the cell processes and – due to the larger diameters of the axons in the optic nerve – are able to resolve individual axons. Alternatively, the innate structural architecture of tissue can be preserved by high pressure freezing and freeze substitution. The samples can thereafter be embedded in EPON and imaged with x-ray nanotomography as demonstrated by Bartels et al. in the sciatic nerve of the mouse [170].

In order to access the morphology of the ECS, higher resolution is needed. The high pressure freezing and freeze substitution approach can be used in EM [55, 171] to preserve the ECS, and is one avenue that could be pursued to accurately estimate the relative volume fractions of all compartments. Another promising method is stimulation emission depleted microscopy and a labelling of the ECS using a fluorophore that does not permeate cells to image the ECS in live brain tissue, as demonstrated by Tønnesen et al. [155] in the hippocampus of the mouse brain. There are additional techniques that could be employed, but their discussion is beyond the scope of this thesis; the review by Soria et al. gives a comprehensive overview of the current (2020) status of ECS imaging [172].

5.3.2 Full segmentation of XNH volumes

Another limitation to characterising the full and innate WM environment is not only the imaging technique, but also the analysis of the obtained images. For example, it is clear that the XNH volumes in Contribution I (Section 5.1) contain more than 54 axons. However, the process of segmenting the axons at 75 nm isotropic resolution and handling the 32 GB large image volumes was time consuming. Although the segmentation was semi-automatic, it relied on a clear myelin boundary between the axoplasm and ECS, and therefore had to be corrected manually in e.g. Nodes of Ranvier or regions of lower contrast.

To obtain more information from the XNH volumes, an MSc project was formulated in connection with the PhD project with the aim of using convolutional neural networks (CNN) to segment as much of the IAS as possible. Figure 5.11 shows the preliminary results of applying a 3D U-Net inspired by [173] to the extended XNH volumes of a crossing fibre region and the splenium region. The network was trained on only the XNH volumes from the organised splenium. The segmentations of splenium axons, cells, blood vessels and vacuoles from Contribution I [44] were used as training and validation data (30% of the volume was reserved for validation and data augmentation). The network was applied to the extended splenium XNH volumes, but also the unseen XNH volumes of the very different crossing fibre region (Figure 5.1) in which it could be validated against the ground truth segmentation of axons presented in Contribution II (Chapter 6).

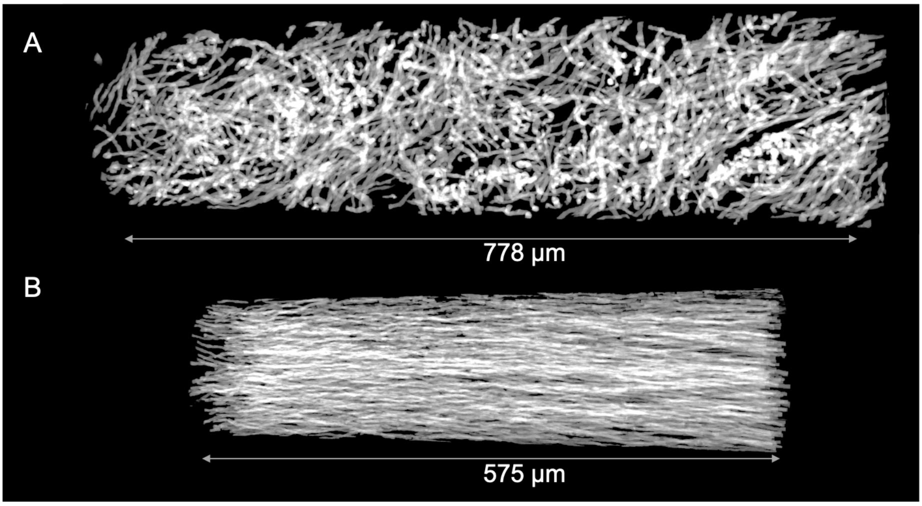

Figure 5.11: 3D U-Net segmentation of axons from the XNH volumes of the A) crossing fibre region and B) splenium regions of the vervet monkey brain in Figure 5.1 and [44]. The U-Net was developed by Harald Løvenskjold Mortensen as part of his MSc thesis.

The automated approach is able to segment thousands of axons from the XNH volumes, that would have taken significantly longer to segment with the approach in Contribution I. It thus shows potential as a tool to more completely segment the IAS for a morphological characterisation and analysis. The use of U-Net CNNs to segment neurons from XNH data has also recently been demonstrated by Kuan et al. [121] for the segmentation of neurons in the fruit fly (*drosophilia*) leg muscle. There already exist several recent automated approaches to segment 3D EM data [17, 18, 174, 175], and automating the image analysis approach provides a solution to handling and analysing the huge image data produced by 3D imaging techniques. Nonetheless, these approaches are not without caveats. It is not always clear how well they generalise to data with a slightly different appearance than that which they are trained on. The sample processing technique, image modality, resolution, sampled anatomy and the type of noise present may all affect their performance. A validation of the segmentations or anatomical metrics produced by such methods is thus needed and, in practise, this demands the use of – often difficult to obtain – ground truth labelled data.

Chapter 6

Investigation into Powder Averaging as a Means of Reducing Bias in Diffusion MRI Axon Diameter Estimates

---

With knowledge of the realistic 3D morphologies of axons in different WM regions, it is possible to validate different diffusion MRI-based methods of measuring axon diameter. Recently, powder averaging (PA) techniques have emerged as a way of removing dispersion related biases in the axon diameter measurement. This chapter, a summary of Contribution II, is devoted to the methodological investigation of two of these methods: the spherical mean technique (SMT) and a power law (PL) implementation. Using the segmented axons from our XNH investigations, the SMT and PL approaches are validated in segmented axons from the splenium and crossing fibre regions of the vervet monkey brain.

Throughout this chapter, we refer to three classes of orientation effects: 1) the macroscopic fibre architecture, describing the the relative orientations of different fibre bundles e.g. in crossing fibre regions; 2) the OD, describing the average dispersion exhibited by axons within each bundle; and 3) the microdispersion, describing the changes in trajectory and curvature along individual axons on the length scale of the measured diffusion.

6.1 Aim

It has been shown that axonal diameter variations, general OD and microscale trajectory variations (referred to hereafter as microdispersion) bias axon diameter measurements with diffusion MRI [18, 44, 111]. Recent work implements a PA approach to disentangle axon diameter from the OD in the entire brain – even in regions of fibre crossings – under in- and ex-vivo conditions. Fan et al. [176] use a multi-compartment SMT approach in the in-vivo human brain, while Veraart et al. [113] model only the IAS by fitting a PL to the PA signal at high b-values that suppress the signal from the ECS [177, 178]. This used $b \geq 20$ ms μm^{-2} for ex vivo experiments and $b \geq 6$ ms μm^{-2} for in vivo experiments. The SMT approach was applied to the in-vivo human brain, and the PL approach to both the in-vivo human and ex-vivo rat brains. Both implementations used a dense sampling of b-values. Although the PA techniques remove fibre architecture and OD effects, they rely on the assumption that the micro-domain probed by diffusing spins is cylindrical.

The theory of the effects of diameter and trajectory variations on estimated axon diameter has been laid out in [111], but the diffusion times and b-values for which the PA-based axon diameter estimate becomes sensitive to the microdispersion in real axons is unknown. The signal-to-noise ratio (SNR) of the signal [96] and the gradient strength of the applied magnetic field [64] also place limits on the upper and lower bounds of measurable axon diameter. How different sequence parameters, the number of gradient directions or the SNRs affect these bounds has not been investigated for PA-based axon diameter estimates. Furthermore, although the PA is expected to factor out the effects of fibre crossings and OD, it has only been validated on segments of axons from the CC [111] in which the fibre architecture is simple and does not contain crossings

In Contribution II, we aimed to investigate the impact of different scanning parameters, SNR and fibre architectures on axon diameter estimates with PA-based approaches. The analysis is restricted to the IAS. The effects of SNR, the number of gradient directions, the selected b-values and the validity of assuming a fixed parallel ADC are explored. To assess the effects of $b-$value, microdispersion, and diffusion time on the estimates of the PL and SMT, we simulated diffusion within segmented axons of minimum length 120 μm from large FOV XNH volumes of the CC splenium and a complex crossing fiber region in the vervet monkey brain. This provided a validation of the PA approaches in both homogenous and complex WM architectures.

6.2 Methods

6.2.1 Simulations

The simulations in this study were divided into two categories: simulations of the signal from cylinders of different diameters and simulations in the IAS of segmented axons from XNH volumes of the vervet monkey brain presented in [44]. We restricted the analysis to signals from the IAS only, and did not model the ECS. Excerpts from the Methods of Contribution II are briefly presented here, but for a complete account of the technical details, the reader is referred to the full manuscript.

6.2.1.1 Simulating the Diffusion MRI Signal from Cylinders

For given PGSE parameters δ, Δ and G, the signal perpendicular to 75 cylinders of diameter 0.2 to 15.0 μm (at 0.2 μm intervals) was calculated using Equation 3.32, giving $D_\perp$ for each cylinder. The ADC in any direction was then calculated from:

$$ADC = \mathbf{G} \times \begin{pmatrix} D_{\|} & 0 & 0 \\ 0 & D_\perp & 0 \\ 0 & 0 & D_\perp \end{pmatrix} \times \mathbf{G}'$$

where $\mathbf{G}$ is the gradient vector and $D_{\|}$ was fixed.

Simulating Diffusion within the Realistic IAS from XNH Images of the Monkey Brain

The segmented axons originated from two different brain regions of the vervet monkey brain from [44]. We segmented 54 axons from the splenium of the CC and 58 axons from a "crossing fiber region", located in the anterior centrum semiovale where the diffusion MRI data indicated the crossing of the corticospinal tract, interhemispheric callosal fibres and association fibres [44]. All of axons were of minimum length 120 μm. Details of the XNH volumes, the segmentation of axons, and the analysis of the axon diameters is given in Section 5.1, Contribution I [44] and Contribution II.

For comparison with the diffusion MRI axon diameter estimates, the volume-weighted axon diameter, d, of each axon was estimated as $d = \sum_{N}^{i=1} 2R_i \cdot$

$\left(\frac{\pi R_i^2}{\sum_N^{i=1} \pi R_i^2}\right)$ where R_i is the ith measured radius of N equidistant measurement points along the axonal trajectories.

The MCDC simulator [133] was used to simulate diffusion within each axon mesh.

The Signal-to-Noise Ratio

The effect of noise on the axon diameter estimation was studied by adding Rician noise of variable SNR to the noise-free, normalised signals. The standard deviation of the noise was defined as $\sigma = \frac{1}{SNR}$. Rician distributed noise was simulated calculating the magnitude of complex Gaussian noise in which the real and imaginary components each had a standard deviation of σ [179].

Distinguishing the Signal from Noise

To assess whether or not a single signal could be distinguished from noise at a given SNR, we used the sensitivity criterion of Nilsson et al. [96] for parallel cylinders. The smallest robustly measurable change of the normalised signal, ΔS was defined as:

$$\Delta S = \frac{z_\alpha}{SNR\sqrt{n}} \tag{6.1}$$

where n was the number of repeated measurements and z_α was the z-threshold for the significance level α. The signal was thus said to be sensitive between the bounds $[\Delta S,\ 1 - \Delta S]$. The diameters that gave rise to the PA signal at these boundaries were defined as the maximum and minimum bounds of the measurable diameter. Here, we choose $\alpha = 0.05$, giving $z_\alpha = 1.64$, as in [96].

To predict whether the PA signal could be distinguished from normally distributed noise, the sensitivity criterion of Nilsson et al. [96] for fully dispersed cylinders was used. It is defined as:

$$\Delta S_{PA} = bD_\perp(d) \cdot \sqrt{\frac{\pi}{4} \frac{erf\left(\sqrt{b(D_\parallel - D_\perp)}\right)}{\sqrt{b(D_\parallel - D_\perp)}}} \tag{6.2}$$

where $D_{\perp}(d)$ is the perpendicular diffusivity of the diameter, d, that is defined as:

$$d = \left(\frac{768}{7}\frac{\Delta S D_0}{\gamma^2 \delta G^2}\right)^{\frac{1}{4}} \tag{6.3}$$

When using Eqs. 6.2 and 6.3, n in Eq. 6.1 was set to the number of unique gradient directions. From ΔS_{PA}, the theoretical range of measurable diameters was calculated as the diameters with PA signals within the range $[\Delta S_{PA}, S_{stick} - \Delta S]$ where S_{stick} is the signal of a cylinder with diameter equal to zero:

$$S_{stick} = \sqrt{\frac{\pi}{4b \cdot D_{||}}} \cdot erf(\sqrt{bD_{||}}) \tag{6.4}$$

Importantly, Eqs. 6.1-6.3 are formulated for single b-values only and assume that the noise follows a normal distribution.

6.2.2 Fitting the Spherical Mean Technique and Power Law to the PA signal

The Spherical Mean Technique Implementation

The SMT equation in Equation 3.36 was fitted to the PA signals with a Matlab-based Levenberg-Marquardt algorithm. Once $D_{\perp}$ had been fitted, the diameter was calculated using Equation 3.32. To assess the robustness of the SMT fit when keeping different variables fixed, three variations of the SMT fit were implemented:

(i) **SMT-1**: a single-shell fit to obtain $D_{\perp}$ in the range $[0, D_{||}]$. Assumes known f_a and $D_{||} = 0.6 \cdot 10^{-9}$ m^{2}s^{-1}.

(ii) **SMT-2**: a multi-shell fit to obtain $D_{\perp}$ in the range $[0, D_{||}]$ and f_a in the range $[0, 1]$. Assumes known $D_{||} = 0.6 \cdot 10^{-9}$ m^{2}s^{-1}.

(iii) **SMT-3**: a multi-shell fit to obtain $D_{\perp}$ in the range $[0, D_0 \cdot 1.5]$, f_a in the range $[0, 1]$ and $D_{||}$ in the range$[D_0/2, D_0 \cdot 1.5]$ where D_0 was the known intrinsic diffusivity of the simulations. For ex vivo simulations, $D_0 = 0.6 \cdot 10^{-9}$ m^{2}s^{-1} was used, while for in vivo simulations $D_0 = 2 \cdot 10^{-9}$ m^{2}s^{-1} was used.

The Power Law Implementation

To assess the diameter estimates from the PL formulation, the expression in Eq. 3.37 was fitted to the PA signal from cylinders of different diameters, providing estimates of $D_\perp$ and β. This allowed for a comparison of the PL-derived diameter, d_{PL}, with those from SMT-2 and SMT-3. To fit the PL the Matlab-based nonlinear least squares estimator provided by Veraart and Novikov [180] was used. This implementation assumed the Neuman limit as in Eq 3.34 to obtain a diameter estimate.

6.3 Results and Discussion

6.3.1 The Diffusion Time and q Influence the Lower and Upper Bounds of Measurable Diameter

At finite SNR – as is always the case experimentally – there are upper and lower bounds of measurable diameter that can be measured from the PA signal as shown in Figure 6.1B. For the high b-value sequence parameters in Figure 6.1A, increasing the SNR widens this range through a reduction of the lower bound and an increase of the upper bound. Increasing the diffusion encoding, $q = \gamma\delta G$ through an increase of the gradient strength lowers the lower bound, in accordance with the findings of Dyrby et al. [64] and Sepehrband et al. [69], but narrows the range of measurable diameters.

In general, the upper and lower bounds span a narrower range than those in methods that estimate axon diameter from measurements perpendicular to axons [13,14,64,65,91,181] (Equation 6.1). The narrower range occurs due to the requirement on the PA signal to be sensitive to all length scales present within an axon, and not only its diameter. The relative angle, α, between the applied gradient and the axis of the cylinder determines the size of the restriction. With increasing SNR (Fig. 6.1C, top row), the sensitivity to both the high and low α increases. Increasing the q-value (bottom row) increases sensitivity to high α, but reduces sensitivity to low α. This is because the q-value and the diffusion time of the acquisition act as spatial filters, restricting the maximum detectable displacements of the spins. A higher q-value increases the sensitivity of the acquisition to smaller length scales in directions perpendicular to the cylinder. However, if the q-value is high enough to cause attenuation of the signal from an ensemble of spins before they have diffused for the entire diffusion time, the acquisition loses sensitivity in the axial direction and the upper bound of measurable diameters decreases. For given PGSE parameters, the sensitivity profiles to axons of different diameter will differ. It is therefore important to keep in mind the range of expected diameters in the substrate when designing an acquisition.

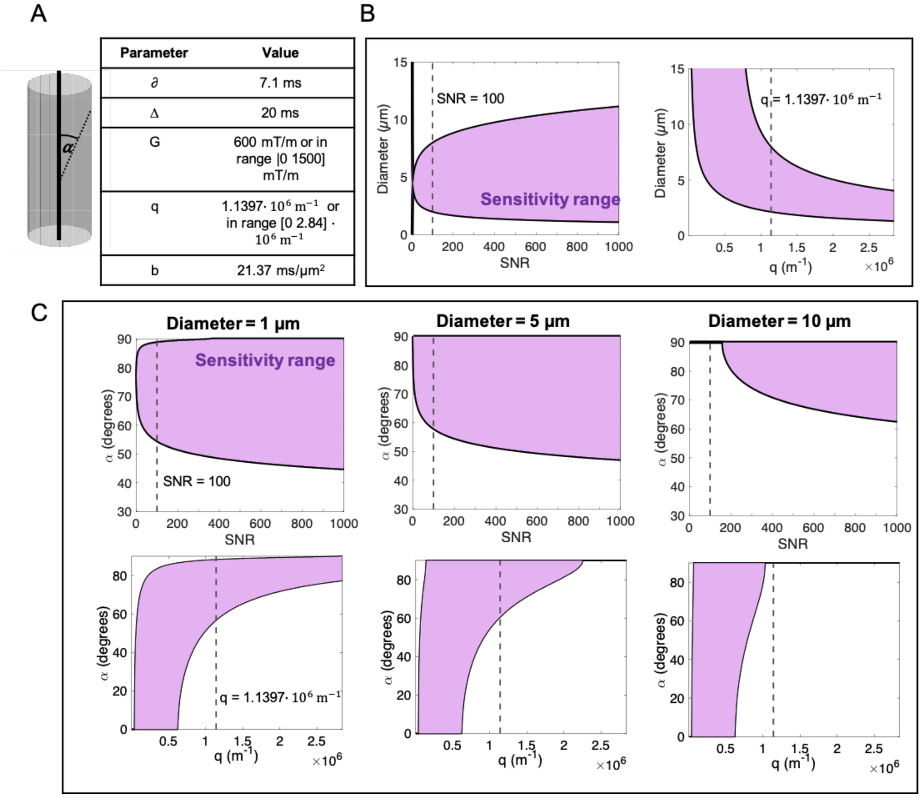

Parameter	Value
∂	7.1 ms
Δ	20 ms
G	600 mT/m or in range |0 1500] mT/m
q	$1.1397 \cdot 10^6\ \mathrm{m}^{-1}$ or in range [0 2.84] $\cdot\ 10^6\ \mathrm{m}^{-1}$
b	21.37 ms/μm²

Figure 6.1: Angular sensitivity of the signal with respect to the cylinder axis A) The angle α is defined as the inclination from the cylinder axis. The PGSE parameters in the table were used for the sensitivity analysis. B) The range of measurable diameters using the PA signal varies with the SNR, as shown using $q = 1.1397 \cdot 10^6\ \mathrm{m}^{-1}$. For SNR=100, the range of measurable diameters varies with the q-value (G is varied to obtain different q, but δ and Δ are as in the table). The sensitivity analysis is based on Eq. 6.2 and assumes 30 gradient directions. C) Variation with SNR and $q-$value of the angular sensitivity range, in terms of α, to which the measurement is sensitive in cylinders of diameter $[1, 5, 10]$ μm for the PGSE parameters in B. This sensitivity criterion is as in Eq. 6.1.

6.3.2 Selecting the Number of Gradient Directions

The angular resolution of the acquisition also placed a lower bound on the measurable diameter, as demonstrated by the diameter estimates at $SNR = \infty$, where an increasing number of directions pushed the lower bound of measurable diameter to lower values. For example, 10 directions were insufficient to resolve diameters smaller than 4 μm in Fig. 6.2, but 30 directions moved the lower bound to ~ 1 μm. This is in line with the findings of Li et al. [182] who show that at SNR= ∞ the number of directions determines how accurately the measured PA signal reflects the ground truth signal. In this sense, the angular resolution places separate limit on the lower bound. Similarly, it has been demonstrated that an increased angular resolution increases the robustness of the PA-derived metrics to different underlying fibre configurations and OD [110, 183].

With Rician noise, the noise-incurred lower bound sometimes masked the benefit of increasing the angular resolution, as evidenced by the the similarity between d_{SMT-1} extracted from 30 directions and 512 directions at SNR=100. At SNR=20, the presence of the Rician bias caused a general underestimation of cylinder diameters, as in Fan et al. [176]. The Rician bias also meant that the theoretical predictions of the upper/lower bounds of measurable diameter were too high/low respectively. This disparity was the clearest using 512 directions. For Gaussian noise (shown in Contribution II), on the other hand, the symmetry of the distribution around the mean entailed that the higher number of sampling points due to the higher angular resolution increased the effective SNR (in line with Equations 6.1-6.3), widening the range of measurable diameters. In this case, the theoretical predictions of the upper and lower bounds agreed with the calculated diameters

The number of gradient directions thus first needs to be sufficient to avoid incurring a limit on the lower bound due to too low angular resolution. As seen in Figure 6.2, 6 and 10 directions are too few to characterise the diameters of segmented axons from the splenium region (with a volume weighted diameter of ~ 3 μm), even at unrealistic SNR=∞. Then, the optimal choice of the number of directions may depend on the SNR of the acquisition, the desired acquisition time (more directions take longer to acquire) and if the magnitude MRI volumes (with Rician noise) are sufficient, or if the real valued images with Gaussian distributed noise will be retrieved. For 30 and 512 gradient directions, the predicted bounds in Figure 6.2 indicate what there is to gain in terms of the measurable range of diameters when moving from Rician noise to Gaussian noise.

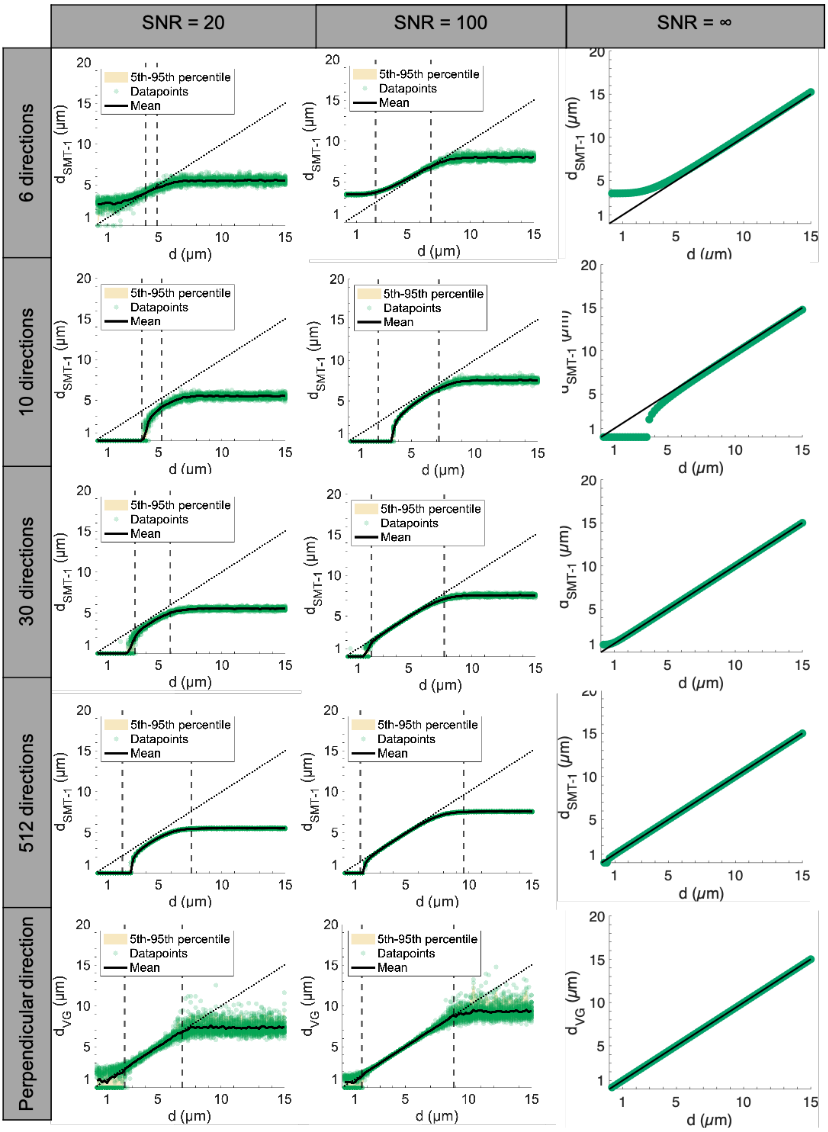

Figure 6.2: Influence of number of directions and SNR (Rician noise) on the single-shell SMT-1 estimated diameter, d_{SMT-1}, in cylinders of diameter between 0.2 and 15.0 μm at 0.2 μm intervals. SMT-1 assumes known $f_a = 1$, $D_{\|} = 0.6 \cdot 10^{-9}\text{m}^2\text{s}^{-1}$. The lower and upper bounds of measurable diameter are sensitive to both SNR and the number of directions. The last row shows the influence of SNR on d_{VG} as calculated using Equation 3.32. $n = 50$ repeats of the acquisition were performed for each diameter, SNR and number of directions. The black striped lines represent the predicted lower and upper bounds of measurable diameter based on Equations 6.1 and 6.2.

6.3.3 Choice, but Not Number, of b-Values Affects the Range of Measurable Diameters

SMT-2 and the PL were fitted to the signal from different high $b-$value shells. All $b-$values were, however, kept $\gtrsim 20$ ms/μm^2, in the regime where the ECS can be said to be suppressed as in [113]. For Rician noise, as in Figure 6.3A, the estimated diameters d_{SMT-2} and d_{PL} dropped to 0 at small and large diameters, and accurately approximated d within a range of intermediate diameters. The underestimation of d_{SMT-2} at large diameters was caused by the attribution of the attenuated signal from large cylinders to an apparent decrease in the IAS volume fraction, f_a, as in [176]. Similarly, the underestimation of d_{PL} could be attributed to a misestimation of β at large diameters. The majority of the underestimation of d_{SMT-2} and f_a disappeared at infinite SNR (see Contribution II), but not for d_{PL}. This could be a consequence of the $b \cdot (D_{\|} - D_{\perp})$ assumption of the PL (Eq. 3.37) not holding at strong diffusion encoding, q, and large d, where the measured $D_{\perp}$ approaches $D_{\|}$.

The use of data with Gaussian distributed noise in Fig. 6.3B produced d_{SMT-2}, f_a and β estimates that were accurate at smaller and larger diameters than with Rician noise, albeit with a high variance beyond the range of robustly measurable diameters. Consequently, at diameters $\gtrsim 7$ μm, the estimates of f_a and β could not be robustly estimated. One contributor to the high variance was that the SMT-2 and PL fits failed for many large diameters, defaulting to 0.

To explore the how $b-$value range and number of shells affected the diameter estimates, the experiments in Fig. 6.3 were repeated for A) three shells that spanned the same range as in Fig. 6.3 with $b = [19.25, 35.79, 63.62]$ ms/μm^2 , B) three closely spaced b-values at the lower end of the range $b = [19.25, 22.90, 26.88]$ ms/μm^2 and C) three closely spaced b-values at the higher end of the range, $b = [51.54, 57.42, 63.62]$ ms/μm^2. The results are shown in Figure 6.4 and indicate that, other than a small decrease in variance, there seemed to be no clear advantage to sampling more shells that cover the same range of $b-$values, as clear from the comparison of the results using ten shells in Fig. 6.4A and using three shells in Fig. 6.3A. This lends support to the approach of ActiveAx [13], where the number of sampled b-values matches the number of parameters that are estimated. Hence, it may not be necessary to perform a dense sampling of b-values as in the SMT implementation of Fan et al. [176], AxCaliber [65] and the PL implementation [113]. This was also recently suggested by Veraaart et al. [184].

Secondly, fitting to the three b-values on the lower end of the range in Fig. 6.4B resulted in a wider range of measurable diameters than fitting to three significantly higher b-values in Fig. 6.4C, although the variance increased somewhat.

A. Rician noise SNR = 100

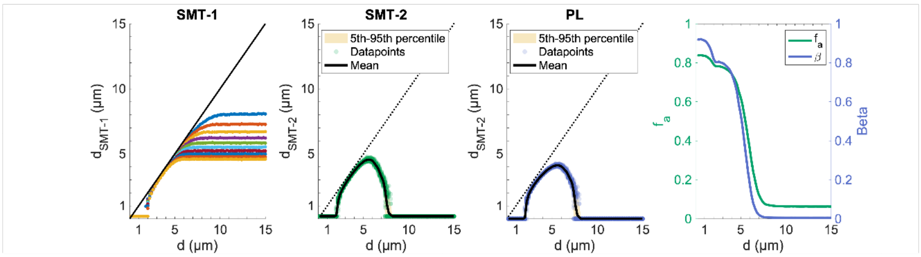

B. Gaussian noise SNR = 100

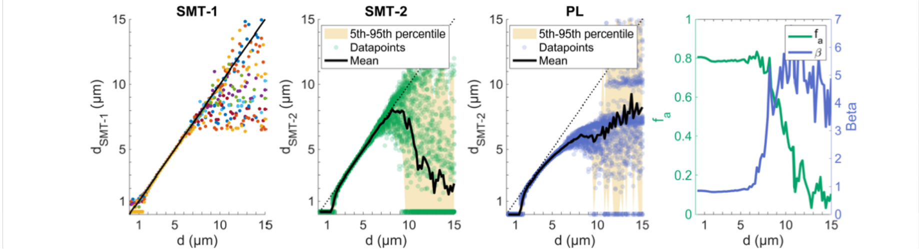

Figure 6.3: Multi-shell fit of SMT and PL to the signal from cylinders of diameter between 0.2 and 15.0 μm at SNR $= 100$ and different noise distributions. Fitted d_{SMT-1}, d_{SMT-2}, d_{PL}, f_a from SMT-2 and β from the PL for A) Rician distributed noise and B) Gaussian distributed noise. The signal is generated using $D_{\|} = 0.6{\cdot}10^{-9}\mathrm{m}^2\mathrm{s}^{-1}$, $f_a = 0.8$, 30 isotropically distributed directions and PGSE parameters $\delta = 7.1$ ms, $\Delta = 20$ ms , 10 b values in the range $[19.25, 63.62]$ ms/μm^2 and linearly spaced values of G in the range $[550, 1000]$ mT/m. $n = 50$ repeats of each acquisition were performed for each diameter.

The equivalent experiments using Gaussian noise are shown in Contribution II. Here, the use of Gaussian noise widened the range of measurable diameters and provided more accurate estimates of f_a. Moreover, while the sensitivity criteria of Nilsson et al. [96] provided good indications of the range of measurable diameter for SMT-1 fits to a single $b-$value (Fig. 6.2), no equivalent metric exists for a multi-shell fit, making simulations of the signal important in predicting the sensitivity of a multi-shell acquisition to diameter.

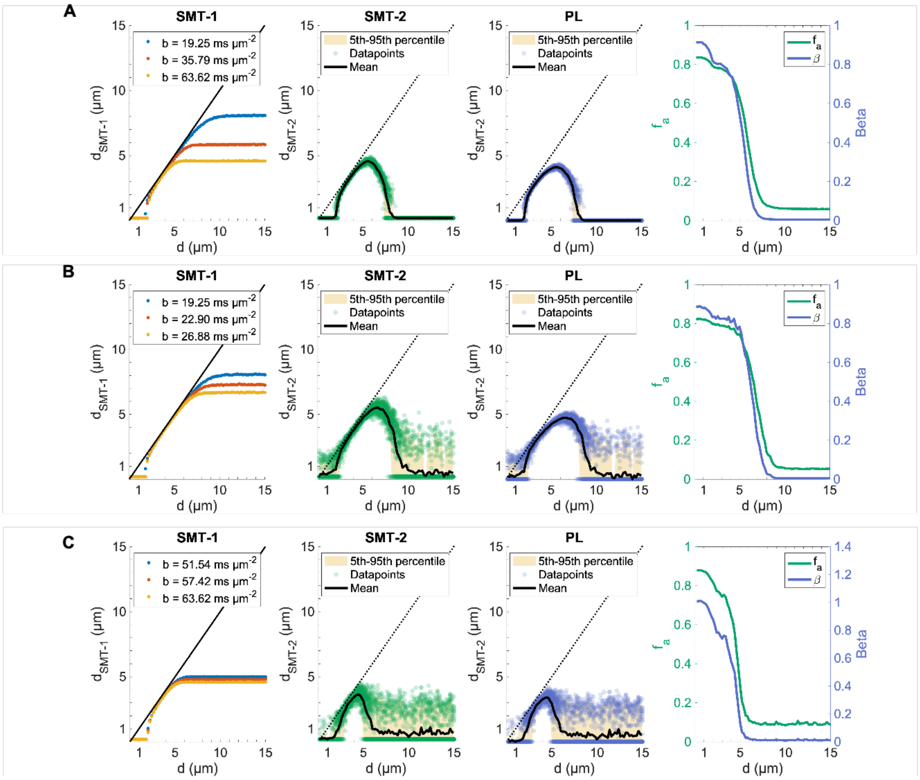

Figure 6.4: The choice of b-values affects the range of measurable diameters. Multi-shell fit of SMT and PL to the signal from cylinders of diameter sbetween 0.2 and 15.0 μm at SNR = 100 (Rician noise) and $f_a = 0.8$. Fitted d_{SMT-1}, d_{SMT-2}, d_{PL}, f_a and β for ground truth A) three shells with $b = [19.25, 35.79, 63.62]$ B) three shells with $b = [19.25, 22.90, 26.88]$ ms/μm^2 and C) three shells with $b = [51.54, 57.42, 63.62]$ ms/μm^2. The signal was generated using $D_{\|} = 0.6 \cdot 10^{-9}\text{m}^2\text{s}^{-1}$, 30 directions, PGSE parameters $\delta = 7.1$ ms, $\Delta = 20$ ms and varying G. $n = 50$ repeats of each acquisition were performed for each diameter.

6.3.4 Microdispersion affects PA-based Axon Diameter Estimates in Segmented Axons from the Vervet Monkey Brain

The axons segmented from the crossing fibre region were significantly larger and exhibited a wider ADD than those from the splenium (Figure 6.5). In comparison to axons from the organised CC environment, they were also very heterogeneous in terms of length, diameter, shape and orientation. The thinnest, thickest and longest axons are shown in Fig. 6.5D-F. To measure the axial diffusivity, the axons were aligned with the z-axis, and the intra-axonal diffusion of spins was simulated for up to 100 ms. From the mean-squared-displacements of the spins, the diffusion coefficient in the z-direction (D_z) was approximated and its variation with diffusion time, t_d, is shown in Fig. 6.5G-E for the splenium and crossing fiber axons respectively. The values of D_z in the splenium axons were lower than those in the crossing fiber region, owing to the more irregular trajectories of the crossing fiber axons, as seen in Fig. 6.5F.

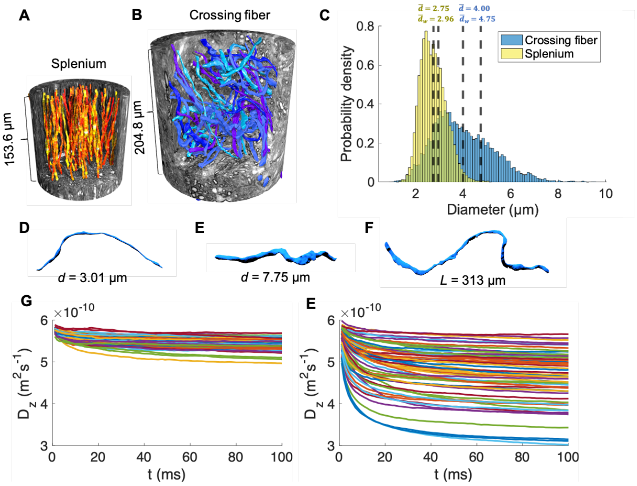

Figure 6.5: 3D reconstructions of A) 54 splenium axons (segmented at 75 nm isotropic resolution) and B) 58 crossing fiber axons (segmented at 500 nm isotropic resolution) in their respective XNH volumes. C) Combined 3D ADD over all measured diameters in the splenium (yellow) and crossing fiber region (blue). The D) thinnest, E) thickest and F) longest axons from the crossing fiber region demonstrate the significant variability of axonal morphology that can exist on the subvoxel scale. The segmented axons were aligned with the z-axis and G) and E) show the variation of the progator-based ADC in the z-direction, D_z, with diffusion time t (data points every 1 ms).

Four different acquisitions were simulated within the axonal IAS, each with three shells. They consisted of one high gradient set and one lower gradient set, each at one short (12.7 ms) and one long (37.7 ms) diffusion time, t_d. For each acquisition, SMT-2, SMT-3 and the PL were fitted to the PA signal to obtain estimates of d_{SMT-3}, $D_{\|}$ from the SMT-3 fit, d_{SMT-2} and d_{PL}, shown in Fig.

6.6.

The simulations within the realistic IAS revealed several interesting properties of PA-based approaches to axon diameter estimation. Firstly, the sensitivity to $D_{||}$, and thus the microdispersion of axons, was low at high $b-$values. Using the set of strong $G = [500, 600, 700]$ mT/m in Figures 6.6A and C, d_{SMT-3} and d_{SMT-2} accurately estimated the axon diameter from both WM regions, regardless of diffusion time. In fact, there was little difference between the measures, suggesting that it is unnecessary to fit $D_{||}$ in SMT-3 at high $b-$values, and that fitting SMT-2 would give equivalent results. An analysis of the dependency of d_{SMT-2} on $D_{||}$ at high $b-$values confirmed this (see Contribution II), and the $D_{||}$ estimates obtained in Figures 6.6A and C did not appear to be meaningful or physically plausible, compared to the estimates of D_z in Figure 6.5. Under the same conditions of high G and q, the PL implementation provided accurate estimates of the diameters in the splenium, but underestimated those in the crossing fibre region.

Secondly, the diameter estimates were sensitive to the microdispersion of real axons at low $b-$values. Using the set of lower gradients $G = [100, 200, 300]$ mT/m in Figures 6.6B and D, d_{SMT-3} exhibited a slight overestimation of the crossing fibre axons that increased with increasing diffusion time. Due to the lower $b-$values, the PL implementation failed to provide accurate estimates of diameter. Furthermore, SMT-3 and SMT-2 did not perform equivalently, and fitting a variable $D_{||}$ was necessary to obtain accurate diameter estimates for the smaller diameters in the splenium region. There was a positive correlation between d and the obtained $D_{||}$. In accordance with D_z in Fig. 6.5G-H, the values of $D_{||}$ were reduced at longer diffusion times and were similar to or larger than D_z, as expected. The time dependence of $D_{||}$ and d_{SMT-3} was due to the microdispersion or diameter variations of the axons, and could potentially be used as biomarkers of changes to axon morphology.

Simulations within the realistic IAS at in vivo diffusivities (see Contribution II) highlight the importance of performing sensitivity analyses and simulations to evaluate the different SMT and PL fits. Even with gradient strengths accessible to human diffusion MRI experiments only via Connectom scanners, the splenium ADs could be accurately estimated only: by SMT-3, at the shortest diffusion time, and provided that $D_{||}$ was fitted.

6.4 Conclusion

In conclusion, we demonstrate that the diameters of axons from diferent fibre architectures, the splenium CC and a crossing fiber region of the vervet monkey brain, can be accurately estimated from their PA diffusion MRI signals. To succeed, the acquisition must have broad sensitivity to different length scales. This is important partly due to the many different axon sizes present within a voxel, as presented here, but also because the powder average by definition probes different length scales. Furthermore, we show how the gradient strength, diffusion time and number of gradient directions, as well as the SNR and noise distribution, influence the lower and upper bounds of measurable diameter. Finally, at low b-values we show that the acquisition becomes sensitive to axonal microdispersion, which could be an interesting biomarker of WM health and pathology.

Here, the behaviours and characteristics of PA-based estimates of axon diameter were studied for the IAS only. It is generally regarded that high b-values suppress the signal contribution from the ECS [177, 178, 185]. However, in the XNH volumes of the WM we observe cell clusters and vacuoles that together constitute 6.1% of the total volume fraction [44]. Recent studies show that the soma of spherical cells could contribute to the PA signal at short diffusion times [186], complicating the SMT and PL fit to the PA signals. The presence of any compartment from which the signal remains at high $b-$values will complicate a multi-shell fit of the SMT and PL implementations, unless the compartments are explicitly modelled. These compartments could include irregularities in the axonal myelin, cellular processes, regions of the ECS in very anisotropic WM regions, or other structures. The observed dot compartment in ex vivo tissue [13, 113] would systematically bias PA-based axon diameter measurements, although its contribution to the signal has been shown to be negligible in in-vivo experiments [178, 187, 188]. At lower b-values, signal contributions from multiple compartments are expected and must be modelled, as in Fan et al. [176]. Thus, the accuracy of the diameter estimation depends not only on how accurately the geometry of other compartments are modelled, but also the compartmental T_2 relaxation times [100] and potential exchange rates. However, assuming that the contribution from the IAS can be reliably isolated at low b-values, the reduced signal attenuation at low b compared to high b-values entails that the diameter estimation may be more robust at finite SNR. Furthermore, the sensitivity to microdispersion and $D_{||}$ is higher for low b-values, and the time-dependence of d_{SMT-3} and $D_{||}$ could provide valuable insight into axonal morphology [18, 93, 94, 96, 111, 189].

Lastly, for the splenium CC and crossing fiber axons in this study, the volume-weighted means of their ADDs are, in general, well approximated by SMT-3 (Fig. 6.6), but this is because the individual axon diameters are generally above the lower bound of measurable diameter. How well the estimated diameter can represent the mean of the ADD when a portion of the ADD is beneath the lower bound, as is expected in MRI voxels, remains to be investigated.

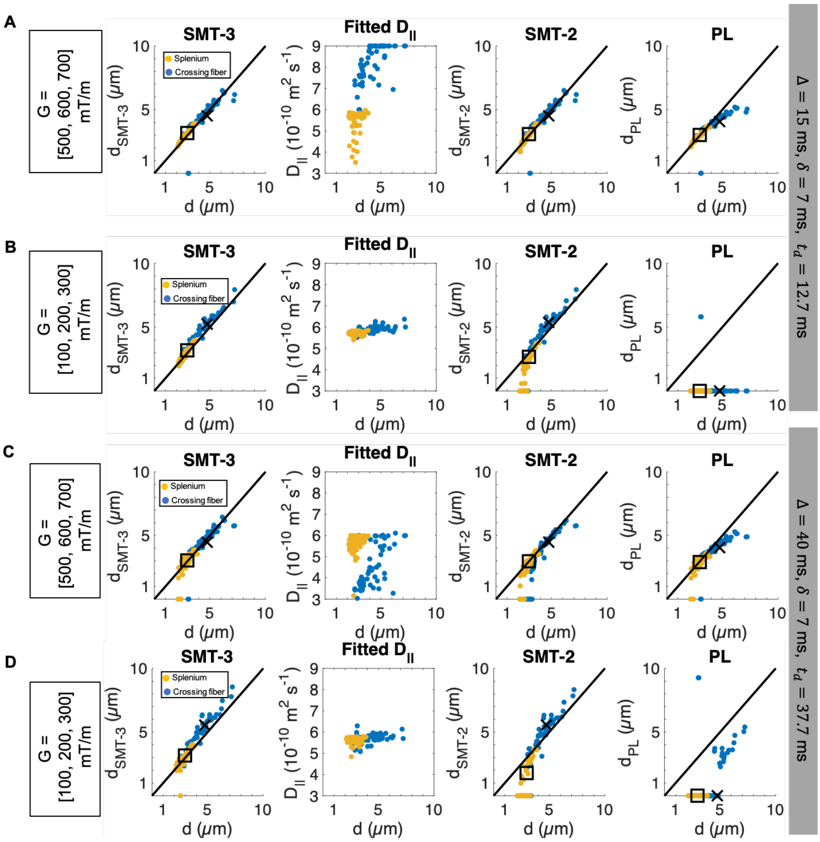

Figure 6.6: The estimated parameters d_{SMT-3}, $D_{\|}$, d_{SMT-2} with assumed $D_{\|} = 0.6 \cdot 10^{-9}$ $\mathrm{m^2 s^{-1}}$ and d_{PL} are plotted against the volume-weighted axon diameter of the 54 axons in the splenium (yellow) and the crossing fiber region (blue). The parameters are calculated for different combinations of short ($\Delta = 15$ ms) and long ($\Delta = 40$ ms) gradient separations with high ($G = [500, 600, 700]$ mT/m) or low ($G = [100, 200, 300]$ mT/m) gradient strengths, as indicated. This gave three-shell acquisitions with A) $b = [11.11, 16.00, 21.77]$ ms/μm^2, B) $b = [0.549, 2.198, 4.945]$ ms/μm^2, C) $b = [33.03, 47, 56, 64.73]$ ms/μm^2 and D) $b = [0.795, 3.180, 7.155]$ ms/μm^2. The signals were generated with MC simulations using $D_0 = 0.6 \cdot 10^{-9} \mathrm{m^2 s^{-1}}$ and were sampled in 30 gradient directions. For all acquisitions, $\delta = 7$ ms and SNR=∞ (barring the intrinsic noise associated with MC simulations). Square marker: volume-weighted axon diameter of splenium axon population, cross marker: volume-weighted axon diameter of crossing fiber population.

CHAPTER 7

Conclusions

The work presented in this thesis aimed to map the 3D microstructural environment of the brain white matter – with a particular focus on the 3D morphologies of axons – and implement the findings in a validation of diffusion MRI approaches to axon diameter estimation. The contributions are both anatomical and technical.

High resolution synchrotron XNH studies of the vervet monkey WM showed that axon morphology is modulated by other structures in the local WM, such as blood vessels, cell clusters and vacuoles. The third dimension of the XNH volumes, beyond the two of classical LM or EM, revealed the highly varying axon diameters along trajectories up to ~ 660 μm in length. The detailed characterisation of axons presented in Contribution I could be thought of as an axonal "recipe" or "fingerprint", which can be used to construct anatomically realistic axon phantoms for use in validation of diffusion MRI models and methods. The quantification of 3D axonal morphology also sheds light on anatomical trends observed in 2D investigations of axon diameter. These include the relationship between axon diameter and myelin sheath thickness in Equation 2.2 [31] and the existence of a sparse population of "giant" axons which might both be driven by local diameter variations of axons. By isolating single internodes, the entire axonal segment between consecutive Nodes of Ranvier, it could be demonstrated that the conduction velocity will vary along the length of an axon according to classical structure-function relations. Furthermore, simulations of diffusion within the intra-axonal space demonstrated that axon diameter estimates based on the diffusion MRI signal perpendicular to the axons, even in the corpus callosum, exhibit a time-dependent overestimation. The findings raise several important questions, which require further investigation. What do the varying morphologies of axons entail for the saltatory conduction process in myelinated axons, and what does this mean for communication within the brain network?

Do the axon morphologies change in diseased tissue, and can we detect those changes with diffusion MRI?

The application of x-ray nanotomography to the mouse white matter in Contribution II demonstrated that axonal connections can be traced with structure tensor tractography in healthy and diseased tissue. This enables a characterisation of the macroscopic organisation of axonal bundles in volumes where the field of view is large enough to cover a significant portion of a WM structure, despite insufficient resolution to segment individual axons. Combined with the high resolution XNH experiments in Contribution I, this approach could provide multi-scale insight into the WM anatomy in volumes representative of MRI voxels. The x-ray nanotomography volume of the hydrated monkey genu in Section 5.3.1 showed clear cellular processes that could not be easily identified in the XNH volumes of dehydrated tissue in Contribution I, indicating a need to image tissue in a closer-to-innate, hydrated state. There is also potential to earn more from the already analysed XNH volumes, as preliminarily exemplified by the application of a CNN segmentation method to the XNH volumes from Contribution I, resulting in the segmentation of thousands of axons.

Using the segmentations of axons from XNH volumes of a splenium and crossing fibre-region, powder average approaches to axon diameter were investigated. Accurate estimates of axon diameter could be made across a range of sequence parameters and diffusion times, even in complex white matter architectures. At sufficiently low b-values, the acquisition became sensitive to axonal microdispersion and the intra-axonal parallel diffusivity showed time dependence, which could be an interesting biomarker of WM health and pathology. Unlike for techniques that base the axon diameter estimation on the signal perpendicular to the axons, the powder averaging approaches require sensitivity to many different length scales and are thus typically subject to a narrower range of measurable diameters. Although the powder average removes dispersion effects, it places higher demands on the MRI hardware and experimental parameters. The q-value, SNR and the noise distribution type (Rician vs. Gaussian) are the key variables that ultimately determine the range of measurable axon diameter. These findings validate the use of powder average approaches even in very complex fibre architectures, and can be used to guide the design of optimised sequences for estimation of axon diameter.

This thesis concludes with a quote whose message is relevant to all aspects of the research presented here: from its aims, to the interpretation of its results, to the identification of its limitations, and lastly – to future research directions.

> “What we observe is not nature itself, but nature exposed to our method of questioning.”
> **Werner Heisenberg (1901-1976)**

On the whole, this thesis work has attempted to bridge the gap between the observations from two different "methods of questioning": the microscale characteristics of axons from synchrotron x-ray imaging and the voxel-scale summary statistics from diffusion MRI. Future research will need to apply other methods of questioning in order to observe the white matter anatomy closer to its inherent state, whether it is with invasive imaging techniques or with diffusion MRI.

Additional Information Figures 2.1, 2.2, 2.3, 2.6, 4.1 and 5.2 were partially created using BioRender.com.

Bibliography

[1] Gaolang Gong, Pedro Rosa-Neto, Felix Carbonell, Zhang J. Chen, Yong He, and Alan C. Evans. Age- and gender-related differences in the cortical anatomical network. *Journal of Neuroscience*, 29(50):15684–15693, 2009.

[2] Bogdan Draganski, Christian Gaser, Volker Busch, Gerhard Schuierer, Ulrich Bogdahn, and Arne May. Changes in grey matter induced by training. *Nature*, 427(6972):311–312, jan 2004.

[3] Hikaru Takeuchi, Atsushi Sekiguchi, Yasuyuki Taki, Satoru Yokoyama, Yukihito Yomogida, Nozomi Komuro, Tohru Yamanouchi, Shozo Suzuki, and Ryuta Kawashima. Training of working memory impacts structural connectivity. *Journal of Neuroscience*, 30(9):3297–3303, 2010.

[4] Arne May. Experience-dependent structural plasticity in the adult human brain. *Trends in Cognitive Sciences*, 15(10):475–482, 2011.

[5] Ni Shu, Yaou Liu, Kuncheng Li, Yunyun Duan, Jun Wang, Chunshui Yu, Huiqing Dong, Jing Ye, and Yong He. Diffusion tensor tractography reveals disrupted topological efficiency in white matter structural networks in multiple sclerosis. *Cerebral Cortex*, 21(11):2565–2577, 2011.

[6] Luis R. Peraza, Antonio Díaz-Parra, Oliver Kennion, David Moratal, John Paul Taylor, Marcus Kaiser, and Roman Bauer. Structural connectivity centrality changes mark the path toward Alzheimer's disease. *Alzheimer's and Dementia: Diagnosis, Assessment and Disease Monitoring*, 11:98–107, 2019.

[7] J. B. Hursh. Conduction Velocity and Diameter of Nerve Fibers. *American Journal of Physiology-Legacy Content*, 127(1):131–139, 1939.

[8] F. K. Sanders and D. Whitteridge. Conduction velocity and myelin thickness in regenerating nerve fibres. *The Journal of Physiology*, 105(2):152–174, 1946.

[9] I. Lorena Arancibia-Cárcamo, Marc C. Ford, Lee Cossell, Kinji Ishida, Koujiro Tohyama, and David Attwell. Node of ranvier length as a potential regulator of myelinated axon conduction speed. *eLife*, 6:1–15, 2017.

[10] Gabriele C. DeLuca, G. C. Ebers, and M. M. Esiri. Axonal loss in multiple sclerosis: A pathological survey of the corticospinal and sensory tracts. *Brain*, 127(5):1009–1018, 2004.

[11] Ranjan Dutta and Bruce D. Trapp. Mechanisms of neuronal dysfunction and degeneration in multiple sclerosis. *Progress in Neurobiology*, 93(1):1–12, 2011.

[12] S. Cluskey and D. B. Ramsden. Mechanisms of neurodegeneration in amyotrophic lateral sclerosis. *Journal of Clinical Pathology - Molecular Pathology*, 54(6):386–392, 2001.

[13] Daniel C. Alexander, Penny L. Hubbard, Matt G. Hall, Elizabeth A. Moore, Maurice Ptito, Geoff J.M. Parker, and Tim B. Dyrby. Orientationally invariant indices of axon diameter and density from diffusion MRI. *NeuroImage*, 52(4):1374–1389, 2010.

[14] Daniel Barazany, Peter J. Basser, and Yaniv Assaf. In vivo measurement of axon diameter distribution in the corpus callosum of rat brain. *Brain*, 132(5):1210–1220, 2009.

[15] Tim B. Dyrby, Giorgio M. Innocenti, Martin Bech, and Henrik Lundell. Validation strategies for the interpretation of microstructure imaging using diffusion MRI. *NeuroImage*, 182(June):62–79, 2018.

[16] Daniel C. Alexander, Tim B. Dyrby, Markus Nilsson, and Hui Zhang. Imaging brain microstructure with diffusion MRI: practicality and applications. *NMR in Biomedicine*, 32(4):e3841, 2019.

[17] Ali Abdollahzadeh, Ilya Belevich, Eija Jokitalo, Jussi Tohka, and Alejandra Sierra. Automated 3D Axonal Morphometry of White Matter. *Scientific Reports*, 9(1):239228, 2019.

[18] Hong Hsi Lee, Katarina Yaros, Jelle Veraart, Jasmine L. Pathan, Feng Xia Liang, Sungheon G. Kim, Dmitry S. Novikov, and Els Fieremans. Along-axon diameter variation and axonal orientation dispersion revealed with 3D electron microscopy: implications for quantifying brain white matter microstructure with histology and diffusion MRI. *Brain Structure and Function*, 224(4):1469–1488, 2019.

[19] Kathleen S. Rockland and Naema Nayyar. Association of type I neurons positive for NADPH-diaphorase with blood vessels in the adult monkey corpus callosum. *Frontiers in Neural Circuits*, 6(FEBRUARY):1–11, 2012.

[20] Eva Syková and Charles Nicholson. Diffusion in brain extracellular space. *Physiological Reviews*, 88(4):1277–1340, 2008.

[21] Inseon Song and Alexander Dityatev. Crosstalk between glia, extracellular matrix and neurons. *Brain Research Bulletin*, 136:101–108, 2018.

[22] D. K. Hartline and D. R. Colman. Rapid Conduction and the Evolution of Giant Axons and Myelinated Fibers. *Current Biology*, 17(1):29–35, 2007.

[23] Dominique Debanne, Emilie Campanac, Andrzej Bialowas, Edmond Carlier, and GISÈLE Alcaraz. Axon physiology. *Physiological Reviews*, 91(2):555–602, 2011.

[24] R. S. Smith and Z. J. Koles. Myelinated nerve fibers: computed effect of myelin thickness on conduction velocity. *The American journal of physiology*, 219(5):1256–1258, 1970.

[25] Taylor Chomiak and Bin Hu. What is the optimal value of the g-ratio for myelinated fibers in the rat CNS? A theoretical approach. *PLoS ONE*, 4(11):e7754, 2009.

[26] A. L. Hodgkin. A note on conduction velocity. *The Journal of Physiology*, 125(1):221–224, 1954.

[27] S. G. Waxman and M. V.I. Bennett. Relative conduction velocities of small myelinated and non-myelinated fibres in the central nervous system. *Nature New Biology*, 238(85):217–219, 1972.

[28] W. A.H. Rushton. A theory of the effects of fibre size in medullated nerve. *The Journal of Physiology*, 115(1):101–122, 1951.

[29] Nikola Stikov, Jennifer S.W. Campbell, Thomas Stroh, Mariette Lavelée, Stephen Frey, Jennifer Novek, Stephen Nuara, Ming Kai Ho, Barry J. Bedell, Robert F. Dougherty, Ilana R. Leppert, Mathieu Boudreau, Sridar Narayanan, Tanguy Duval, Julien Cohen-Adad, Paul Alexandre Picard, Alicja Gasecka, Daniel CÔté, and G. Bruce Pike. Quantitative analysis of the myelin g-ratio from electron microscopy images of the macaque corpus callosum. *Data in Brief*, 4:368–373, 2015.

[30] Giorgio M. Innocenti, Alessandro Vercelli, and Roberto Caminiti. The diameter of cortical axons depends both on the area of origin and target. *Cerebral Cortex*, 24(8):2178–2188, 2014.

[31] C H Berthold, I Nilsson, and M Rydmark. Axon diameter and myelin sheath thickness in nerve fibres of the ventral spinal root of the seventh lumbar nerve of the adult and developing cat. *Journal of anatomy*, 136(Pt 3):483–508, 1983.

[32] G. J. Little and J. W. Heath. Morphometric analysis of axons myelinated during adult life in the mouse superior cervical ganglion. *Journal of Anatomy*, 184(2):387–398, 1994.

[33] R. L. Friede and W. Beuche. Combined scatter diagrams of sheath thickness and fibre calibre in human sural nerves: Changes with age and neuropathy. *Journal of Neurology, Neurosurgery and Psychiatry*, 48(8):749–756, 1985.

[34] B Y A F Huxley and A D R Stampfli. Evidence for Saltatory Conduction in. *J. Physiol.*, 108(1946):315–339, 1948.

[35] Reinhard L. Friede. The significance of internode length for saltatory conduction: Looking back at the age of 90. *Journal of Neuropathology and Experimental Neurology*, 76(4):258–259, apr 2017.

[36] A. G. Richardson, C. C. McIntyre, and W. M. Grill. Modelling the effects of electric fields on nerve fibres: Influence of the myelin sheath. *Medical and Biological Engineering and Computing*, 38(4):438–446, 2000.

[37] Helmut Schmidt and Thomas R. Knösche. Action potential propagation and synchronisation in myelinated axons. *PLoS Computational Biology*, 15(10):1–33, 2019.

[38] Giorgio M. Innocenti, Marie Carlén, and Tim B. Dyrby. The Diameters of Cortical Axons and Their Relevance to Neural Computing. *Axons and Brain Architecture*, pages 317–335, 2016.

[39] Giorgio M. Innocenti. Network causality, axonal computations, and Poffenberger. *Experimental Brain Research*, 235(8):2349–2357, 2017.

[40] Ariane Saliani, Blanche Perraud, Tanguy Duval, Nikola Stikov, Serge Rossignol, and Julien Cohen-Adad. Axon and myelin morphology in animal and human spinal cord. *Frontiers in Neuroanatomy*, 11(December):1–19, 2017.

[41] Simone Tomasi, Roberto Caminiti, and Giorgio M. Innocenti. Areal differences in diameter and length of corticofugal projections. *Cerebral Cortex*, 22(6):1463–1472, 2012.

[42] Laurent Tettoni, Patricia Lehmann, Jean Christophe Houzel, and Giorgio M. Innocenti. Maxsim, software for the analysis of multiple axonal arbors and their simulated activation. *Journal of Neuroscience Methods*, 67(1):1–9, 1996.

[43] Roberto Caminiti, Hassan Ghaziri, Ralf Galuske, Patrick R. Hof, and Giorgio M. Innocenti. Evolution amplified processing with temporally dispersed slow neuronal connectivity in primates. *Proceedings of the National Academy of Sciences*, 106(46):19551–19556, nov 2009.

[44] Mariam Andersson, Hans Martin Kjer, Jonathan Rafael-Patino, Alexandra Pacureanu, Bente Pakkenberg, Jean-Philippe Thiran, Maurice Ptito, Martin Bech, Anders Bjorholm Dahl, Vedrana Andersen Dahl, and Tim B. Dyrby. Axon morphology is modulated by the local environment and impacts the noninvasive investigation of its structure–function relationship. *Proceedings of the National Academy of Sciences*, 117(52):33649–33659, 2020.

[45] Jan Pielage, Ling Cheng, Richard D. Fetter, Pete M. Carlton, John W. Sedat, and Graeme W. Davis. A Presynaptic Giant Ankyrin Stabilizes the NMJ through Regulation of Presynaptic Microtubules and Transsynaptic Cell Adhesion. *Neuron*, 58(2):195–209, 2008.

[46] Milton L. Greenberg, Jason G. Weinger, Melanie P. Matheu, Kevin S. Carbajal, Ian Parker, Wendy B. Macklin, Thomas E. Lane, and Michael D. Cahalan. Two-photon imaging of remyelination of spinal cord axons by engrafted neural precursor cells in a viral model of multiple sclerosis. *Proceedings of the National Academy of Sciences of the United States of America*, 111(22):2349–2355, 2014.

[47] Jaime Imitola, Daniel Coˆté, Stine Rasmussen, X. Sunney Xie, Yingru Liu, Tanuja Chitnis, Richard L. Sidman, Charles. P. Lin, and Samia J. Khoury. Multimodal coherent anti-Stokes Raman scattering microscopy reveals microglia-associated myelin and axonal dysfunction in multiple sclerosis-like lesions in mice. *Journal of Biomedical Optics*, 16(2):021109, 2011.

[48] Yong Zhang, Xiaobo Zhou, Ju Lu, Jeff Lichtman, Donald Adjeroh, and Stephen T.C. Wong. 3D axon structure extraction and analysis in confocal fluorescence microscopy images. *Neural Computation*, 20(8):1899–1927, 2008.

[49] Emmanouil D. Karagiannis and Edward S. Boyden. Expansion microscopy: development and neuroscience applications. *Current Opinion in Neurobiology*, 50:56–63, 2018.

[50] Miriam Menzel, Markus Axer, Katrin Amunts, Hans De Raedt, and Kristel Michielsen. Diattenuation Imaging reveals different brain tissue properties. *Scientific Reports*, 9(1):1–12, 2019.

[51] Veijo Hukkanen and Matias Röyttä. Autolytic changes of human white matter: An electron microscopic and electrophoretic study. *Experimental and Molecular Pathology*, 46(1):31–39, 1987.

[52] Elizabeth McInnes. Artefacts in histopathology. *Comparative Clinical Pathology*, 13(3):100–108, sep 2005.

[53] C H Fox, F B Johnson, J Whiting, and P P Roller. Formaldehyde fixation. *Journal of Histochemistry & Cytochemistry*, 33(8):845–853, aug 1985.

[54] Asena Abay, Greta Simionato, Revaz Chachanidze, Anna Bogdanova, Laura Hertz, Paola Bianchi, Emile Van Den Akker, Marieke Von Lindern, Marc Leonetti, Giampaolo Minetti, Christian Wagner, and Lars Kaestner. Glutaraldehyde - A subtle tool in the investigation of healthy and pathologic red blood cells. *Frontiers in Physiology*, 10(MAY):1–14, 2019.

[55] Paul Walther and A. Ziegler. Freeze substitution of high-pressure frozen samples: The visibility of biological membranes is improved when the substitution medium contains water. *Journal of Microscopy*, 208(1):3–10, 2002.

[56] Danielle L. Brown. Bias in image analysis and its solution: Unbiased stereology. *Journal of Toxicologic Pathology*, 30(3):183–191, 2017.

[57] Michael S. Gazzaniga. Cerebral specialization and interhemispheric communication. Does the corpus callosum enable the human condition? *Brain*, 123(7):1293–1326, 2000.

[58] Francisco Aboitiz, Arnold B. Scheibel, Robin S. Fisher, and Eran Zaidel. Fiber composition of the human corpus callosum. *Brain Research*, 598(1-2):143–153, 1992.

[59] Roberto Caminiti, Filippo Carducci, Claudia Piervincenzi, Alexandra Battaglia-Mayer, Giuseppina Confalone, Federica Visco-Comandini, Patrizia Pantano, and Giorgio M. Innocenti. Diameter, length, speed, and conduction delay of callosal axons in macaque monkeys and humans: Comparing data from histology and magnetic resonance imaging diffusion tractography. *Journal of Neuroscience*, 33(36):14501–14511, 2013.

[60] A. S Lamantia and P. Rakic. Cytological and quantitative characteristics of four cerebral commissures in the rhesus monkey. *Journal of Comparative Neurology*, 291(4):520–537, 1990.

[61] Jack Hou and Bente Pakkenberg. Age-related degeneration of corpus callosum in the 90+ years measured with stereology. *Neurobiology of Aging*, 33(5):1009.e1–1009.e9, 2012.

[62] Stephen G. Waxman and Harvey A. Swadlow. Ultrastructure of visual callosal axons in the rabbit. *Experimental Neurology*, 53(1):115–127, 1976.

[63] Jesper Riise and Bente Pakkenberg. Stereological estimation of the total number of myelinated callosal fibers in human subjects. *Journal of Anatomy*, 218(3):277–284, 2011.

[64] Tim B. Dyrby, Lise V. Søgaard, Matt G. Hall, Maurice Ptito, and Daniel C. Alexander. Contrast and stability of the axon diameter index from microstructure imaging with diffusion MRI. *Magnetic Resonance in Medicine*, 70(3):711–721, 2013.

[65] Yaniv Assaf, Tamar Blumenfeld-Katzir, Yossi Yovel, and Peter J. Basser. AxCaliber: A method for measuring axon diameter distribution from diffusion MRI. *Magnetic Resonance in Medicine*, 59(6):1347–1354, 2008.

[66] Susie Y. Huang, Aapo Nummenmaa, Thomas Witzel, Tanguy Duval, Julien Cohen-Adad, Lawrence L. Wald, and Jennifer A. McNab. The impact of gradient strength on in vivo diffusion MRI estimates of axon diameter. *NeuroImage*, 106:464–472, 2015.

[67] Susie Y. Huang, Qiuyun Fan, Natalya Machado, Ani Eloyan, John D. Bireley, Andrew W. Russo, Sean M. Tobyne, Kevin R. Patel, Kristina Brewer, Sarah F. Rapaport, Aapo Nummenmaa, Thomas Witzel, Janet C. Sherman, Lawrence L. Wald, and Eric C. Klawiter. Corpus callosum axon diameter relates to cognitive impairment in multiple sclerosis. *Annals of Clinical and Translational Neurology*, 6(5):882–892, 2019.

[68] Ricardo Olivares, Juan Montiel, and Francisco Aboitiz. Species differences and similarities in the fine structure of the mammalian corpus callosum. *Brain, Behavior and Evolution*, 57(2):98–105, 2001.

[69] Farshid Sepehrband, Daniel C. Alexander, Kristi A. Clark, Nyoman D. Kurniawan, Zhengyi Yang, and David C. Reutens. Parametric probability distribution functions for axon diameters of corpus callosum. *Frontiers in Neuroanatomy*, 10:59, 2016.

[70] Albert Einstein. On the theory of the brownian movement. *Ann. Phys.*, 19(4):371–381, 1906.

[71] Jörg Kärger and Wilfried Heink. The propagator representation of molecular transport in microporous crystallites. *Journal of Magnetic Resonance (1969)*, 51(1):1–7, 1983.

[72] P.J. Basser, James Mattiello, and D. Lebihan. Estimation of the Effective Self-Diffusion Tensor from the NMR Spin Echo. *Journal of Magnetic Resonance, Series B*, 103(3):247–254, mar 1994.

[73] I. I. Rabi, J. R. Zacharias, S. Millman, and P. Kusch. A New Method of Measuring Nuclear Magnetic Moment. *Physical Review*, 53(4):318–318, feb 1938.

[74] F. Bloch. Nuclear induction. *Physical Review*, 70(7-8):460–474, oct 1946.

[75] E. L. Hahn. Nuclear induction due to free larmor precession. *Physical Review*, 77(2):297–298, 1950.

[76] E. L. Hahn. Spin echoes. *Physical Review*, 80(4):580–594, 1950.

[77] H. Y. Carr and E. M. Purcell. Effects of diffusion on free precession in nuclear magnetic resonance experiments. *Physical Review*, 94(3):630–638, 1954.

[78] H. C. Torrey. Bloch Equations with Diffusion Terms. *Physical Review*, 104(3):563–565, nov 1956.

[79] E. O. Stejskal and J. E. Tanner. Spin diffusion measurements: Spin echoes in the presence of a time-dependent field gradient. *The Journal of Chemical Physics*, 42(1):288–292, 1965.

[80] J.E. Tanner. *Use of a Pulsed Magnetic-field Gradient for Measurements of Self-diffusion by Spin-echo Nuclear Magnetic Resonance with Applications to Restricted Diffusion in Several Tissues and Emulsions.* PhD thesis, The University of Wisconsin, University Microfilms, Ann Arbor, 1967.

[81] C. H. Neuman. Spin echo of spins diffusing in a bounded medium. *The Journal of Chemical Physics*, 4508(September 1973):4508–4511, 1974.

[82] Hong Hsi Lee, Els Fieremans, and Dmitry S. Novikov. What dominates the time dependence of diffusion transverse to axons: Intra- or extra-axonal water? *NeuroImage*, 182(July 2017):500–510, 2018.

[83] P. Van Gelderen, D. Des Pres, P. C.M. Van Zijl, and C. T.W. Moonen. Evaluation of Restricted Diffusion in Cylinders. Phosphocreatine in Rabbit Leg Muscle. *Journal of Magnetic Resonance, Series B*, 103(3):255–260, 1994.

[84] Eleftheria Panagiotaki, Torben Schneider, Bernard Siow, Matt G. Hall, Mark F. Lythgoe, and Daniel C. Alexander. Compartment models of the diffusion MR signal in brain white matter: A taxonomy and comparison. *NeuroImage*, 59(3):2241–2254, 2012.

[85] Uran Ferizi, Torben Schneider, Eleftheria Panagiotaki, Gemma Nedjati-Gilani, Hui Zhang, Claudia A.M. Wheeler-Kingshott, and Daniel C. Alexander. A ranking of diffusion MRI compartment models with in vivo human brain data. *Magnetic Resonance in Medicine*, 72(6):1785–1792, 2014.

[86] Yaniv Assaf, Raisa Z. Freidlin, Gustavo K. Rohde, and Peter J. Basser. New modeling and experimental framework to characterize hindered and restricted water diffusion in brain white matter. *Magnetic Resonance in Medicine*, 52(5):965–978, 2004.

[87] Yaniv Assaf and Peter J. Basser. Composite hindered and restricted model of diffusion (CHARMED) MR imaging of the human brain. *NeuroImage*, 27(1):48–58, 2005.

[88] Daniel C. Alexander. A general framework for experiment design in diffusion MRI and its application in measuring direct tissue-microstructure features. *Magnetic Resonance in Medicine*, 60(2):439–448, 2008.

[89] P. J. Basser, J. Mattiello, and D. LeBihan. MR diffusion tensor spectroscopy and imaging. *Biophysical Journal*, 66(1):259–267, 1994.

[90] Aaron Szafer, Jianhui Zhong, and John C. Gore. Theoretical Model for Water Diffusion in Tissues. *Magnetic Resonance in Medicine*, 33(5):697–712, may 1995.

[91] Hui Zhang, Penny L. Hubbard, Geoff J.M. Parker, and Daniel C. Alexander. Axon diameter mapping in the presence of orientation dispersion with diffusion MRI. *NeuroImage*, 56(3):1301–1315, 2011.

[92] Markus Nilsson, Jimmy Lätt, Freddy Ståhlberg, Danielle van Westen, and Håkan Hagslätt. The importance of axonal undulation in diffusion MR measurements: A Monte Carlo simulation study. *NMR in Biomedicine*, 25(5):795–805, 2012.

[93] Jan Brabec, Samo Lasič, and Markus Nilsson. Time-dependent diffusion in undulating thin fibers: Impact on axon diameter estimation. *NMR in Biomedicine*, 33(3):1–19, 2020.

[94] Hong Hsi Lee, Antonios Papaioannou, Sung Lyoung Kim, Dmitry S. Novikov, and Els Fieremans. A time-dependent diffusion MRI signature of axon caliber variations and beading. *Communications Biology*, 3(1), 2020.

[95] Lorenza Brusini, Gloria Menegaz, and Markus Nilsson. Monte Carlo simulations of water exchange through myelin wraps: Implications for diffusion MRI. *IEEE Transactions on Medical Imaging*, 38(6):1438–1445, 2019.

[96] Markus Nilsson, Samo Lasič, Ivana Drobnjak, Daniel Topgaard, and Carl Fredrik Westin. Resolution limit of cylinder diameter estimation by diffusion MRI: The impact of gradient waveform and orientation dispersion. *NMR in Biomedicine*, 30(7):1–13, 2017.

[97] Jelle Veraart, Dmitry S. Novikov, and Els Fieremans. TE dependent Diffusion Imaging (TEdDI) distinguishes between compartmental T2 relaxation times. *NeuroImage*, 182:360–369, 2018.

[98] Isidro Bonilla and Richard E. Synder. Transverse relaxation in rat optic nerve. *NMR in Biomedicine*, 20(2):113–120, 2007.

[99] Sharon Peled, David G. Cory, Stephen A. Raymond, Daniel A. Kirschner, and Ferenc A. Jolesz. Water diffusion, T2, and compartmentation in frog sciatic nerve. *Magnetic Resonance in Medicine*, 42(5):911–918, 1999.

[100] Björn Lampinen, Filip Szczepankiewicz, Mikael Novén, Danielle van Westen, Oskar Hansson, Elisabet Englund, Johan Mårtensson, Carl Fredrik Westin, and Markus Nilsson. Searching for the neurite density with diffusion MRI: Challenges for biophysical modeling. *Human Brain Mapping*, 40(8):2529–2545, 2019.

[101] Sune Nørhøj Jespersen, Henrik Lundell, Casper Kaae Sønderby, and Tim B. Dyrby. Orientationally invariant metrics of apparent compartment eccentricity from double pulsed field gradient diffusion experiments. *NMR in Biomedicine*, 26(12):1647–1662, 2013.

[102] Enrico Kaden, Frithjof Kruggel, and Daniel C Alexander. Quantitative mapping of the per-axon diffusion coefficients in brain white matter. *Magn. Reson. Med.*, 75(4):1752–1763, April 2016.

[103] Enrico Kaden, Nathaniel D. Kelm, Robert P. Carson, Mark D. Does, and Daniel C. Alexander. Multi-compartment microscopic diffusion imaging. *NeuroImage*, 139:346–359, 2016.

[104] Filip Szczepankiewicz, Samo Lasič, Danielle van Westen, Pia C. Sundgren, Elisabet Englund, Carl Fredrik Westin, Freddy Ståhlberg, Jimmy Lätt, Daniel Topgaard, and Markus Nilsson. Quantification of microscopic diffusion anisotropy disentangles effects of orientation dispersion from microstructure: Applications in healthy volunteers and in brain tumors. *NeuroImage*, 104:241–252, 2015.

[105] Samo Lasič, Filip Szczepankiewicz, Stefanie Eriksson, Markus Nilsson, and Daniel Topgaard. Microanisotropy imaging: Quantification of microscopic diffusion anisotropy and orientational order parameter by diffusion MRI with magic-angle spinning of the q-vector. *Frontiers in Physics*, 2(February):1–14, 2014.

[106] Kasper Winther Andersen, Samo Lasič, Henrik Lundell, Markus Nilsson, Daniel Topgaard, Finn Sellebjerg, Filip Szczepankiewicz, Hartwig Roman Siebner, Morten Blinkenberg, and Tim B Dyrby. Disentangling white-matter damage from physiological fibre orientation dispersion in multiple sclerosis. *Brain Communications*, 2(2), 2020.

[107] Stefanie Eriksson, Samo Lasic, and Daniel Topgaard. Isotropic diffusion weighting in PGSE NMR by magic-angle spinning of the q-vector. *Journal of Magnetic Resonance*, 226:13–18, 2013.

[108] Rafael Neto Henriques, Sune N. Jespersen, and Noam Shemesh. Microscopic anisotropy misestimation in spherical-mean single diffusion encoding MRI. *Magnetic Resonance in Medicine*, 81(5):3245–3261, 2019.

[109] Marco Pizzolato, Demian Wassermann, Rachid Deriche, Jean Philippe Thiran, and Rutger Fick. Orientation-Dispersed Apparent Axon Diameter via Multi-Stage Spherical Mean Optimization. *Mathematics and Visualization*, (226249):91–101, 2019.

[110] Henrik Lundell, Carson Ingo, Tim B. Dyrby, and Itamar Ronen. Cytosolic diffusivity and microscopic anisotropy of N-acetyl aspartate in human white matter with diffusion-weighted MRS at 7 T. *NMR in Biomedicine*, (September 2019):1–14, 2020.

[111] Hong Hsi Lee, Sune N. Jespersen, Els Fieremans, and Dmitry S. Novikov. The impact of realistic axonal shape on axon diameter estimation using diffusion MRI. *NeuroImage*, 223(August):117228, 2020.

[112] Christopher D Kroenke, Joseph J H Ackerman, and Dmitriy A Yablonskiy. On the nature of the NAA diffusion attenuated MR signal in the central nervous system. *Magn. Reson. Med.*, 52(5):1052–1059, November 2004.

[113] Jelle Veraart, Daniel Nunes, Umesh Rudrapatna, Els Fieremans, Derek K. Jones, Dmitry S. Novikov, and Noam Shemesh. Noninvasive quantification of axon radii using diffusion MRI. *eLife*, 9:1–27, 2020.

[114] Tim Salditt and Mareike Töpperwien. Holographic imaging and tomography of biological cells and tissues. In Tim Salditt, Alexander Egner, and D. Russell Luke, editors, *Nanoscale Photonic Imaging*, pages 339–376. Springer International Publishing, Cham, 2020.

[115] Atsushi Momose and Jun Fukuda. Phase-contrast radiographs of nonstained rat cerebellar specimen. *Medical Physics*, 22(4):375–379, apr 1995.

[116] Matthias Bartels. *Cone-beam x-ray phase contrast tomography of biological samples*, volume 013 of *Göttingen Series in X-ray Physics*. Universitätsverlag Göttingen, Göttingen, 2013.

[117] P. Cloetens, W. Ludwig, J. Baruchel, D. Van Dyck, J. Van Landuyt, J. P. Guigay, and M. Schlenker. Holotomography: Quantitative phase tomography with micrometer resolution using hard synchrotron radiation x rays. *Applied Physics Letters*, 75(19):2912–2914, 1999.

[118] A. Groso, R. Abela, and M. Stampanoni. Implementation of a fast method for high resolution phase contrast tomography. *Opt. Express*, 14(18):8103–8110, Sep 2006.

[119] Yoni De Witte, Matthieu Boone, Jelle Vlassenbroeck, Manuel Dierick, and Luc Van Hoorebeke. Bronnikov-aided correction for x-ray computed tomography. *J. Opt. Soc. Am. A*, 26(4):890–894, Apr 2009.

[120] Mareike Töpperwien. *3d virtual histology of neuronal tissue by propagation-based x-ray phase-contrast tomography*, volume 025 of *Göttingen Series in X-ray Physics*. Universitätsverlag Göttingen, Göttingen, 2018.

[121] Aaron T. Kuan, Jasper S. Phelps, Logan A. Thomas, Tri M. Nguyen, Julie Han, Chiao Lin Chen, Anthony W. Azevedo, John C. Tuthill, Jan Funke, Peter Cloetens, Alexandra Pacureanu, and Wei Chung Allen Lee. Dense neuronal reconstruction through X-ray holographic nano-tomography. *Nature Neuroscience*, 2020.

[122] Mareike Töpperwien, Martin Krenkel, Kristin Müller, and Tim Salditt. Phase-contrast tomography of neuronal tissues: from laboratory- to high resolution synchrotron CT. *Developments in X-Ray Tomography X*, 9967:99670T, 2016.

[123] Mareike Töpperwien, Franziska van der Meer, Christine Stadelmann, and Tim Salditt. Three-dimensional virtual histology of human cerebellum by X-ray phase-contrast tomography. *Proceedings of the National Academy of Sciences of the United States of America*, 115(27):6940–6945, 2018.

[124] Diego F. Silva, Vinícius M.A. Souza, Daniel P.W. Ellis, Eamonn J. Keogh, and Gustavo E.A.P.A. Batista. Exploring Low Cost Laser Sensors to Identify Flying Insect Species: Evaluation of Machine Learning and Signal Processing Methods. *Journal of Intelligent and Robotic Systems: Theory and Applications*, 80:313–330, 2015.

[125] Maxime Hubert, Alexandra Pacureanu, Cyril Guilloud, Yang Yang, Julio C. Da Silva, Jerome Laurencin, Florence Lefebvre-Joud, and Peter Cloetens. Efficient correction of wavefront inhomogeneities in X-ray holographic nanotomography by random sample displacement. *Applied Physics Letters*, 112(20):203704, 2018.

[126] Mareike Töpperwien, Andrea Markus, Frauke Alves, and Tim Salditt. Contrast enhancement for visualizing neuronal cytoarchitecture by propagation-based x-ray phase-contrast tomography. *NeuroImage*, 199(March):70–80, 2019.

[127] Merrick C. Strotton, Andrew J. Bodey, Kazimir Wanelik, Michele C. Darrow, Esau Medina, Carl Hobbs, Christoph Rau, and Elizabeth J. Bradbury. Optimising complementary soft tissue synchrotron X-ray microtomography for reversibly-stained central nervous system samples. *Scientific Reports*, 8(1):1–18, 2018.

[128] S. Zabler, P. Cloetens, J. P. Guigay, J. Baruchel, and M. Schlenker. Optimization of phase contrast imaging using hard x rays. *Review of Scientific Instruments*, 76(7), 2005.

[129] H M Kjer, M Andersson, Yi He, M Elkjaer, A Pacureanu, Z Illes, B Pakkenberg, A Bjorholm Dahl, V Andersen Dahl, and T B Dyrby. Streamline tractography for 3D mapping of axon bundle organization in one MRI voxel using ultra-high resolution synchrotron radiation imaging, 2020.

[130] Jelle Veraart, Els Fieremans, and Dmitry S. Novikov. Diffusion MRI noise mapping using random matrix theory. *Magnetic Resonance in Medicine*, 76(5):1582–1593, 2016.

[131] Elias Kellner, Bibek Dhital, Valerij G. Kiselev, and Marco Reisert. Gibbs-ringing artifact removal based on local subvoxel-shifts. *Magnetic Resonance in Medicine*, 76(5):1574–1581, 2016.

[132] J. Donald Tournier, Fernando Calamante, and Alan Connelly. MRtrix: Diffusion tractography in crossing fiber regions. *International Journal of Imaging Systems and Technology*, 22(1):53–66, 2012.

[133] Jonathan Rafael-Patino, David Romascano, Alonso Ramirez-Manzanares, Erick Jorge Canales-Rodríguez, Gabriel Girard, and Jean Philippe Thiran. Robust Monte-Carlo Simulations in Diffusion-MRI: Effect of the Substrate Complexity and Parameter Choice on the Reproducibility of Results. *Frontiers in Neuroinformatics*, 14:8, 2020.

[134] S.K. Ludwin. *"Pathology of the myelin sheath" in The Axon: Structure, Function and Pathophysiology.* Oxford University Press, 1995.

[135] Fwu Tarng Dun. The Length and Diameter of the Node of Ranvier. *IEEE Transactions on Biomedical Engineering*, BME-17(1):21–24, 1970.

[136] Marc C. Ford, Olga Alexandrova, Lee Cossell, Annette Stange-Marten, James Sinclair, Conny Kopp-Scheinpflug, Michael Pecka, David Attwell, and Benedikt Grothe. Tuning of Ranvier node and internode properties in myelinated axons to adjust action potential timing. *Nature Communications*, 6, 2015.

[137] A. Reles and R. L. Friede. Axonal cytoskeleton at the nodes of Ranvier. *Journal of Neurocytology*, 20(6):450–458, 1991.

[138] Ana Rita Costa, Rita Pinto-Costa, Sara Castro Sousa, and Mónica Mendes Sousa. The Regulation of Axon Diameter: From Axonal Circumferential Contractility to Activity-Dependent Axon Swelling. *Frontiers in Molecular Neuroscience*, 11:319, 2018.

[139] Anthony Fan, Alireza Tofangchi, Mikhail Kandel, Gabriel Popescu, and Taher Saif. Coupled circumferential and axial tension driven by actin and myosin influences in vivo axon diameter. *Scientific Reports*, 7(1):14188, 2017.

[140] Sérgio Carvalho Leite, Paula Sampaio, Vera Filipe Sousa, Joana Nogueira-Rodrigues, Rita Pinto-Costa, Luanne Laurel Peters, Pedro Brites, and Mónica Mendes Sousa. The Actin-Binding Protein α-Adducin Is Required for Maintaining Axon Diameter. *Cell Reports*, 15(3):490–498, 2016.

[141] R. Douglas Fields. Signaling by neuronal swelling. *Science Signaling*, 4(155):tr1–tr1, 2011.

[142] Ronan Chéreau, G. Ezequiel Saraceno, Julie Angibaud, Daniel Cattaert, and U. Valentin Nägerl. Superresolution imaging reveals activity-dependent plasticity of axon morphology linked to changes in action potential conduction velocity. *Proceedings of the National Academy of Sciences of the United States of America*, 114(6):1401–1406, 2017.

[143] Christopher K. Glass, Kaoru Saijo, Beate Winner, Maria Carolina Marchetto, and Fred H. Gage. Mechanisms Underlying Inflammation in Neurodegeneration. *Cell*, 140(6):918–934, 2010.

[144] Santa Mammana, Paolo Fagone, Eugenio Cavalli, Maria Sofia Basile, Maria Cristina Petralia, Ferdinando Nicoletti, Placido Bramanti, and Emanuela Mazzon. The role of macrophages in neuroinflammatory and neurodegenerative pathways of alzheimer's disease, amyotrophic lateral sclerosis, and multiple sclerosis: Pathogenetic cellular effectors and potential therapeutic targets. *International Journal of Molecular Sciences*, 19(3):1–20, 2018.

[145] Matthew D. Budde and Joseph A. Frank. Neurite beading is sufficient to decrease the apparent diffusion coefficient after ischemic stroke. *Proceedings of the National Academy of Sciences of the United States of America*, 107(32):14472–14477, 2010.

[146] János A. Perge, Jeremy E. Niven, Enrico Mugnaini, Vijay Balasubramanian, and Peter Sterling. Why do axons differ in caliber? *Journal of Neuroscience*, 32(2):626–638, 2012.

[147] A. A. Harper and S. N. Lawson. Conduction velocity is related to morphological cell type in rat dorsal root ganglion neurones. *The Journal of Physiology*, 359(1):31–46, 1985.

[148] Hiroko Sakai and Charles D. Woody. Relationships between axonal diameter, soma size, and axonal conduction velocity of HRP-filled, pyramidal tract cells of awake cats. *Brain Research*, 460(1):1–7, 1988.

[149] M. J. Katz. How straight do axons grow? *Journal of Neuroscience*, 5(3):589–595, 1985.

[150] Assaf Horowitz, Daniel Barazany, Ido Tavor, Moran Bernstein, Galit Yovel, and Yaniv Assaf. In vivo correlation between axon diameter and conduction velocity in the human brain. *Brain Structure and Function*, 220(3):1777–1788, 2015.

[151] Hui Zhang, Torben Schneider, Claudia A. Wheeler-Kingshott, and Daniel C. Alexander. NODDI: Practical in vivo neurite orientation dispersion and density imaging of the human brain. *NeuroImage*, 61(4):1000–1016, 2012.

[152] Nicolas Kunz, Stéphane V. Sizonenko, Petra S. Hüppi, Rolf Gruetter, and Yohan Van de Looij. Investigation of field and diffusion time dependence of the diffusion-weighted signal at ultrahigh magnetic fields. *NMR in Biomedicine*, 26(10):1251–1257, 2013.

[153] Els Fieremans, Lauren M. Burcaw, Hong Hsi Lee, Gregory Lemberskiy, Jelle Veraart, and Dmitry S. Novikov. In vivo observation and biophysical interpretation of time-dependent diffusion in human white matter. *NeuroImage*, 129:414–427, 2016.

[154] Natalya Korogod, Carl C.H. Petersen, and Graham W. Knott. Ultrastructural analysis of adult mouse neocortex comparing aldehyde perfusion with cryo fixation. *eLife*, 4(AUGUST2015), 2015.

[155] Jan Tønnesen, V. V.G.Krishna Inavalli, and U. Valentin Nägerl. Super-Resolution Imaging of the Extracellular Space in Living Brain Tissue. *Cell*, 172(5):1108–1121.e15, 2018.

[156] Glenn K. Matsushima and Pierre Morell. The neurotoxicant, cuprizone, as a model to study demyelination and remyelination in the central nervous system. *Brain Pathology*, 11(1):107–116, 2001.

[157] Jose M. Vega-Riquer, Gerardo Mendez-Victoriano, Raul A. Morales-Luckie, and Oscar Gonzalez-Perez. Five Decades of Cuprizone, an Updated Model to Replicate Demyelinating Diseases. *Current Neuropharmacology*, 17(2):129–141, 2019.

[158] Ahmad Raza Khan, Anda Cornea, Lindsey A. Leigland, Steven G. Kohama, Sune Nørhøj Jespersen, and Christopher D. Kroenke. 3D structure tensor analysis of light microscopy data for validating diffusion MRI. *NeuroImage*, 111:192–203, 2015.

[159] C.-F. Westin, S.E. Maier, H. Mamata, A. Nabavi, F.A. Jolesz, and R. Kikinis. Processing and visualization for diffusion tensor MRI. *Medical Image Analysis*, 6(2):93–108, jun 2002.

[160] Susumu Mori and Jiangyang Zhang. Principles of Diffusion Tensor Imaging and Its Applications to Basic Neuroscience Research. *Neuron*, 51(5):527–539, 2006.

[161] J. Donald Tournier, Robert Smith, David Raffelt, Rami Tabbara, Thijs Dhollander, Maximilian Pietsch, Daan Christiaens, Ben Jeurissen, Chun Hung Yeh, and Alan Connelly. MRtrix3: A fast, flexible and open software framework for medical image processing and visualisation. *NeuroImage*, 202(January):116137, 2019.

[162] Eleftherios Garyfallidis, Matthew Brett, Marta Morgado Correia, Guy B. Williams, and Ian Nimmo-Smith. QuickBundles, a Method for Tractography Simplification. *Frontiers in Neuroscience*, 6(December):1–13, 2012.

[163] C. Leuze, M. Goubran, M. Barakovic, M. Aswendt, Q. Tian, B. Hsueh, A. Crow, E. M.M. Weber, G. K. Steinberg, M. Zeineh, E. D. Plowey, A. Daducci, G. Innocenti, J. P. Thiran, K. Deisseroth, and J. A. McNab. Comparison of diffusion MRI and CLARITY fiber orientation estimates in both gray and white matter regions of human and primate brain. *NeuroImage*, 228(December 2020), 2021.

[164] Trygve B. Leergaard, Nathan S. White, Alex De Crespigny, Ingeborg Bolstad, Helen D'Arceuil, Jan G. Bjaalie, and Anders M. Dale. Quantitative histological validation of diffusion MRI fiber orientation distributions in the rat brain. *PLoS ONE*, 5(1), 2010.

[165] Sune Nrhøj Jespersen, Lindsey A. Leigland, Anda Cornea, and Christopher D. Kroenke. Determination of axonal and dendritic orientation distributions within the developing cerebral cortex by diffusion tensor imaging. *IEEE Transactions on Medical Imaging*, 31(1):16–32, 2012.

[166] Kurt Schilling, Vaibhav Janve, Yurui Gao, Iwona Stepniewska, Bennett A. Landman, and Adam W. Anderson. Comparison of 3D orientation distribution functions measured with confocal microscopy and diffusion MRI. *NeuroImage*, 129:185–197, 2016.

[167] Kurt G. Schilling, Vaibhav Janve, Yurui Gao, Iwona Stepniewska, Bennett A. Landman, and Adam W. Anderson. Histological validation of diffusion MRI fiber orientation distributions and dispersion. *NeuroImage*, 165(August 2017):200–221, 2018.

[168] Kurt G. Schilling, Yurui Gao, Iwona Stepniewska, Vaibhav Janve, Bennett A. Landman, and Adam W. Anderson. Histologically derived fiber response functions for diffusion MRI vary across white matter fibers—An ex vivo validation study in the squirrel monkey brain. *NMR in Biomedicine*, 32(6):1–17, 2019.

[169] Raimo A. Salo, Ilya Belevich, Eija Jokitalo, Olli Gröhn, and Alejandra Sierra. Assessment of the structural complexity of diffusion MRI voxels using 3D electron microscopy in the rat brain. *NeuroImage*, 225(October 2020), 2021.

[170] M. Bartels, M. Krenkel, P. Cloetens, W. Möbius, and T. Salditt. Myelinated mouse nerves studied by X-ray phase contrast zoom tomography. *Journal of Structural Biology*, 192(3):561–568, 2015.

[171] Wiebke Möbius, Klaus Armin Nave, and Hauke B. Werner. Electron microscopy of myelin: Structure preservation by high-pressure freezing. *Brain Research*, 1641:92–100, 2016.

[172] Federico N. Soria, Cristina Miguelez, Olga Peñagarikano, and Jan Tønnesen. Current Techniques for Investigating the Brain Extracellular Space. *Frontiers in Neuroscience*, 14(October):1–15, 2020.

[173] Özgün Çiçek, Ahmed Abdulkadir, Soeren S. Lienkamp, Thomas Brox, and Olaf Ronneberger. 3D U-Net: Learning Dense Volumetric Segmentation from Sparse Annotation. In Sebastien Ourselin, Leo Joskowicz, Mert R. Sabuncu, Gozde Unal, and William Wells, editors, *Medical Image Computing and Computer-Assisted Intervention*, Lecture Notes in Computer Science, pages 424–432. Springer International Publishing, Cham, 2016.

[174] Ali Abdollahzadeh, Ilya Belevich, Eija Jokitalo, Alejandra Sierra, and Jussi Tohka. DeepACSON automated segmentation of white matter in 3D electron microscopy. *Communications Biology*, 4(1):179, dec 2021.

[175] Tao Zeng, Bian Wu, and Shuiwang Ji. DeepEM3D: approaching human-level performance on 3D anisotropic EM image segmentation. *Bioinformatics (Oxford, England)*, 33(16):2555–2562, 2017.

[176] Qiuyun Fan, Aapo Nummenmaa, Thomas Witzel, Ned Ohringer, Qiyuan Tian, Kawin Setsompop, Eric C. Klawiter, Bruce R. Rosen, Lawrence L. Wald, and Susie Y. Huang. Axon diameter index estimation independent of fiber orientation distribution using high-gradient diffusion MRI. *NeuroImage*, 222(June):117197, 2020.

[177] Emilie T. McKinnon, Jens H. Jensen, G. Russell Glenn, and Joseph A. Helpern. Dependence on b-value of the direction-averaged diffusion-weighted imaging signal in brain. *Magnetic Resonance Imaging*, 36:121–127, 2017.

[178] Jelle Veraart, Els Fieremans, and Dmitry S. Novikov. On the scaling behavior of water diffusion in human brain white matter. *NeuroImage*, 185(October 2018):379–387, 2019.

[179] HáKon Gudbjartsson and Samuel Patz. The rician distribution of noisy mri data. *Magnetic Resonance in Medicine*, 34(6):910–914, dec 1995.

[180] Jelle Veraart and Dmitry Novikov. Axon radius mapping, 2019. https://github.com/NYU-DiffusionMRI/AxonRadiusMapping.

[181] Hui Zhang, Tim B. Dyrby, and Daniel C. Alexander. Axon diameter mapping in crossing fibers with diffusion MRI. In *Lecture Notes in Computer Science (including subseries Lecture Notes in Artificial Intelligence and Lecture Notes in Bioinformatics)*, volume 6892 LNCS, pages 82–89, 2011.

[182] Hua Li, Ho Ming Chow, Diane C Chugani, and Harry T Chugani. Minimal number of gradient directions for robust measurement of spherical mean diffusion weighted signal. *Magn. Reson. Imaging*, 54:148–152, December 2018.

[183] Derek K Jones. The effect of gradient sampling schemes on measures derived from diffusion tensor MRI: a monte carlo study. *Magn. Reson. Med.*, 51(4):807–815, April 2004.

[184] Jelle Veraart, Erika P. Raven, Luke J. Edwards, Nikolaus Weiskopf, and Derek K. Jones. The variability of mr axon radii estimates in the human white matter. *Human Brain Mapping*, 2021.

[185] Jens H. Jensen, G. Russell Glenn, and Joseph A. Helpern. Fiber ball imaging. *NeuroImage*, 124:824–833, 2016.

[186] Marco Palombo, Andrada Ianus, Michele Guerreri, Daniel Nunes, Daniel C. Alexander, Noam Shemesh, and Hui Zhang. SANDI: A compartment-based model for non-invasive apparent soma and neurite imaging by diffusion MRI. *NeuroImage*, 215(March), 2020.

[187] Bibek Dhital, Marco Reisert, Elias Kellner, and Valerij G. Kiselev. Intra-axonal diffusivity in brain white matter. *NeuroImage*, 189(June 2018):543–550, 2019.

[188] Chantal M.W. Tax, Filip Szczepankiewicz, Markus Nilsson, and Derek K. Jones. The dot-compartment revealed? Diffusion MRI with ultra-strong gradients and spherical tensor encoding in the living human brain. *NeuroImage*, 210(September 2019), 2020.

[189] Evren Özarslan, Cem Yolcu, Magnus Herberthson, Hans Knutsson, and Carl Fredrik Westin. Influence of the size and curvedness of neural projections on the orientationally averaged diffusion MR signal. *Frontiers in Physics*, 6(MAR):1–10, 2018.

Contribution I

Axon morphology is modulated by the local environment and impacts the noninvasive investigation of its structure–function relationship

Mariam Andersson[a,b,1], **Hans Martin Kjer**[a,b], **Jonathan Rafael-Patino**[c], **Alexandra Pacureanu**[d], **Bente Pakkenberg**[e], **Jean-Philippe Thiran**[c,f,g], **Maurice Ptito**[h,i], **Martin Bech**[j], **Anders Bjorholm Dahl**[b], **Vedrana Andersen Dahl**[b], **and Tim B. Dyrby**[a,b,1]

[a]Danish Research Centre for Magnetic Resonance, Centre for Functional and Diagnostic Imaging and Research, Copenhagen University Hospital Hvidovre, 2650 Hvidovre, Denmark; [b]Department of Applied Mathematics and Computer Science, Technical University of Denmark, 2800 Kongens Lyngby, Denmark; [c]Signal Processing Laboratory (LTS5), École Polytechnique Fédérale de Lausanne, 1015 Lausanne, Switzerland; [d]The European Synchrotron, 38000 Grenoble, France; [e]Research Laboratory for Stereology and Neuroscience, Copenhagen University Hospital, Bispebjerg, 2400 Copenhagen, Denmark; [f]Radiology Department, Centre Hospitalier Universitaire Vaudois and University of Lausanne, 1011 Lausanne, Switzerland; [g]Center for Biomedical Imaging, 1015 Lausanne, Switzerland; [h]School of Optometry, University of Montreal, Montreal, QC H3T 1P1, Canada; [i]Department of Neuroscience, Faculty of Health Science, University of Copenhagen, 2200 Copenhagen, Denmark; and [j]Division of Medical Radiation Physics, Department of Clinical Sciences, Lund University, 221 85 Lund, Sweden

Edited by Marcus E. Raichle, Washington University in St. Louis, St. Louis, MO, and approved November 15, 2020 (received for review July 3, 2020)

Axonal conduction velocity, which ensures efficient function of the brain network, is related to axon diameter. Noninvasive, in vivo axon diameter estimates can be made with diffusion magnetic resonance imaging, but the technique requires three-dimensional (3D) validation. Here, high-resolution, 3D synchrotron X-ray nano-holotomography images of white matter samples from the corpus callosum of a monkey brain reveal that blood vessels, cells, and vacuoles affect axonal diameter and trajectory. Within single axons, we find that the variation in diameter and conduction velocity correlates with the mean diameter, contesting the value of precise diameter determination in larger axons. These complex 3D axon morphologies drive previously reported 2D trends in axon diameter and *g*-ratio. Furthermore, we find that these morphologies bias the estimates of axon diameter with diffusion magnetic resonance imaging and, ultimately, impact the investigation and formulation of the axon structure–function relationship.

axon morphology | conduction velocity | myelination | brain | MRI

Axons form the communication infrastructure of the brain network. Upon their initial discovery by Otto Friedrich Karl Deiters circa 1860, they were described as "cylinders"—a description still widely used today. The saltatory conduction velocity (CV) of action potentials along myelinated axons depends on their morphology, including axon diameter (AD) (1) and thickness of the CV-boosting, insulating myelin sheath (2). The ratio of AD to the outer fiber diameter, the *g*-ratio, is thought to be fixed to an optimal value that promotes high CVs and minimizes energy consumption (3). Simulation studies (4, 5) predict optimal *g*-ratios around 0.7 in the central nervous system (CNS), matching histological data (6, 7). The concept of a given *g*-ratio along straight, cylindrical axons enables an inference of the outer fiber diameter from the inner AD, allowing classical structure–function relations between outer fiber diameter and CV (8, 9) to be reformulated in terms of AD and a constant *g*-ratio (8, 9). This makes an investigation of brain network function accessible with techniques that can measure AD.

Histological tracer studies of axons between brain sites reveal that the diameter, and thus CV, of an axon depends on its origin (10) and target (7), corroborating the functional significance of AD. AD is potentially also a biomarker for neurodegenerative diseases like multiple sclerosis, which has been shown to preferentially attack smaller axons (11). To provide useful diagnostic information, the white matter (WM) microstructure and axon morphology must be characterized in vivo. Diffusion magnetic resonance imaging (MRI) uses the diffusion of water molecules to noninvasively probe the WM microstructure in the living brain. Although MRI voxels are typically on the scale of ∼1 mm, it is possible to estimate axonal dispersion (12), the axon diameter distribution (ADD) (13), and the mean of the ADD (14) by fitting three-dimensional (3D) biophysical models to the acquired diffusion signal (15). However, diffusion MRI-based AD estimates (14, 16, 17) are larger than those obtained by histology (15, 18). Potential causes include the following: limited gradient strength in the diffusion MRI acquisition (19), sequence parameters (15), tissue shrinkage in histology (17), and—as discussed here—inaccurate modeling of the WM compartments, including the century-old representation of myelinated axons as cylinders. A validation of the 3D WM anatomy could thus improve diffusion MRI-based AD estimations (17) and shed light on the validity of enforcing a cylindrical geometry and constant *g*-ratio in axonal structure–function relations. Recent 3D electron

Significance

Axons, the brain's communication cables, have been described as cylinders since their discovery in 1860. Their structure is linked to how fast they conduct signals and is thus indicative of brain health and function. Here, we demonstrate an interplay between the micromorphology of axons and other extra-axonal structures, showing that axons are noncylindrical and exhibit environment-dependent diameter and trajectory variations. The nonspecificity in diameter, and thus conduction velocity, challenges the current knowledge of how axons communicate signals. Diffusion magnetic resonance imaging can be used to measure axon diameter in the living brain in order to explore the brain network and detect potential biomarkers of disease, but we show here that the observed complex morphologies of axons bias these measurements.

Author contributions: M.A., H.M.K., and T.B.D. designed research; M.A., H.M.K., J.R.-P., A.P., B.P., J.-P.T., M.P., M.B., A.B.D., V.A.D., and T.B.D. performed research; H.M.K., A.B.D., and V.A.D. contributed new reagents/analytic tools; M.P. provided tissue materials; M.A., H.M.K., J.R.-P., and T.B.D. analyzed data; M.A. and T.B.D. wrote the paper; and H.M.K., J.R.-P., A.P., B.P., J.-P.T., M.P., M.B., A.B.D., and V.A.D. revised the paper.

The authors declare no competing interest.

This article is a PNAS Direct Submission.

[1]To whom correspondence may be addressed. Email: mariama@drcmr.dk or timd@drcmr.dk.

This article contains supporting information online at https://www.pnas.org/lookup/suppl/doi:10.1073/pnas.2012533117/-/DCSupplemental.

microscopy (EM) studies on axon morphology of the mouse reveal, in high resolution, nonuniform ADs and trajectories (20, 21). However, axons are only tracked for up to 20 μm, a fraction of their length in MRI voxels.

Here, we characterize the long-range micromorphologies of axons against the backdrop of the complex 3D WM environment consisting of blood vessels, cells, and vacuoles. With synchrotron X-ray nano-holotomography (XNH), we acquire MRI measurements of the WM from the same monkey brain as in Alexander et al. (14) and Dyrby et al. (19), in which the MRI-derived AD estimates were larger than those estimated by histology. The 3D WM environment is mapped at a voxel size of 75 nm and volume of ~150 × 150 × 150 μm^3. By combining adjacent XNH volumes, we extract axons >660 μm in length and show that AD, axon trajectory, and *g*-ratio depend on the local microstructural environment. The 3D measurements shed light on the interpretation of 2D measurements, highlighting the importance of the third dimension for a robust description of single-axon structure and function. Last, by performing Monte Carlo (MC) diffusion simulations on axonal substrates with morphological features deriving from the XNH-segmented axons, we show that geometrical deviations from cylinders cause an overestimation of AD with diffusion MRI.

Results

Volumetric Mesoscopic White Matter Features. The mean AD indices in the corpus callosum (CC) were fitted on diffusion MRI volumes of the monkey brain and exhibited the expected trend in diameter from the splenium to the genu, but with overestimated diameters (19) (Fig. 1*A*). In the splenium, along the interhemispheric connection between visual cortices V1/V2, the mean AD index was 1.3 μm. The connection length was delineated by tractography to 49.7 mm (SD = 1.9 mm) as described in *Materials and Methods*, resulting in a conduction delay of 4.8 ms.

To further investigate the microstructure underlying the diffusion MRI estimates with XNH, we extracted and processed cylindrical tissue volumes of 1 mm in diameter. Tissue was taken from the CC and a crossing fiber region, located in the anterior centrum semiovale at a point where the diffusion MRI data indicated the existence of crossing axon bundles (*SI Appendix*, Fig. S2). Four tissue structures were examined, as shown in an XNH volume of the CC splenium in Fig. 1 *B*–*D*: 1) long-range myelinated axons, 2) blood vessels, 3) cells, and 4) vacuoles.

Myelinated axons were identifiable as bright, tubular shapes with dark contours. The contrast was given by the electron density of the sample, with bright regions corresponding to low-density structures, while the dark borders were due to the binding of electron-dense osmium tetroxide to myelin. Axons exhibited varying diameters throughout the volume. Like axons, blood vessels appeared as bright, tubular structures. Their larger diameters and ability to branch distinguished them from axons. Blood cells were rarely detected since they were flushed out during the perfusion process. Cell nuclei were distinguishable by their DNA inclusions (Fig. 1*D*). Due to its high electron density, DNA—seen with a Nissl stain in Fig. 1*E*—gave rise to round, dark structures, contained within a less dense nucleoplasm. Generally, the cells clustered and aligned with the axons/blood vessels in the CC samples. The majority are believed to be glial cells, but the existence of neuronal cell bodies cannot be ruled out, as shown in the macaque CC (22). Vacuoles appeared as hyperintense spheroids and could be located within axons (Fig. 1*C*).

A volumetric quantification of the cell nuclei, vacuoles, and blood vessels was performed within an extended cylindrical volume, composed of four stitched XNH volumes having a combined diameter of 153.6 μm and length of 584.5 μm, as in Fig. 2*A*. The tissue compartments were segmented and are shown in Fig. 2.

Generally, the cell clusters, blood vessels, and vacuoles were evenly distributed throughout the volumes, as shown in Fig. 2*B*.

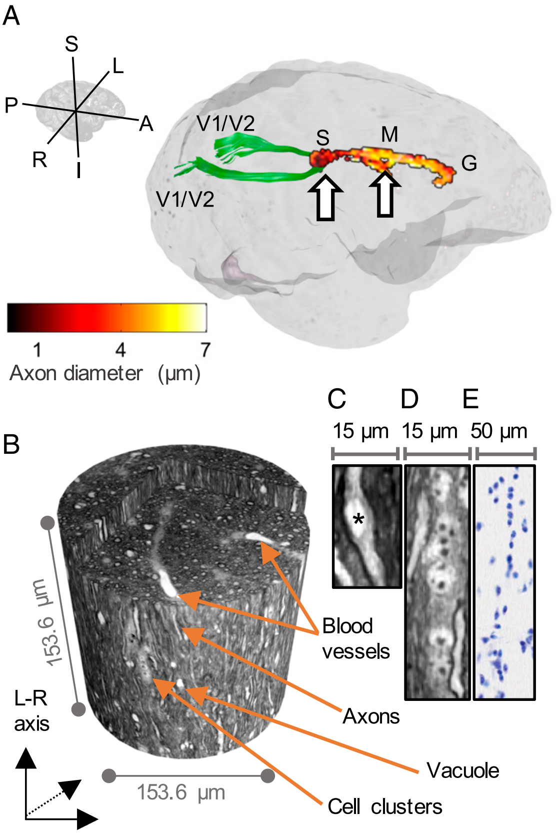

Fig. 1. Observed anatomical microstructures within the white matter of the monkey brain. (*A*) Diffusion-MRI mean AD estimations with the ActiveAx method in the midsagittal plane of corpus callosum (CC) of the monkey brain spanning the splenium (S), midbody (M), and genu (G). The arrows show biopsy locations. The interhemispheric callosal connection between primary visual cortices (V1/V2) is delineated with tractography and is shown in green. (*B*) Three-dimensional XNH volume from the splenium with an isotropic voxel size of 75 nm, showing detectable anatomical features. The volume interior is exposed to reveal the vessels. (*C*) Close-up of a vacuole (asterisk). (*D*) Close-up of a cell cluster. (*E*) Nissl stain light microscopy image showing nuclei in the same splenium region as *D* in an age-matched monkey (BrainMaps: An Interactive Multiresolution Brain Atlas; brainmaps.org).

The average volume fractions of the quantified structures in the splenium were 4.6%, 0.6%, and 1.5% for the cell clusters, blood vessels, and vacuoles, respectively. The extracellular space (ECS) could not be distinguished. Since the samples were dehydrated during tissue processing, it may have shrunk considerably, and the remaining volume fraction is thought to be occupied mostly by myelinated axons. The blood vessels were few but occupied the largest volume fraction after the axons with diameters between 4 and 10 μm.

Morphological characteristics of the cell clusters are shown in Fig. 2*E*. The cell nuclei had a mean diameter of 5.5 μm (SD = 0.73 μm; *N* = 38). Assuming spherical nuclei, the average cell cluster of volume 1,057 μm^3 contained 12 cells. They could be represented by tensors whose principal axes often aligned with the axons or nearest blood vessels. The typical cell cluster tensor shape, produced by averaging the first, second, and third principal axis lengths of all clusters, is shown in Fig. 2*C* and has a

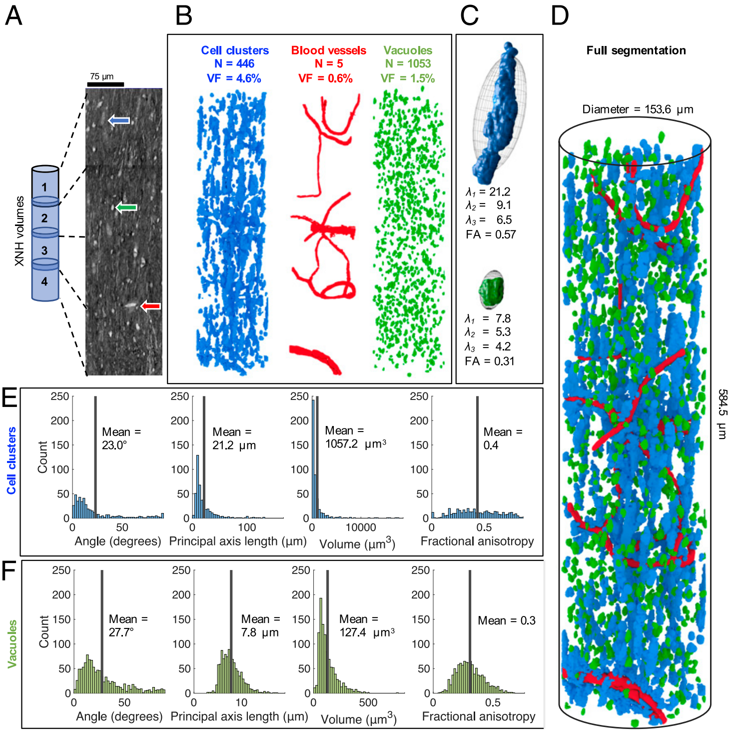

Fig. 2. Volumetric quantification of cell clusters, vessels, and vacuoles. (*A*) Two-dimensional slice through four overlapping XNH volumes (13.6-µm overlap) of the monkey brain splenium. Blue arrow, cell body. Green arrow, vacuole. Red arrow, blood vessel. (*B*) Three-dimensional reconstructions of the cell clusters (blue), blood vessels (red), and vacuoles (green) within the cylindrical volume of length 584.4 µm and diameter 153.6 µm. (*C*) λ_1, λ_2, and λ_3 denote the average first, second, and third principal-component lengths of tensors fitted to the cell cluster/vacuole structures. These are visualized by ellipsoids. In blue/green: examples of an individual cell cluster/vacuole. (*D*) Three-dimensional visualization of cell cluster, blood vessel, and vacuole segmentations. (*E* and *F*) Histograms showing the mean values and distributions of the following: inclination angle (compared to the axon population direction), principal axis length, mean volume, and FA across the cellular (blue) and vacuole (green) components, respectively.

fractional anisotropy (FA) of 0.57 and principal axis lengths between 6.5 and 21.2 µm. The morphological characteristics of the smaller vacuoles are shown in Fig. 2*F*. The typical vacuole tensor shape (Fig. 2*C*) had FA = 0.31 and principal axis lengths ranging between 4.2 and 7.8 µm. The vacuoles were scattered throughout the XNH volume, with some situated within the axons (Fig. 1*C*).

Axonal Micromorphology in 3D: Diameters and Dispersion. Axons differed from cylinders in terms of diameter and trajectory changes. Axons ($N = 54$) with mean diameters between 2.1 and 3.8 µm were segmented from the XNH volume in Fig. 1*B* as described in *Materials and Methods*. The 54-axon population, shown in Fig. 3*A*, had a mean diameter of 2.7 µm and a volume-weighted mean diameter of 2.9 µm, both significantly larger than the diffusion MRI estimate of 1.3 µm. This was expected, since the diffusion MRI estimate was based on modeling of the signal from all axons in the image voxels, small and large, while the XNH estimate was extracted solely from the geometries of larger axons. Smaller axons were observable, but the image resolution and signal-to-noise level of the XNH volumes challenged a robust segmentation. In general, large-diameter (>2 µm) axons were evenly distributed throughout the tissue at a density of $0.0123/\mu m^2$ and were surrounded by smaller axons. The midbody CC and the crossing fiber region were similarly organized (*SI Appendix*, Fig. S3).

Longitudinal AD variations. The trajectories of the 54 segmented axons, shown in Fig. 3*B*, ranged in length between 124 and 170 µm, with a combined length of 8.36 mm. Their diameters varied nonsystematically along their lengths. We define AD to be the equivalent diameter, the diameter of a circle with the same area as the axonal cross-section perpendicular to its local trajectory, as in Abdollahzadeh et al. (20). The combined 3D ADD, representing all diameters measured at 150-nm intervals along all 54 axons, had a mean diameter of 2.7 µm, and followed a gamma distribution with parameters $a = 27$ and $b = 0.2$ (Fig. 3*C*).

We use the terms "longitudinal" AD and ADD to describe the ADs and ADDs along single axons. Gamma distributions were fitted to the individual longitudinal ADDs of the largest and smallest mean diameter axons, respectively. The longitudinal ADD of the largest axon was similar in width to that of the combined 3D ADD, while that of smallest axon was significantly narrower (Fig. 3*C*). A weak linear relationship ($R^2 = 0.29$) was found between the mean AD and the SD of the longitudinal AD (Fig. 3*D*), suggesting that larger axons exhibit larger diameter variations than small axons, but with significant variability. The maximum encountered SD of 0.5 µm (Fig. 3*D*) entails that the majority of diameter fluctuations occur within ±0.5 µm of the mean AD.

To compare with measurements from 2D techniques, we calculated the slice-wise ADs for the 1,139 slices in which all 54 axons were present. The conventional 2D ADDs from six of

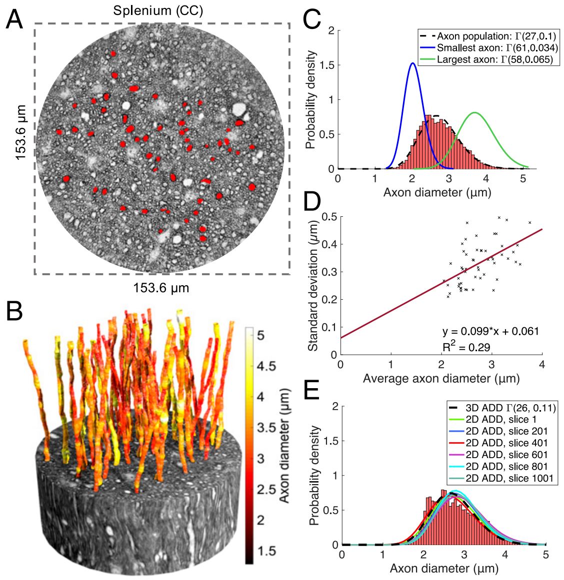

Fig. 3. Distribution and morphology of large axons. (*A*) Distribution of 54 large axons (red) in a 2D slice of the monkey splenium. (*B*) Fifty-four segmented axons from the monkey splenium. The axon lengths range from 124 to 170 µm, with average ADs between 2.1 and 3.8 µm. (*C*) Combined 3D ADD consisting of diameter measurements every 150 nm along all 54 axons and associated gamma distribution fit (black). For comparison, the fits of the longitudinal ADDs of the thinnest (blue) and thickest axon (green) are shown. (*D*) The SD of the longitudinal AD correlates positively with average AD. (*E*) Histogram and gamma distribution fit (black striped line) of combined 3D ADD, along with gamma distribution fits of the 2D ADD, sampled every 200 slices of the image subvolume in which all 54 axons were present.

these slices are shown in Fig. 3*E* and overlap with the combined 3D ADD. The mean 2D diameter of the fiber population throughout their common volume was 2.9 µm; from slice to slice, this value varied at most ±150 nm.

Axonal dispersion. Axonal dispersion is a measure of disorder of the axonal trajectories. On the bundle level, 54 axons, the orientation dispersion (OD) describes the angular spread of the axons around the main bundle direction. Although axons in the CC were expected to be aligned and straight, the mean OD was 7° (Fig. 4 *A* and *B*).

On the single-axon level, we used microdispersion to quantify dispersion on different length scales as described in *Materials and Methods*. The microdispersion describes the angle between the main axon direction and axon segments of certain lengths. The microdispersion decayed smoothly with increasing sampling length (Fig. 4*C*). Between sampling lengths of 1 and 30 µm, the average microdispersion decreased from 14 to 7°.

The longitudinal ADD, and not the myelin thickness, dominates longitudinal g-ratio variations. We investigated how the *g*-ratio, and consequently the CV, varied along axonal internodes—the axon segment between consecutive nodes of Ranvier—by mapping the long-range behavior of six axons (>580-µm length) in the monkey splenium, as shown in Fig. 5*A*. The equivalent inner AD and equivalent outer fiber diameter were evaluated by manual segmentation at *N* randomly generated locations along the axonal internodes (Fig. 5*B*). This revealed a linear correlation between the inner and outer longitudinal diameters, suggesting a constant myelin thickness. The distributions of CVs along the internodes of axons 1, 2, and 6 (Fig. 5*C*) were calculated using the classical relationship (8) CV = 5.5·*D*, where *D* is the outer fiber diameter. Using the tract length of 49.7 mm from tractography, the mean conduction delays along the respective fibers were 2.0, 2.4, and 1.9 ms.

Fig. 5*D* depicts the morphological changes occurring over the 662-µm-long trajectory of axon 5. Its diameter varied between 1.5 and 5.3 µm, and averaged at 3.3 µm. Of nine selected regions of interest (ROIs) labeled r1 to r9, local diameter minima occurred at points r1, r6, r7, and r9. At r1 and r7, we identified nodes of Ranvier (black stars), separated by 348 µm. At r6, the reduced diameter was caused by two vacuoles. The *g*-ratio was evaluated at the nine ROIs shown in Fig. 5, and at 10 randomly chosen positions inside and outside the internode, respectively. As expected of a constant myelin thickness, the g-ratio followed the trend in diameter, with the exception of the nodes of Ranvier at points r1 and r7.

In contrast to the 54-axon population for which the mean diameter did not deviate more than ±150 nm in any slice of the volume, the mean AD in a single axon could not be reliably established from one measurement. As a measure of stability of the AD, we calculated the cumulative mean AD along axon 5 in Fig. 5*D*. The point at which the cumulative mean diameter became stable to within ±150 nm depended on the position along the axon at which measurements were commenced and was up to 200 µm for some positions.

Local obstacles such as vacuoles, blood vessels, cell clusters, and crossing axon bundles alter the morphology of axons. The presence of certain extra-axonal obstacles gave rise to noticeable trajectory changes. For example, blood vessels visibly warped the surrounding microstructure and disrupted axon trajectories as illustrated in Fig. 6 *A*–*C*.

A subvolume spanning 690 slices and containing a blood vessel of diameter ∼10 µm was isolated (Fig. 6 *A* and *B*). The expected linear trajectories of the axons, based on their positions in the first and last 75 slices of the volume, were calculated. The axon trajectories exhibited maximum deviations from their expected trajectories between 2 and 9 µm, with the most significant deviations occurring along axon segments within ±10 µm of the blood vessel (Fig. 6*C*). Axonal trajectory changes were also found in

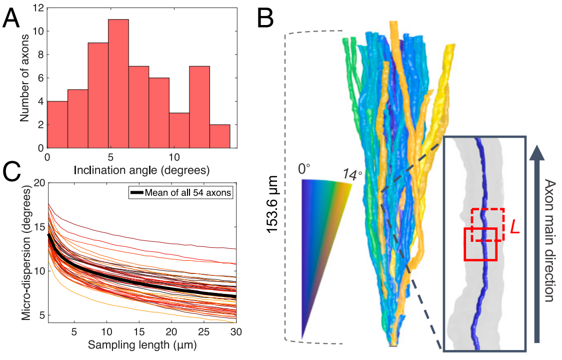

Fig. 4. Trajectory variations of large axons. (*A*) Histogram of the OD—the axonal inclination with respect to the main bundle direction—within the axon population. (*B*) Fifty-four axons from the splenium of the monkey brain translated to a common origin to illustrate the mesoscopic dispersion within the volume. Axon color represents inclination angle compared to the *z* axis. The *Inset* shows the quantification of microdispersion along axons: The axon is aligned with the *z* axis and a window of length *L* slides along the axon centerline (blue) at intervals of *L*/4. A principal-component analysis is performed on points within the window to determine their directionality. The inclination angle to the *z* axis is calculated and averaged over all windows. (*C*) Variation of microdispersion relative to main axon direction with sampling length, *L* (data points every 1 µm).

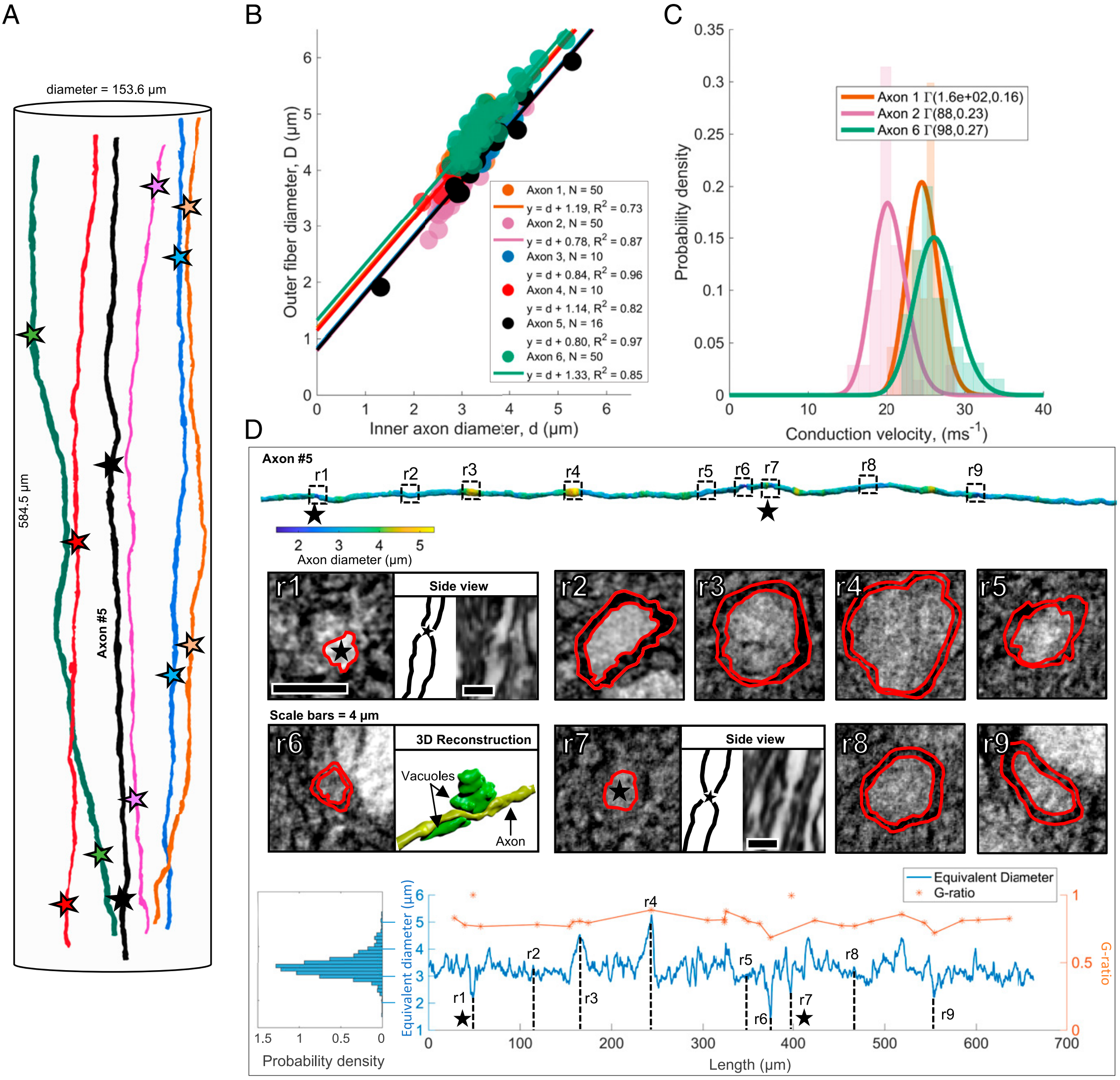

Fig. 5. Long-range quantification of axon morphology and myelination. (*A*) Six long axons segmented from the extended cylindrical XNH volume of the monkey splenium shown in Fig. 2 *A* and *D*. The stars mark identified nodes of Ranvier. (*B*) Inner AD vs. outer fiber diameter (including myelin sheath) at *N* randomly sampled points along the internodes of the six axons. Straight lines represent linear fits to the six datasets. The high linear correlation suggests that the myelin thickness remains approximately constant along the internodes, and that the *y* intercept is representative of twice the myelin thickness. (*C*) Histograms and associated gamma distribution fits of CVs along the internodes of axons 1, 2, and 6. (*D*) Row 1: segmentation of long axon (number 5, black, in *A* and *B*), colored according to diameter. The dotted squares marked r1–r9 indicate nine ROIs. Black stars mark the positions of the nodes of Ranvier. Row 2: ROI intensity images. The red lines show a manual segmentation of the inner axonal boundary and the outer myelin boundary, respectively. At r1 and r7, nodes of Ranvier are shown in an orthogonal view. At r6, the axon (yellow) is squeezed by two vacuoles (green). Row 3: on *Left*: ADD along axon. Blue line: the longitudinal equivalent AD measured every 150 nm along the axonal trajectory. In orange, the *g*-ratio for the 9 marked ROIs and 20 additional randomly generated positions along the axon.

response to cell clusters (Fig. 6*D*) and other axons in a crossing fiber region (Fig. 6*F*), in which two axons were found to twist around each other three times within the available volume. Although vacuoles did not cause trajectory variations, they caused a reduction in AD as shown in Fig. 5*D* (point r6) where two vacuoles cause a local decrease in AD, and in Fig. 6*E*.

The influence of axon morphology on diffusion MRI measurements. To assess how axon morphology influences noninvasive diffusion MRI estimates of mean AD, we performed MC simulations of the diffusion process in six different 54-axon substrates (see *Materials and Methods* for details). The substrates differed in morphological complexity, ranging from the simplest geometry, G1, parallel cylinders, to G6, the XNH segmentation (Fig. 7*A*). Each axon in each substrate inherited its morphological properties (OD, microdispersion, and mean diameter/longitudinal diameter) from the respective XNH-segmented axons.

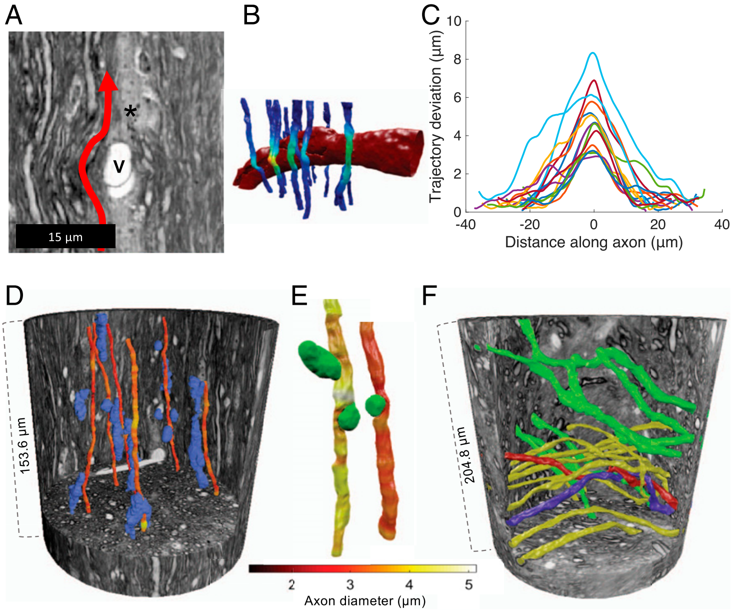

Fig. 6. Blood vessels, vacuoles, and crossing axons cause axonal trajectory variations. (*A*) XNH image looking into a vessel, marked V. Cell nuclei, marked by an asterisk, cluster around the vessel. The vessel significantly impacted the nearby axonal trajectories, depicted by the red arrow. (*B*) Three-dimensional reconstruction of *A*. Fifteen segmented axons are colored according to the deviation from their expected linear trajectories (a linear interpolation of the axon centerline above and below the blood vessel). Yellow, strong deviation; dark blue, little/no deviation. (*C*) Deviation from expected linear trajectory as a function of distance along the axon, centered on the maximum deviation. (*D* and *E*) Three-dimensional reconstructions of select cell clusters (blue), vacuoles (green), and axons, whose diameters are given by the color bar, in the XNH volume of the monkey splenium shown in Fig. 3*B*. The axon trajectories are impacted by the presence of cell clusters, and their diameters and shapes are impacted by neighboring vacuoles. (*F*) Three-dimensional reconstruction of axons in an XNH volume of a crossing fiber region. Two different projection directions are marked by green and yellow. Two axons, colored red and blue, twist around each other.

After an initial diffusion time of 6 ms, the mean AD in the parallel cylinders remained constant, as expected, at the true volume-weighted mean AD of 2.9 µm. For the other substrates, however, AD was overestimated. The degree of overestimation increased with diffusion time and substrate complexity (Fig. 7*B*). The simulations also demonstrated the effects of OD (G2) on AD and revealed that the overestimation of AD is more significant when there is microdispersion than diameter variations (G3 vs. G4).

The parallel apparent diffusion coefficient (ADC) describes the rate of diffusion along a cylinder, or axon, and is often assumed to be a fixed value in MRI-based AD estimation. Our results show parallel ADC in parallel cylinders (G1) was constant and equal to the chosen intrinsic diffusivity of 6×10^{-10} m^2/s. However, for substrates that exhibited OD, microdispersion, and/or diameter variations, the parallel ADC decreased with diffusion time and substrate complexity. Substrates with longitudinal AD variations (G4, G5, G6) exhibited particularly steep decreases in the parallel ADC with diffusion time. The 3D effects of AD variation and dispersion (OD and microdispersion) could thus be distinguished from each other based on the time dependence of the parallel ADC.

Discussion

By performing high-resolution 3D XNH on intact white matter samples from a monkey brain, we demonstrate the interplay between extra-axonal structures (blood vessels, cells, vacuoles) and the micromorphology of axons. Contrary to Deiters' century-old description of axons as cylinders, we find that AD and trajectory vary along the length of the axon, often due to obstacles in the local microstructural environment. These morphological changes entail that large axons are nonspecific in terms of diameter and CV. We thus question the value of precisely measuring their diameters and the validity of enforcing cylindrical geometries in axonal structure–function relationships. Furthermore, we show that the 3D morphologies of axons may drive previously reported trends in 2D AD distributions and *g*-ratio distributions. Our results have significant impact for AD determination with 2D techniques and—as we show here—diffusion MRI. We foresee that a thorough morphological characterization of axons and their structural context will guide the noninvasive investigation of axon morphology with diffusion MRI and, consequently, the investigation of brain network function.

The Nonspecificity of the Diameters and *g*-Ratios of Large Axons. Single axons lack well-defined diameters, and this has implications for the interpretation of 2D ADDs. Our findings show that individual axons exhibit longitudinal ADDs whose widths correlate with AD. Controversially, single axons are not always well described by classical 2D histological measurements. For one 662-µm-long axon, we show that a robust characterization of its mean diameter demands that AD be sampled for up to 200 µm at intervals of 0.15 µm. However, we find the opposite for a quantification of population mean AD. In axon populations, the 2D slice-wise ADDs match the 3D ADD, indicating that the 3D longitudinal AD variations are represented in the 2D ADDs. This has two consequences. First, it entails that previously reported 2D ADDs from EM (23) and light microscopy (7) also reflect the 3D ADD of the axon population if quantified over a sufficiently large volume. Second, contrary to the conventional

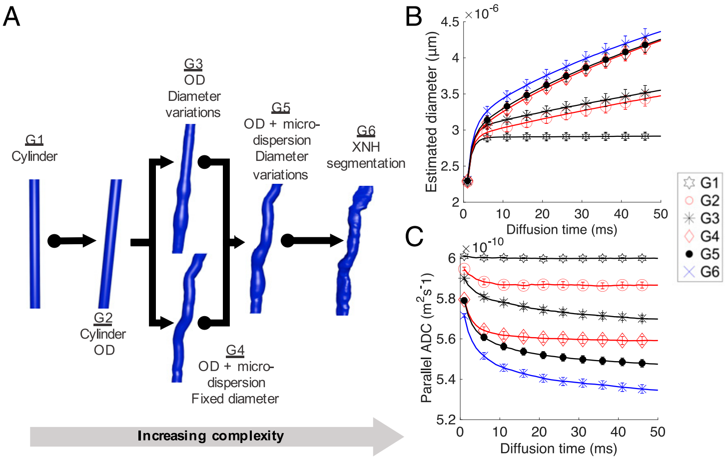

Fig. 7. Examining the diffusion properties of different axonal geometries. (*A*) The morphological features of the XNH-segmented axons in Figs. 3 and 4 are directly mapped to the six different axon classes generated for MC simulations. G1, straight cylinders of diameter corresponding to XNH axon mean diameters; G2, same as G1 plus segmented OD; G3, segmented OD and longitudinal ADD; G4, segmented OD and microdispersion; G5, segmented OD, microdispersion, and longitudinal ADD; and G6, the XNH segmentation. (*B*) The variation of estimated AD and (*C*) parallel intra-axonal ADC with diffusion time for geometries G1–G6. Error bars represent the SE, reflecting the spread in diameters/ADCs across the individual axons.

interpretation of the ADD, it implies that the 2D ADDs are not directly representative of individual ADs. Instead, the 2D ADD may be interpreted as the sampling of the longitudinal ADD of each axon. We thus propose that the characteristic tail of the 2D ADD may arise as a result of the broad longitudinal ADDs of large axons. Therefore, observations of "giant axons" (15, 23) may not indicate the presence of very large axons, but instead the local AD variations along large axons.

The morphological nonspecificity of large axons may indicate that they have different functions to smaller axons. Their wide and overlapping longitudinal ADDs entail that their mean diameters are less defined than those of smaller axons, which exhibit narrower longitudinal ADDs. Given these effects, we suggest a categorization of axons into "large" and "small." Similar categorizations are made in the peripheral nervous system (PNS). The fast-conducting, larger Alpha/Beta axons of the sciatic nerve have a broad ADD that partially overlaps the narrower ADD of the smaller, slower C and Alpha/Delta fibers (24). Although the structure–function relationship of CNS axons is not as well described as that of the sciatic nerve, it has been shown that CNS AD correlates with neuron soma size (25). ADs may thus be cell type specific. The possibility that smaller and larger axons may encode different functional features (26) further supports a size-specific axon categorization. Hence, we suggest that it may be meaningful to pursue a size-specific axon categorization, although explicit definitions of the "large" and "small" categories are yet to be established—and may possibly overlap, similar to the PNS categorization.

The longitudinal ADDs drive variations in *g*-ratio, while myelin remains stable between nodes of Ranvier. Along single internodes, we found a linear relationship between the inner AD and outer fiber diameter, entailing a nonlinear relationship between *g*-ratio and AD. Interestingly, this trend is of similar shape to that observed in 2D EM measurements of *g*-ratios in populations of CNS axons (27). For such 2D measurements, Berthold et al. (28) formulated a log-linear relationship between the number of myelin lamellae (proportional to myelin thickness, assuming a constant lamellar spacing) and the inner AD. For single axons, however, we did not find that the myelin thickness varied as a function of local AD within internodes. Instead, the linear correlation between the longitudinal inner AD and outer fiber diameter indicated that the myelin thickness along internodes was constant. Deviations from the linear trend could be due to too few sampling points, the myelin wrapping mechanism (29), measurement uncertainty in the inner and outer ADs, or myelin-disturbing vacuoles or fixation effects. Histological studies suggest that the myelin thickness shows a stronger correlation to CV than the AD (2), while simulation studies report that myelin is energetically inefficient, and potentially time consuming, to remodel (30). A constant myelin thickness along internodes is thus motivated from a signal timing and energy perspective, entailing that the longitudinal *g*-ratio variation can be driven by the longitudinal ADD. We expect the 2D *g*-ratio distributions to represent a sampling of the 3D longitudinal *g*-ratio distribution, in the same way as the 2D ADDs reflect the longitudinal AD variations. Consequently, Berthold's log-linear relationship relating the number of myelin lamellae to the AD may also be partially driven by longitudinal variations in AD. Furthermore, although large *g*-ratios can be detected in 2D images, these may be confined to local axonal segments. The *g*-ratio measurements of individual axons are therefore not meaningful on their own, since they capture only a snapshot of the 3D axon morphology. Indeed, our findings here apply only to large axons with diameters >2 μm, and smaller axons remain to be investigated.

Longitudinally varying axon morphologies suggest that individual myelinated axons exhibit varying CVs. The calculated mean conduction delays along three axons in the interhemispheric, callosal V1/V2 connection were between 1.9 and 2.4 ms, contrasting with our diffusion MRI-estimated conduction delay of 4.8 ms. The longer delay of 4.8 ms agrees with the calculated conduction delay within the same tract in the larger macaque brain, where the tract length was estimated with tracers to 63.4 mm, the average AD to be 0.95 μm, and the calculated conduction delay to be 4.6 ms (SD = 1.2 ms) (31). As expected from the literature (31), we conclude that the same tract can contain many different-sized axons, resulting in a range of conduction delays. Further demonstrating the nonspecificity of large axons, the range of CVs along single internodes is large, ranging, for example, between 22 and 35 m/s in axon 6 of Fig. 5. Additionally, we note that diffusion MRI and tracer-based histology calculations of CV reformulate Waxman's classical relation to incorporate a constant *g*-ratio (9, 18), which we show is not the case. Other factors, such as the internodal spacing, also affect the saltatory CV along an entire axon (32). Nodes of Ranvier were identifiable and internodal distances could be measured in the long axons in Fig. 5, but such an analysis was beyond the scope of this study. Several studies have investigated the relationship between CV and axon morphology, e.g., AD (3), node of Ranvier length (30), internodal length (30), *g*-ratio (4, 5), and a longitudinally varying AD (33), but none have yet considered the effects of a longitudinal distribution of *g*-ratios.

Changes to Axonal Morphology May Be Caused by Extra-axonal Obstacles. The longitudinal variations in AD and trajectory in the vicinity of extra-axonal structures could contribute to the high intracellular volume fraction of around 80% in the brain (34). In the extended volume of the monkey splenium, the blood vessels, cell clusters, and vacuoles accounted for 6.7% of the volume. Aside from the cells clustering parallel to the axons and blood vessels in the CC, the extra-axonal structures occupied space independently of the surrounding axons in the midbody CC, splenium, and the crossing fiber region. Morphological variations and spatial distributions of the extra-axonal compartments could not be linked to the presence of axons. On the other hand, the diameter and trajectory variations of axons could be linked to the presence of extra-axonal structures.

Local AD minima were at times associated with the presence of vacuoles. Vacuoles have been reported in EM studies of the healthy CC (20) and described in ref. 35, but it is possible that vacuolation occurs as a fixation or embedding artifact (36). Reduced ADs were also observed at nodes of Ranvier, as described in the literature. It has been described that AD is regulated by the axonal cytoskeleton (37), which maintains axon shape and consists of nanometer-thick neurofilaments. Decreases in AD have been shown to occur when axons are subjected to axial or circumferential tension, or microtubule disruption (38). Similarly, a reduction of tension through disruption of the axonal actin filaments or myosin II causes a diameter increase (38, 39). Adjacent structures such as vacuoles and neighboring axons may place local circumferential tension on the axons, affecting the organization of microtubules and possibly causing the diameter decreases we observe. This could not be confirmed in the XNH volumes as the microtubules and neurofilaments were too small to be resolved. Furthermore, in unmyelinated axons, local AD increases occur in conjunction with signal firing (40). Consequently, the signal conduction process itself may modulate AD in myelinated axons, meaning that the XNH volumes reveal only a structural snapshot of a truly complex and dynamic tissue environment.

Axonal trajectory changes were caused by blood vessels (Fig. 6 *A*–*C*), cells (Fig. 6*D*), and other crossing axons (Fig. 6*F*). The 54-axon population exhibited both low- and high-frequency trajectory changes. We quantified the dispersion effects across length scales from the microscopic (1 μm) to the mesoscopic (30 μm). Nonstraight trajectories are commonly observed in tracer-labeled axonal projections over long distances (9, 10, 18), and axonal growth has been shown to follow nonstraight trajectories in axons from the frog and chick (17, 41). Although axons may have predefined targets during axonal growth, we postulate that their trajectories are modified by the extra-axonal environment. In our data, the axons skirt around extra-axonal obstacles, i.e., cell clusters and blood vessels ranging in size from 4 to 10 μm, and this effect may be a major contributor to the meso-dispersion. The microdispersion could be a characteristic of axonal growth, or simply a consequence of the meso-dispersion, which, by definition, gives rise to microdispersion.

The quantification of axon OD is based on the trajectories of the 54 axons from the CC splenium and the results from their analysis are supported by inspection of XNH volumes of the CC midbody. Axons in crossing fiber regions exhibited similar nonstraight trajectories and also intertwining; such effects have previously been observed histologically in tracer-labeled axons (42). Previously, we have detected indications of local undulations in the CC [results presented in Dyrby et al. (43)] with histology, and other studies have derived the theoretical impact of sinusoidal undulation on the diffusion signal for AD estimation (44). The axon trajectories observed here, however, were irregular. Our 3D XNH data suggest that mesoscopic dispersion can occur due to axons projecting around large obstacles, e.g., blood vessels. If these obstacles are aligned and evenly distributed, they may result in the appearance of axonal "undulation."

Impacts on AD Estimation with Diffusion MRI. Our findings on the longitudinal ADD and *g*-ratio variations, as well as the relationship between axon morphology and extra-axonal obstacles, impact microstructural MRI techniques for noninvasive AD estimation. Our MC simulations show that any morphological variation from parallel cylinders incurs an overestimation of AD. This will be the case for all diffusion MRI models that assume a cylindrical axonal geometry and base the AD estimation on measurements perpendicular to the axon population, confirming the need to account for fiber dispersion effects (14, 16, 19, 45). Some studies implement biophysical models to account for axon dispersion or crossing axon effects (12, 46), but the intra-axonal MRI signal profile intermingles with that of the ECS, challenging a robust fitting (47). We could not extract the ECS from our XNH data due to insufficient resolution and shrinkage caused by the tissue processing. As such, we simulated only diffusion within the intra-axonal space. A recent study uses spherical averaging of the diffusion MRI signal to eliminate OD effects with sequence parameters that suppress the ECS signal (48). Although there exist methods to remove the bias caused by OD, none accounts for the effects of microdispersion that we see in Fig. 7. Further challenging accurate AD estimates with diffusion MRI, we found that the parallel ADC is time dependent for realistic axonal substrates. Consequently, measured values of the parallel ADC are likely lower than the true intrinsic diffusivity of the tissue. This potentially influences the ActiveAx-estimated mean AD of 1.3 μm that we present here, since the model assumes that the parallel ADC and intrinsic diffusivity of the tissue are equivalent (14). Simulated substrates with longitudinal AD variations (G3 and G5 in Fig. 7) exhibited stronger time dependence of the parallel ADC than substrates with constant ADs (G2, G4), suggesting that diameter variations could be a potential source of the axial time dependence observed in other studies (49), in line with the suggestions of Fieremans et al. (50).

To ensure robust fitting of the axon model to the diffusion MRI data in Alexander et al. (14) and Dyrby et al. (19), one had to account for a "dot" compartment that represented a small fraction of isotropically restricted water molecules. From the XNH volumes, possible dot compartments could potentially be the cell clusters (4.6% volume fraction) and, assuming their presence in hydrated tissue, the vacuoles (1.4% volume fraction).

Future Directions. Synchrotron XNH of the monkey WM provides anatomical information within volumes approaching the size of MRI voxels, including the micromorphologies of axons and the volume fractions and morphologies of cells, vacuoles, and blood vessels. However, the ECS is not visible, perhaps due to tissue shrinkage, insufficient signal-to-noise ratio (SNR) and limited resolution at 75 nm. Although scaling factors can be employed to compensate for shrinkage, it is not known if shrinkage affects all WM compartments equally (17). To fully reconstruct the volume fractions of the respective WM compartments, including the ECS, cryo-techniques could be implemented to preserve the hydrated microstructure. Both cryo-EM (51) and cryo-XNH provide alternatives to do so.

The tissue analyzed here belongs to one female, 32-mo-old vervet monkey. Given that 3D EM studies of the mouse CC (20, 21) also demonstrate morphological variations in axons, we expect that the modulation of axonal morphology by extra-axonal structures is present in the WM regions of other individuals and species. However, the "fingerprints" of axonal diameter and trajectory variation (Figs. 3*C* and 4*C*) may differ with species, age, gender, and disease, and it is relevant to pursue further studies into this matter.

As with many imaging techniques, XNH is subject to a tradeoff between the size of the image volume and the resolution. The image quality depends on the acquisition time and sample processing, including the sample size, staining, and smoothness of the embedding medium. We imaged at voxel sizes of 75 nm (splenium) and 100 nm (crossing fiber and midbody), but the SNR challenged the segmentation of axons with mean diameters smaller than ∼2 μm. The morphological behavior of smaller axons thus remains to be studied. This is possible with XNH, given that one prioritizes resolution and optimizes the sample preparation. However, EM provides superior resolution and there are ongoing efforts to develop large-scale 3D mapping of neural tissue by stacking 2D EM images (52). Still, EM is time demanding and there is a need to combine techniques that bridge different resolutions and volumes. Di-attenuation imaging has recently been demonstrated on sections of the vervet monkey brain at an effective resolution of 27 μm/pixel, and shows sensitivity to fiber orientation, diameter, and myelin sheath thickness (53). Further combination of XNH with EM and di-attenuation imaging would be valuable for mapping fiber microstructure, and the whole-brain network architecture.

Last, the axonal diameter variations and dispersion behavior presented here could act as an axonal "fingerprint" to guide the construction of anatomically informed axonal phantoms for MC simulations. Existing frameworks to model morphological features such as fiber undulation (44, 54) (although we do not observe periodic undulations in our data) and diameter variations (55, 56) exist. Others allow for the generation of a more complex WM environment with beaded axons and cells (57). None, however, has yet imposed anatomically realistic trajectory patterns or longitudinal ADDs.

Materials and Methods

Monkey Brain Tissue. The tissue came from a 32-mo-old female perfusion fixated vervet (*Chlorocebus aethiops*) monkey brain, obtained from the Montreal Monkey Brain Bank. The monkey, cared for on the island of St. Kitts, had been treated in line with a protocol approved by The Caribbean Primate Center of St. Kitts. The brain had previously been stored and prepared according to Dyrby et al. (58) and ex vivo MRI scanned using the optimized ActiveAx framework for volume-weighted mean AD estimation from previous work (14, 19). Prior to synchrotron XNH, the tissue was prepared for whole-brain ex vivo MRI for the estimation of AD and the segmentation of interhemispheric callosal fibers with tractography, as described in the following.

MRI Scanning, AD Estimation, and Tractography.

MRI scanning. The diffusion MRI dataset was collected on an experimental 4.7-tesla Agilent MRI scanner with a maximum gradient strength of 600 mT/m. An optimized three-shell ActiveAx MRI protocol based on a maximal gradient strength of 300 mT/m for ex vivo tissue as in Dyrby et al. (19) was used. The noncollinear diffusion weighting encoding directions were obtained from the Camino Toolbox (RRID: SCR_001638) (59). Further details of the protocol are included in *SI Appendix*. Prior to AD fitting and tractography, the diffusion MRI datasets were denoised (60) and processed to remove Gibbs ringing artifacts (61) in the MRTrix3 software toolbox (RRID: SCR_006971).

AD estimation. AD estimation was performed using the ActiveAx framework, based on the four-compartment minimal model of white matter diffusion (MMWMD) as described in ref. 14.

The MMWMD model was fitted to the diffusion MRI data with the same parameter settings and multistage fitting method as in Dyrby et al. (19) using the ActiveAx implementation of the Camino Toolbox. Since MRI probes volumes, larger axons contribute more to the intra-axonal signal than smaller ones. Hence, the estimated mean AD using diffusion MRI is a volume-weighted index (14). A ROI was manually drawn to cover the midsagittal plane of the CC within which the volume-weighted mean AD was calculated voxelwise as the average of 100 repeated estimations.

Segmentation of interhemispheric brain connections with tractography-based MRI. Streamline-based tractography was used to estimate the length of the interhemispheric connection that, via the splenium in the CC, connects the two primary visual cortical areas at the V1/V2 border that represents the vertical in meridian in most species including cats, monkeys, and humans (62). We used a constrained spherical deconvolution method (63) implemented in MRTrix3 to obtain voxelwise multifiber reconstructions of the whole brain. Probabilistic streamline tractography was then implemented with the SD-STREAM function in MRtrix3 using standard parameters to extract 2,000 streamlines (64). Further details are included in *SI Appendix*.

Tractography-based estimation of conduction velocity. To estimate the end-to-end conduction delay of the interhemispheric connection between the V1/V2 border regions and passing through the splenium, the tract was assumed to have a *g*-ratio, *g*, of 0.7 as in other studies (10, 31). The CV was calculated according to the following (9): $CV = 5.5/g \cdot d$, where d is the inner AD. The inner AD used was the AD index obtained by fitting ActiveAx to the diffusion MRI dataset of the monkey brain, as previously described. Together with the tract length from tractography, L, the conduction delay (t) was given by the following: $t = L/CV$.

Synchrotron XNH Imaging and Segmentation.

Tissue preparation for XNH imaging. After MRI acquisition, the whole monkey brain was agar-embedded for mechanical stability and cut into sagittal slices at thicknesses between 2 and 4 mm in a mold. Samples from the midsagittal CC and crossing fiber regions were extracted with a biopsy punch of diameter 1 mm and fixed in 2.5% glutaraldehyde before being stained with 0.5% osmium tetroxide (OsO_4) at room temperature for 2 h. The OsO_4 did not fully penetrate the tissue sample. However, the stained peripheries of the samples were large enough to cover the XNH field of view. The stained tissue was dehydrated with an alcohol series and embedded in EPON resin. Excess EPON was removed to produce blocks of approximately 1 × 1 × 4 mm.

Synchrotron XNH imaging. XNH was performed at beamline ID16A of the European Synchrotron Research Facility (ESRF). Samples were imaged using a nano-focused cone beam (65, 66) of energy 17 keV. Holograms of the samples were recorded at different distances with respect to the focus and the detector to obtain phase maps (66, 67). In practice, sequential tomographic scans were acquired at four different propagation distances by rotating the samples over 180°, and corresponding angular holographic projections were aligned and combined to generate phase maps of the sample. For each tomographic scan, 1,800 projections were acquired with exposure times of 0.22 s using a pixel size of 75 nm. The reconstructed image volumes were cylindrical, with dimensions 2,048 × 2,048 × 2,048 voxels. Acquiring one full scan took ∼4 h.

Segmentation of cell clusters, blood vessels, and vacuoles. We implemented an in-house intensity- and morphology-based approach in MATLAB to segment the cell clusters, blood vessels, and vacuoles from the four consecutively acquired XNH volumes (Fig. 2*A*). This used classic low-level image analysis operations such as intensity thresholds, morphological operations, and connected components analysis. Further information can be found in *SI Appendix*.

Segmentation of axon diameters. The XNH volumes were downsampled by a factor of 5 by extracting every fifth slice, and performing a slicewise cubic interpolation and Gaussian smoothing (kernel width of 5 pixels) in MATLAB (version 2019b) to achieve volumes of dimension 410 × 410 × 410 voxels with isotropic voxel size of 375 nm. A rough segmentation of the axons from these volumes was then performed using the adaptive paintbrush in ITK-Snap (RRID: SCR_002010). This allowed for the extraction of an approximate centerline by a simple slicewise estimate of the axon centroid. With the centerline as input, we employed a MATLAB-based, in-house segmentation method to extract the axons and update their centerlines from the high-resolution volumes of voxel size 75 nm. This is described in *SI Appendix*.

Quantification of Axonal Dispersion of Segmented Axons. For each of the 54 axons, the point-to-point vectors within their centerlines were averaged to obtain a main axon direction. The average of all 54 main axon directions was defined as the main bundle direction. The OD of each axon was defined as the inclination angle between the main bundle direction and the main axon direction.

We introduced the concept of microdispersion at different length scales, *L*, to quantify the deviation of axons from their linear main directions. To calculate the microdispersion, we first aligned the axons with the *z* axis. Then, the cumulative distance along the centerline was calculated, and the centerline was divided into segments of length, *L*, corresponding to the sampling length. A principal-component analysis was performed on the set of points within each segment to determine the segment direction in MATLAB. Thereafter, the inclination angle between the segment direction and the main axon direction was calculated. The average inclination angle of all segments (weighted according to the number of points in each segment) was defined to be the mean inclination angle of the axon at a length scale *L*. For a robust quantification, the axon skeleton was queried four times for each length scale *L* by shifting the starting position of the quantification by *L*/4 as shown in Fig. 4*B*. We studied length scales, *L*, ranging between 1 and 30 μm.

MC Simulations of the Diffusion Process in Synthetic Axons. Substrates G1–G5 in Fig. 7 were based on the 54 segmented axons (substrate G6). The 54 axons in geometries G1–G5 inherited one or more of the following from the segmented axons in G6: mean AD, longitudinal diameter variation, OD, microdispersion (trajectory). This was attained through modeling of the axons as deformed cylinders.

Prior to simulations, the XNH segmentations were meshed and post-processed as described in *SI Appendix*.

Simulations were performed using the Monte Carlo Diffusion and Collision simulator from Rafael-Patino et al. (54). Each axon in each geometry was simulated separately, and the intra-axonal diffusivity was set to 6.0×10^{-10} $m^2 \cdot s^{-1}$ as measured in ref. 19, as is conventional for ex vivo diffusion MRI. Particles were initialized uniformly within the central region of the axon meshes at a minimum distance of 20 μm from the axon ends. This confined initialization ensured that virtually no particle was able to diffuse outside the mesh. Perfectly elastic mesh boundaries were implemented, as in ref. 54. The number of particles and time-step duration were chosen using a bootstrap-based analysis of the convergence of the simulation as explained in ref. 54. In this investigation, we studied diffusion times, D_t, between 1 and 50 ms at intervals of 1 ms and used 2×10^5 particles and 5×10^5 time steps with a duration of 1×10^{-5} s. The simulator output the mean-squared displacement, $\langle(\Delta x)^2\rangle$, of the particles in the directions parallel and perpendicular to the main bundle direction.

The reported ADCs were calculated from $\langle(\Delta x)^2\rangle$ by the Einstein relationship (68):

$$\langle(\Delta x)^2\rangle = 2 \cdot ADC \cdot D_t.$$

The AD estimations were based on the analytical expression for diffusion perpendicular to cylinders (69): $\lambda^2 = R^2/2$, where λ^2 is the mean-squared displacement perpendicular to the cylinder and *R* is its radius.

Data Availability. The four XNH image volumes of the monkey brain splenium and the segmentation of cells, vacuoles and blood vessels are publicly available on the download center of the Danish Research Centre for Magnetic Resonance (https://www.drcmr.dk/axon-morphology-dataset). The diffusion MRI datasets of the same brain as the XNH image volumes are also available on the same link and include the raw diffusion MRI data covering the mid sagittal region of the corpus callosum, used for axon diameter fitting, and the whole-brain diffusion MRI data set used for tractography.

ACKNOWLEDGMENTS. M.A. and H.M.K. were supported by Capital Region Research Foundation Grant A5657 (principal investigator: T.B.D.). M.B. was supported by Swedish Research Council Grants E0605401 and E0605402. We acknowledge ESRF for providing beamtime for the experiment LS2702 at ID16A. We thank Henrik Lundell for valuable discussions and Susanne Sørensen for her assistance with the tissue preparation.

1. J. B. Hursh, Conduction velocity and diameter of nerve fibers. *Am. J. Physiol.* **127**, 131–139 (1939).
2. F. K. Sanders, D. Whitteridge, Conduction velocity and myelin thickness in regenerating nerve fibres. *J. Physiol.* **105**, 152–174 (1946).
3. W. A. H. Rushton, A theory of the effects of fibre size in medullated nerve. *J. Physiol.* **115**, 101–122 (1951).
4. R. S. Smith, Z. J. Koles, Myelinated nerve fibers: Computed effect of myelin thickness on conduction velocity. *Am. J. Physiol.* **219**, 1256–1258 (1970).
5. T. Chomiak, B. Hu, What is the optimal value of the *g*-ratio for myelinated fibers in the rat CNS? A theoretical approach. *PLoS One* **4**, e7754 (2009).
6. N. Stikov *et al*., Quantitative analysis of the myelin *g*-ratio from electron microscopy images of the macaque corpus callosum. *Data Brief* **4**, 368–373 (2015).
7. G. M. Innocenti, A. Vercelli, R. Caminiti, The diameter of cortical axons depends both on the area of origin and target. *Cereb. Cortex* **24**, 2178–2188 (2014).
8. S. G. Waxman, M. V. Bennett, Relative conduction velocities of small myelinated and non-myelinated fibres in the central nervous system. *Nat. New Biol.* **238**, 217–219 (1972).
9. L. Tettoni, P. Lehmann, J. C. Houzel, G. M. Innocenti, Maxsim, software for the analysis of multiple axonal arbors and their simulated activation. *J. Neurosci. Methods* **67**, 1–9 (1996).
10. S. Tomasi, R. Caminiti, G. M. Innocenti, Areal differences in diameter and length of corticofugal projections. *Cereb. Cortex* **22**, 1463–1472 (2012).
11. G. C. DeLuca, G. C. Ebers, M. M. Esiri, Axonal loss in multiple sclerosis: A pathological survey of the corticospinal and sensory tracts. *Brain* **127**, 1009–1018 (2004).
12. H. Zhang, T. Schneider, C. A. Wheeler-Kingshott, D. C. Alexander, NODDI: Practical in vivo neurite orientation dispersion and density imaging of the human brain. *Neuroimage* **61**, 1000–1016 (2012).
13. Y. Assaf, T. Blumenfeld-Katzir, Y. Yovel, P. J. Basser, AxCaliber: A method for measuring axon diameter distribution from diffusion MRI. *Magn. Reson. Med.* **59**, 1347–1354 (2008).
14. D. C. Alexander *et al*., Orientationally invariant indices of axon diameter and density from diffusion MRI. *Neuroimage* **52**, 1374–1389 (2010).
15. D. C. Alexander, T. B. Dyrby, M. Nilsson, H. Zhang, Imaging brain microstructure with diffusion MRI: Practicality and applications. *NMR Biomed.* **32**, e3841 (2019).
16. D. Barazany, P. J. Basser, Y. Assaf, In vivo measurement of axon diameter distribution in the corpus callosum of rat brain. *Brain* **132**, 1210–1220 (2009).
17. T. B. Dyrby, G. M. Innocenti, M. Bech, H. Lundell, Validation strategies for the interpretation of microstructure imaging using diffusion MRI. *Neuroimage* **182**, 62–79 (2018).
18. R. Caminiti, H. Ghaziri, R. Galuske, P. R. Hof, G. M. Innocenti, Evolution amplified processing with temporally dispersed slow neuronal connectivity in primates. *Proc. Natl. Acad. Sci. U.S.A.* **106**, 19551–19556 (2009).
19. T. B. Dyrby, L. V. Sogaard, M. G. Hall, M. Ptito, D. C. Alexander, Contrast and stability of the axon diameter index from microstructure imaging with diffusion MRI. *Magn. Reson. Med.* **70**, 711–721 (2013).
20. A. Abdollahzadeh, I. Belevich, E. Jokitalo, J. Tohka, A. Sierra, Automated 3D axonal morphometry of white matter. *Sci. Rep.* **9**, 6084 (2019).
21. H.-H. Lee *et al*., Along-axon diameter variation and axonal orientation dispersion revealed with 3D electron microscopy: Implications for quantifying brain white matter microstructure with histology and diffusion MRI. *Brain Struct. Funct.* **224**, 1469–1488 (2019).
22. K. S. Rockland, N. Nayyar, Association of type I neurons positive for NADPH-diaphorase with blood vessels in the adult monkey corpus callosum. *Front. Neural Circuits* **6**, 4 (2012).
23. A. S. Lamantia, P. Rakic, Cytological and quantitative characteristics of four cerebral commissures in the rhesus monkey. *J. Comp. Neurol.* **291**, 520–537 (1990).
24. A. A. Harper, S. N. Lawson, Conduction velocity is related to morphological cell type in rat dorsal root ganglion neurones. *J. Physiol.* **359**, 31–46 (1985).
25. H. Sakai, C. D. Woody, Relationships between axonal diameter, soma size, and axonal conduction velocity of HRP-filled, pyramidal tract cells of awake cats. *Brain Res.* **460**, 1–7 (1988).
26. J. A. Perge, J. E. Niven, E. Mugnaini, V. Balasubramanian, P. Sterling, Why do axons differ in caliber? *J. Neurosci.* **32**, 626–638 (2012).
27. T. FitzGibbon, Z. Nestorovski, Human intraretinal myelination: Axon diameters and axon/myelin thickness ratios. *Indian J. Ophthalmol.* **61**, 567–575 (2013).
28. C. H. Berthold, I. Nilsson, M. Rydmark, Axon diameter and myelin sheath thickness in nerve fibres of the ventral spinal root of the seventh lumbar nerve of the adult and developing cat. *J. Anat.* **136**, 483–508 (1983).
29. J. P. Fraher, Quantitative studies on the maturation of central and peripheral parts of individual ventral motoneuron axons. I. Myelin sheath and axon calibre. *J. Anat.* **126**, 509–533 (1978).
30. I. L. Arancibia-Cárcamo *et al*., Node of Ranvier length as a potential regulator of myelinated axon conduction speed. *eLife* **6**, e23329 (2017).
31. R. Caminiti *et al*., Diameter, length, speed, and conduction delay of callosal axons in macaque monkeys and humans: Comparing data from histology and magnetic resonance imaging diffusion tractography. *J. Neurosci.* **33**, 14501–14511 (2013).
32. M. H. Brill, S. G. Waxman, J. W. Moore, R. W. Joyner, Conduction velocity and spike configuration in myelinated fibres: Computed dependence on internode distance. *J. Neurol. Neurosurg. Psychiatry* **40**, 769–774 (1977).
33. H. A. Swadlow, J. D. Kocsis, S. G. Waxman, Modulation of impulse conduction along the axonal tree. *Annu. Rev. Biophys. Bioeng.* **9**, 143–179 (1980).
34. E. Syková, C. Nicholson, Diffusion in brain extracellular space. *Physiol. Rev.* **88**, 1277–1340 (2008).
35. S. K. Ludwin, "Pathology of the myelin sheath" in *The Axon: Structure, Function, and Pathophysiology*, S. G. Waxman, J. D. Kocsis, P. K. Stys, Eds. (Oxford University Press, 1995), pp. 412–437.
36. E. McInnes, Artefacts in histopathology. *Comp. Clin. Pathol.* **13**, 100–108 (2005).
37. A. R. Costa, R. Pinto-Costa, S. C. Sousa, M. M. Sousa, The regulation of axon diameter: From axonal circumferential contractility to activity-dependent axon swelling. *Front. Mol. Neurosci.* **11**, 319 (2018).

38. A. Fan, A. Tofangchi, M. Kandel, G. Popescu, T. Saif, Coupled circumferential and axial tension driven by actin and myosin influences in vivo axon diameter. *Sci. Rep.* **7**, 14188 (2017).
39. S. C. Leite *et al*., The actin-binding protein α-adducin is required for maintaining axon diameter. *Cell Rep.* **15**, 490–498 (2016).
40. R. D. Fields, Signaling by neuronal swelling. *Sci. Signal.* **4**, tr1 (2011).
41. M. J. Katz, How straight do axons grow? *J. Neurosci.* **5**, 589–595 (1985).
42. K. Rockland, “White matter tracts visualized by parvalbumin in nonhuman primates” in *Primates*, M. Burke, M. Ptito, Eds. (IntechOpen, 2017), pp. 163–178.
43. T. B. Dyrby, M. Burke, D. C. Alexander, M. Ptito, "Undulating and crossing axons in the corpus callosum may explain the overestimation of axon diameters with ActiveAx" in Proceedings of the Joint Annual Meeting of ISMRM-ESMRMB (International Society for Magnetic Resonance in Medicine, 2014), Abstract 2619.
44. M. Nilsson, J. Lätt, F. Ståhlberg, D. van Westen, H. Hagslätt, The importance of axonal undulation in diffusion MR measurements: A Monte Carlo simulation study. *NMR Biomed.* **25**, 795–805 (2012).
45. A. Horowitz *et al*., In vivo correlation between axon diameter and conduction velocity in the human brain. *Brain Struct. Funct.* **220**, 1777–1788 (2015).
46. H. Zhang, P. L. Hubbard, G. J. M. Parker, D. C. Alexander, Axon diameter mapping in the presence of orientation dispersion with diffusion MRI. *Neuroimage* **56**, 1301–1315 (2011).
47. D. Romascano *et al*., ActiveAx$_{\mathrm{ADD}}$: Toward non-parametric and orientationally invariant axon diameter distribution mapping using PGSE. *Magn. Reson. Med.* **83**, 2322–2330 (2020).
48. J. Veraart *et al*., Nonivasive quantification of axon radii using diffusion MRI. *eLife* **9**, e49855 (2020).
49. N. Kunz, S. V. Sizonenko, P. S. Hüppi, R. Gruetter, Y. van de Looij, Investigation of field and diffusion time dependence of the diffusion-weighted signal at ultrahigh magnetic fields. *NMR Biomed.* **26**, 1251–1257 (2013).
50. E. Fieremans *et al*., In vivo observation and biophysical interpretation of time-dependent diffusion in human white matter. *Neuroimage* **129**, 414–427 (2016).
51. N. Korogod, C. C. H. Petersen, G. W. Knott, Ultrastructural analysis of adult mouse neocortex comparing aldehyde perfusion with cryo fixation. *eLife* **4**, e05793 (2015).
52. A. L. Eberle *et al*., High-resolution, high-throughput imaging with a multibeam scanning electron microscope. *J. Microsc.* **259**, 114–120 (2015).
53. M. Menzel, M. Axer, K. Amunts, H. De Raedt, K. Michielsen, Diattenuation Imaging reveals different brain tissue properties. *Sci. Rep.* **9**, 1939 (2019).
54. J. Rafael-Patino *et al*., Robust Monte-Carlo simulations in diffusion-MRI: Effect of the substrate complexity and parameter choice on the reproducibility of results. *Front. Neuroinform.* **14**, 8 (2020).
55. M. D. Budde, J. A. Frank, Neurite beading is sufficient to decrease the apparent diffusion coefficient after ischemic stroke. *Proc. Natl. Acad. Sci. U.S.A.* **107**, 14472–14477 (2010).
56. R. Callaghan, D. C. Alexander, M. Palombo, H. Zhang, ConFiG: Contextual Fibre growth to generate realistic axonal packing for diffusion MRI simulation. *Neuroimage* **220**, 117107 (2020).
57. K. Ginsburger *et al*., MEDUSA: A GPU-based tool to create realistic phantoms of the brain microstructure using tiny spheres. *Neuroimage* **193**, 10–24 (2019).
58. T. B. Dyrby *et al*., An ex vivo imaging pipeline for producing high-quality and high-resolution diffusion-weighted imaging datasets. *Hum. Brain Mapp.* **32**, 544–563 (2011).
59. P. A. Cook *et al*., “Camino: Open-source diffusion-MRI reconstruction and processing” in *14th Scientific Meeting of the International Society for Magnetic Resonance in Medicine* (International Society for Magnetic Resonance in Imaging, 2006), p. 2759.
60. J. Veraart, E. Fieremans, D. S. Novikov, Diffusion MRI noise mapping using random matrix theory. *Magn. Reson. Med.* **76**, 1582–1593 (2016).
61. E. Kellner, B. Dhital, V. G. Kiselev, M. Reisert, Gibbs-ringing artifact removal based on local subvoxel-shifts. *Magn. Reson. Med.* **76**, 1574–1581 (2016).
62. M. Pietrasanta, L. Restani, M. Caleo, The corpus callosum and the visual cortex: Plasticity is a game for two. *Neural Plast.* **2012**, 838672 (2012).
63. J.-D. Tournier, F. Calamante, A. Connelly, Determination of the appropriate b value and number of gradient directions for high-angular-resolution diffusion-weighted imaging. *NMR Biomed.* **26**, 1775–1786 (2013).
64. J.-D. Tournier, F. Calamante, A. Connelly, MRtrix: Diffusion tractography in crossing fiber regions. *Int. J. Imaging Syst. Technol.* **22**, 53–66 (2012).
65. J. C. da Silva *et al*., Efficient concentration of high-energy x-rays for diffraction-limited imaging resolution. *Optica* **4**, 492–495 (2017).
66. M. Hubert *et al*., Efficient correction of wavefront inhomogeneities in X-ray holographic nanotomography by random sample displacement. *Appl. Phys. Lett.* **112**, 203704 (2018).
67. P. Cloetens *et al*., Holotomography: Quantitative phase tomography with micrometer resolution using hard synchrotron radiation x rays. *Appl. Phys. Lett.* **75**, 2912–2914 (1999).
68. A. Einstein, On the motion of small particles suspended in liquids at rest required by the molecular-kinetic theory of heat. *Ann. Phys.* **17**, 549–560 (1906).
69. P. van Gelderen, D. DesPres, P. C. van Zijl, C. T. Moonen, Evaluation of restricted diffusion in cylinders. Phosphocreatine in rabbit leg muscle. *J. Magn. Reson. B.* **103**, 255–260 (1994).

PNAS
www.pnas.org

Supplementary Information for
Axon morphology is modulated by the local environment and impacts the non-invasive investigation of its structure-function relationship

Mariam Andersson[1,2*], Hans Martin Kjer[1,2], Jonathan Rafael-Patino[3], Alexandra Pacureanu[4], Bente Pakkenberg[5], Jean-Philippe Thiran[3,6,7], Maurice Ptito[8,9], Martin Bech[10], Anders Bjorholm Dahl[2], Vedrana Andersen Dahl[2], Tim B. Dyrby[1,2*]

1. Danish Research Centre for Magnetic Resonance, Centre for Functional and Diagnostic Imaging and Research, Copenhagen University Hospital Hvidovre, 2650 Hvidovre, Denmark
2. Department of Applied Mathematics and Computer Science, Technical University of Denmark, 2800 Kongens Lyngby, Denmark
3. Signal Processing Laboratory (LTS5), École Polytechnique Fédérale de Lausanne, 1015 Lausanne, Switzerland
4. European Synchrotron Research Facility, 38000 Grenoble, France
5. Research Laboratory for Stereology and Neuroscience, Copenhagen University Hospital, Bispebjerg, 2400-Copenhagen, Denmark
6. Radiology Department, Centre Hospitalier Universitaire Vaudois and University of Lausanne, 1011 Lausanne, Switzerland
7. Center for Biomedical Imaging (CIBM), 1015 Lausanne, Switzerland
8. School of Optometry, University of Montreal, Montreal, Canada
9. Department of Neuroscience, Faculty of Health Science, University of Copenhagen, 2200 Copenhagen, Denmark
10. Division of Medical Radiation Physics, Department of Clinical Sciences, Lund University, 221 85 Lund, Sweden

* Mariam Andersson **Email:** mariama@drcmr.dk
* Tim B. Dyrby **Email:** timd@drcmr.dk

This PDF file includes:

- Supplementary Methods
- Figures S1 to S4
- SI References

Other supplementary materials for this manuscript include the following:

- Datasets S1

Supplementary Methods

MRI scanning, axon diameter estimation and tractography

Tissue preparation for MRI

The brain tissue was sealed in a double plastic bag with minimal free fluid and placed for temperature stabilization at room temperature overnight prior to scanning. It was then positioned in a quadrature volume RF coil on a mechanical stable set up using LEGO^{TM} to minimize short-term instabilities, seen as a non-linear decreasing motion artifacts in the first hours of an MRI acquisition (1). A temperature-stabilized environment was ensured by a constant influx of airflow at room temperature, producing stable diffusion MRI images.

MRI scanning

The diffusion MRI dataset was collected on an experimental 4.7 Tesla Agilent MRI scanner with a maximum gradient strength of 600 mT/m. An optimized ActiveAx MRI protocol based on a maximal gradient strength of 300 mT/m for ex vivo tissue as in Dyrby et al. (2013) (2) was used. The protocol was based on a 2D T2-weighted Pulsed-Gradient-Spin-Echo (PGSE) sequence with a single-line readout to reduce geometric image distortions. The optimized ActiveAx diffusion MRI protocol included three unique *b*-values $[2011, 2957, 9259]$ s/mm^2 obtained by the following sequence parameters: Gradient pulse duration (δ) $[5.6, 7.0, 10.5]$ ms, time between onset of gradient pulses (Δ) $[12.1, 20.4, 16.9]$ ms and gradient strength $[300, 219, 300]$ mT/m. The *b*-values were acquired as shells including $[84, 87, 68]$ non-collinear diffusion weighting encoding directions obtained from the Camino Toolbox. For each shell $[15, 16, 13]$ repeats of $b = 0$ s/mm^2 were collected. All shells used the same echo time (TE) of 36 ms and a repetition time (TR) of $[4200, 4200, 7200]$ ms. For whole-brain coverage at an isotropic 0.5 mm^3 image resolution, a matrix size of 128×256 was used and 100 sagittal slices were acquired in an interleaved manner. The total scan time, excluding a dummy prescan of >6 hours to reduce short-term instability artifacts, was 50 hours. Prior to axon diameter fitting and tractography the diffusion MRI data sets were denoised (3) and processed to remove Gibbs ringing artifacts (4) using the method implementations available in the MRTrix3 software toolbox (RRID: SCR_006971).

Axon Diameter estimation

Axon diameter estimation was performed using the ActiveAx framework which is based on the minimal model of white matter diffusion (MMWMD) – a four compartment biophysical model – as described in detail in (5). In short, the compartments and their respective volume fractions (VF) are:

(i) the VF of the extraaxonal space modeled as a symmetric tensor.

(ii) the VF of intraaxonal space modeled as a single cylinder with a mean diameter that best fits the diffusion signal.

(iii) the VF of the “dot” compartment reflecting a small fraction of stationary water likely trapped inside vacuoles and cell bodies.

(iv) the VF of free diffusion modeled as an isotropic tensor coming from surrounding fluid around the CC.

The MMWMD model was fitted to the diffusion MRI data with the same model parameter settings and multi-stage fitting method as in Dyrby et al. (2013) (2) using the ActiveAx implementation as part of the Camino Toolbox. Since MRI probes volumes, larger axons contribute more to the intra-axonal signal than smaller ones. Hence, the estimated mean AD using diffusion MRI is a volume-weighted index (5) A region-of-interest (ROI) was manually drawn to cover the midsagittal plane of the CC within which the volume-weighted mean AD was calculated voxel-wise as the average of 100 repeated estimations.

Segmentation of interhemispheric brain connections with tractography-based MRI

Streamline-based tractography was used to segment and estimate the length of the interhemispheric connection that, via the splenium in the CC, connects the two primary visual cortical areas at the V1/V2 border that represents the vertical in meridian in most species including cats, monkeys and humans (6). We used a probabilistic streamline approach based on a voxel multi-fiber reconstruction method. First, a constrained spherical deconvolution (CSD) method (7) implemented in MRTrix3 was fitted to the $b = 2957$ s/mm^2 shell dataset to give a voxel-wise multi-fiber reconstruction of the whole brain. Thereafter, probabilistic streamline tractography was implemented with the SD-STREAM function in MRtrix3 using standard parameters to extract 2000 streamlines (8). The probabilistic tractography was initialized in a broad seed region covering the splenium of the midsagittal CC. To obtain only streamlines that projected towards both V1/V2 of each hemisphere, we defined two inclusive regions through which valid streamlines had to project. These regions were manually drawn to be symmetrical in both hemispheres and cover a broad region in the most anterior coronal slice at which V2 starts. The seed and inclusive regions were manually defined on the $b = 0$ s mm^{-2} using the FSLeyes software. The mean streamline length and its variation were calculated using the TCKSTATS method in MRTrix3. Visualization of tractography results used MRtrix3 tools and Blender (RRID: SCR_008606).

Segmentation of XNH volumes

Segmentation of cell clusters, blood vessels and vacuoles

The intensity- and morphology-based segmentation of cell clusters, blood vessels and vacuoles from the downsampled XNH volumes was performed for one class at a time, in the order of their perceived difficulty, starting with the easiest class. The information gained in previous steps served as fixed prior information in the more difficult later steps e.g., once a voxel was classified, it could not be re-classified as something else. This approach was taken since it is simpler to tune parameters for one class at a time, inspect and manually correct the result until it is satisfactory, and then proceed to the next class. The tuning of parameters and segmentation of XNH volumes could be performed and visualized in a matter of minutes. This made it simpler to a) fine-tune the parameters and b) quality control the final solution, helping to minimize errors.

In order of decreasing average brightness the segmented compartments could be ordered as: blood vessels, vacuoles, and cells. The shape criteria for the different classes were as follows:

- Blood vessels: large, tubular connected regions (volumes>730 µm^3), with no specific structures or branching patterns.
- Vacuoles: relatively spherical (minimum elongation, described below, of $e = 0.4$) with volumes ranging between $[15, 600]$ µm^3 and spanning maximum 25 µm in the longest direction.
- Cell nuclei clusters: typically appear in relatively large connected regions (estimated to span at least 60 µm in the longest direction with volumes ranging between $[75, 2300]$ µm^3) and containing dark DNA inclusions.

If a connected component spans $S_{CC} = [s_1, s_2, s_3]$ unique rows, columns and slices of the volume respectively, the elongation of the component is here calculated as $e = \frac{\inf(S_{CC})}{\sup(S_{CC})}$. A score of 1 can roughly be interpreted as a perfect spherical component.

The blood vessels, vacuoles and cell nuclei clusters were large compared to the voxel size of 75 nm. Each of the four XNH volumes was therefore downsampled by a factor of 5 to improve signal-to-noise ratio and speed up computations. Downsampling involved extracting every 5th slice and performing a slice-wise cubic interpolation and Gaussian smoothing (kernel width of 5 pixels) in MATLAB (ver. 2019b) to achieve volumes of dimension $410 \times 410 \times 410$ voxels with isotropic voxel size 375 nm. These were then individually segmented to avoid errors due to slightly differing contrasts in the separate volumes. Finally, the segmentations were combined as in Figure 2D, manually corrected and analyzed by a connected components analysis which rejected the smallest, falsely segmented components.

Segmentation of axon diameters

Given their varying intensities, morphologies and occasional nodes of Ranvier, segmentation of the axons required a geometrically constrained method, i.e. a segmentation approach which could enforce a closed tubular output. Axons were first preliminarily segmented from downsampled volumes, and thereafter segmented from the high-resolution volumes with voxel size 75 nm.

The image volumes from the XNH were downsampled to volumes of dimension $410 \times 410 \times 410$ voxels and isotropic voxel size of 375 nm as above. Each slice was filtered with a Gaussian kernel of width 5 pixels in MATLAB (ver. 2019b). A rough segmentation of the axons was then performed using the adaptive paintbrush in the program ITK-Snap (RRID: SCR_002010) (9). This allowed for the extraction of a centerline by a simple slice-wise centroid estimate from the segmentation.

Given such a centerline, we employed the following MATLAB-based, in-house segmentation method on the original, high resolution volumes:

1. Sub-volume extraction: Radial image resampling centered from each individual centerline point to construct a small fiber-unfolded sub-volume. Here, the axon-myelin interface can be seen as a surface with a strong negative gradient (going from bright axon to dark myelin).

2. Sub-volume layered segmentation: Perform layered surface segmentation on gradient-based cost-function of the sub-volume, using a graph cut approach (10).

3. Volume labelling: Unfold the solution to the original volume coordinate system to obtain the final geometrically enforced solution.

The method is robust towards noise and image intensity variations. Furthermore, it is computationally efficient because the centerline serves to provide a much smaller sub-volume, in which we can build and solve the graph.

Segmentation of g-ratios along single internodes

Within the four overlapping XNH volumes depicted in Figure 2, we performed a rough manual segmentation of 6 axons with two visible nodes of Ranvier using the adaptive paintbrush in ITK-Snap and extracted their centerlines by estimating their slice-wise centroids.

Thereafter, we generated *N* random points between the two nodes of Ranvier in MATLAB along each axon. We then extracted the relevant slices in which the randomly generated points could be found and performed a manual segmentation of the inner axonal and outer myelin boundaries with the “roipoly” tool in MATLAB. The g-ratio estimation could be performed slice-wise and not perpendicular to the local axon trajectory because – as the ratio between the inner and outer axon boundaries – it is insensitive to skewed axons, unlike the equivalent AD.

Monte Carlo Simulations of Diffusion

Post-processing of XNH axon segmentations for Monte Carlo simulations

Firstly, the raw binary reconstructions were meshed using an octree-based surface extraction (11) to ensure a closed surface and high-polygonal density. Secondly, to reduce small irregularities arising from the surface reconstruction, the meshes were smoothed using an algorithm as in Desbrun et al. (1999) (12), which ensures volume preservation while reducing high-frequency changes along the volumetric contour. Finally, the resulting meshes were triangulated and decimated to reduce the computational burden for the simulation.

SI Figures

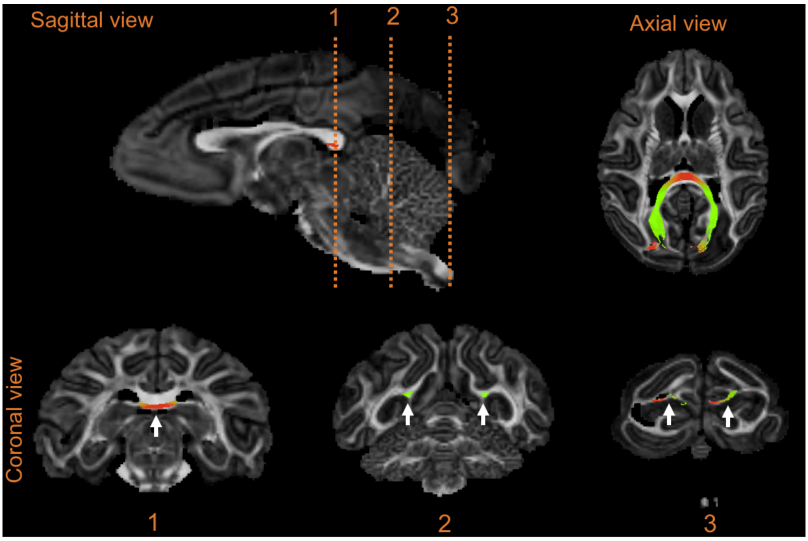

Fig. S1. Sagittal, axial and coronal views of monkey brain MRI volume and tractography of the interhemispheric connection between the V1/V2 visual cortices, passing through the splenium of the corpus callosum.

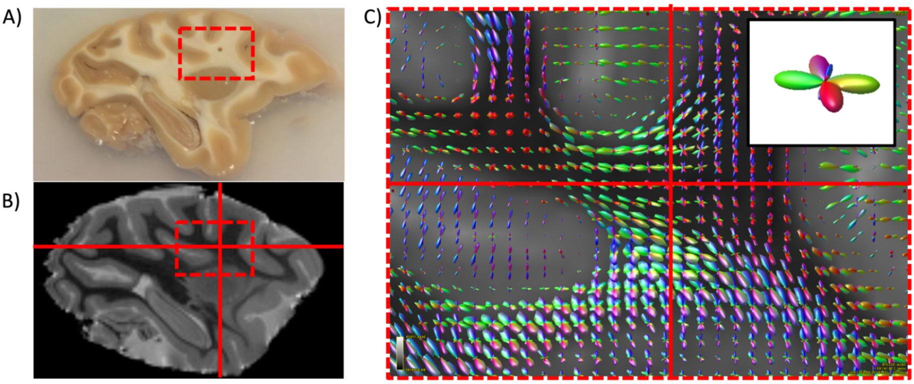

Fig. S.2. **A)** The location of the “crossing fiber region” biopsy in a sagittal slice of the monkey brain, marked by the hole. The biopsy was taken from the anterior centrum semiovale. **B)** The equivalent location in the MRI data. **C)** Multi-fiber reconstruction of the axonal pathways in the diffusion weighted images, showing the crossing of different tracts believed to be the corticospinal tract, interhemispheric callosal fibers and association fibers. Inset: multi-fiber reconstruction at red cross. The red striped box marks the approximate field-of-view of C). The crossing of the red lines marks the approximate biopsy location.

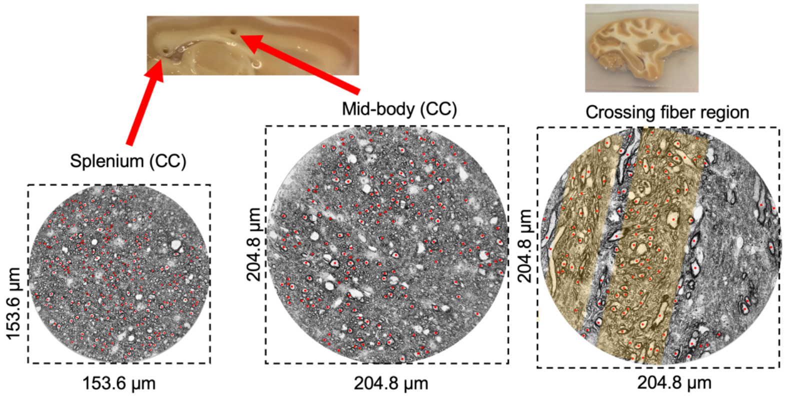

Number density (large axons per μm^2)	**0.0123**	**0.0055**	**0.0038**

Fig. S.3. 2D cross sections of XNH-volumes from the splenium (75 nm voxel size), mid-body (100 nm voxel size) and crossing fiber (100 nm voxel size) regions. Axons with estimated equivalent diameters larger than 2 µm are marked by red dots. The large axons appear to be evenly distributed throughout the splenium and mid-body samples but are organized in bands (yellow) in the crossing fiber region. Of the three samples, the number density of large axons is highest in the splenium and lowest in the mid-body. Photograph inserts show the positions at which 1 mm biopsies were extracted from the sagittal slices.

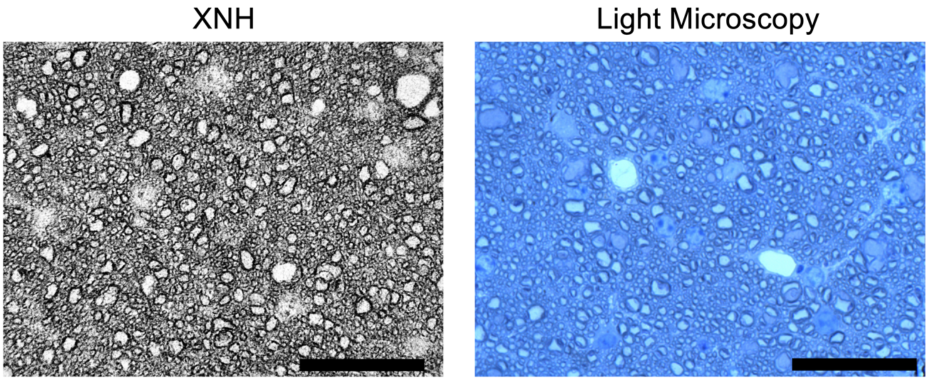

XNH

Light Microscopy

Fig. S.4. *Left*: 2D cross section of the XNH-volume from the splenium (75 nm voxel size). *Right*: Light microscope image of a section from the same EPON-embedded sample of the splenium. A Toluidine blue stain is used for visualization. The scale bars represent 30 µm.

Dataset S1 (separate files). The following datasets are publicly available on https://www.drcmr.dk/axon-morphology-dataset

1. Four XNH volumes from the vervet monkey splenium
2. High resolution (75 nm) 3D segmentation of axons in one XNH volume of splenium
3. Low resolution (375 nm) 3D segmentation of cells, blood vessels and vacuoles in all four XNH volumes of splenium.
4. Diffusion MRI volume used for tractography of the interhemispheric V1/V2 connection through the vervet monkey splenium.
5. Diffusion MRI subvolumes used for ActiveAx axon diameter estimation in the vervet monkey corpus callosum.

Info files are provided to guide the user and provide more details about the data formats.

SI References

1. T. B. Dyrby, W. F. C. Baaré, D. C. Alexander, An ex vivo imaging pipeline for producing high-quality and high-resolution diffusion-weighted imaging datasets. *Hum. Brain Mapp.* (2011).

2. T. B. Dyrby, L. V. Sogaard, M. G. Hall, M. Ptito, D. C. Alexander, Contrast and stability of the axon diameter index from microstructure imaging with diffusion MRI. *Magn. Reson. Med.* **70**, 711–721 (2013).

3. J. Veraart, E. Fieremans, D. S. Novikov, Diffusion MRI noise mapping using random matrix theory. *Magn. Reson. Med.* **76**, 1582–1593 (2016).

4. E. Kellner, B. Dhital, V. G. Kiselev, M. Reisert, Gibbs-ringing artifact removal based on local subvoxel-shifts. *Magnetic Resonance in Medicine* **76**, 1574–1581 (2016).

5. D. C. Alexander, *et al.*, Orientationally invariant indices of axon diameter and density from diffusion MRI. *Neuroimage* **52**, 1374–1389 (2010).

6. M. Pietrasanta, L. Restani, M. Caleo, The corpus callosum and the visual cortex: plasticity is a game for two. *Neural Plast.* **2012**, 838672 (2012).

7. J.-D. Tournier, J. -Donald Tournier, F. Calamante, A. Connelly, Determination of the appropriatebvalue and number of gradient directions for high-angular-resolution diffusion-weighted imaging. *NMR in Biomedicine* **26**, 1775–1786 (2013).

8. J.-D. Tournier, F. Calamante, A. Connelly, MRtrix: Diffusion tractography in crossing fiber regions. *Int. J. Imaging Syst. Technol.* **22**, 53–66 (2012).

9. P. A. Yushkevich, *et al.*, User-guided 3D active contour segmentation of anatomical structures: significantly improved efficiency and reliability. *Neuroimage* **31**, 1116–1128 (2006).

10. K. Li, X. Wu, D. Z. Chen, M. Sonka, Optimal surface segmentation in volumetric images--a graph-theoretic approach. *IEEE Trans. Pattern Anal. Mach. Intell.* **28**, 119–134 (2006).

11. M. Kazhdan, A. Klein, K. Dalal, H. Hoppe, Unconstrained isosurface extraction on arbitrary octrees in *Symposium on Geometry Processing*, (2007).

12. M. Desbrun, M. Meyer, P. Schröder, A. H. Barr, Implicit fairing of irregular meshes using diffusion and curvature flow in *Proceedings of the 26th Annual Conference on Computer Graphics and Interactive Techniques*, SIGGRAPH '99., (Citeseer, 1999), pp. 317–324.

Contribution II

Does powder averaging remove dispersion bias in diameter estimates within realistic axonal architectures?

Status: *In preparation*

Author list

Mariam Andersson[1,2]*, Marco Pizzolato[1,2,3], Hans Martin Kjer[1,2], Katrine Forum Skodborg[1,2], Henrik Lundell[2], Tim B. Dyrby[1,2]*

1. Danish Research Centre for Magnetic Resonance, Center for Functional and Diagnostic Imaging and Research, Copenhagen University Hospital Hvidovre, 2650 Hvidovre, Denmark
2. Department of Applied Mathematics and Computer Science, Technical University of Denmark, 2800 Kongens Lyngby, Denmark
3. Signal Processing Laboratory (LTS5), Ecole Polytechnique Fédérale de Lausanne, 1015 Lausanne, Switzerland

* Corresponding authors Contact: mariama@drcmr.dk and timd@drcmr.dk

Abstract

Noninvasive estimation of axon diameter with diffusion MRI holds potential to investigate the timing properties of the brain network and pathology of neurodegenerative diseases. Recent methods use powder averaging to account for complex white matter architectures, such as fibre crossing regions. Here, we investigate the influence of the sequence parameters, signal-to-noise ratio, number of gradient directions and assumed intra-axonal parallel diffusivity on the range and accuracy of diameter estimates from powder average approaches. We show that a broad sensitivity to different length scales is required to accurately estimate diameter, demonstrating how the range of measurable diameters is regulated by the SNR and $q-$value. The powder averaging approaches are then investigated within complex and realistic fibre architectures by Monte Carlo simulations of diffusion within $120 - 313$ μm long sections of segmented axons from X-ray Nano-Holotomography volumes of a splenium and crossing fibre region of a vervet monkey brain. Our simulations show that powder averaging techniques succeed in providing accurate estimates of axon diameter across a range of sequence parameters and diffusion times, even in complex white matter architectures. At sufficiently low b-values, the acquisition becomes sensitive to axonal microdispersion and the intra-axonal parallel diffusivity shows time dependency at both in vivo and ex vivo intrinsic diffusivities. This could be an interesting biomarker of WM health and pathology.

Introduction

Axons propagate action potentials along their lengths to enable communication between different neurons. Their morphology is crucial for the signal conduction process [1–3] and determines the conduction velocity (CV) with which signals are propagated. By electrophysiological modelling of the axon, Drakesmith et al. showed that axon diameter (AD) is the most important determinant of CV in myelinated axons [4]. AD is also a potential biomarker of neurodegenerative diseases such as Amyotrophic Lateral Sclerosis [5] and Multiple Sclerosis (MS) [6], and has been suggested to correlate with clinical scores of cognitive impairment in MS patients [7]. Thus, AD sheds light on brain health, as well as the structural and functional properties of the brain network.

Diffusion Magnetic Resonance Imaging (MRI) non-invasively probes the microstructural brain tissue environment by measuring the diffusion of water molecules across millisecond time scales. By fitting multi-compartment biophysical models that describe the underlying tissue microstructure to the diffusion MRI signal, AD can be estimated.

The AxCaliber method [8, 9] uses pulsed gradient spin echo (PGSE) measurements with numerous combinations of gradient strengths and diffusion times to output the AD distribution (ADD), as demonstrated in vivo in the rat [8] and human [10] brains. AxCaliber requires prior knowledge of the axon orientation since it relies on measurements being made perpendicular to the axons. The ActiveAx approach has been demonstrated in vivo in humans and ex vivo in primates [11, 12] and outputs a mean AD index. Contrary to AxCaliber, ActiveAx is invariant to the orientation of the main fibre direction and implements an optimised acquisition consisting of three $b-$value shells, the minimum number of shells required to fit the three parameters in the signal model used by ActiveAx. These are sampled in ~ 90 unique directions distributed uniformly on the unit sphere. These two methods have in common that they do not account for non-parallel axons, i.e. orientation dispersion (OD), or multiple bundles of crossing axons, factors which bias the AD measurement. Zhang et al. extended the ActiveAx approach in two approaches. They relaxed the assumption of a single main fibre direction to enable AD estimation in regions of the ex vivo monkey brain in which there were crossing axon bundles [13], but the OD within those bundles was not taken into account. Later, Zhang et al. modelled the OD as a Watson distribution to fit AD in the in vivo human brain [14], but the method assumed a single main bundle direction. As such, diffusion MRI-based AD studies have mostly targeted the corpus callosum (CC), an organised white matter (WM) region that consists of aligned interhemispheric axonal connections. The homogeneous architecture of the CC has also made it the subject of light and electron microscopy (EM) studies on AD, and these have been used as validation for the diffusion MRI-based AD metrics [8,15,16]. However, recent 3D imaging studies in the monkey and mouse CC demonstrate the complex morphologies, OD and trajectory variations of axons [17–19], and show how – even in the highly organised CC – these will bias AD measurements [17,18,20,21]. Diffusion MRI-based estimates of AD should thus take into account three different classes of orientation effects: 1) the macroscopic fibre architecture, describing the the relative orientations of different fibre bundles e.g. in crossing fibre regions; 2) the OD, describing the average dispersion exhibited by axons within each bundle; and 3) the microdispersion, describing the changes in trajectory and curvature along individual axons on the length scale of the measured diffusion.

The effects of the macroscopic fibre architecture and OD can be removed by powder averaging (PA). The PA involves calculating the arithmetic mean of the diffusion MRI signal in isotropically distributed directions on the unit sphere. Each diffusing spin can be described as probing a micro-domain – a microscopic region of the tissue environment within a voxel. The PA signal thus represents the spherical mean of the set of micro-domains, regardless of their individual orientation or organisation within the voxel. Several studies have used the PA to disentangle the effects of fibre architecture and OD from diffusion metrics [20, 22–31], and it has recently been implemented to estimate AD in the entire brain WM [32,33]. To obtain estimates of AD index in the in vivo human brain, Fan et al. [32] fitted a multi-compartment spherical mean technique (SMT) model to the PA signal. The signal was sampled in up to 64 uniformly distributed directions for two diffusion times. In total, 16 unique $b-$values up to $b =\sim 20$ ms μm^{-2} were acquired, enabled by the high in vivo gradient strengths of up to 300 mT/m of the Connectom scanner [34–36]. Veraart et al. [33], on the other hand, modelled only the intra-axonal space (IAS) by fitting a power law (PL) to the PA signal at high $b-$values that suppress the signal from the extra-axonal space (EAS) [37,38]. This used $b \geq 20$ ms μm^{-2} for ex vivo experiments and $b \geq 6$ ms μm^{-2} for in vivo experiments. The signal was measured along 60 uniformly distributed gradient directions at a single diffusion time for up to 18 b-values. AD was calculated for the ex vivo rat brain and, also using a Connectom scanner, the in vivo human brain.

Although the PA techniques remove fibre architecture and OD effects, they rely on the assumption that the micro-domain probed by diffusing spins is cylindrical. With increasing diffusion times, the spins diffuse further and increasingly probe the microdispersion of the axons, violating the assumption of a cylindrical micro-domain and making the AD estimate time-dependent. The theory of the effects of diameter and trajectory variations on estimated AD has been laid out in [20], but the diffusion times and b-values for which the PA-based AD estimate becomes sensitive to the microdispersion in axons is unknown. The signal-to-noise ratio (SNR) of the signal [39] and the gradient strength of the applied magnetic field [12] affect the sensitivity profile of the acquisition, placing limits on the upper and lower bounds of measurable AD. How different sequence parameters, the number of gradient directions or the SNRs affect these bounds has not been investigated for PA-based AD estimates.

Validating the estimated ADs from the PA methods for different sequence parameters and in realistic axons is therefore important. The PL implementation from Veraart et al. was evaluated within the axon segments of length ~ 20 μm from electron microscopy (EM) of the mouse CC using Monte Carlo (MC) simulations of diffusion in [20]. Given that non-axonal structures in the EAS can impact the trajectories of axons for up to 20 μm [17], longer axonal segments may to a greater extent represent the characteristics of the IAS. Notably, although the PA is expected to factor out the effects of fibre crossings and OD, it has only been validated on segments of axons from the CC in which the fibre architecture is simple and does not contain crossings.

In this study, we adopt a simulation-based modus operandi to investigate the impact of different scanning parameters, SNR and fibre architectures on AD estimates with PA-based approaches. We restrict the analysis to the IAS to analyse how accurately it is represented by the PA signal at different b-values, and the results are relevant to both multi-compartment and single-compartment models that include the IAS. Firstly, we consider how the SNR, gradient strength (hence, also b-value) and number of unique gradient directions interplay to determine the bounds and range of measurable AD. Secondly, we demonstrate the impact (or lack thereof) on estimated AD of using inaccurate assumptions of the parallel diffusivity in the SMT and PL implementations for different b-values. Lastly, large field of view (FOV) X-ray nano-holotomography (XNH) volumes of the vervet monkey brain provided access to long axon segments, between 120 and 313 μm in length, from two inherently different fibre architectures: a) the ordered CC of the splenium and b) a heterogeneous crossing fibre region. We validated the AD estimates from the SMT and PL at different diffusion times, gradient strengths, diffusivities (in vivo/ex vivo) and, pertinently, within the complex IAS of the primate brain where ADs are similar to those of the human brain [40].

Theory

To model the IAS, the SMT and PL approaches both assume that the microdomains probed by spins within the IAS are cylindrical. Here, we present an outline of the origins of the SMT expression for cylinders, based on the theory presented elsewhere in [41,42]. It is this expression that is used to represent the IAS in the SMT-based approach of Fan et al. [32]. From the SMT expression, the assumption of high $b-$values entails that the SMT can be formulated as a PL, as that in Veraart et al. [33].

Modelling the PA signal of a cylinder

In a cylinder, the apparent diffusion coefficient (ADC) at any angle α to its axis is [43]:

$$D(\alpha) = \cos^2(\alpha)D_{\parallel} + \sin^2(\alpha)D_{\perp} \tag{1}$$

where $D_{\parallel}$ is the ADC parallel to the cylinder axis and $D_{\perp}$ is that perpendicular to it, and carries the information regarding cylinder diameter. Powder averaging of the diffusion MRI signal involves integrating it over an infinite number of uniformly distributed angles α [41] to give the powder averaged signal, $\overline{S}_{SMT}$:

$$\begin{aligned}\overline{S}_{SMT}(b) &= \int_0^{\pi} P(\alpha)e^{-b(\cos^2(\alpha)D_{\parallel}+\sin^2(\alpha)D_{\perp})}d\alpha \\ &= \left(e^{-bD_{\perp}} \cdot \sqrt{\frac{\pi}{4b\cdot(D_{\parallel}-D_{\perp})}} \cdot erf(\sqrt{b\cdot(D_{\parallel}-D_{\perp})}\right)\end{aligned} \tag{2}$$

where $P(\alpha) = \frac{\sin(\alpha)}{2}$ ensures that the weighting of the angles is uniform, $erf(x)$ is the error function of x, and b is the diffusion weighting. Equation 2 is what is here referred to as the "SMT implementation" and is the analytical description of the spherically averaged signal within a cylinder. Aside from the $b-$value, the signal depends on two variables: $D_{\parallel}$ and $D_{\perp}$. Only a finite number of directions, N, can be used in practise. As such, N is one of the variables that determines the accuracy of the measurement.

In cylinders, where $D_{\parallel} > D_{\perp}$ and at high $b-$values, it can be assumed that $b \cdot (D_{\parallel} - D_{\perp}) \gg 1$. In these conditions, $erf(x) = 1$ and Equation 2 can be rearranged to take the form of a PL:

$$\overline{S}_{PL}(b) = \beta e^{-bD_{\perp}} b^{-0.5} \tag{3}$$

where $\beta = \sqrt{\frac{\pi}{4(D_{\parallel} - D_{\perp})}}$. Equation 3 is what is here referred to as the "PL implementation" and is an alternative representation of the SMT at high $b-$values.

In practise, whether using single- or multi-compartment models of the WM, the fraction of the total signal that the IAS represents, f_a, is unknown. It thus needs to be included as a multiplicative constant in Equations 2 or 3. This introduces an additional third variable into the SMT implementation in Equation 2, such that the signal depends on f_a, $D_{\parallel}$ and $D_{\perp}$. In the case of the PL, f_a can simply be incorporated into the existing constant β such that $\beta = f_a \cdot \sqrt{\frac{\pi}{4(D_{\parallel} - D_{\perp})}}$. This removes the need to fit a third parameter to the PA signal.

Converting $D_{\perp}$ into diameter

By fitting Equations 2 or 3 to the PA signal, the ADC perpendicular to the cylindrical micro-domains, $D_{\perp}$, is obtained. The cylinder diameter can be calculated from $D_{\perp}$ using [43, 44]:

$$\begin{aligned} &- bD_{\perp} = \ln S_{\perp} = \\ &\qquad \ln S_0 - 2\gamma G^2 \sum_{m=1}^{\inf} \frac{1}{D_0^2 \alpha_m^6 (R^2 \alpha_m^2 - 1)} \\ &\cdot [2D_f \alpha_m^2 \delta - 2 + 2e^{-D_0 \alpha_m^2 \delta} + 2e^{-D_0 \alpha_m^2 \Delta} - e^{-D_0 \alpha_m^2 (\Delta - \delta)} - e^{-D_0 \alpha_m^2 (\Delta + \delta)}] \end{aligned} \tag{4}$$

where $S_{\perp}$ is the diffusion-weighted signal perpendicular to the cylinder, S_0 is the signal with no diffusion weighting, γ is the gyromagnetic ratio, G is the strength of the gradient pulse, D_0 is the intrinsic diffusivity, δ is the duration of the gradient pulse, Δ is the separation of the gradient pulses and α_m is the mth root of $J_1'(\alpha_m R) = 0$ where J_1' is the derivative of the first order Bessel function of the first kind. In this case, Eq. 4 is calculated up to $m = 6$.

If $\delta \gg \frac{R^2}{D_0}$, as is in practise the case for most axons [33], the cylinders are said to fall within the Neuman limit [44, 45] and Equation 4 simplifies to:

$$\ln S_{\perp} = -\frac{7}{48} \frac{\delta g^2 R^4}{D_0} \tag{5}$$

Importantly, both the SMT and PL require knowledge – or an assumption – of D_0 in order to estimate a diameter from $D_\perp$. However, since $R \sim (D_0)^{\frac{1}{4}}$ in Equation 5, R is relatively insensitive to small inaccuracies of D_0.

Materials and Methods

Simulations

The simulations in this study are divided into two categories: simulations of the diffusion MRI signal from cylinders of different diameters and simulations in the IAS of segmented axons from XNH volumes of the vervet monkey brain presented in [17]. By simulating the signal from cylinders, the impact of scanning parameters, SNR and model assumptions on estimated diameter could be isolated. By simulating diffusion within segmented axons from the splenium and crossing fibre regions, the impact on the estimated AD of realistic fibre architectures, OD and microdispersion was investigated.

Simulating the Diffusion MRI Signal from Cylinders

The signals arising from cylinders of different diameter, aligned with the z-axis, were generated analytically. For given PGSE parameters δ, Δ and G and radius R, Equation 4 was used to calculate $D_\perp$ for each cylinder. From this, the ADC and signal in any direction $\mathbf{G} = [G_x, G_y, G_z]$ could be calculated from

$$ADC = \mathbf{G} \times \begin{pmatrix} D_\| & 0 & 0 \\ 0 & D_\perp & 0 \\ 0 & 0 & D_\perp \end{pmatrix} \times \mathbf{G}'.$$

Simulating Diffusion within the Realistic IAS from XNH Volumes of the Monkey Brain

We used segmented axons from the brain of a 32-month female vervet monkey, imaged with 3D synchrotron XNH acquired at the European Synchrotron Research Facility, beamline ID16A. The axons originated from two different brain regions: the splenium of the CC and a "crossing fiber region", located in a position of the anterior centrum semiovale where the diffusion MRI data indicated the crossing of the corticospinal tract, interhemispheric callosal fibres and association fibres [17]. A description of both XNH volumes, as well as the segmentation and analysis of splenium axons is given in Andersson et al [17]. In short, the XNH volume of the splenium had an isotropic voxel size of 75 nm and cylindrical FOV of diameter and length 153.6 μm. From the splenium, 54 axons of minimum length 120 μm were segmented at the native 75 nm image resolution. The XNH volume of the crossing fibre region had an isotropic voxel size of 100 nm and cylindrical FOV of diameter and length 204.8 μm. The much larger diameters of axons in this region entailed that the segmentation of 58 axons of minimum length 120 μm could be manually performed in ITK-Snap (RRID:SCR_002010) at a downsampled isotropic voxel size of 500 nm. This was significantly less time consuming than segmenting the axons at higher resolution. Smaller axons were present in both XNH volumes, but could not be segmented due to their small diameters in comparison to the voxel size and low SNR [17]. After segmentation, the equivalent diameters of the axons were quantified in the plane perpendicular to their local trajectory [17]. The volume-weighted AD, d, of each axon was estimated as $d = \sum_{N}^{i=1} 2R_i \cdot \left(\frac{\pi R_i^2}{\sum_{i=1}^{N} \pi R_i^2} \right)$ where R_i is the ith measured radius of N equidistant measurement points along the axonal trajectories. The volume-weighted mean diameters of the population of splenium axons and crossing fibre axons were similarly calculated.

The axon segmentations were converted to triangulated surface meshes, after which the Monte Carlo Diffusion and Collision (MCDC) framework [46] was used to simulate diffusion within each axon mesh. The simulations used an intrinsic ex vivo diffusivity of $D_0 = 0.6 \cdot 10^{-9}$ m^{2}s^{-1}, $2 \cdot 10^5$ uniformly distributed spins per axon (with initialisation at least 20 μm from the ends of the axons) and $1 \cdot 10^{-5}$ seconds per time step, as in Andersson et al [17]. Simulations were also performed using an in vivo diffusivity of $D_0 = 2 \cdot 10^{-9}$ m^{2}s^{-1}, but with $3.4 \cdot 10^{-6}$ seconds per time step to ensure the same step length at the higher diffusivity. The $2 \cdot 10^5$ uniformly distributed spins were initialised at least 30 μm from the ends of the axons to prevent their escape from the IAS with regards to the diffusivity and maximum diffusion time probed.

Diffusion MRI Scanning Parameters

For all experiments, the PGSE waveform was used. Throughout the investigation, different sequence parameters were varied to isolate the effects of different variables on the estimated diameter.

In the simulations on cylinders, a gradient duration of $\delta = 7.1$ ms was used, similar to in [32, 33]. The gradient separation was kept at $\Delta = 20$ ms, and the effective diffusion time, t_d, was given by $t_d = \Delta - \frac{\delta}{3}$. The simulations on cylinders used only ex vivo diffusivities, and b-values were referred to as "high" if they surpassed $\gtrsim 20$ ms μm^{-2}, the value at which the EAS was said to be suppressed in [33]. Most simulations in cylinders used high b-values in the range of $b = [19.25, 63.62]$ ms μm^{-2} to allow a direct comparison between the SMT and PL implementations, the latter of which required the use of high b-values. Different b-values were obtained by varying the gradient strength, G, given that $b = q^2 t_d$ where q is the diffusion encoding $q = \gamma\delta G$. In the simulations of the realistic IAS, $\delta = 7$ ms was used. Both G and Δ were varied to assess the effects of different diffusion times. In these simulations, the SMT and PL were fitted to many different b-values, ranging between $b = [0.55, 65]$ ms μm^{-2} for ex vivo diffusivities and $b = [0.44, 11.89]$ ms μm^{-2} for in vivo diffusivities.

For the most part, fits of the SMT and PL to the PA signal from several b-values used three shells, similar to ActiveAx [11, 12], since three was the minimum number of shells needed to calculate f_a, $D_{\|}$ and $D_{\perp}$ in the SMT implementation. Uniformly distributed directions on the unit sphere were generated according to the electrostatic repulsion method in [47, 48].

The Signal-to-Noise Ratio

The effect of noise on the AD estimation was studied by adding Rician noise of variable SNR to the noise-free, normalised signals. The total variance of the noise was defined as $\sigma^2 = \frac{1}{SNR^2}$. Rician distributed noise was simulated calculating the magnitude of complex Gaussian noise in which the real and imaginary components each had a standard deviation of $\frac{1}{SNR}$ [49].

Distinguishing the Signal from Noise

To assess whether or not a single signal could be distinguished from noise at a given SNR, we used the sensitivity criterion of Nilsson et al. [39] for parallel cylinders. The smallest robustly measurable change of the normalised signal, ΔS was defined as:

$$\Delta S = \frac{z_\alpha}{SNR\sqrt{n}} \tag{6}$$

where n was the number of repeated measurements and z_α was the z-threshold for the significance level α. The signal was thus said to be sensitive between the bounds $[\Delta S,\ 1-\Delta S]$. The diameters that gave rise to the PA signal at these boundaries were defined as the maximum and minimum bounds of the measurable diameter. Here, we choose $\alpha = 0.05$, giving $z_\alpha = 1.64$, as in [39].

To predict whether the PA signal could be distinguished from normally distributed noise, the sensitivity criterion of Nilsson et al. [39] for fully dispersed cylinders was used. It is defined as:

$$\Delta S_{PA} = bD_\perp(d) \cdot \sqrt{\frac{\pi}{4}\frac{erf\left(\sqrt{b(D_\parallel - D_\perp)}\right)}{\sqrt{b(D_\parallel - D_\perp)}}} \tag{7}$$

where $D_\perp(d)$ is the perpendicular diffusivity of the diameter, d, that is defined as:

$$d = \left(\frac{768}{7}\frac{\Delta S D_0}{\gamma^2 \delta G^2}\right)^{\frac{1}{4}} \tag{8}$$

When using Eqs. 7 and 8, n in Eq. 6 was set to the number of unique gradient directions. From ΔS_{PA}, the theoretical range of measurable diameters was calculated as the diameters with PA signals within the range $[\Delta S_{PA}, S_{stick} - \Delta S]$ where S_{stick} is the signal of a cylinder with diameter equal to zero:

$$S_{stick} = \sqrt{\frac{\pi}{4b \cdot D_\parallel}} \cdot erf(\sqrt{bD_\parallel}) \tag{9}$$

Importantly, Eqs. 6-8 are formulate for single b-values only and assume that the noise follows a normal distribution.

Fitting the Spherical Mean Technique and Power Law to the PA signal

The Spherical Mean Technique Implementation

The volume fraction of the IAS, f_a, was incorporated into the SMT formulation in Equation 2 such that:

$$\overline{S} = f_a \left(e^{-bD_\perp} \cdot \sqrt{\frac{\pi}{4b \cdot (D_\| - D_\perp)}} \cdot \Phi(\sqrt{b \cdot (D_\| - D_\perp)} \right) \tag{10}$$

The SMT was fitted to the PA signals with a Matlab-based Levenberg-Marquardt algorithm. Once $D_\perp$ had been fitted, the diameter was calculated using Equation 4. To assess the robustness of the SMT fit when keeping different variables fixed, we implemented three different variations of the SMT fit:

(i) **SMT-1**: a single-shell fit to obtain $D_\perp$ in the range $[0, D_\|]$. Assumes known f_a and $D_\| = 0.6 \cdot 10^{-9}$ $\mathrm{m}^2\mathrm{s}^{-1}$.

(ii) **SMT-2**: a multi-shell fit to obtain $D_\perp$ in the range $[0, D_\|]$ and f_a in the range $[0, 1]$. Assumes known $D_\| = 0.6 \cdot 10^{-9}$ $\mathrm{m}^2\mathrm{s}^{-1}$.

(iii) **SMT-3**: a multi-shell fit to obtain $D_\perp$ in the range $[0, D_0 \cdot 1.5]$, f_a in the range $[0, 1]$ and $D_\|$ in the range$[D_0/2, D_0 \cdot 1.5]$ where D_0 was the known intrinsic diffusivity of the simulations. For ex vivo simulations, $D_0 = 0.6 \cdot 10^{-9}$ $\mathrm{m}^2\mathrm{s}^{-1}$ was used, while for in vivo simulations $D_0 = 2 \cdot 10^{-9}$ $\mathrm{m}^2\mathrm{s}^{-1}$ was used.

SMT-1 was used to assess the effect of the number of directions and SNR on the estimated diameter in the best case scenario in which f_a and $D_\|$ are known. Moving to a more realistic scenario, SMT-2 was used to assess the accuracy of SMT-based diameter estimation at different, unknown values of f_a. SMT-2 was also used to investigate the consequences of enforcing an incorrect value of $D_\|$ at different $b-$values and SNRs. Lastly, SMT-3 placed no assumptions on any of the variables, similar to the PL implementation. SMT-3 was used to investigate the ability of the SMT to estimate AD in real axons for in vivo and ex vivo intrinsic D_0, assuming no prior knowledge of diffusivities (other than their upper and lower bounds). SMT-3 also outputted estimates of $D_\|$ in the axons.

The Power Law Implementation

To assess the diameter estimates from the PL formulation, the expression in Eq. 3 was fitted to the PA signal from cylinders of different diameters, providing estimates of $D_\perp$ and β. This allowed for a comparison of the PL-derived diameter, d_{PL}, with those from SMT-2 and SMT-3. To fit the PL the Matlab-based nonlinear least squares estimator provided by Veraart and Novikov [50] was used. This implementation assumed the Neuman limit as in Eq 5 to obtain a diameter estimate.

Results

The Results section is organised as follows. First, we examine the effects of the number of gradient directions and SNR on the estimated diameter, d_{SMT-1}, from SMT-1 of cylinders. This is done for both Rician and Gaussian noise. Next, we relax the assumption of the known volume fraction, and investigate the range of measurable diameters obtained by fitting SMT-2 and the PL to different sets of high b-values. We then investigate the validity of assuming a known parallel diffusivity in SMT-2 for low and high b-values. Moving away from the assumption of a cylindrical microdomain, we present segmentations of axons from the splenium and a crossing fibre region of the monkey brain. In these, we then investigate the ability of the SMT-2, SMT-3 and PL implementations to estimate the volume-weighted ADs within real axonal geometries for in/ex vivo diffusivities, different gradient strengths and diffusion times between $\sim 10-40$ ms.

Angular sensitivity of the diffusion MRI signal in cylinders

Diameter estimates using the PA demand that the diffusion MRI signal is sensitive to the different length scales probed by measuring the signal at angles α relative to the cylinder axis. The range of diameters that can be measured with the PA can be predicted from Eq. 7, and are shown in Fig. 1B for a range of SNRs and q-values. The widening/narrowing of the sensitivity range can be explained by the sensitivity of the PGSE acquisition to different angles α. As shown in Fig. 1C, the range of α that ensures a sensitive signal varies with the SNR and the diffusion encoding q (and hence the gradient strength). Sensitivity of the signal was defined according to Eq. 6. For the same parameters, angular sensitivity profiles were different for cylinders of different diameter. With increasing SNR (Fig. 1C, top row), the sensitivity to both the high and low α increased. At SNR $= 100$, an increasing q increased the sensitivity to high α, but the additional attenuation of the signal caused by the higher diffusion weighting decreased the sensitivity to small α.

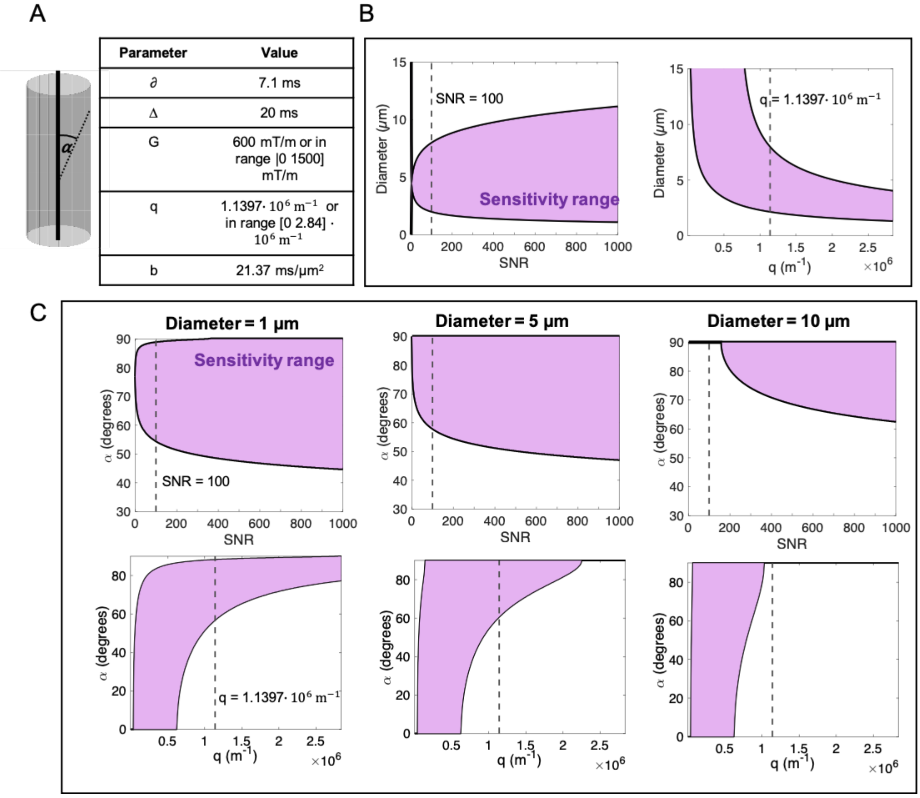

Parameter	Value
∂	7.1 ms
Δ	20 ms
G	600 mT/m or in range [0 1500] mT/m
q	$1.1397 \cdot 10^{6}$ m^{-1} or in range [0 2.84] $\cdot$ 10^{6} m^{-1}
b	21.37 ms/µm²

Fig. 1: Angular sensitivity of the signal with respect to the cylinder axis A) The angle α is defined as the inclination from the cylinder axis. The PGSE parameters in the table were used for the sensitivity analysis. B) The range of measurable diameters using the PA signal varies with the SNR, as shown using $q = 1.1397 \cdot 10^{6}$ m^{-1}. For SNR=100, the range of measurable diameters varies with the q-value (G is varied to obtain different q, but δ and Δ are as in the table). The sensitivity analysis is based on Eq. 7 and assumes 30 gradient directions. C) Variation with SNR and $q-$value of the angular sensitivity range, in terms of α, to which the measurement is sensitive in cylinders of diameter $[1, 5, 10]$ μm for the PGSE parameters in B. This sensitivity criterion is as in Eq. 6.

Effect of Number of Gradient Directions and SNR

The number of uniformly distributed directions affects the accuracy of the PA signal in describing the underlying microstructure, but also determines the total scan time. The signals from cylinders of different diameters with different numbers of gradient directions and different levels of Rician noise were generated, emulating the noise distribution present in magnitude diffusion MRI images. The sequence parameters were the same as in Fig. 1 and SMT-1 was fitted to the PA signal, giving a diameter estimate d_{SMT-1}, as shown in Figure 2. For comparison, the diameter estimated from a single measurement perpendicular to the cylinders, d_{VG}, was also calculated from Eq. 4. The theoretical upper and lower bounds of d_{SMT-1} were calculated from Eq. 7, while those of d_{VG} were calculated from Eq. 6.

At $SNR = \infty$, the higher the number of directions, the more accurate d_{SMT-1} was at smaller diameters. At low SNRs <2, the asymmetric Rician noise is known to introduce a bias [49]. Even at high SNRs of 100 in non-diffusion weighted $b = 0$ images, considerable signal attenuation in cylinders with large diameters incurs a low effective SNR of the measurement. This, combined with the Rician bias, caused an underestimation of large diameters in Fig. 2. Similarly, the Rician bias caused the PA signal of small cylinders to appear as sticks (Eq. 9), resulting in $d_{SMT-1} = 0$. In general, the theoretical lower and upper bounds agreed well with the diameter trend using an intermediate number of directions; in this case 30. Due to the assumption of normally distributed noise in the sensitivity criteria, the theoretical lower bound should decrease with increasing number of directions. The advantage of using a higher number of directions was masked by the Rician bias. For example, at SNRs $= [20, 100]$, there appeared to be no significant difference between d_{SMT-1} extracted from 30 directions or 512 directions. In general, the higher the number of directions, the smaller the variance in the estimate. The diameter calculated from the direction perpendicular to the cylinders, d_{VG}, accurately estimated the diameters of smaller cylinders than d_{SMT-1} without underestimation, but had a higher variance owing to the fewer sampling points.

Furthermore, the behaviour of d_{SMT-1} at small diameters varied when few directions were used. It either plateaued (as it did using 6 directions) or dropped to 0 (as it did using 10 directions). This indicated a dependence of the PA signal on the orientation of the gradient sets relative to the cylinder axis. The sensitivity of d_{SMT-1} to the orientation of the direction sets was examined by generating the signals of cylinders that were rotated around the y-axis at 1 deg intervals between $[0, 90]$ deg. Fig. S2 shows the standard deviation and mean of d_{SMT-1} estimated from these 91 orientations. In general, the estimated diameter was more rotationally invariant (the standard deviation was lower) the higher the higher the angular resolution.

To mitigate the effects of the Rician bias on the signal, it is possible to extract the real-valued diffusion MRI data in which the noise distribution is Gaussian. We thus repeated the experiments in Fig. 2 for Gaussian distributed noise, and the results are shown in Fig. S1. The Gaussian distributed noise allowed for more accurate estimates of the diameter at both smaller and larger diameters than with Rician noise, for 30 or more directions. The theoretical upper and lower bounds gave accurate predictions of sensitivity, but beyond these, the variance of the measurements was significantly higher due to the difference in variance between the Gaussian and Rician distributions.

Estimating Diameter and Intra-Axonal Volume Fraction from Multiple High $b-$Value Shells

The impact of different b-values on diameter estimation was studied by fitting SMT-2 and the PL to the PA signals from cylinders with ground truth values of $f_a = 0.8$, an approximation of the expected axonal volume fraction. The b-values were chosen to cover a similar range to those in the ex vivo acquisition in [33], and all were $\gtrsim 20$ ms μm^{-2} to simulate suppression of the ECS. For one set of b-values, Fig. 3 shows the estimated parameters from the SMT-1, SMT-2 and PL fits at SNR=100 with Rician and Gaussian distributed noise.

For Rician noise in Fig. 3A, d_{SMT-2} and d_{PL} exhibited parabolic shapes, dropping to 0 at small and large diameters, in contrast to the single shell SMT-1 which plateaued at large diameters. At large diameters, the underestimation of diameter was accompanied by a reduction of the f_a estimate for the SMT-2 approach, and a reduction in β by the PL approach, as the significant attenuation at large diameters was instead attributed to a smaller volume fraction. The use of data with Gaussian distributed noise in Fig. 3 produced d_{SMT-2}, f_a and β estimates that were accurate at smaller and larger diameters than with Rician noise, albeit with a high variance (at large diameters). Consequently, at diameters $\gtrsim 7$ μm, the estimates of f_a and β could not be robustly estimated, even with the mean of $n = 50$ repeats. One contributor to the high variance was that the SMT-2 and PL fits failed for many large diameters, defaulting to 0.

To explore the how $b-$value range and number of shells affected the diameter estimates, the experiments in Fig. 3A were repeated for A) three shells that spanned the same range as in Fig. 3 with $b = [19.25, 35.79, 63.62]$ ms/μm^2 , B) three closely spaced b-values at the lower end of the range $b = [19.25, 22.90, 26.88]$ ms/μm^2 and C) three closely spaced b-values at the higher end of the range,

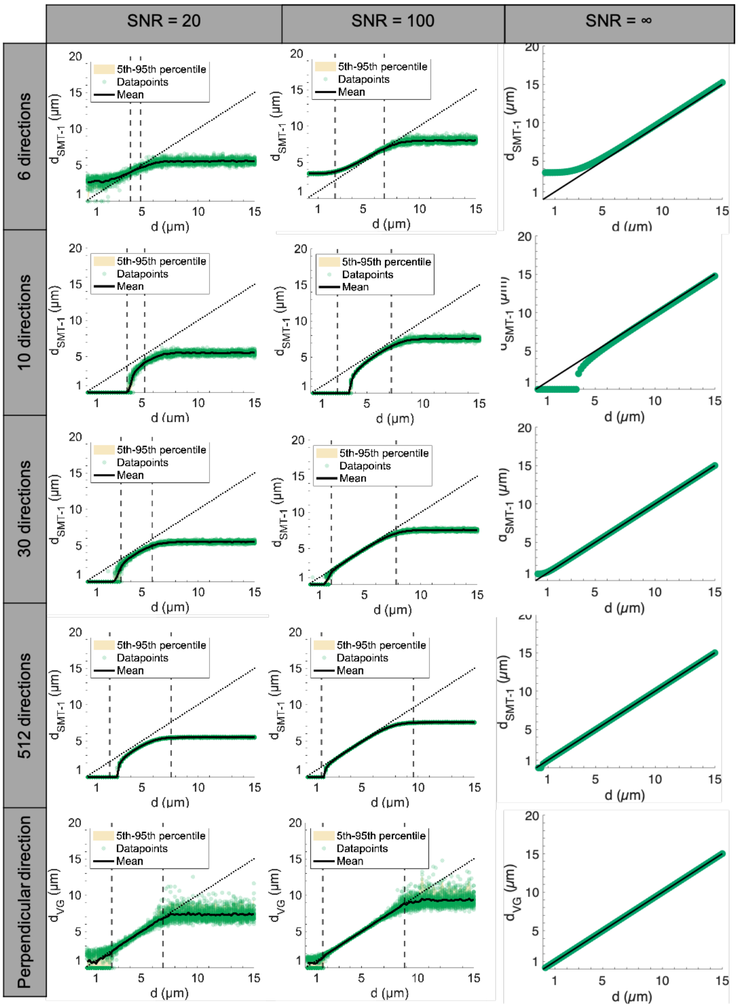

Fig. 2: Influence of number of directions and SNR (Rician noise) on the single-shell SMT-estimated diameter, d_{SMT-1}, in cylinders of diameter between 0.2 and 15.0 μm at 0.2 μm intervals. The single-shell SMT assumes known $f_a = 1$, $D_{\|} = 0.6 \cdot 10^{-9}\text{m}^2\text{s}^{-1}$. The lower and upper bounds of measurable diameter are sensitive to both SNR and the number of directions and calc. The last row shows the influence of SNR on d_{VG} as calculated using Equation 4. $n = 50$ repeats of the acquisition were performed for each diameter, SNR and number of directions. The black striped lines represent the predicted lower and upper bounds of measurable diameter.

$b = [51.54, 57.42, 63.62]$ ms/μm^2. The results are shown in Fig. 4. Other than

A. Rician noise SNR = 100

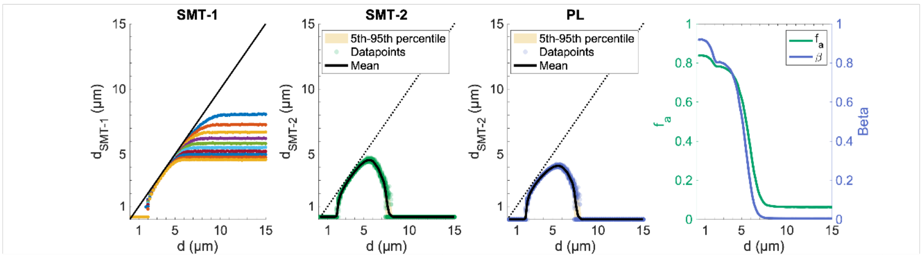

B. Gaussian noise SNR = 100

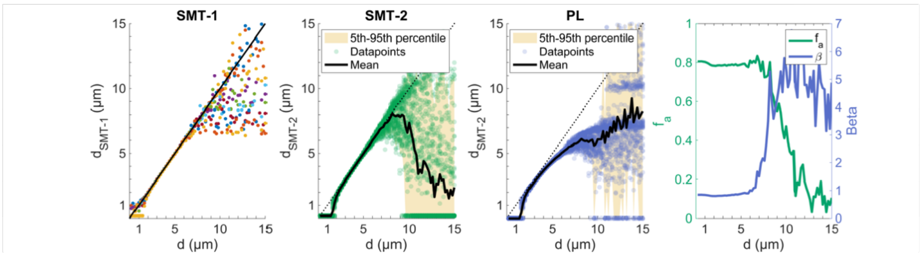

Fig. 3: Multi-shell fit of SMT and PL to the signal from cylinders of diameter between 0.2 and 15.0 μm at SNR = 100 and different noise distributions. Fitted d_{SMT-1}, d_{SMT-2}, d_{PL}, f_a from SMT-2 and β from the PL for A) Rician distributed noise and B) Gaussian distributed noise. The signal is generated using $D_{\|} = 0.6 \cdot 10^{-9}\text{m}^2\text{s}^{-1}$, $f_a = 0.8$, 30 isotropically distributed directions and PGSE parameters $\delta = 7.1$ ms, $\Delta = 20$ ms , 10 b values in the range $[19.25, 63.62]$ ms/μm^2 and linearly spaced values of G in the range $[550, 1000]$ mT/m. $n = 50$ repeats of each acquisition were performed for each diameter.

a very small decrease in variance, there seemed to be no clear advantage to sampling more shells that cover the same range of $b-$values, as clear from the comparison of the results using ten shells in Fig. 4A and using three shells in Fig. 3A. Secondly, fitting to the three b-values on the lower end of the range in Fig. 4B resulted in a wider range of measurable diameters than fitting to three significantly higher b-values in Fig. 4C, although the variance increased somewhat. The equivalent experiments using Gaussian noise are shown in Fig. 3. Here, the use of Gaussian noise widened the range of measurable diameters and provided more accurate estimates of f_a.

How different noise levels influenced the diameter estimates from the SMT-2 and PL fits was examined by repeating the experiment in Fig. 4B for SNR $= [\infty, 20]$, as shown in Fig. S4. At SNR$= \infty$, d_{SMT-2} and f_a were accurate estimated up to ~ 13 μm, aside from at the very smallest diameters, but d_{PL} underestimated diameters $\gtrsim 5$ μm. At SNR=20 with Rician noise in Fig. S4B

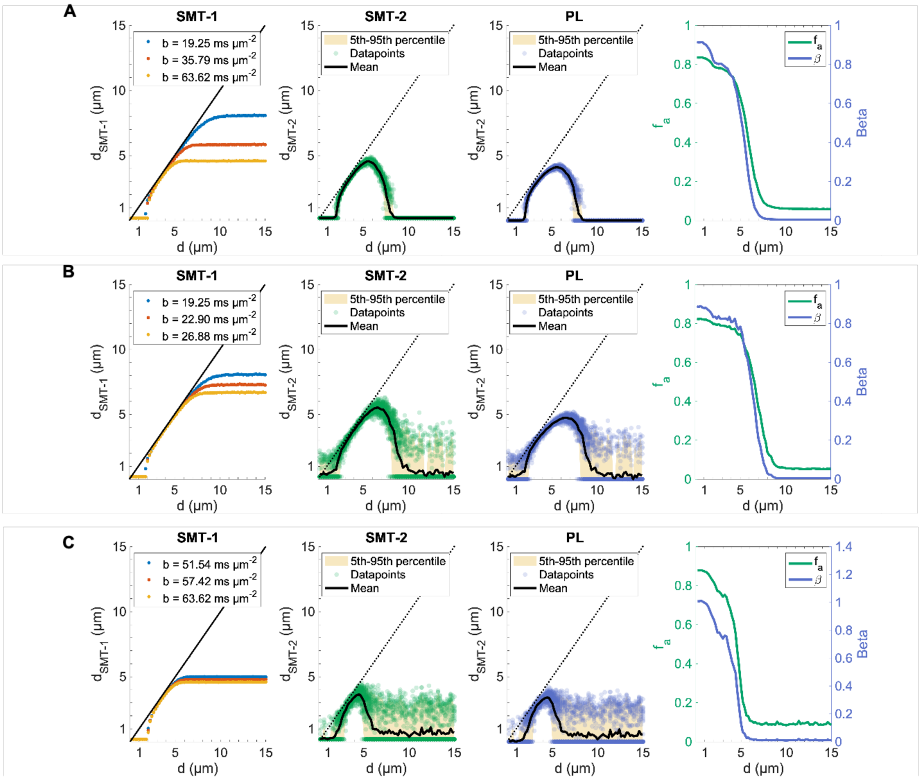

Fig. 4: The choice of b-values affects the range of measurable diameters. Multi-shell fit of SMT and PL to the signal from cylinders of diameter sbetween 0.2 and 15.0 μm at SNR = 100 (Rician noise) and $f_a = 0.8$. Fitted d_{SMT-1}, d_{SMT-2}, d_{PL}, f_a and β for ground truth A) three shells with $b = [19.25, 35.79, 63.62]$ B) three shells with $b = [19.25, 22.90, 26.88]$ ms/μm^2 and C) three shells with $b = [51.54, 57.42, 63.62]$ ms/μm^2. The signal was generated using $D_{\parallel} = 0.6 \cdot 10^{-9}$m^{2}s^{-1}, 30 directions, PGSE parameters $\delta = 7.1$ ms, $\Delta = 20$ ms and varying G. $n = 50$ repeats of each acquisition were performed for each diameter.

the range of measurable diameters narrowed significantly as the lower and upper bounds of measurable diameter approached each other, and the estimate of f_a was highly dependent on the diameter. At SNR=20 with Gaussian noise in Fig. S4C, the variance in the parameter estimates was higher than at SNR=100 in Fig. S3A and at diameters $\gtrsim 6$ μm, the estimates of f_a and β could not be robustly estimated from the mean of $n = 50$ repeats. Furthermore, an increase/decrease in ground truth f_a had the same effect on the fitted parameters as an increased/decreased SNR as shown in Fig. S5, either widening or narrowing the range of measurable diameters.

The Dependence of Estimated Diameter on $D_{||}$

The validity of fitting SMT-2 to a multi-shell acquisition depends on how accurately $D_{||}$ must be approximated. The percentage errors in d_{SMT-2} and d_{VG} for different assumed values of $D_{||}$ are shown in Fig. 5, with ground truth $D_{||} = 0.6 \cdot 10^{-9}\text{m}^2\text{s}^{-1}$. For the diameter estimation, it was assumed that $D_{||} = D_0$ for all $D_{||}$. The range $D_{||} \pm 15\%$ is marked and approximately covers the spread of in- and ex vivo axial diffusivities reported in the literature [51–53].

Using an incorrect value of $D_{||}$ to within $\pm 15\%$ of the ground truth did not noticeably change the percentage error of d_{SMT-2} for cylinders with $d > 2$ μm at high $b-$values and infinite SNR in Fig. 5A. For diameters > 2 μm, there was thus little dependence of d_{SMT-2} on the value of $D_{||}$. For cylinders with $d = 2$ μm, the use of a larger-than ground truth $D_{||}$ caused the SMT-2 fit to fail. Diameters of 1 μm could not be resolved, regardless of the assumed value of $D_{||}$. The value of d_{VG} showed little sensitivity to the assumed value of D_0. The inclusion of Rician noise in Fig. 5B caused a somewhat increased dependency of d_{SMT-2} on the assumed value of $D_{||}$, apparent from the increased slope of the plots. As expected from Fig. 3, the Rician noise caused a general underestimation of all diameters, particularly evident in the larger diameters for which the fit misattributed the large signal attenuation to a decreased volume fraction (e.g. 7 μm in Fig. 5B). For the low $b-$values in Figs. 5C-D, there was a much clearer time dependence of d_{SMT-2} on $D_{||}$ for all but the largest cylinders. The trends were almost identical for the noise-free/noisy conditions. Although d_{VG} was very unstable for $d = 1$ μm, it again showed little dependence on D_0. From these results, it is clear that the dependence of estimated diameter on the assumed value of $D_{||}$ depends on the b-values used.

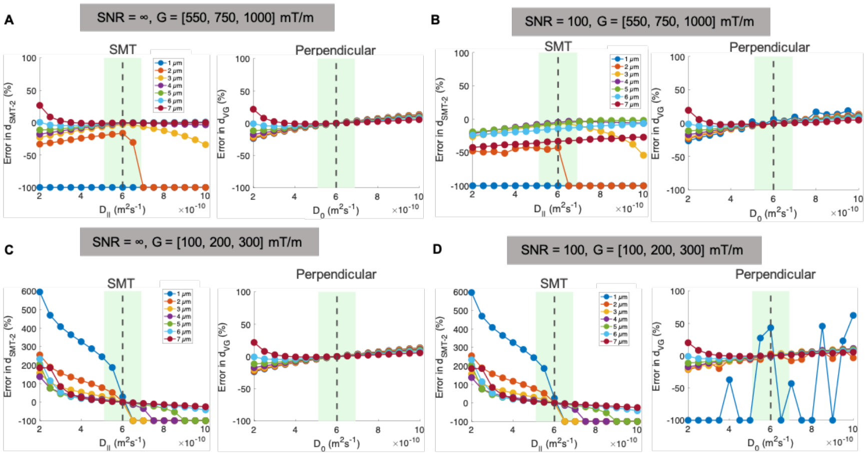

Fig. 5: The sensitivity of d_{SMT-2} and d_{VG} to assumed value of $D_{\|}$ depends on b-value RANGE. Percentage error in estimated d_{SMT-2} and d_{VG} in cylinders vs. assumed value of $D_{\|}$ for high diffusion weighting A) $b = [19.25, 35.79, 63.62]$ ms/μm^2 and SNR=∞ , B) $b = [19.25, 35.79, 63.62]$ ms/μm^2 and SNR=100 (Rician), and lower diffusion weighting C) $b = [0.636, 2.545, 5.726]$ ms/μm^2 and SNR=∞ and D) $b = [0.636, 2.545, 5.726]$ ms/μm^2 and SNR = 100 (Rician). The signal was generated using 30 isotropically distributed directions, $f_a = 1$ and PGSE parameters $\delta = 7.14$ ms and $\Delta = 20$ ms. The higher b shells use $G = [550, 750, 1000]$ mT/m and the "low b" shells use $G = [100, 200, 300]$ mT/m. The true $D_{\|} = 0.6 \cdot 10^{-9}$m^{2}s^{-1} is marked by the black striped line, and $D_{\|} \pm 15\%$ is represented by the green shaded area. The datapoints represent the mean of $n = 50$ repeats.

Diameter estimation in realistic axons

Fibre architecture, axonal OD and axonal microdispersion differed considerably between the splenium and crossing fibre regions of the vervet monkey brain. The axons segmented from the splenium region, shown in Fig. 6A, were significantly smaller (mean AD= 2.75 μm, SD = 0.53 μm) and exhibited a narrower ADD than those from the crossing fibre region (mean AD= 4.00 μm, SD = 1.26 μm) in Fig. 6B. In comparison to axons from the organised CC environment, the axons from the crossing fibre region were very heterogeneous in terms of length, diameter, shape and OD. The thinnest, thickest and longest axons are shown in Fig. 6D-F. To measure the axial diffusivity, the main direction of the axons, calculated via a principal component analysis of their trajectories, were aligned with the z-axis. Intra-axonal diffusion of spins was simulated for up to 100 ms. From the mean-squared-displacements of the spins, the diffusion coefficient in the z-direction (D_z) was approximated and its variation with diffusion time, t_d, is shown in Fig. 6G-E for the splenium and crossing fiber axons respectively. The values of D_z in the splenium axons were higher than those in the crossing fiber region, owing to the more irregular trajectories of the crossing fiber axons as seen in Fig. 6F.

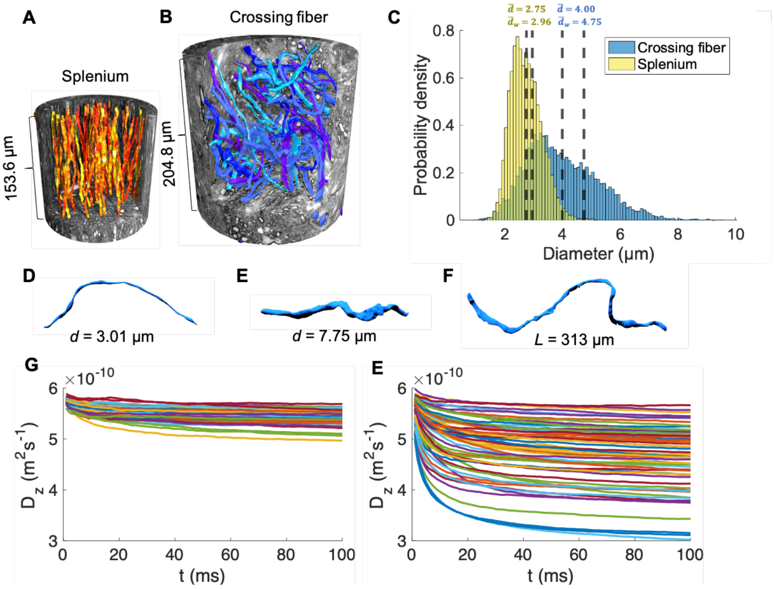

Fig. 6: Properties of realistic axons from different WM fiber architectures in the vervet monkey brain. 3D reconstructions of A) 54 splenium axons (segmented at 75 nm isotropic resolution) and B) 58 crossing fiber axons (segmented at 500 nm isotropic resolution) in their respective XNH volumes. C) Combined 3D AD distributions over all measured diameters in the splenium (yellow) and crossing fiber region (blue). The striped lines mark the means, $\overline{d}$, or weighted means $\overline{d_w}$, of the distributions. The D) thinnest, E) thickest and F) longest axons from the crossing fiber region demonstrate the significant variability of axonal morphology that can exist on the subvoxel scale. The segmented axons were aligned with the z-axis and G) and E) show the variation of the progator-based ADC in the z-direction, D_z, with diffusion time t_d (data points every 1 ms per axon).

For evaluation of the SMT and PL implementations in the realistic IAS and under different conditions, we simulated four acquisitions within the axons from the splenium and crossing fibre regions. To isolate the effects of the realistic axonal geometries on the estimated diameter, the SNR was set to ∞. The four acquisitions consisted of three shells sampled in 30 gradient directions each and used either a high or low gradient strength set, and either a short (t_d = 12.7

ms) or a long ($t_d = 37.7$ ms) diffusion time. The intrinsic diffusivity D_0 was set to an ex vivo diffusivity of $6 \cdot 10^{-9}$ m^{2}s^{-1}. SMT-2, SMT-3 and the PL were fitted to the PA signals to obtain estimates of d_{SMT-3}, $D_{||}$ from the SMT-3 fit, d_{SMT-2} and d_{PL}, as shown in Fig. 7.

At high b (Fig. 7A,C), d_{SMT-3} and d_{SMT-2} provided accurate approximations of both the individual AD and the volume-weighted mean AD of the splenium/crossing fiber axon populations at short and long diffusion times. d_{PL} provided accurate estimates of the diameters of the splenium axons, but underestimated those of the larger crossing fibre axons. For all methods, the only visible difference due to diffusion time was the underestimation of some of the smallest diameters at longer diffusion times. The $D_{||}$ estimates from the SMT-3 fit either defaulted to D_0 as some did in Fig. 7C, or were scattered over the range of possible $D_{||}$ values. As a result of the unexpected distribution of $D_{||}$ at high b, the fitted values of f_a were studied for three different diffusion times in Fig. S7. For all diffusion times, the f_a of the splenium axons were accurately estimated. The f_a values of the crossing fibre axons, on the other hand, were underestimated at large diameters and short diffusion times, but were mostly accurate at longer diffusion times.

Using lower b and short diffusion times, as in Fig. 1B, d_{SMT-3} slightly overestimated the diameters of all axons. There was a subtle positive correlation between d and $D_{||}$, the values of which were similar to or higher than D_z in Fig. 6G-H. d_{SMT-2} underestimated the diameters of the smaller splenium axons, but overestimated those from the crossing fibre region. The PL fit failed for all but one of the axons, which was greatly overestimated (Fig. 7B). Interestingly, at longer diffusion time, as in Fig. 7D, there was a further overestimation of d_{SMT-3} for the crossing fibre axons and a shift in $D_{||}$ towards lower values. In d_{SMT-2}, the under- and overestimation of the splenium and crossing fibre axons respectively were both enhanced. At this longer diffusion time, d_{PL} was non-zero for some of the larger crossing fibre axons, but was significantly underestimated. The effects of a finite SNR=100 on the AD estimates are shown for the short diffusion times in Fig. S6; they produces very similar results to Fig. 7A-B.

To evaluate the methods of AD estimation with in vivo diffusivities, the simulations were repeated for $G = [100, 200, 300]$ mT/m and different diffusion times, using an intrinsic diffusivity of $D_0 = 2 \cdot 10^{-9}$ m^{2}s^{-1}. The results are shown in Fig. 8. Strikingly, the volume-weighted mean diameter of the splenium axon population was only non-zero for one metric and under one condition: it was accurate for d_{SMT-3} at the shortest investigated diffusion time $t_d = 12.7$ ms in Fig. 8A. At longer diffusion times, d_{SMT-3} provided accurate estimates of a subset of the individual axons, but the mean of the population could not be fitted. The individual and population mean ADs of the splenium axons could not be

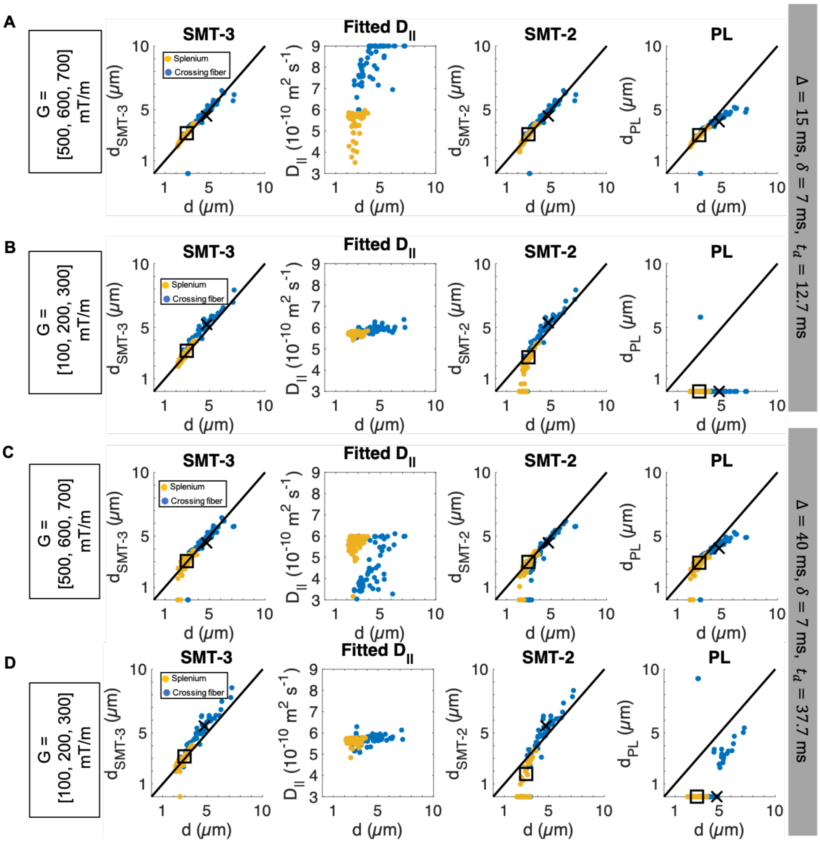

Fig. 7: In realistic axons, a fixed $D_\parallel$ can be assumed at high b and short t_d. The estimated parameters d_{SMT-3}, $D_\parallel$, d_{SMT-2} with assumed $D_\parallel = 0.6 \cdot 10^{-9}$ m^{2}s^{-1} and d_{PL} are plotted against the volume-weighted AD of the 54 axons in the splenium (yellow) and the crossing fiber region (blue). The parameters are calculated for different combinations of short ($\Delta = 15$ ms) and long ($\Delta = 40$ ms) gradient separations with high ($G = [500, 600, 700]$ mT/m) or low ($G = [100, 200, 300]$ mT/m) gradient strengths, as indicated. This gave three-shell acquisitions with A) $b = [11.11, 16.00, 21.77]$ ms/μm^2, B) $b = [0.549, 2.198, 4.945]$ ms/μm^2, C) $b = [33.03, 47, 56, 64.73]$ ms/μm^2 and D) $b = [0.795, 3.180, 7.155]$ ms/μm^2. The signals were generated with MC simulations using $D_0 = 0.6 \cdot 10^{-9}$m^{2}s^{-1} and were sampled in 30 gradient directions. For all acquisitions, $\delta = 7$ ms and SNR=∞ (barring the intrinsic noise associated with MC simulations). Square marker: volume-weighted AD of splenium axon population, cross marker: volume-weighted AD of crossing fiber population.

estimated using the SMT-2 or PL approaches for any parameter combinations. The ADs of the crossing fibre axons were generally somewhat overestimated by SMT-3 at all diffusion times. Contrary to the splenium axons, SMT-2 could fit the ADs of the largest crossing fibre axons, but failed for more axons the longer the diffusion time was. The PL implementation could fit only very few axons at short diffusion times (Fig. 8A), but its performance improved with increasing diffusion time (Fig. 8C). As for the simulations using the ex vivo diffusivities, the values of of $D_{||}$ decreased with increasing diffusion time.

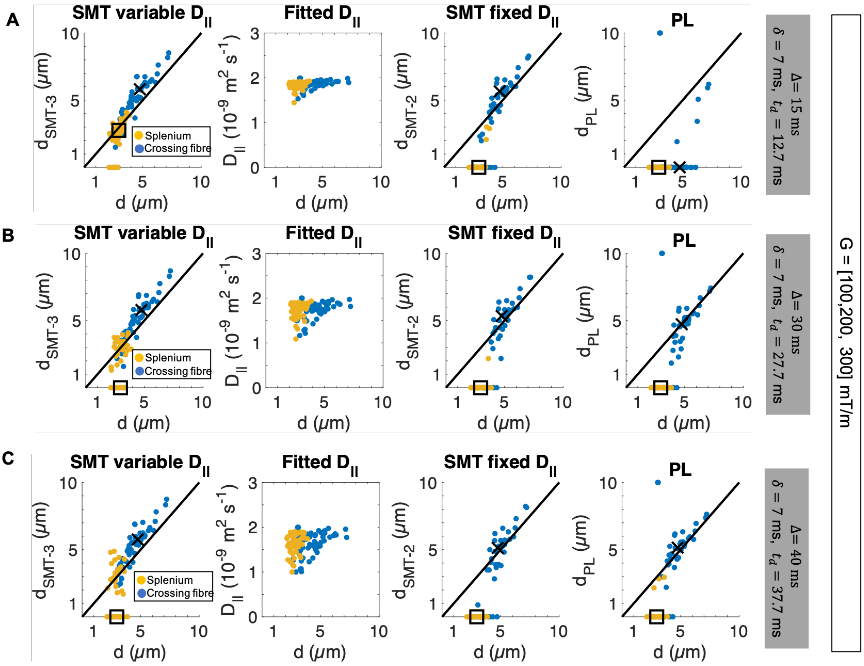

Fig. 8: Axon diameter estimation in realistic axons using in vivo intrinsic diffusivity $D_0 = 2 \cdot 10^{-9}$ m^{2}s^{-1}. The estimated parameters d_{SMT-3}, $D_{||}$, d_{SMT-2} and d_{PL} are plotted against the volume-weighted AD of the 54 axons in the splenium (yellow) and the crossing fibre region (blue). The parameters are calculated for acquisitions with A) $\Delta = 15$ ms and $b = [0.44, 1.78, 4.00]$ ms μm^{-2}, B) $\Delta = 30$ ms and $b = [0.97, 3.88, 8.73]$ ms μm^{-2}, and C) $\Delta = 40$ ms and $b = [1.32, 5.28, 11.89]$ ms μm^{-2}. Each acquisition consisted of three shells with 30 gradient directions, $G = [100, 200, 300]$ mT/m, $\delta = 7$ ms and SNR=∞. Square marker: volume-weighted AD of splenium axon population, cross marker: volume-weighted AD of crossing fiber population.

Discussion

By segmenting axons from a crossing fibre region of the vervet monkey, we demonstrate that axons significantly larger than those in the corpus callosum exist in other white matter regions. Despite the extremely complex morphologies of the axons, accurate measures of diameter could be obtained with powder averaging approaches, in axons from both the splenium and crossing fibre region. At low b-values, we fit the intra-axonal parallel diffusivities and show how the diameter estimates exhibit time dependence. The analysis of sequence parameters reveals that the accuracy of a powder average-based diameter estimation depends on the sensitivity of the acquisition to different length scales. Although, the lower and upper bounds depend on the gradient strength, as in Dyrby et al. [12], they also depend on the diffusion time and number of gradient directions. Ultimately, the SNR is a key limiting variable of measurable diameter, and we show the importance of removing Rician bias from the diffusion MRI signal.

The diffusion time and q influence the lower and upper bounds of measurable diameter

We find that PA-based estimates of AD are subject to lower and upper bounds that are determined by the angular sensitivity profile of the acquisition (Fig. 1C). The q-value and the diffusion time of the acquisition act as spatial filters, restricting the maximum detectable displacements of the spins. A higher q-value increases the sensitivity of the acquisition to smaller length scales in directions perpendicular to the cylinder. However, if the q-value is high enough to cause attenuation of the signal from an ensemble spin before it has diffused for the entire diffusion time, the acquisition loses sensitivity in the axial direction. For a given diffusion time and SNR, an increase in q often narrows the angular sensitivity profile. Although an increased gradient strength will move the lower bound to smaller diameters, in accordance with the findings of Dyrby et al. [12] and Sepehrband et al. [54], this will narrow the range of measurable diameters. This is true also for methods that estimate AD from measurements perpendicular to axons [8, 9, 11–14], but the increased attenuation of the PA due to its averaging across many directions and length scales demands a higher q-value or effective SNR to achieve the same lower bound.

Choosing the number of gradient directions

The number of uniformly distributed gradient directions is shown here to influence lower bound of measurable AD, with smaller diameters demanding measurements with higher angular resolution. This is in line with the findings of Li et al. [55] who show that at SNR$= \infty$, the number of directions determines how accurately the measured PA signal reflects the ground truth signal. The angular resolution thus places a lower bound on the measurable AD, separate to that incurred by the SNR and sequence parameters. Too low an angular resolution will shift the lower bound of measurable AD to higher diameters, regardless of SNR. For example, 10 directions are insufficient to resolve diameters smaller than 4 μm in Fig. 2, while 30 directions move the lower bound to ~ 1 μm. With Rician noise, increasing the angular resolution cannot decrease the SNR-incurred lower bound. For Gaussian noise, however, the higher number of sampling points given by the higher angular resolution may increase the effective SNR and provide access to smaller diameters. In practise, if an increased sampling is required, it is better to increase the number of directions, as opposed to performing many repeats of the same shell [56]. Both will have the same effect on the precision of the measurement, but acquisitions with a higher angular resolution hold the potential to resolve smaller diameters the real valued images with a Gaussian noise distribution are retrieved (Fig. 2 vs. Fig. 1). Furthermore, an increased angular resolution increases the robustness of the AD estimate to different underlying fibre configurations and OD, as seen in Fig. S2. This agrees with the findings of Lundell et al. [31] who showed more gradient directions lower the variance in parameter estimates from the PA signal. Our results also indicate that an increased angular resolution does not yield a significantly more robust estimate after a certain number of directions, similar to the findings of [57] where the rotational invariance of the fractional anisotropy measurement improved with increasing angular resolution, although little improvement was found beyond 20 directions at $b = 1$ ms μm^{-2}.

All simulations on cylinders in this investigation assume a single cylinder direction. In practise, this is not realistic even in the CC [17,18]. For methods that assume a single fibre direction [8,9,11,12], this is a limitation. For PA methods, it is the opposite and the single cylinder direction presents a worst case scenario. The less anisotropy there is on the voxel scale, the fewer directions are required to obtain rotational invariance of the PA [55,57]. If the voxel-scale anisotropy is so low that the sub-voxel structures can be approximated to be uniformly distributed as in Palombo et al. [58], few gradient directions are needed, saving scan time.

Is it necessary to fit the intra-axonal parallel diffusivity?

We show here that the need to fit $D_{||}$ depends on the b-value regime. At high b-values, the signals at low α (roughly parallel to the cylinder axis) are heavily attenuated and contribute little to the overall PA. The dependency of the estimated diameter on $D_{||}$ is therefore low and the assumption of erroneous $D_{||}$ and D_0 did not have a significant impact on the estimated diameter (Fig. 5A-B). At lower b, as in Fig. 5C-D, on the other hand, the contribution of the low α signals to the overall PA is more significant and the dependency on $D_{||}$ cannot not be ignored. Some AD estimation methods, such as ActiveAx [11] and the SMT implementation by Fan et al. [32] assume a value of $D_{||}$ based on previous literature. Other methods e.g. AxCaliber [8,9] and the PL implementation [33] (either directly or indirectly) fit it. For PA methods, this entails that estimates of $D_{||}$ reported in literature or calculated from the diffusion tensor images are likely to be sufficient at ex vivo intrinsic diffusivities at least for $b \geq 20$ ms μm^2, but potentially also for smaller $b-$values as in Fig. 7A where SMT-2 and SMT-3 both provided accurate estimates of AD.

The importance of the Signal-to-Noise Ratio and Noise Distribution

We show here how an increase in SNR increases the angular sensitivity range of the acquisition (Fig. 1). As such, increasing SNR decreases the lower bound and increases the upper bound (Fig. 2, Fig. S4, Fig. S6), provided that the angular resolution is sufficiently high. The increased sensitivity to smaller length scales is expected from the senstivity criteria presented in [39]. In combination with D_0 and diffusion time, the SNR also determines whether or not there is sensitivity to $D_{||}$, and hence if it needs to be fitted.

We found that Gaussian distributed noise prevented the systematic underestimation of diameter at high b-values (Fig. 3, Fig. S1) seen with Rician noise. This agrees with the findings of Fan et al. [32], in which it is also argued that the use of real-valued diffusion MRI data with Gaussian noise is more independent of the underlying fiber orientation distributions. Importantly, we show that Gaussian distributed noise results in a wider range of measurable diameters when fitting PA approaches to multi-shell data (Fig. 3 and provide more accurate estimates of intra-axonal volume fraction. The advantages of analysing signals with Gaussian noise are therefore similar to increasing the SNR of the measurement. In light of this, recovery of the the real-valued diffusion MRI data with Gaussian distributed noise by performing a phase correction [59] is likely an important step in improving both the range and accuracy of measurable ADs. However, in Fan et al. [32] and in this investigation, the variance of the estimated diameters using Gaussian distributed noise were higher than those obtained when using Rician distributed noise, especially for large diameters. This stems from the higher variance of the Gaussian distribution compared to the Rician distribution. Under time constrains where few measurement points (either in the form of gradient directions or repeats) are available, but SNR is high, it may be advantageous to analyse the magnitude data with Rician distributed noise.

Choice, but not number, of b-values affects measurable range of diameter

Fitting the SMT and PL implementations to the signal from different sets of b-values (all $b \gtrsim 20$ ms μm^2 to simulate suppression of the ECS signal [33]) showed that there may be little advantage to increasing the $q-$value (and thus the $b-$value) of an acquisition. This supports the trend in Fig. 1B, in which an increase in q-value after a certain point does little to lower the lower bound, but narrows the range of measurable diameter. Furthermore, the finding of no noticeable advantage of densely sampling many b-values lends support to the approach of ActiveAx [11], where the number of sampled b-values matches the number of parameters that are estimated. This suggests that it may not be necessary to perform a dense sampling of b-values as in the SMT implementation of Fan et al. [32], AxCaliber [9] and the PL implementation [33]. This was also recently suggested by Veraaart et al. [60]. Moreover, while the sensitivity criteria of Nilsson et al. [39] provided good indications of the range of measurable diameter for SMT-1 fits to a single $b-$value (Fig. 2, Fig. S1), no equivalent metric exists for a multi-shell fit, making simulations of the signal important in predicting the sensitivity of a multi-shell acquisition to diameter.

The parabolic shapes of estimated diameter resulting from multi-shell fits in Fig. 3 introduce a problematic degeneracy: two different diameters may estimated to be the same. As in Fan et al. [32], we observed a correlation between estimated diameter and IAS volume fraction at high diameters. This correlation mostly disappeared at infinite SNR, indicating that it may not be an issue at lower b-values, where the signal attenuation is not as large. We demonstrate here a similar trend for the PL, in which diameter and the parameter β are underestimated at large diameters. The underestimation remains at infinite SNR and may be a result of the assumption $b \cdot (D_{\parallel} - D_{\perp} \gg 1)$ (Eq. 3) does not holding for large diameters and strong diffusion encoding, q, where the measured $D_\perp$ approaches $D_\parallel$. When interpreting the fitted metrics – from either the SMT or the PL – it is integral to consider if they may be correlated. For example, estimates of large diameters are sometimes accompanied by an apparent, but erroneous, decrease in the volume fraction. Ideally, simulations should be performed to predict the diameter responses as in Fig. 3 to aid choice of implementation to use and interpretation of the metrics.

Microdispersion affects PA-based Axon Diameter Estimates in Segmented Axons from the Vervet Monkey Brain

The SMT and PL approaches were both able to recover the ADs from complex WM architectures given the correct conditions. At high b-values and ex vivo intrinsic diffusivities, we show that AD could be accurately estimated using the SMT implementation for axons from both WM architectures, regardless of diffusion time. The PL underestimated some of the larger crossing fibre axons. Unlike Lee et al. [20], we did not observe an overestimation of AD. The sensitivity to $D_\parallel$ was low at the high $b-$values, as evidenced by the similarity between the SMT-2 and SMT-3 fits. Due to the insensitivity of the signal in the parallel direction, the fitted values of $D_\parallel$ in Figs. 7A and C did not appear to be meaningful.

At lower b-values, the effects of axonal microdispersion manifested as a slight overestimation of the crossing fibre axon ADs that increased with increasing diffusion time. Fitting $D_\parallel$ was necessary to obtain accurate AD estimates for the smaller splenium axons. Despite the extremely tortuous trajectories of the crossing fibre axons, their fitted $D_\parallel$ were generally higher than those of the smaller splenium axons. It is possible that axons exhibit similar microdispersion somewhat independently of the fibre architecture, given that axonal trajectories are modulated by obstacles in the local environment [17]. If so, the correlation between $D_\parallel$ and diameter could be due to spins in smaller axons probing the curvature of the IAS to a greater extent. The reduction of $D_\parallel$ could be caused by microdispersion and diameter variations [17, 20, 61, 62]. In contrast to the PA estimates of $D_\parallel$, the diffusivities measured in the single main direction of each axon (D_z) were markedly lower in the crossing fibre region than in the splenium (Figs. 6G,E). This further corroborates the need for PA methods to remove macroscale fibre architecture and OD effects to obtain an accurate characterisation of the IAS. Lastly, we observed a decrease in $D_\parallel$ at longer diffusion times, agreeing with the time-dependence of D_z in Fig. 6. The nature of this time dependence could be indicative of the diameter variations and degree of microdispersion of the axons [17,61], and thus also an indication of the density of cells or other extra-axonal structures in the WM [17]. The time dependence of both $D_{||}$ and the diameter could potentially act as biomarkers of situations where the WM cell density is expected to change, such as in pathology or inflammation.

The simulations within the realistic IAS at in vivo diffusivities (Fig. 8) highlight the importance of performing sensitivity analyses and simulations to evaluate the different SMT and PL fits. Even with gradient strengths accessible to human diffusion MRI experiments only via Connectom scanners, the splenium ADs could be accurately estimated only: by the SMT, at the shortest diffusion time, and provided that $D_{||}$ was fitted. At increasing diffusion times, the volume-weighted mean AD of the splenium population could not be estimated. Additionally, the overestimation of the ADs of the crosssing fibre axons at all diffusion times could be explained by the high in vivo intrinsic diffusivity entailing that spins probe larger distances, and thus more microdispersion, than at ex vivo intrinsic diffusivities. The lack of time-dependence in the crossing fibre ADs could be due to the spatial filtering effect of the q-value.

Limitations

This investigation restricted the analysis of PA-based AD estimates to the IAS, for different sequence parameters and SNRs. At high b-values, the observation of a signal decay proportional to $b^{-0.5}$ at indicates that the signal mostly arises from thin, cylindrical structures [37, 38, 63], and that the ECS is suppressed. However, in the splenium XNH volume, we observed cell clusters and vacuoles that together constituted 6.1% of the total volume fraction [17]. Recent studies show that the cell somas could contribute to the PA signal at short diffusion times [64], complicating the SMT and PL fit to the PA signals. The presence of any restricted or hindered compartment from which the signal remains at high $b-$values will complicate the fits, unless it is explicitly modelled. These compartments could include e.g. irregularities in the axonal myelin or cellular processes. The observed dot compartment in ex vivo tissue [11,33] – completely restricted in all directions – will systematically bias PA-based AD measurements, although its contribution to the signal has been shown to be negligible in vivo [38, 52, 65].

Furthermore, use of the single-compartment PL implementation as in Veraart et al. [33] requires high b-values both for the suppression of the ECS and to fulfil the assumptions of the PL model. In Fan et al. [36] and Veraart et al. [33], the use of Connectom scanners for the in vivo applications enabled high gradient strengths, and thus high q and b-values. On regular clinical scanners with limited gradient strengths, high b-values could be achieved with longer diffusion times, but this would be at the cost of a reduced sensitivity to small diameters and a long echo time that would reduce the SNR of the acquisition.

At lower b-values, only the SMT implementation provides an adequate fit to the PA signals and the signal contributions from other compartments must be modelled, as in Fan et al. [32]. The the accuracy of the AD estimate thus depends not only on how accurately the geometry of other compartments are modelled, but also the compartmental T_2 relaxation times [66] and potential exchange rates. Assuming that the contribution from the IAS can be accurately separated from other compartments at low b-values, the reduced signal attenuation at low b entails that the AD estimation may be more robust. Furthermore, the sensitivity to microdispersion and $D_{||}$ at low b-values is higher, and the time-dependence of d_{SMT-3} and $D_{||}$ could provide valuable insight into axonal morphology [18, 20, 39, 61, 67, 68].

One key challenge to AD estimation with diffusion MRI is that real WM voxels contain a an ADD, and not single diameters. The contribution of each axon to the overall signal scales as a function of its radius $\sim R^4$ in Equation 5 and as R^2 due to the volume-weighting [11, 69]. The diffusion MRI-based estimates of diameter are thus heavily weighted by the tail of the ADD [33, 70] and the larger axons – like those presented in this study – significantly contribute to the signal. On the other hand, the insensitivity to smaller diameters complicates the interpretation of the estimated AD. In a complex substrate with many ADs, axons below the lower bound of measurable diameter still contribute to the total signal and will cause an underestimation of the average AD index, as seen for the splenium axons at in vivo diffusivities.

Lastly, we have not investigated whether the conversion of perpendicular diffusivity to a diameter estimate with the assumption of the Neuman limit in Eq. 5 (used in the PL implementation) differs to that of the full expression in Eq. 4 (which we use here in the SMT implementation), although the expressions are generally considered to be equivalent for typical ADs [33]. To obtain a diameter estimate, both expressions assume a value of the intrinsic diffusivity. One new study suggests that it is meaningful to interpret the perpendicular diffusivity independently [71]. While this is true, the diameter metric carries direct anatomical significance and can be used for neuroscience applications e.g. estimations of axonal conduction velocities.

Conclusion

We demonstrate that powder averaging techniques can succeed in providing accurate estimates of axon diameter, even in a complex crossing fibre region of the vervet monkey brain. To succeed, the acquisition must have broad sensitivity to different length scales. This is important partly due to the many different axon sizes present within a voxel, as presented here, but also because the powder average by definition probes different length scales in anisotropic micro-domains. Furthermore, we show how the gradient strength, diffusion time and number of gradient directions, as well as the SNR and noise distribution, influence the lower and upper bounds of measurable diameter. Finally, at low b-values we show that the acquisition becomes sensitive to axonal microdispersion, which could be an interesting biomarker of WM health and pathology. We foresee that this characterisation of the limits and potential of PA-based approaches to AD estimation will contribute to the development of new methods and models to study the WM microstructure with diffusion MRI.

References

[1] J B Hursh. CONDUCTION VELOCITY AND DIAMETER OF NERVE FIBERS. *American Journal of Physiology-Legacy Content*, 127(1):131–139, July 1939.

[2] F K Sanders and D Whitteridge. Conduction velocity and myelin thickness in regenerating nerve fibres. *J. Physiol.*, 105:152–174, September 1946.

[3] I Lorena Arancibia-Cárcamo, Marc C Ford, Lee Cossell, Kinji Ishida, Koujiro Tohyama, and David Attwell. Node of ranvier length as a potential regulator of myelinated axon conduction speed. *Elife*, 6, January 2017.

[4] Mark Drakesmith, Robbert Harms, Suryanarayana Umesh Rudrapatna, Greg D Parker, C John Evans, and Derek K Jones. Estimating axon conduction velocity in vivo from microstructural MRI. *Neuroimage*, 203:116186, December 2019.

[5] S Cluskey and D B Ramsden. Mechanisms of neurodegeneration in amyotrophic lateral sclerosis. *Mol. Pathol.*, 54(6):386–392, December 2001.

[6] G C DeLuca, G C Ebers, and M M Esiri. Axonal loss in multiple sclerosis: a pathological survey of the corticospinal and sensory tracts. *Brain*, 127(Pt 5):1009–1018, May 2004.

[7] Susie Y Huang, Qiuyun Fan, Natalya Machado, Ani Eloyan, John D Bireley, Andrew W Russo, Sean M Tobyne, Kevin R Patel, Kristina Brewer, Sarah F Rapaport, Aapo Nummenmaa, Thomas Witzel, Janet C Sherman, Lawrence L Wald, and Eric C Klawiter. Corpus callosum axon diameter relates to cognitive impairment in multiple sclerosis. *Ann Clin Transl Neurol*, 6(5):882–892, May 2019.

[8] Daniel Barazany, Peter J Basser, and Yaniv Assaf. In vivo measurement of axon diameter distribution in the corpus callosum of rat brain. *Brain*, 132(Pt 5):1210–1220, May 2009.

[9] Yaniv Assaf, Tamar Blumenfeld-Katzir, Yossi Yovel, and Peter J. Basser. Axcaliber: A method for measuring axon diameter distribution from diffusion MRI. *Magnetic Resonance in Medicine*, 59(6):1347–1354, jun 2008.

[10] Assaf Horowitz, Daniel Barazany, Ido Tavor, Moran Bernstein, Galit Yovel, and Yaniv Assaf. In vivo correlation between axon diameter and conduction velocity in the human brain. *Brain Structure and Function*, 220(3):1777–1788, 2015.

[11] Daniel C Alexander, Penny L Hubbard, Matt G Hall, Elizabeth A Moore, Maurice Ptito, Geoff J M Parker, and Tim B Dyrby. Orientationally invariant indices of axon diameter and density from diffusion MRI. *Neuroimage*, 52(4):1374–1389, October 2010.

[12] Tim B Dyrby, Lise V Sogaard, Matt G Hall, Maurice Ptito, and Daniel C Alexander. Contrast and stability of the axon diameter index from microstructure imaging with diffusion MRI. *Magn. Reson. Med.*, 70(3):711–721, September 2013.

[13] Hui Zhang, Tim B. Dyrby, and Daniel C. Alexander. Axon diameter mapping in crossing fibers with diffusion MRI. In *Lecture Notes in Computer Science (including subseries Lecture Notes in Artificial Intelligence and Lecture Notes in Bioinformatics)*, volume 6892 LNCS, pages 82–89, 2011.

[14] Hui Zhang, Penny L. Hubbard, Geoff J.M. Parker, and Daniel C. Alexander. Axon diameter mapping in the presence of orientation dispersion with diffusion MRI. *NeuroImage*, 56(3):1301–1315, 2011.

[15] A. S Lamantia and P. Rakic. Cytological and quantitative characteristics of four cerebral commissures in the rhesus monkey. *Journal of Comparative Neurology*, 291(4):520–537, 1990.

[16] Francisco Aboitiz, Arnold B. Scheibel, Robin S. Fisher, and Eran Zaidel. Fiber composition of the human corpus callosum. *Brain Research*, 598(1-2):143–153, 1992.

[17] Mariam Andersson, Hans Martin Kjer, Jonathan Rafael-Patino, Alexandra Pacureanu, Bente Pakkenberg, Jean-Philippe Thiran, Maurice Ptito, Martin Bech, Anders Bjorholm Dahl, Vedrana Andersen Dahl, and Tim B Dyrby. Axon morphology is modulated by the local environment and impacts the noninvasive investigation of its structure–function relationship, 2020.

[18] Hong-Hsi Lee, Katarina Yaros, Jelle Veraart, Jasmine L Pathan, Feng-Xia Liang, Sungheon G Kim, Dmitry S Novikov, and Els Fieremans. Along-axon diameter variation and axonal orientation dispersion revealed with 3D electron microscopy: implications for quantifying brain white matter microstructure with histology and diffusion MRI. *Brain Struct. Funct.*, 224(4):1469–1488, May 2019.

[19] Ali Abdollahzadeh, Ilya Belevich, Eija Jokitalo, Jussi Tohka, and Alejandra Sierra. Automated 3D Axonal Morphometry of White Matter. *Scientific Reports*, 9(1):239228, 2019.

[20] Hong-Hsi Lee, Sune N Jespersen, Els Fieremans, and Dmitry S Novikov. The impact of realistic axonal shape on axon diameter estimation using diffusion MRI. *Neuroimage*, 223:117228, December 2020.

[21] Itamar Ronen, Matthew Budde, Ece Ercan, Jacopo Annese, Aranee Techawiboonwong, and Andrew Webb. Microstructural organization of axons in the human corpus callosum quantified by diffusion-weighted magnetic resonance spectroscopy of N-acetylaspartate and post-mortem histology. *Brain structure & function*, 219(5):1773–1785, 2014.

[22] Sune Nørhøj Jespersen, Henrik Lundell, Casper Kaae Sønderby, and Tim B. Dyrby. Orientationally invariant metrics of apparent compartment eccentricity from double pulsed field gradient diffusion experiments. *NMR in Biomedicine*, 26(12):1647–1662, 2013.

[23] Enrico Kaden, Frithjof Kruggel, and Daniel C Alexander. Quantitative mapping of the per-axon diffusion coefficients in brain white matter. *Magn. Reson. Med.*, 75(4):1752–1763, April 2016.

[24] Enrico Kaden, Nathaniel D Kelm, Robert P Carson, Mark D Does, and Daniel C Alexander. Multi-compartment microscopic diffusion imaging. *Neuroimage*, 139:346–359, October 2016.

[25] Filip Szczepankiewicz, Samo Lasič, Danielle van Westen, Pia C. Sundgren, Elisabet Englund, Carl Fredrik Westin, Freddy Ståhlberg, Jimmy Lätt, Daniel Topgaard, and Markus Nilsson. Quantification of microscopic diffusion anisotropy disentangles effects of orientation dispersion from microstructure: Applications in healthy volunteers and in brain tumors. *NeuroImage*, 104:241–252, 2015.

[26] Samo Lasič, Filip Szczepankiewicz, Stefanie Eriksson, Markus Nilsson, and Daniel Topgaard. Microanisotropy imaging: Quantification of microscopic diffusion anisotropy and orientational order parameter by diffusion MRI with magic-angle spinning of the q-vector. *Frontiers in Physics*, 2(February):1–14, 2014.

---

[27] Kasper Winther Andersen, Samo Lasič, Henrik Lundell, Markus Nilsson, Daniel Topgaard, Finn Sellebjerg, Filip Szczepankiewicz, Hartwig Roman Siebner, Morten Blinkenberg, and Tim B Dyrby. Disentangling white-matter damage from physiological fibre orientation dispersion in multiple sclerosis. *Brain Communications*, 2(2), 2020.

[28] Stefanie Eriksson, Samo Lasic, and Daniel Topgaard. Isotropic diffusion weighting in PGSE NMR by magic-angle spinning of the q-vector. *Journal of Magnetic Resonance*, 226:13–18, 2013.

[29] Rafael Neto Henriques, Sune N. Jespersen, and Noam Shemesh. Microscopic anisotropy misestimation in spherical-mean single diffusion encoding MRI. *Magnetic Resonance in Medicine*, 81(5):3245–3261, 2019.

[30] Marco Pizzolato, Demian Wassermann, Rachid Deriche, Jean-Philippe Thiran, and Rutger Fick. Orientation-Dispersed apparent axon diameter via Multi-Stage spherical mean optimization. In *Computational Diffusion MRI*, pages 91–101. Springer International Publishing, 2019.

[31] Henrik Lundell, Carson Ingo, Tim B. Dyrby, and Itamar Ronen. Cytosolic diffusivity and microscopic anisotropy of N-acetyl aspartate in human white matter with diffusion-weighted MRS at 7 T. *NMR in Biomedicine*, (September 2019):1–14, 2020.

[32] Qiuyun Fan, Aapo Nummenmaa, Thomas Witzel, Ned Ohringer, Qiyuan Tian, Kawin Setsompop, Eric C Klawiter, Bruce R Rosen, Lawrence L Wald, and Susie Y Huang. Axon diameter index estimation independent of fiber orientation distribution using high-gradient diffusion MRI. *Neuroimage*, 222:117197, November 2020.

[33] Jelle Veraart, Daniel Nunes, Umesh Rudrapatna, Els Fieremans, Derek K Jones, Dmitry S Novikov, and Noam Shemesh. Nonivasive quantification of axon radii using diffusion MRI. *Elife*, 9, February 2020.

[34] Jennifer A. McNab, Brian L. Edlow, Thomas Witzel, Susie Y. Huang, Himanshu Bhat, Keith Heberlein, Thorsten Feiweier, Kecheng Liu, Boris Keil, Julien Cohen-Adad, M. Dylan Tisdall, Rebecca D. Folkerth, Hannah C. Kinney, and Lawrence L. Wald. The Human Connectome Project and beyond: Initial applications of 300mT/m gradients. *NeuroImage*, 80:234–245, 2013.

[35] K. Setsompop, R. Kimmlingen, E. Eberlein, T. Witzel, J. Cohen-Adad, J.A. McNab, B. Keil, M.D. Tisdall, P. Hoecht, P. Dietz, S.F. Cauley, V. Tountcheva, V. Matschl, V.H. Lenz, K. Heberlein, A. Potthast, H. Thein, J. Van Horn, A. Toga, F. Schmitt, D. Lehne, B.R. Rosen, V. Wedeen, and L.L. Wald. Pushing the limits of in vivo diffusion mri for the human connectome project. *NeuroImage*, 80:220 – 233, 2013. Mapping the Connectome.

[36] Qiuyun Fan, Thomas Witzel, Aapo Nummenmaa, Koene R.A. Van Dijk, John D. Van Horn, Michelle K. Drews, Leah H. Somerville, Margaret A. Sheridan, Rosario M. Santillana, Jenna Snyder, Trey Hedden, Emily E. Shaw, Marisa O. Hollinshead, Ville Renvall, Roberta Zanzonico, Boris Keil, Stephen Cauley, Jonathan R. Polimeni, Dylan Tisdall, Randy L. Buckner, Van J. Wedeen, Lawrence L. Wald, Arthur W. Toga, and Bruce R. Rosen. MGH-USC Human Connectome Project datasets with ultra-high b-value diffusion MRI. *NeuroImage*, 124:1108–1114, 2016.

[37] Emilie T. McKinnon, Jens H. Jensen, G. Russell Glenn, and Joseph A. Helpern. Dependence on b-value of the direction-averaged diffusion-weighted imaging signal in brain. *Magnetic Resonance Imaging*, 36:121–127, 2017.

[38] Jelle Veraart, Els Fieremans, and Dmitry S. Novikov. On the scaling behavior of water diffusion in human brain white matter. *NeuroImage*, 185(October 2018):379–387, 2019.

[39] Markus Nilsson, Samo Lasič, Ivana Drobnjak, Daniel Topgaard, and Carl-Fredrik Westin. Resolution limit of cylinder diameter estimation by diffusion MRI: The impact of gradient waveform and orientation dispersion. *NMR Biomed.*, 30(7), July 2017.

[40] Roberto Caminiti, Hassan Ghaziri, Ralf Galuske, Patrick R. Hof, and Giorgio M. Innocenti. Evolution amplified processing with temporally dispersed slow neuronal connectivity in primates. *Proceedings of the National Academy of Sciences*, 106(46):19551–19556, nov 2009.

[41] Christopher D Kroenke, Joseph J H Ackerman, and Dmitriy A Yablonskiy. On the nature of the NAA diffusion attenuated MR signal in the central nervous system. *Magn. Reson. Med.*, 52(5):1052–1059, November 2004.

[42] Dmitriy A Yablonskiy, Alexander L Sukstanskii, Jason C Leawoods, David S Gierada, G Larry Bretthorst, Stephen S Lefrak, Joel D Cooper, and Mark S Conradi. Quantitative in vivo assessment of lung microstructure at the alveolar level with hyperpolarized 3he diffusion MRI. *Proc. Natl. Acad. Sci. U. S. A.*, 99(5):3111–3116, March 2002.

[43] P van Gelderen, D DesPres, P C van Zijl, and C T Moonen. Evaluation of restricted diffusion in cylinders. phosphocreatine in rabbit leg muscle. *J. Magn. Reson. B*, 103(3):255–260, March 1994.

[44] C H Neuman. Spin echo of spins diffusing in a bounded medium. *J. Chem. Phys.*, 60(11):4508–4511, June 1974.

[45] Hong Hsi Lee, Els Fieremans, and Dmitry S. Novikov. What dominates the time dependence of diffusion transverse to axons: Intra- or extra-axonal water? *NeuroImage*, 182(July 2017):500–510, 2018.

[46] Jonathan Rafael-Patino, David Romascano, Alonso Ramirez-Manzanares, Erick Jorge Canales-Rodríguez, Gabriel Girard, and Jean-Philippe Thiran. Robust Monte-Carlo simulations in Diffusion-MRI: Effect of the substrate complexity and parameter choice on the reproducibility of results. *Front. Neuroinform.*, 14:8, 2020.

[47] Mads Bak and Niels Chr Nielsen. Repulsion, A Novel Approach to Efficient Powder Averaging in Solid-State NMR. *Journal of Magnetic Resonance*, 125(1):132–139, 1997.

[48] D. K. Jones, M. A. Horsfield, and A. Simmons. Optimal strategies for measuring diffusion in anisotropic systems by magnetic resonance imaging. *Magnetic Resonance in Medicine*, 42(3):515–525, 1999.

[49] HáKon Gudbjartsson and Samuel Patz. The rician distribution of noisy mri data. *Magnetic Resonance in Medicine*, 34(6):910–914, dec 1995.

[50] Jelle Veraart and Dmitry Novikov. Axon radius mapping, 2019. https://github.com/NYU-DiffusionMRI/AxonRadiusMapping.

[51] Emilie T. McKinnon, Joseph A. Helpern, and Jens H. Jensen. Modeling white matter microstructure with fiber ball imaging. *NeuroImage*, 176(April):11–21, 2018.

[52] Bibek Dhital, Marco Reisert, Elias Kellner, and Valerij G. Kiselev. Intra-axonal diffusivity in brain white matter. *NeuroImage*, 189(June 2018):543–550, 2019.

[53] Shu Wei Sun, Jeffrey J. Neil, and Sheng Kwei Song. Relative indices of water diffusion anisotropy are equivalent in live and formalin-fixed mouse brains. *Magnetic Resonance in Medicine*, 50(4):743–748, 2003.

[54] Farshid Sepehrband, Daniel C. Alexander, Nyoman D. Kurniawan, David C. Reutens, and Zhengyi Yang. Towards higher sensitivity and stability of axon diameter estimation with diffusion-weighted MRI. *NMR in Biomedicine*, 29(3):293–308, 2016.

[55] Hua Li, Ho Ming Chow, Diane C Chugani, and Harry T Chugani. Minimal number of gradient directions for robust measurement of spherical mean diffusion weighted signal. *Magn. Reson. Imaging*, 54:148–152, December 2018.

[56] Karen S. Ambrosen, Simon F. Eskildsen, Max Hinne, Kristine Krug, Henrik Lundell, Mikkel N. Schmidt, Marcel A.J. van Gerven, Morten Mørup, and Tim B. Dyrby. Validation of structural brain connectivity networks: The impact of scanning parameters. *NeuroImage*, 204(April 2019), 2020.

---

[57] Derek K Jones. The effect of gradient sampling schemes on measures derived from diffusion tensor MRI: a monte carlo study. *Magn. Reson. Med.*, 51(4):807–815, April 2004.

[58] Marco Palombo, Clemence Ligneul, and Julien Valette. Modeling diffusion of intracellular metabolites in the mouse brain up to very high diffusion-weighting: Diffusion in long fibers (almost) accounts for non-monoexponential attenuation. *Magn. Reson. Med.*, 77(1):343–350, January 2017.

[59] Marco Pizzolato, Guillaume Gilbert, Jean Philippe Thiran, Maxime Descoteaux, and Rachid Deriche. Adaptive phase correction of diffusion-weighted images. *NeuroImage*, 206(November 2018):116274, 2020.

[60] Jelle Veraart, Erika P. Raven, Luke J. Edwards, Nikolaus Weiskopf, and Derek K. Jones. The variability of mr axon radii estimates in the human white matter. *Human Brain Mapping*, 2021.

[61] Hong Hsi Lee, Antonios Papaioannou, Sung Lyoung Kim, Dmitry S. Novikov, and Els Fieremans. A time-dependent diffusion MRI signature of axon caliber variations and beading. *Communications Biology*, 3(1), 2020.

[62] Matthew D. Budde and Joseph A. Frank. Neurite beading is sufficient to decrease the apparent diffusion coefficient after ischemic stroke. *Proceedings of the National Academy of Sciences of the United States of America*, 107(32):14472–14477, 2010.

[63] Jens H. Jensen, G. Russell Glenn, and Joseph A. Helpern. Fiber ball imaging. *NeuroImage*, 124:824–833, 2016.

[64] Marco Palombo, Andrada Ianus, Michele Guerreri, Daniel Nunes, Daniel C. Alexander, Noam Shemesh, and Hui Zhang. SANDI: A compartment-based model for non-invasive apparent soma and neurite imaging by diffusion MRI. *NeuroImage*, 215(March), 2020.

[65] Chantal M.W. Tax, Filip Szczepankiewicz, Markus Nilsson, and Derek K. Jones. The dot-compartment revealed? Diffusion MRI with ultra-strong gradients and spherical tensor encoding in the living human brain. *NeuroImage*, 210(September 2019), 2020.

[66] Björn Lampinen, Filip Szczepankiewicz, Mikael Novén, Danielle van Westen, Oskar Hansson, Elisabet Englund, Johan Mårtensson, Carl Fredrik Westin, and Markus Nilsson. Searching for the neurite density with diffusion MRI: Challenges for biophysical modeling. *Human Brain Mapping*, 40(8):2529–2545, 2019.

[67] Jan Brabec, Samo Lasič, and Markus Nilsson. Time-dependent diffusion in undulating thin fibers: Impact on axon diameter estimation. *NMR in Biomedicine*, 33(3):1–19, 2020.

[68] Evren Özarslan, Cem Yolcu, Magnus Herberthson, Hans Knutsson, and Carl Fredrik Westin. Influence of the size and curvedness of neural projections on the orientationally averaged diffusion MR signal. *Frontiers in Physics*, 6(MAR):1–10, 2018.

[69] K. J. Packer and C. Rees. Pulsed NMR studies of restricted diffusion. I. Droplet size distributions in emulsions. *Journal of Colloid And Interface Science*, 40(2):206–218, 1972.

[70] Lauren M Burcaw, Els Fieremans, and Dmitry S Novikov. Mesoscopic structure of neuronal tracts from time-dependent diffusion. *Neuroimage*, 114:18–37, July 2015.

[71] Kevin D. Harkins, Christian Beaulieu, Junzhong Xu, John C. Gore, and Mark D. Does. A simple estimate of axon size with diffusion MRI. *NeuroImage*, 227(May 2020):117619, 2021.

Supplementary Materials

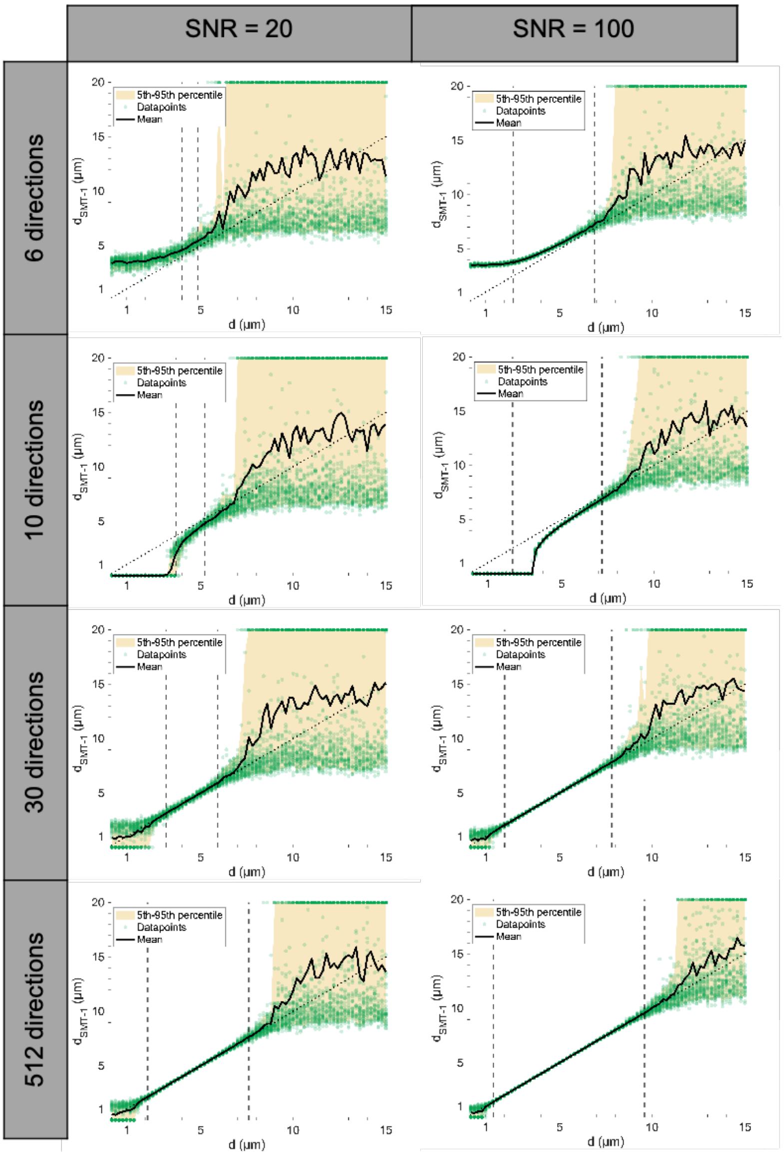

Fig S. 1: Influence of Gaussian noise and number of directions and on the single-shell SMT-estimated diameter, d_{SMT-1}, in cylinders of diameter between 0.2 and 15.0 μm. The single-shell SMT assumes known $f_a = 1, D_{\|} = 0.6 \cdot 10^{-9}\text{m}^2\text{s}^{-1}$. The last row shows the influence of SNR on d_{VG} as calculated using Eq 4. $n = 50$ repeats of the acquisition were performed for each diameter, SNR and number of directions. The black striped lines represent the predicted lower and upper bounds of measurable diameter.

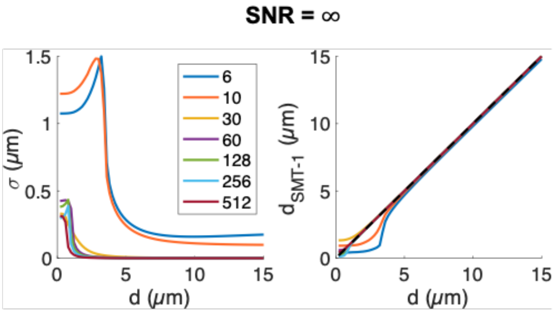

Fig S. 2: The PA is sensitive to fibre direction. The standard deviation of d_{SMT-1} of cylinders rotated around the y-axis in the interval $[0, 90]^\circ$ at 1° intervals, and the estimated mean diameter d_{SMT-1}, depend on the number of gradient directions. PGSE parameters $\delta = 7.1$ ms, $\Delta = 20$ ms and $G = 600$ mT/m were used.

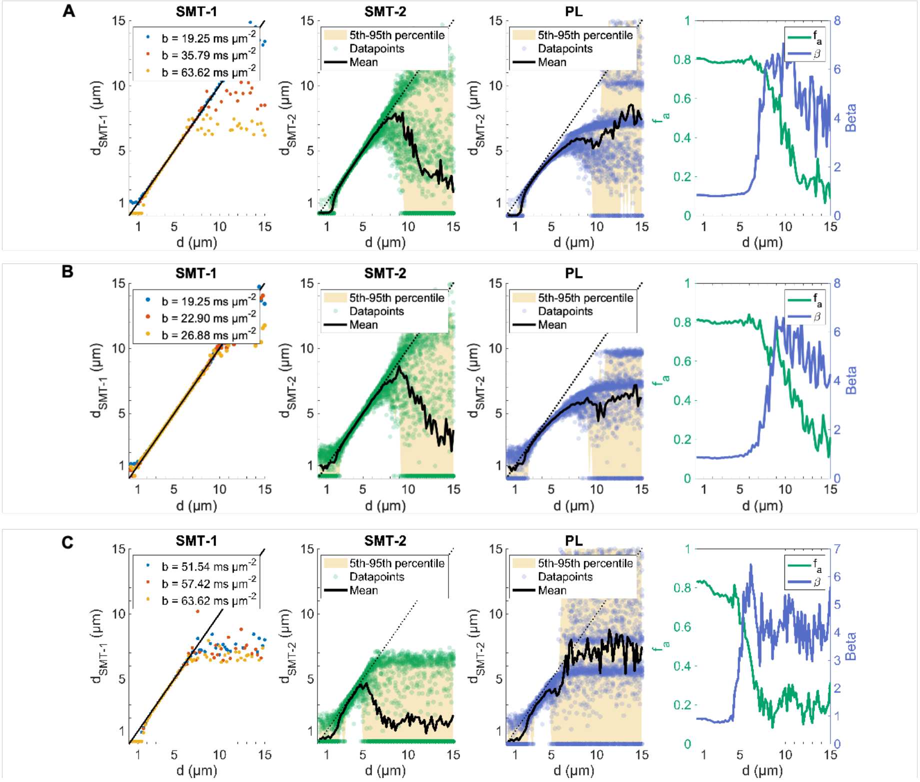

Fig S. 3: Multi-shell fits with different b-shell and Gaussian noise. Multi-shell fit of SMT and PL to the signal from cylinders of diameter between 0.2 and 15.0 μm at SNR = 100 (Gaussian noise) and $f_a = 0.8$. Fitted d_{SMT-1}, d_{SMT-2}, d_{PL}, f_a and β for ground truth A) 3 with $b = [19.25, 35.79, 63.62]$ B) three shells with $b = [19.25, 22.90, 26.88]$ ms/μm^2 and C)three shells with $b = [51.54, 57.42, 63.62]$ ms/μm^2. The signal is generated using $D_{\parallel} = 0.6 \cdot 10^{-9}\mathrm{m}^2\mathrm{s}^{-1}$, 30 directions, PGSE parameters $\delta = 7.1$ ms, $\Delta = 20$ ms and varying G. $n = 50$ repeats of each acquisition were performed for each diameter.

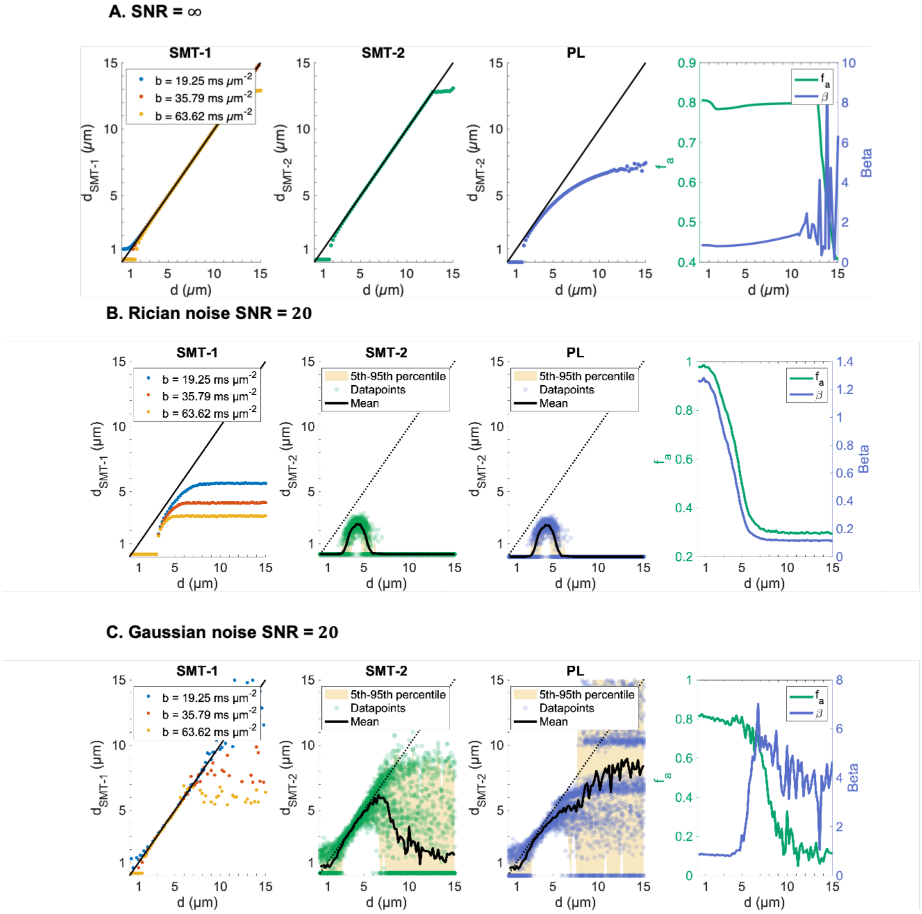

Fig S. 4: Multi-shell fit at A) SNR $= \infty$, B) SNR $= 20$ with Rician noise and C) SNR $= 20$ with Gaussian noise . Fitted d_{SMT-1}, d_{SMT-2}, d_{PL}, f_a and β for

$$b = [19.25, 35.79, 63.62]$$

ms/μm^2 in cylinders of varying diameter. The signal is generated using $D_{\parallel} = 0.6 \cdot 10^{-9}\text{m}^2\text{s}^{-1}$, 30 directions and PGSE parameters $\delta = 7.1$ ms, $\Delta = 20$ ms and $G = [550, 750, 1000]$ mT/m. $n = 50$ repeats of each acquisition were performed for each diameter.

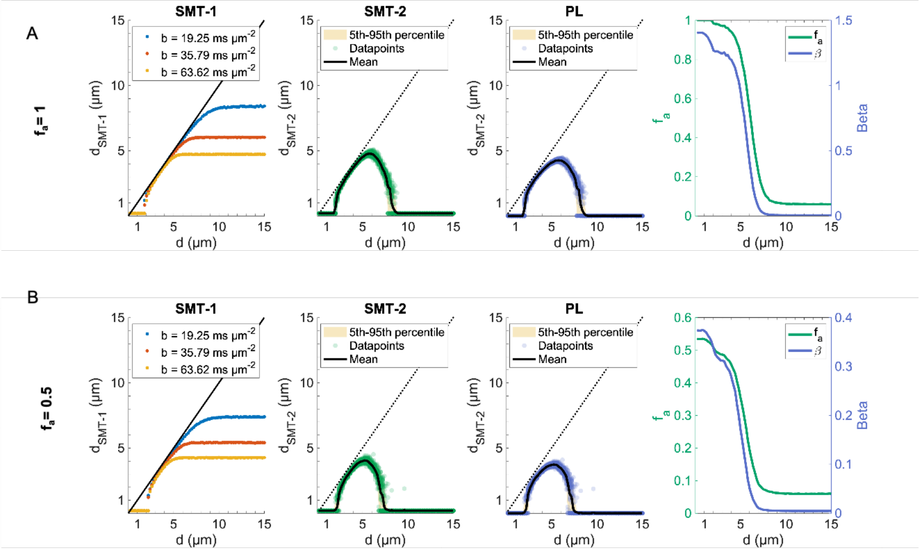

Fig S. 5: Multi-shell fit of SMT and PL to the signal from cylinders of diameter between 0.2 and 15.0 μm at SNR $=$ 100 (Rician noise) and different f_a. Fitted d_{SMT-1}, d_{SMT-2}, d_{PL}, f_a and β for ground truth A) $f_a = 1$ B) $f_a = 0.8$ and C) $f_a = 0.5$. The signal is generated using $D_{\|} = 0.6 \cdot 10^{-9}\text{m}^2\text{s}^{-1}$, 30 isotropically distribued directions and PGSE parameters $\delta = 7.1$ ms, $\Delta = 20$ ms , $G = [550, 600, 650]$ mT/m, $b = [19.25, 22.90, 26.88]$ ms/μm^2. $n = 50$ repeats of each acquisition were performed for each diameter.

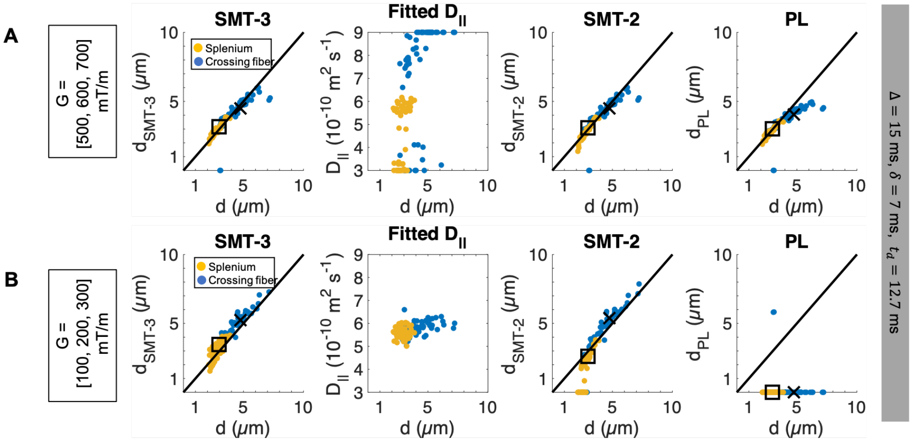

Fig S. 6: Axon diameter estimation in realistic axons at finite SNR=100 (Rician noise). The estimated parameters d_{SMT-3}, $D_{\|}$, d_{SMT-2} and d_{PL} are plotted against the volume-weighted AD of the 54 axons in the splenium (yellow) and the crossing fibre region (blue). The parameters are calculated for A) heavy diffusion weighting $b = [11.11, 16.00, 21.77]$ ms/μm^2 and B) weaker diffusion weighting $b = [0.549, 2.198, 4.945]$ ms/μm^2. For the heavy diffusion weighting, $G = [500, 600, 700]$ mT/m, and for the lower diffusion weighting, $G = [100, 200, 300]$ mT/m, as indicated. For all acquisitions, $\delta = 7$ ms, $\Delta = 15$ ms and SNR=100. An ex-vivo difusivity of $D_0 = 0.6 \cdot 10^{-9}$ m^{2}s^{-1} was used for the simulations. Square marker: volume-weighted AD of splenium axon population, cross marker: volume-weighted AD of crossing fiber population.

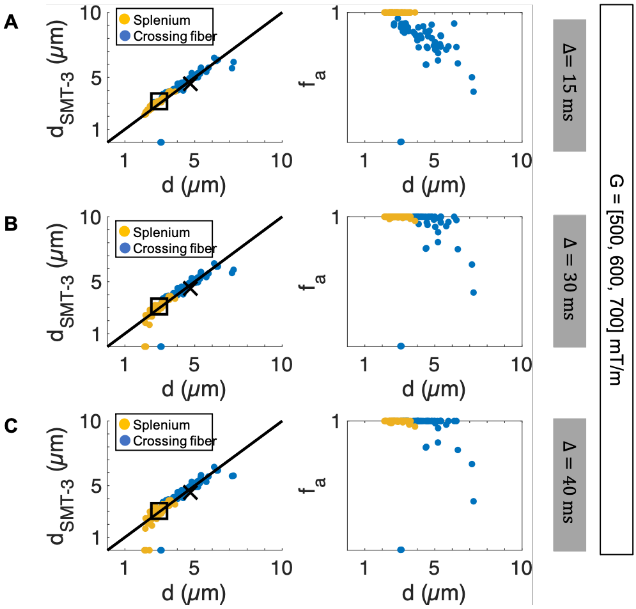

Fig S. 7: The time-dependence of f_a estimates from high b-value acquisitions. A) The estimated d_{SMT-3} and f_a plotted against the volume-weighted AD of the 54 axons in the splenium (yellow) and the crossing fiber region (blue) with A) $\Delta = 15$ ms, B) $\Delta = 30$ ms and C) $\Delta = 40$ ms. For all acquisitions, ground truth $f_a = 1$, $G = [500, 600, 700]$ mT/m and $\delta = 7$ ms. An ex-vivo difusivity of $D_0 = 0.6 \cdot 10^{-9}$ m^{2}s^{-1} was used for the simulations. Square marker: volume-weighted AD of splenium axon population, cross marker: volume-weighted AD of crossing fiber population.

Contribution III

0727

Streamline tractography for 3D mapping of axon bundle organization in one MRI voxel using ultra-high resolution synchrotron radiation imaging

Hans Martin Kjer[1,2], Mariam Andersson[1,2], Yi He[2], Marie Louise Elkjaer[3], Alexandra Pacureanu[4,5], Zsolt Illes[3], Bente Pakkenberg[6], Anders Bjorholm Dahl[1], Vedrana Andersen Dahl[1], and Tim B. Dyrby[1,2]
[1]DTU Compute, Technical University of Denmark, Kgs. Lyngby, Denmark, [2]Danish Research Centre for Magnetic Resonance, Hvidovre, Denmark, [3]Department of Neurology, Odense University Hospital, Odense, Denmark, [4]X-ray Nanoprobe Group, ID16A, The European Synchrotron, Grenoble, France, [5]University College London, London, United Kingdom, [6]Research Laboratory for Stereology and Neuroscience, Bispebjerg University Hospital, Copenhagen NV, Denmark

Synopsis

We present an efficient image analysis pipeline that enables us to reveal white matter organization in high-resolution 3D non-MRI structural datasets, in cases where a strict image segmentation is not required nor possible. We apply the method to a synchrotron X-ray holographic tomography scan from a healthy mouse sample, and show the organization of axon bundles in a region covering parts of the corpus callosum and the cingulum. The method has a potential to improve our general understanding of white matter organization and our ability to generate realistic phantoms for validation of microstructure modelling from low-resolution diffusion MRI scans.

Introduction

Diffusion-weighted MRI (DWI) allows us to probe and model the microstructure of white matter tissues from in-vivo scans. Validation of those models is an on-going and crucial challenge for the community. The key is to work on a ground truth structural data set. Phantom-based validation is typically the go-to option, but they are in themselves simplified models of the real anatomy! Eventually, we end up studying high-resolution volumetric datasets of microstructure. In this context, a high resolution corresponds to images with enough detail, so that individual axons and other microstructures can be resolved.

Making a thorough data analysis of these large volumes is required, but too time consuming and difficult to do manually. Semi- or fully automated segmentation approaches are being developed[1,2]. However, they are challenging to make generally applicable and work best at really high resolutions, where all structural boundaries are clearly defined. Another downside is that the high resolution typically is traded for a smaller field-of-view (FOV) and this obscures the ability to study the larger organization of tissues and the long-range behavior of white matter bundles etc.

Clearly, we need to deal with a class of white matter structural datasets, where axons are resolved almost as streamlines. Tracking and segmentation of an individual axon is in such a case almost impossible to achieve reliably. However, as we will show, it is possible to extract information about the organization in a relatively simple manner, by the use of structure tensor analysis and tractography as illustrated in Figure 1.

Methods

Data Acquisition: In this preliminary study, we demonstrate the method using a single healthy mouse sample. After perfusion fixation, the brain was sliced and a biopsy (approx. 2.5 x 0.7 x 0.7 mm) extracted from a region covering the splenium in Corpus Callosum (CC) and cingulum. The biopsy was stained with osmium (OsO_4, 0.5%), and embedded in EPON. Imaging of the sample took place at the European Synchrotron and Radiation Facility (ESRF) at beamline ID16A using X-ray holographic nano-tomography. The obtained volume used in this study, see Figure 2, covers an extended FOV of 0.24 x 0.24 x 0.24 mm in a voxel resolution of 75 nm.

Structure Tensor: The primary workhorse for the data analysis is the 3D structure tensor estimation[3], here using a local Matlab implementation. In short, the image gradients in all three axis directions are measured in a small neighborhood around each voxel and collected in a 3x3 matrix. Using an Eigen-decomposition, we extract information about the local orientation. In the case of a fiber-like material such as white matter, we can estimate a clear dominant direction aligned with the main fiber orientation, see Figure 3. The concept is very similar to DTI[4], but based on structural data content and not a diffusion MR signal.

Tractography: While the structure tensor provides an estimate of the orientation information in all voxels, it does not reveal how structures are connected. That we have to probe using deterministic tractography, here using the MRTrix implementation[5]. The inspiration comes from DWI-based connectivity data analysis, but the application to structural data is still novel. Based on a seed point, a particle trajectory through the volume is simulated using the local main orientation for direction until some stopping mask or criteria is met, see Figure 4.

Clustering: The output of the tractography is a large number of unorganized streamlines without a direct biological interpretation. It is then beneficial to apply a streamline clustering method, which collects multiple streamlines into meaningful axonal-bundles. We use the QuickBundles method[6] for its simplicity and scalability, and the result can be seen on Figure 1.

Results

Axon-bundles are clearly revealed both within the CC and cingulum. An immediate observation is that bundles trajectories are non-parallel and perform subtle bends and dispersions to move around cellular structures. An analysis on the cluster centroid trajectories, shows that bundles turn with angles up to 28.6 and 7.8 degrees in CC and cingulum respectively. Such information is valuable in the design of realistic white matter phantoms.

Discussion

While we demonstrate our method on a synchrotron X-ray tomography dataset, it is in principle no hindrance to apply it to other structural and volumetric modalities. The synchrotron is a good option, as it provides relatively large FOVs with enough resolution to generate the streamline characteristic in white matter that our method targets. It is further a non-destructive technique, allowing us to cover an even larger volume with overlapping FOVs. Extensions to our work includes exploring more white matter regions of the brain and comparing healthy vs. diseased samples. More advanced approaches of both tractography and clustering can be investigated, which might be beneficial in crossing fibers regions.

Conclusion

We have demonstrated an efficient image analysis pipeline based on structure tensor and tractography to investigate the 3D white matter organization. The method is ideally applied to high-resolution 3D structural datasets, in cases where a strict image segmentation is not required nor possible. It can serve to improve our general understanding of white matter organization and our ability to generate realistic phantoms for validation of microstructure modelling from low-resolution diffusion MRI scans.

Acknowledgements

M. Andersson and H.M. Kjer were supported by the Capital Region Research Foundation (grant number: A5657) (PI: T. Dyrby).

References

[1] Abdollahzadeh A, Belevich I, Jokitalo E, Tohka J, Sierra A. Automated 3D Axonal Morphometry of White Matter. Scientific reports. 2019;9(1):6084.

[2] Zaimi A, Wabartha M, Herman V, Antonsanti PL, Perone CS, Cohen-Adad J. AxonDeepSeg: Automatic Axon and Myelin Segmentation From Microscopy Data Using Convolutional Neural Networks. Scientific reports. 2018;8(1):3816.

[3] Khan AR, Cornea A, Leigland LA, Kohama SG, Jespersen SN, Kroenke CD. 3D Structure Tensor Analysis of Light Microscopy Data for Validating Diffusion MRI. NeuroImage. 2015;111:192-302.

[4] Mori S, Zhang J. Principles of Diffusion Tensor Imaging and Its Applications to Basic Neuroscience Research. Neuron. 2006;51(5):527-539

[5] Tournier JD, Smith RE, Raffelt D, Tabbara R, Dhollander T, Pietsch M, Christiaens D, Jeurissen B, Yeh CH, Connelly A. MRtrix3: A Fast, Flexible and Open Software Framework for Medical Image Processing and Visualisation. NeuroImage. 2019;202:116-37.

[6] Garyfallidis E, Brett M, Correia MM, Williams GB, Nimmo-Smith I. QuickBundles, a Method for Tractography Simplification. Front Neurosci. 2012;6:175.

Figures

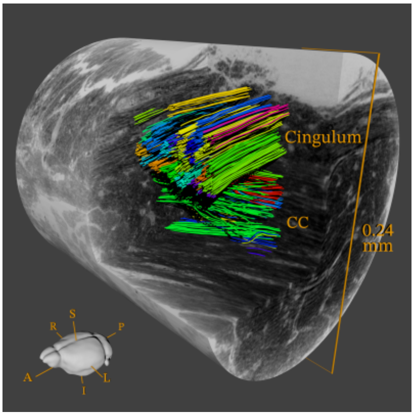

Figure 1: The concept of this study: Given a high resolution 3D structural dataset where axons are seen as steamlines. We present a method that can find realistic axon-bundles using structure tensor, tractography and clustering techniques.

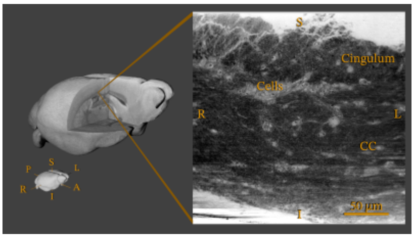

Figure 2: Location of sample biopsy position shown in a mouse brain MRI (MPRAGE), and a corresponding coronal slice from the synchrotron FOV (coronal slice). Fatty tissues (myelin and cell nuclei) appear dark due to osmium staining. The synchrotron FOV would correspond to approximately 3x3x3 voxels in the shown MRI dataset.

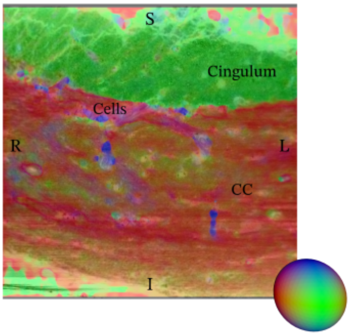

Figure 3: Structure tensor output overlaid on the corresponding image slice from Figure 2. Coloring is according to the local main direction, as shown on the spherical widget (bottom right), so that red corresponds to R-L direction, green is A-P direction and blue is I-S direction.

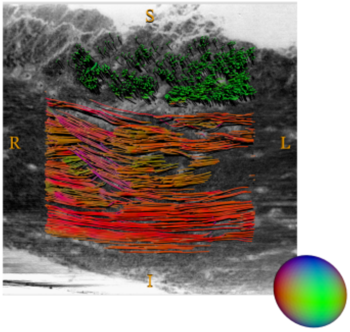

Figure 4: All tractography streamlines close to the corresponding image slice from Figure 2 and 3. Streamlines are colored according their local main direction, as shown on the spherical widget (bottom right).

Proc. Intl. Soc. Mag. Reson. Med. 28 (2020)
0727